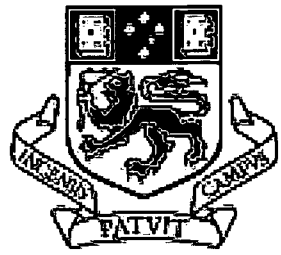

UNIVERSITY OF TASMANIA

SPARK IGNITION ENGINE PORT AIR MASS FLOW PREDICTION USING ARTIFICIAL NEURAL NETWORKS

Nicholas Richard Jones

BE (Hons) *Mech*

Submitted in fulfilment of the requirements for the degree of Masters of Engineering Science (MEngSc)

February 2003

DECLARATION & AUTHORITY OF ACCESS

This thesis contains no material that has been accepted for a degree or diploma by the University of Tasmania or any other institution, except by way of background information and has been duly acknowledged in the thesis, and to the best of the author's knowledge and belief no material has been previously published or written by another person except where due acknowledgment is made in the text of the thesis.

This thesis contains confidential information and is not to be disclosed or made available for loan or copy without the expressed permission of the University of Tasmania (i). Once released the thesis may be made available for loan and limited copying in accordance with the Copyright Act 1968.

Inquires should be directed to the Research and Development Office.

Signed:_____

Dated this seventeen day of February 2003

ACKNOWLEDGMENTS

Firstly, I would like to thank my supervisor Associate Professor Vishy Karri for his guidance, support and friendship throughout the completion of this project.

I thank the workshop staff for their patience, assistance and advice throughout the duration of this project. In particular, I would like to thank Peter Seward for manufacturing and constructing the various components of the inlet manifold. I would like to thank the electrical technical staff for their assistance also.

I would like to extend my gratitude to the members of the 2001 & 2002 University of Tasmania FSAE team. In particular David Butler, Garth Heron, Cranston Polson, Helen Cunnignham, Robert Neben, Bent Rosenkilde and Nick Dwyer deserve a special mention for their efforts in developing the 2001 car.

I owe a special debt of gratitude to Mr John White, Managing Director of Delta Hydraulics and Hot White Racing, who kindly donated the use of his excellent chassis dynamometer. I also wish to thank Mr David Griffards of Hot White Racing who provided assistance in using the chassis dynamometer and advice in the experimental data collection. I also wish to thank Cranston Polson and George Ivkovic for their help in the collection of the necessary experimental data.

I wish to thank Cathy Sugden for tolerating my "unusual filing practices" in our shared room. I also extend thanks to Tossapol Kiatcharoenpol for answering any questions I had relating to ANN's in general and the associated ANN analysing software. I also wish to thank Oliver Pechan for entertaining me with many interesting lunch time discussions.

Finally, I would like to thank my family, for their care, endless support and encouragement throughout the completion of this project.

ABSTRACT

In order to maintain the air fuel ratio within the stoichiometric operating window, which is necessary for efficient catalytic converter operation an accurate estimation of the mass airflow at the engine ports is critical. It is difficult to accurately represent the port air mass flow of an Internal Combustion Spark Ignition engine as reciprocating engines are complex non-linear systems based on a large number of interrelated parameters.

Conventional air fuel ratio control strategies use a number of three dimensional feedforward look up tables to represent these complex nonlinear engine functions. These look up tables are usually functions of only two engine variables, engine speed and engine load. Engine load is either, calculated from the speed density relationship using an absolute manifold air pressure sensor or measured directly using a mass air flow sensor. Conventional AFR control algorithms perform poorly during transient conditions as the strategies inherent in look up tables, are based on stationary or non-dynamic modelling techniques. Modern air fuel ratio control strategies employ a large number of correction factors to compensate for transient engine operation.

This research is a preliminary investigation into the feasibility of using Artificial Neural Networks to represent transient nonlinear engine functions. This research develops offline artificial neural network models of the port air mass flow of a Spark Ignition, based on Hendricks' et al [1] accepted mean value engine model description of the manifold filling phenomena. In particular two different Artificial Neural Network paradigms, namely the Backpropagation algorithm and the fast converging Optimise Layer by Layer algorithm will be trained on data collected through both steady state and transient chassis dynamometer testing.

Both steady state and transient air mass flow models will be developed in this investigation. The accuracy of the Backpropagation and Optimised Layer by Layer models will be analysed both qualitatively and quantitatively and compared in terms of the Root Mean Squared percentage error and computational time in an effort to evaluate the most appropriate model for future online engine implementation.

CONTENTS

INTRODUCTION

In the 1950's the products of the engine combustion process were formally identified as being a major source of urban air pollution. Consequently, governments around the world began to implement exhaust gas emission legislation in an attempt to reduce automobile generated air pollution. The advent of such legislation prompted automobile manufactures to improve the designs of engine intake manifolds and fuel mixture systems in order to comply with the new emission laws. Since the introduction of emission legislation four decades ago, there have been significant improvements in the techniques used to deliver fuel to Internal Combustion engines.

Successive amendments to the exhaust gas emission legislation have resulted in the continual need for automotive manufactures to improve fuelling technology. In the late 1970's and early 1980's emission legislation eventually reached a level where automotive manufactures where no longer able to simply improve existing technologies and this encouraged research and development into more reliable and accurate systems for controlling the air fuel ratio. This meant the carburettor, which for so long had been used by automotive manufactures for fuel-metering purposes could no longer be further improved to meet future emission requirements. This led to the development of new fuel metering techniques and additional hardware components to reduce harmful automotive emissions. The carburettor system was replaced firstly by mechanical and then electronic fuel injection systems and catalytic converters were developed to further reduce exhaust emissions. These advancements not only reduced exhaust gas emissions but also had the added benefit of improving engine power, enhancing drivability and decreasing engine fuel consumption.

Currently automobile emissions are regulated by using an electronic fuel injection system using both feedforward and feedback control coupled with a three-way catalytic converter. The typical feedback control arrangement uses a proportional integral term and the information regarding the state of the air fuel ratio is supplied by an exhaust gas oxygen sensor [2]. An electronic control unit controls the fuel injection timing, ignition timing and load control through exhaust gas recirculation for emission management purposes.

The critical device in this control arrangement is the catalytic converter as its emission conversion efficiency is highly sensitive to excursions in the air fuel ratio and is maximum only when a stoichiometric air fuel ratio is used. Even a 1 % deviation in the air fuel ratio can cause up to a 50 % reduction in the conversion efficiency of the catalytic converter in reducing pollutants [3] [4]. Consequently, in order to maintain maximum operating efficiency of the catalytic converter, precise control of the air fuel ratio is needed in all driving conditions. Current air fuel ratio control strategies are able to meet these requirements only during steady state driving conditions as fuelling is primarily based on feedforward look up tables which are developed from stationary experimental engine testing. Correction factors are introduced into the control algorithm in an attempt to compensate for transient driving conditions and currently this overall arrangement is sufficient to comply with today's transient emission test cycles.

In reality current air fuel ratio control algorithms are unable to avoid large excursions in the air fuel ratio during normal transient driving conditions. Research done by Rototest suggests that the accelerations during normal driving conditions are far more rapid and severe than the accelerations in the actual test cycles [5], [6]. Consequently real transient automotive emissions for some exhaust gases are approximately ten times higher than what is reported in the European test cycle [5], [6].

Many researchers have examined why AFR variations occur during transient driving conditions [7] [8], [9], [10]. The main reason for the existence of AFR deviations is due to the fact it is very difficult to accurately estimate the air flow at the actual engine cylinder ports especially during transient operating conditions [11]. It is also difficult to place the fuel in the intake manifold at the necessary location and at that instant [12]. This is because during transient conditions the fuel injected does not equal the fuel flow into the cylinders of the engine and the air mass flow either calculated or measured upstream of the throttle does not correspond to the actual air mass flow inducted into the engine.

Future exhaust gas emission legislation will further reduce the tolerated levels of exhaust gas pollution being emitted to the atmosphere. To illustrate this trend in 2003 the Californian government will require 10 % of all new vehicles to be zero emission vehicles while the remaining 90 % will have to reduce noxious emissions substantially [4], [13]. This trend is also a concern for Australia as Australian emission standards for vehicles are generally based

on obsolete European standards and U.S. emission legislation. Consequently, within the next few years accurate air fuel ratio control will be required during both steady state and transient driving conditions.

This can be achieved in one of three ways, by increasing the complexity of the existing hardware that is used in the control system, by developing and designing new algorithms for the control or a combination of both techniques. Up until now, automotive manufactures have focused on improving the hardware side of the control problem, such as producing sensors that are more sophisticated and implementing faster microprocessors for control purposes. Over the past ten years, there have not been significant improvements made to the actual algorithms used to control the fuel injection actuators. In order to comply with increasing exhaust gas emission legislation requirements automotive manufactures have simply incorporated additional look up tables to compensate for various dynamic effects. Such an approach is labour intensive and expensive as the engine mapping process is based on extensive engine dynamometer testing and associated complex engine tuning. The results of this approach has seen only marginal improvements in air fuel control, sufficient only to met new introduced emission legislation. Therefore there is a need for more sophisticated and adaptive control algorithms than what is currently used in automobiles, that will not only meet the requirements of future exhaust gas emission legislation, but will also have reduced developmental times [14].

This study has been conducted as part of the "Intelligent Car Research Project" at the University of Tasmania, which aims to investigate the feasibility of applying artificial intelligent tools for potential automotive control applications. Previous research from this project has primarily concerned the application of Artificial Neural Networks to chassis parameter prediction [15], [16], [17].

This study is a preliminary investigation into developing nonlinear engine models using artificial neural networks. Specifically a neural network port air mass flow engine model is developed based on Hendricks' et al [1] first order differential port air mass flow mathematical equation. The intention of this research is to determine the feasibility of using neural networks as potential alternatives to engine look up tables, firstly by developing stationary port air mass flow models and then developing transient port air mass flow engine models. Two different types of feedforward neural networks architectures are applied in this

research, namely the backpropagation algorithm and a fast converging optimised layer by layer algorithm. The research entails developing offline artificial neural network engine models using only chassis dynamometer collected data.

The inputs to the developed neural network models are based on those engine parameters identified by Hendricks' et al [1] to model the air mass flow inducted into an engine. The rate of change of throttle position is also included as a model input to provide representative information on the rate of change of manifold pressure and hence compensate for the manifold filling phenomena during transient testing conditions.

The performance of the individual ANN architectures in the estimation of the port air mass flow is compared both qualitatively and quantitatively. Histograms are used to compare the accuracy of the developed models and statistical techniques are used to determine if there is a significant difference between the mean errors of the developed models. For each model, a comprehensive investigation is carried out to determine the optimum model architecture. This involves manipulating the number of nodes of each model over a suitable range in an endeavour to find the optimum model, which has minimum Root Mean Squared (RMS) prediction error, while at the same time having an acceptable model computational time. An analysis is also undertaken to determine the number of training iterations that is required for the convergence of model error. The overall aim of this investigation is to identify the most appropriate model for future online learning and prediction purposes.

The following chapter of this thesis, Chapter Two, is a literature survey discussing the fundamental operating principals of Internal Combustion Spark Ignition engines. This chapter also describes the conventional techniques used for air fuel ratio and engine emission control purposes. Chapter Three, is a review of Hendricks' [1] Mean Value Engine Models (MVEM) and presents the potential advantages of applying Artificial Neural Networks to nonlinear engine modelling. This chapter also provides a review of recent research that has been published in the field of engine modelling using ANN and describes the features of the Backpropagation and Optimised Layer by Layer network algorithms. Chapter Four, explains the rationale behind this research, describes the selection of the model input parameters and proposes the practical implications of this research. Chapter Five, gives a description of the experimental test rig, which will be used in the collection of a reliable knowledge data base for neural network testing and training. Chapter Six is a qualitative and quantitative analysis

of the developed steady state and transient port mass air flow neural network models with the intention of determining the most appropriate model for future online training and prediction purposes. Chapter Seven provides the final concluding remarks of this research and provides recommendations into possible future work.

2 LITERATURE SURVEY

The first section of this chapter discusses the fundamentals of Internal Combustion spark Ignition engines. It introduces how and where Spark Ignition engines are used and the major components of a Spark Ignition engine. This chapter describes the operation of the four-stroke engine and briefly explains the combustion process. The concept of the air fuel ratio is presented highlighting its significance in reliable engine operation, and its importance in engine fuel consumption and power. The review also describes the conventional technologies, strategies and specialised components used to deliver the fuel to the engine, manage the exhaust gas emissions and maintain control of the air fuel ratio. The chapter concludes by providing an explanation as to why conventional engine control strategies are unable to avoid deviations in the air fuel ratio under particular driving conditions.

2.1 Introduction to Internal Combustion Engines

Combustion engines are designed to convert chemical energy contained within certain substances into mechanical energy, by igniting the substance in the presence of air by some means. The ignitable substance that contains the chemical energy is referred to as a fuel. Automotive combustion is achieved by mixing some air with a small amount of fuel in a enclosed space and igniting it to produce an "explosion" which releases an incredible amount of energy in the form of hot expanding gases [18]. The increase in energy from the hot expanding gases produces mechanical motion. At the completion of this energy conversion process the gases are discharged to the atmosphere.

The most outstanding application of Internal Combustion (IC) engines is for transportation – in automobiles, trucks and aeroplanes [19]. Small IC engines are used in many applications: in the home (eg. lawn mowers, chain saws), in portable power generation, as outboard motorboat engines and in motorbike engines [20]. Gas turbines can also be regarded as IC engines, however the name is usually applied to reciprocating internal combustion engines [21].

Reciprocating IC engines are typically used as the power generation facilities in cars, trucks, buses and some trains. Reciprocating combustion engines consist of a piston that moves up and down inside a special volume of space called the engine cylinder. The periodic linear movement of the piston inside the engine cylinder generates an enclosed region of space with a constantly changing volume. This region of space is called the combustion chamber and is where the air fuel mixture is ignited and combustion takes place.

Internal Combustion (IC) engines are engines in which the combustion chamber is located inside the actual boundaries of the engine. If the combustion chamber is foreign or lies outside the boundaries of the engine, the engine is referred to as an External Combustion (EC) engine. IC engines usually incorporate more than one combustion chamber in their design and these types of engines are commonly referred to as multicylinder engines.

Reciprocating IC Engines may be subdivided into different categories in a number of ways [22]. However the most general method of classification is according to their cycle of operation (method of air charging) or by their combustion mode (method of ignition). There are two cycles of operation, namely, the two-stroke cycle and the four-stroke cycle [23]. The cycle of operation refers to how many strokes are required for the completion of one power cycle.

There are two modes of combustion, namely, Spark Ignition (SI) and Compression Ignition (CI) [20]. SI engines use a device called a spark plug that generates an electric discharge in the combustion chamber in order to ignite the air fuel mixture. In a CI engine the rise in temperature and pressure during compression is sufficient to cause spontaneous ignition of the fuel [24].

SI and CI engines use fuels with different combustion characteristics. Petrol also referred to as gasoline is used in SI engine operation. Because of this SI engines are also commonly referred to as petrol engines, gasoline or gas engines. Petrol fuels are designed to resist combustion during piston compression (under conditions of increased pressure and temperature) and are intended to combust only in the presence of an electric spark. Diesel also known as fuel oil is used in the operation of CI engines. Diesel fuels are manufactured so that they spontaneously combust in the high pressure and temperature environments associated with piston compression.

Reciprocating Internal Combustion (IC) Spark Ignition (SI) four stroke cycle engines, are the focus of this research and will be discussed in more detail below, beginning with a description of the major components that make up an IC SI engine, special terms associated with their use and how IC SI engines work.

2.1.1 Major Components of the Reciprocating IC SI Engine

The reciprocating internal combustion engine is composed of one or more combustion chambers or cylinders inside which a single piston moves with reciprocating motion (upwards and downwards). Each cylinder is fitted with a spark plug and a minimum of two valves, the inlet valve and the exhaust valve. Each piston is independently attached to a shaft called a crankshaft by means of a connecting rod. The connecting rod facilities the transmission of the reciprocating motion of the piston into crankshaft rotary motion. Figure 2-1, below depicts the general configuration of a single engine cylinder showing its major components. Section 2.1.2 describes some special terms that are frequently used to describe reciprocating IC SI engines.

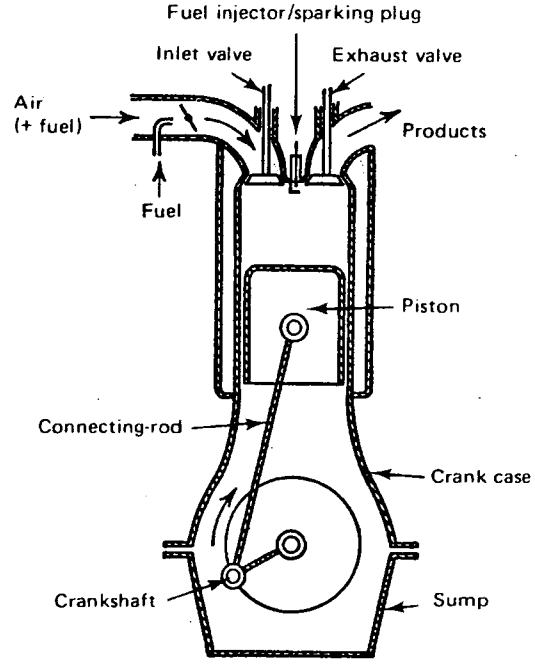

Figure 2-1 A four stroke IC SI engine, displaying important components [21]

2.1.2 Special Terms Associated with the Reciprocating IC SI Engine

The diameter of the combustion chamber or cylinder of a reciprocating IC SI engine is referred to as the bore. The term engine stroke is defined as the total distance the piston travels between Top Dead Centre (TDC) and Bottom Dead Centre (BDC). TDC refers to the piston position associated with minimum cylinder volume. This volume is called the clearance volume. BDC refers to the piston position associated with maximum cylinder volume. The compression ratio of an engine, usually denoted by r, is defined as the ratio of maximum cylinder volume (piston at BDC) to minimum cylinder volume (piston at TDC). The crankangle is measured from the vertical, in a clockwise direction to the point at which the connecting rod is fixed to the crankshaft. TDC is equivalent to 0 crankangle degrees and BTC is equivalent to 90 crankangle degrees. One revolution of the crankshaft equates to 360 crankangle degrees. These terms are labelled in Figure 2-2 below.

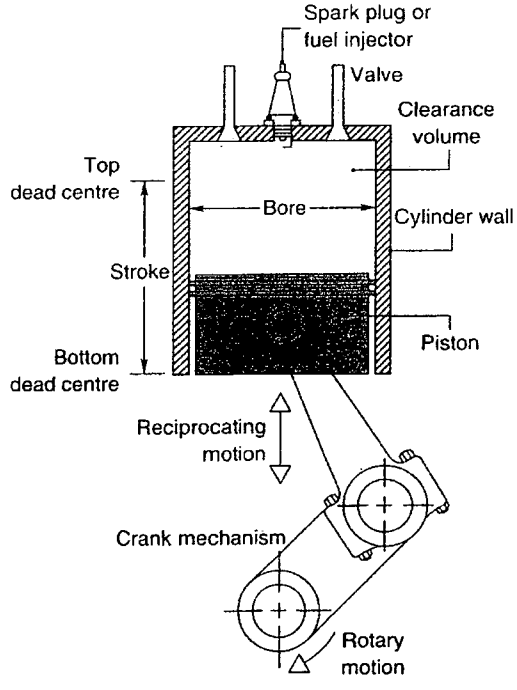

Figure 2-2 Nomenclature for reciprocating SI engine [18]

2.1.3 Operation of an IC SI Four Stroke Cycle Engine

SI engines convert chemical energy into mechanical energy by inducting a hydrocarbon fuel and air mixture into the combustion chamber of the engine and igniting the mixture by an electric discharge produced by a spark plug. The heat that is released from the combustion reaction causes a large increase in the pressure within the cylinder, forcing the piston to move downwards [25]. In a four-stroke cycle engine this process is achieved in four piston strokes.

The four-stroke engine cycle is also commonly referred to as the Otto Cycle after its inventor Nicolaus Otto. Each cylinder requires four strokes of its piston – two revolutions of the crankshaft or 720 crankangle degrees– to complete the sequence of events that produces one power stroke [17]. The four-stroke cycle comprises of an induction stroke, compression stroke, expansion or power stroke and an exhaust stroke. The execution of each stroke is described below with reference to engine combustion chamber volume and engine piston and valve movement.

The Induction Stroke

During this stroke the inlet valve is open and the piston travels down the cylinder to BDC resulting in an increase in the volume of the combustion chamber. The rapid downward motion of the piston creates a vacuum that draws (sucks) a pre-mixed air fuel mixture into the combustion chamber.

The Compression Stroke

Both the inlet and exhaust valves are closed during this stroke and the piston inside the cylinder travels upward to TDC. This piston movement reduces the volume of the combustion chamber. The rapid upward motion of the piston compresses the air fuel mixture, which increases the pressure and temperature of the air fuel mixture inside the combustion chamber. At a certain angle before TDC, the compressed air fuel mixture is ignited by an electric discharge from a spark plug.

The Expansion, Power or Working Stroke

The spark produced by the spark plug ignites the air fuel mixture contained within the cylinder and combustion commences. The combustion reaction between the air and fuel results in a rapid increase in the temperature and pressure inside the cylinder due to bonds being broken and new compounds being formed. The increase in temperature and pressure forces the piston downwards producing rotary motion of the crankshaft.

The Exhaust Stoke

After the combustion process has been completed the exhaust valve opens and the piston travels upwards forcing the combustion products (the exhaust gases) from the cylinder through the opening produced by the exhaust valve movement. The products of the combustion process are forced into the exhaust manifold at high speeds, which discharges them to the atmosphere.

Table 2-1 below summarises the four-stroke cycle with reference to the position of the intake and exhaust valve, the movement of the piston and the onset of combustion.

STROKE	INTAKE VALVE	EXHAUST VALVE	PISTON MOVEMENT	COMBUSTION
Induction	*Open*	*Closed*	*Downwards*	*None*
Compression	*Closed*	*Closed*	*Upwards*	*Ignition*
Power	*Closed*	*Closed*	*Downwards*	*Completed*
Exhaust	*Closed*	*Open*	*Upwards*	*None*

Table 2-1 A summary of valve movement, piston movement and combustion in a four cycle SI engine

Figure 2-3, below shows qualitatively the pressure-displacement variation of the combustion chamber, for the four-stroke engine cycle described above, with induction, compression, power and exhaust strokes depicted on the diagram.

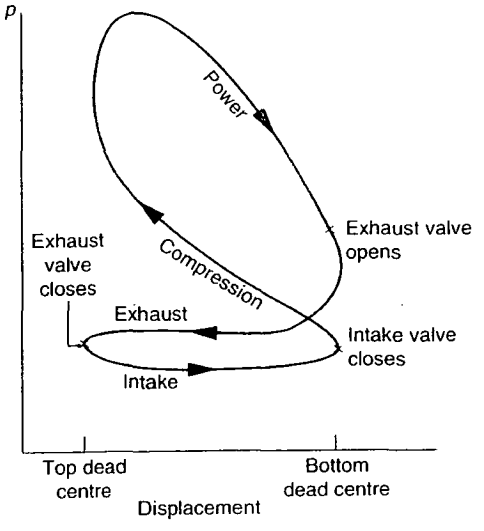

Figure 2-3 Pressure-displacement diagram for a reciprocating IC engine [18]

Section 2.1.4, below describes the advantages of multicylinder engines over single cylinder engines.

2.1.4 Advantages of Multicylinder Engines

The basic operating principals of an IC SI engine have been described assuming an engine comprised of a single cylinder (single combustion chamber) only. However, multicylinder engines are by far the most common configurations of IC SI engines used in automobiles and other transportation vehicles.

The main advantage of multicylinder engines compared with single cylinder engines is in terms of improved engine balance, smoothness in operation and the advantage of smaller engine cylinder volume required to produce the equivalent amount of power. This is mainly due to a higher power stroke frequency in multicylinder engines, resulting in smoother torque characteristics [17]. This is because multicylinder engines simultaneously have many cylinders executing the four-stroke cycle of operation, which produces more power, more power stokes per revolution of the crankshaft. The other major benefit is that the inertial forces present from the accelerating and decelerating motion of the piston between TDC and

BDC can be balanced by running the pistons one stroke out of phase with each another. Because of this reason even multiples (ie 2,4,6,8,10,12) engine cylinders are usually coupled together.

The most common engine configurations used by the automotive industry are the four, six and eight multicylinder engines. Four, six and eight cylinder engines produce two, three and four power strokes also referred to as torque pulses respectively per engine revolution. Multicylinder engine configurations can be arranged in a number of ways, including in-line, V or flat [15]. These configurations will not be discussed here. Section 2.1.5, below presents a basic overview of the combustion process in SI engines, describing normal and abnormal combustion and some of the critical parameters that effect combustion quality and hence torque generation.

2.1.5 Combustion Formation in Spark Ignition Engines

The combustion formation in spark ignition engines is complex and a complete and full understanding of all the processes involved is still unknown. Therefore, only a simplified description will be provided here.

Combustion in SI engines may occur in one of two ways, either normally or abnormally [21]. Normal or controlled combustion in SI engines is initiated by an electric discharge from a spark plug near the conclusion of the compression stroke. The electric discharge is a single high intensity spark of high temperature that passes from one electrode of the spark plug to the other. The effect of this spark is that it leaves behind a small flame, in much literature referred to as the flame nucleus [19], [21], [26] that propagates steadily throughout the entire air fuel mixture enclosed in the combustion chamber until the entire air fuel mixture has been consumed or burnt. The zone of active burning is known as the flame front which burns the end gas [27]. The end gas is the unburnt air fuel mixture that is ahead of the flame front.

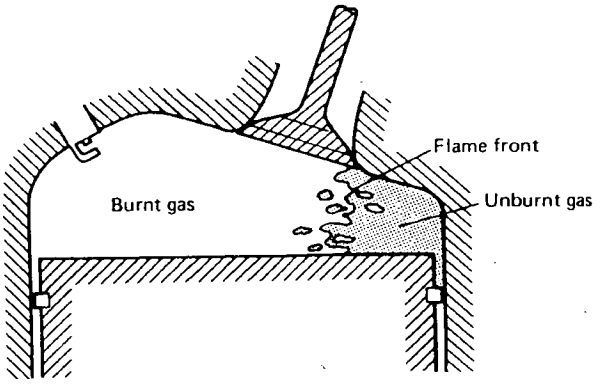

Figure 2-4 Combustion in a SI engine [21]

The normal combustion process is generally considered to develop in two distinct stages. The first stage (AB) corresponds to the time of formation of the self propagating nucleus of the flame and the second stage (BC) the propagation of the flame throughout the combustion chamber [19]. Figure 2-5 below qualitatively shows the pressure-crank angle variation before and after ignition, highlighting the combustion formation characteristics AB, BC described above.

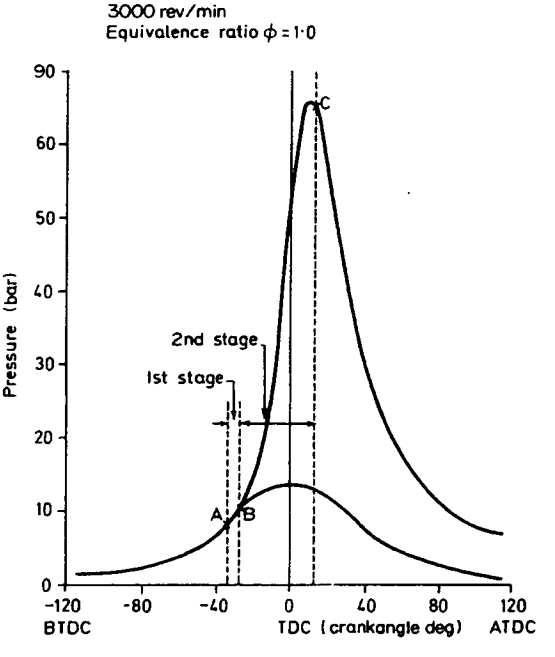

Figure 2-5 Indicator diagram showing two stages of combustion in a SI engine [19]

Point C in Figure 2-5 above represents peak cylinder pressure and the completion of the flame propagation phase of combustion. Turbulence that exists inside the combustion chamber due to the reciprocating motion of the piston has a significant effect on the rate at which the combustion reaction proceeds in both stages.

Abnormal combustion can occur in a number of different ways namely in the form of pre-ignition and self-ignition. Pre-ignition occurs when the air fuel mixture makes contact with a hot surface or body inside the engine cylinder and not initiated from the electrical discharge of the sparkplug. Common hot surfaces that have been known to prompt ignition are the exhaust valve(s) or products left over from previous combustion reactions usually in the form carbon deposits. Self-ignition also known as knocking occurs when the pressure and temperature inside the combustion chamber is sufficient to spontaneously ignite unburnt regions of the air fuel mixture, this can occur before or after the firing of the spark plug. Pre-ignition can lead to self-ignition and vice versa [21].

The firing time of spark plug is determined over a wide range of engine speeds and loads and is usually set at a crank angle just before the occurrence of Maximum Brake Torque (MBT) timing, the point at which mechanical power output from the engine is maximum. Figure 2-6 below shows that more advanced timing or retarded timing than the optimum value gives lower power output [17].

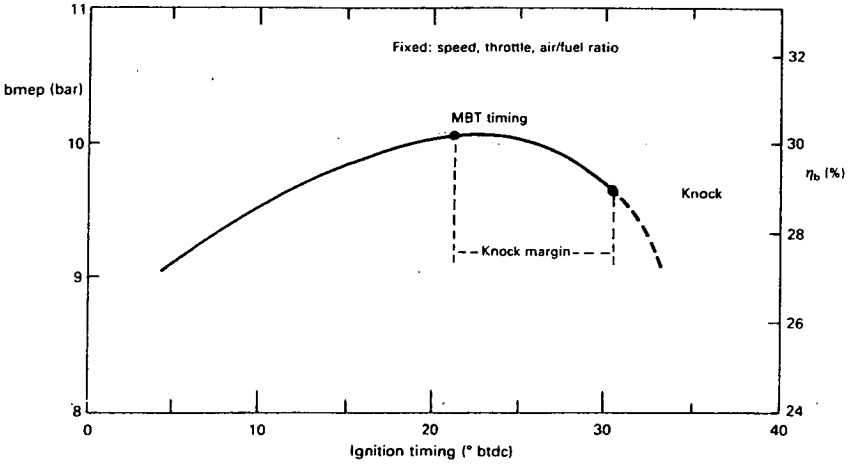

Figure 2-6 The effect of ignition timing on the output and efficiency of a spark ignition engine [21]

Engine ignition timing is advanced slightly from the MBT timing as a precautionary measure to allow for cycle to cycle variations, variation in manufacturing tolerances and engine aging. This is known as the knock margin and is shown in Figure 2-6 above. This practice prevents the likelihood of self-ignition or knock from occurring from engine to engine and during the engine wearing process. Ignition timing effects the pressure and temperature development inside the combustion chamber and is often varied to reduce the production of certain emissions, especially NO_x, which forms because of high combustion temperatures. If the ignition timing is too early then the work done by the piston in compressing the air fuel mixture is reduced, but so is the work done on the piston during the expansion stroke [17], [21]. If ignition timing is too late, it may not leave sufficient time for the completion of the combustion reaction before the exhaust valve opens. This will result in the exhaust valve becoming unnecessarily heated which is undesirable, as it may lead to pre-ignition of the air fuel mixture on the surface of the hot exhaust valve during future engine cycles. If ignition is too late there will be too much pressure rise before the end of the compression stroke and power will be reduced [21].

As engine speed increases, the spark ignition timing is advanced to provide sufficient time for the completion of the combustion reaction. That is at low speeds the ignition timing occurs at a crankangle relatively close to TDC, while ignition timing at high speeds occurs at a more advanced crankangle. Under normal driving conditions, the mixture is ignited around 15-30 degrees before the piston has reached TDC [28].

Ignition timing and the quality of the air fuel mixture influence many combustion characteristics. In order to highlight the effect the air fuel mixture has on the combustion process, it is necessary to look at the chemical reactions involved.

2.1.6 An Introduction to Combustion Chemistry

A description of the physical processes that occur inside the engine cylinder during combustion formation was provided above. Combustion will now be looked at from a chemical perspective. The combustion process is a chemical reaction in which chemical energy stored within the reactants is released in order to produce motion. In all chemical reactions bonds within the reactants are broken and atoms and electrons are rearranged to

form products [18]. Oxygen and ignitable compounds called fuels are the reactants in combustion reactions. The source of the oxygen is usually atmospheric air, consisting of approximately 21% oxygen and 79% nitrogen on a molar basis. Automotive fuels are often mixtures of hydrocarbons, with bonds between carbon atoms and between hydrogen and carbon atoms [21]. Gasoline or petrol, used in the operation of SI engines, are mixtures of paraffins, naphthenes and aromatics.

During the combustion process the hydrogen and carbon elements present in the fuel chemically combine with oxygen to produce compounds ideally consisting of only carbon dioxide water and nitrogen. This is shown below in Figure 2-7

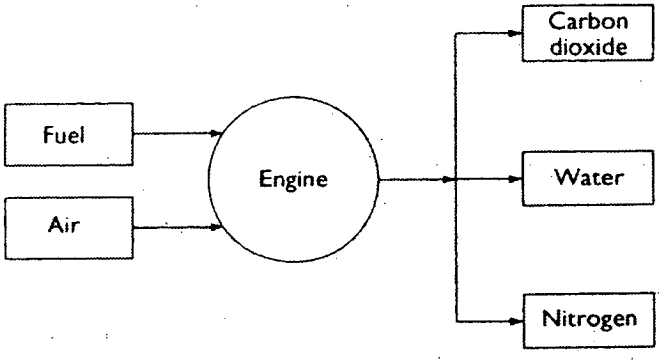

Figure 2-7 The theoretical combustion products for burning a hydrocarbon fuel [23]

During the formation of the new compounds, energy is released and this is apparent as a rise in temperature and pressure (expansion) of the products. Figure 2-8 below shows the conversion of chemical energy into mechanical energy. Due to this increase in temperature, combustion reactions are referred to as exothermic reactions, reactions that transfer heat to their surroundings.

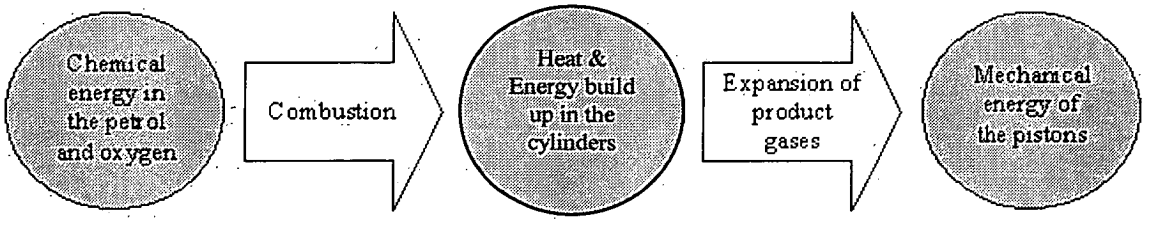

Figure 2-8 The conversion of chemical energy into mechanical energy

The relative portions and quality of the reactants used in SI combustion, determines the types and quantities of products formed and the quantity of energy released by the reaction. The Air Fuel Ratio parameter is a convenient way in expressing the relative proportions of the combustion reactants. This parameter will be defined below.

2.2 Air Fuel Ratio

2.2.1 Definition of Air Fuel Ratio

The Air Fuel Ratio (AFR) is defined as being the ratio of the air mass flow rate ($\dot{m}_a$) to the fuel mass flow rate ($\dot{m}_f$) inducted into the engine for combustion purposes. Mathematically this is expressed as:

$$\textbf{Air/Fuel Ratio (AFR)} = \left(\frac{\dot{m}_a}{\dot{m}_f}\right) \qquad \text{Equation 2-1}$$

2.2.2 Definition of the Stoichiometric Air Fuel Ratio

As mention above, IC engines generate power by relying on the energy that is released when a mixture of air and a hydrocarbon fuel is ignited undergoing an exothermic chemical reaction. The air fuel mixture before combustion and the burned products after combustion are the actual working fluids of the energy conversion process [17]. The work transfer that provides the desired power output occurs directly between these working fluids and the mechanical components of the engine [17].

The stoichiometric AFR, is defined as the chemically correct or the theoretical proportions of air and fuel that is required for the full conversion of all the fuel into completely oxidised products [17]. This means that there is an optimum amount of air that can mix with a specific hydrocarbon compound for the combustion reaction to completely burn all the carbon and

hydrogen, to produce reactants ideally consisting of only CO_2, H_2O, and N_2. The air fuel ratio can be determined from a balanced chemical equation for any hydrocarbon fuel that reacts with air.

The chemical equations shown below describe this combustion process for a SI engine between air (consisting of oxygen and nitrogen components, $O_2 + 3.773N_2$) and a generally represented hydrocarbon fuel (C_aH_b), assuming sufficient oxygen is available to completely oxidise the hydrocarbon fuel.

$$C_aH_b + \left(a + \frac{b}{4}\right)(O_2 + 3.773\,N_2) = aCO_2 + \frac{b}{2}H_2O + 3.773\left(a + \frac{b}{4}\right)N_2 + Energy$$

Equation 2-2

The stoichiometric AFR is therefore:

$$\left(\frac{A}{F}\right)_S = \frac{\left(1 + \frac{y}{4}\right)(O_2 + 3.772N_2)}{C + 1.008y}$$

Equation 2-3

where $y = \frac{b}{a}$

Substituting the molecular weights of carbon (12.011), hydrogen (1.008), oxygen (32) and nitrogen (28.16) into equation 2 above one obtains,

$$\left(\frac{A}{F}\right)_S = \frac{\left(1 + \frac{y}{4}\right)(32 + 3.772 \times 28.16)}{12.011 + 1.008y}$$

Equation 2-4

$$\left(\frac{A}{F}\right)_S = \frac{34.56(4 + y)}{12.011 + 1.008y}$$

Equation 2-5

Equation 2-5, above is the generic relationship for the stoichiometric AFR for any hydrocarbon (C_aH_b) fuel. The actual stoichiometric AFR depends on the type of the fuel

used, however for a SI engine (gasoline or petrol) it normally lies within the range of 14.4 to 14.7 [17]. The stoichiometric value also depends on the quality of the gasoline used [29]. The typical stoichiometric AFR value for gasoline is 14.6, however a value between 14.57-14.7 is common to characterise the stoichiometric AFR value for petrol [17]. In this study a value of 14.64 will be used to represent the stoichiometric AFR as this value was identified by Falck et al [3] to be the AFR at which maximum conversion efficiency of the catalytic converter occurs. The importance of the stoichiometric air fuel ratio on the efficiency of the catalytic converter is discussed in detail in Section 2.6.2.

2.2.3 Actual Air Fuel Ratio Relative to Stoichiometric Air Fuel Ratio

The importance of the air fuel ratio on the combustion reaction, in particular regarding the formation of fully oxidised products was described above. In the automotive industry a far more informative parameter for defining mixture composition is the air fuel ratio that has been normalised by the stoichiometric air fuel ratio for that particular fuel [17]. There are two generally accepted methods in describing an engines actual AFR relative to the ideal stoichiometric ratio. These are the Relative AFR also known as Lambda Ratio and the Fuel/Air Equivalence Ratio. These two parameters will be defined below.

The relative AFR or lambda ratio (λ) refers to the ratio between the actual AFR and stoichiometric AFR (AFR_S). Mathematically λ is expressed as:

Lambda Value $$\lambda = \frac{\left(\frac{\dot{m}_a}{\dot{m}_f}\right)_{actual}}{\left(\frac{\dot{m}_a}{\dot{m}_f}\right)_S} = \frac{(AFR)_{actual}}{14.64}$$ Equation 2-6

The fuel air equivalence ratio is alternative way of describing the reactant mixture composition relative to the air fuel ratio. The fuel/air equivalence ratio is symbolised by ϕ and is simply the inverse or reciprocal of the lambda ratio, λ^{-1}. Mathematically the fuel air equivalence ratio is expressed as:

$$\phi = \lambda^{-1} = \frac{(FAR)_{actual}}{(FAR)_S} = \frac{(FAR)_{actual}}{\left(\frac{1}{14.64}\right)} \quad \text{Equation 2-7}$$

The lambda ratio and equivalence ratio provide exactly the same information regarding the fuel mixture composition relative to the stoichiometric mixture and both will be used throughout this study. The significance of a using different lambda and equivalence ratio values on engine performance will be described below.

2.2.4 The Significance of Lambda and Air Fuel Equivalence Ratio Values

A λ ratio or ϕ ratio of unity corresponds to the actual air fuel ratio mixture inducted into the engine being equal to the ideal stoichiometric ratio. If the λ ratio exceeds unity (ϕ ratio less than unity) the mixture is referred to as being lean containing excess air in comparison to the stoichiometric value (the actual air fuel ratio is greater than the typical value of 14.64). On the other hand, if λ is less than unity (ϕ ratio greater than unity) then the actual AFR is said to be rich, which means the air fuel mixture composition is air deficient (the actual AFR that is less than 14.64). The air/fuel mixture has to be close to stoichiometric (chemically correct) for satisfactory spark ignition and flame propagation. [21]. The chemical compounds that are actually produced as a result of automotive combustion will be described below, with emphasis on those additional non oxidised compounds that are formed. Chemical and physical reasons for the formation of these additional compounds will be presented, highlighting those compounds that are regarded as pollutants.

2.2.5 Actual SI Combustion Formation and Products

The combustion process, so far, has been discussed from an ideal perspective based on elementary combustion chemistry ignoring many of the complexities actually involved. Combustion inside the engine cylinder is a result of a series of complicated and rapid chemical reactions and the products that are formed depend on many factors [18]. In practical engine operation it is impossible to control the combustion reaction to an extent to ensure that

all combustion products are fully oxidised. This leads to the exhaust gas composition always being a mixture of fully oxidised compounds and small traces of compounds that have not been completely oxidised usually referred to as being pollutants. There are chemical and physical explanations for this occurrence and these will be described below.

In Section 2.1.6 above, the theoretical products of the combustion were examined, namely carbon dioxide, water and nitrogen, assuming complete combustion. During actual combustion, the products differ from these theoretical results. Figure 2-9 below shows the actual products of combustion including carbon dioxide, water nitrogen, and not fully oxidised compounds consisting of carbon monoxide, nitric oxides, hydrocarbons and particulate matter.

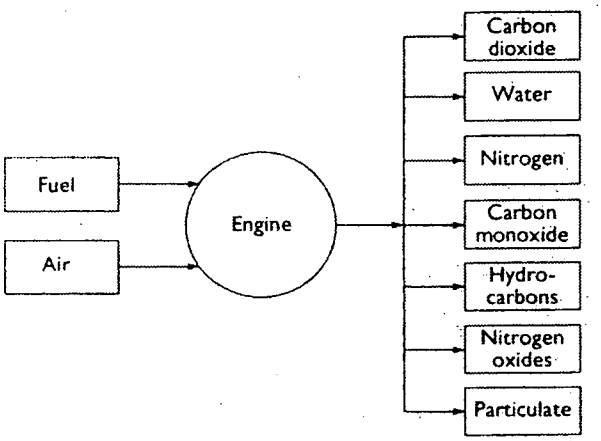

Figure 2-9 The actual products of hydrocarbon combustion [23]

The occurrence and reasons for the formation of these non-oxidised compounds will be briefly explained below.

In practical engine operation the rate of formation of products from the reactants is retarded by the rate of dissociation of the products back to the original reactants [19]. Energy is released when combustion takes place due to oxygen atoms combining with carbon and hydrogen atoms to form primarily carbon dioxide and water molecules. For a molecule to break into atoms, an equivalent amount of energy must be consumed [30]. Dissociation occurs when there is sufficient energy available to reverse the forward reaction ie break the covalent bonds of the carbon dioxide and water molecules and return the molecules into other

not fully oxidised compounds. Dissociation reactions normally occur after ignition when there is a sharp rise in temperature and pressure inside the combustion chamber. This temperature rise is sufficient to provide what is called the molar heat of dissociation or bond dissociation energy, which is required, for dissociation to proceed. The dissociation reactions for carbon dioxide, water and oxygen are provided below for completeness.

$$CO + 1/2O_2 \Leftrightarrow CO_2 + energy \qquad \text{Equation 2-8}$$

$$CO_2 + H_2 \Leftrightarrow CO + H_2O + energy \qquad \text{Equation 2-9}$$

$$O_2 \Leftrightarrow 2O + energy \qquad \text{Equation 2-10}$$

The sign $\Leftrightarrow$ used in the above equations illustrates that the chemical equations can be reversed if the required bond dissociation energy is available. At the onset of combustion the above dissociation reactions proceed until equilibrium is reached and the final reaction composition is a mixture of both the reactants and products of the above equations. Dissociation ceases when the energy available is less than the bond dissociation energy. This usually occurs during the expansion stroke when the temperature of the combustion products decreases. Equilibrium thermodynamics is used to determine the degree of dissociation. The dissociation process is in equilibrium when the Gibbs function is minimum. The existence of dissociation during combustion, means that engine operation even with a stoichiometric AFR ie λ = 1, still results in combustion products containing small traces of non oxidised products. Dissociation of carbon dioxide means that carbon monoxide will be present, even for the combustion of weak mixtures [21].

Nitric oxides are generated, not as a result of the actual chemical combustion reaction, but as a result of the environment that is created by the combustion reaction [17]. Nitric oxides, generally represented by NO_x, form after the onset of combustion in the high temperature regions in the combustion chamber left behind by the flame front. The formation of nitric oxides is due to the Zeldovich mechanism, a series of complex chemical reactions involving oxygen and nitrogen. The formation rate of nitric oxides is dependent upon both flame temperature and flame speed. High temperatures and low flame speeds result in maximum nitric oxide formation. There are a number of methods used to reduce nitric oxide formation

in SI engines. One popular method is to employ Exhaust Gas Recirculation (EGR). This involves mixing a fraction of the exhaust gases with the future inducted air fuel mixture. This reduces the peak temperature inside the combustion chamber thus reducing the quantity of nitric oxides produced.

Hydrocarbons are a product of combustion due to some of the fuel not being completely burnt during the process. This may be due to some of the air fuel mixture entering crevices inside the combustion chamber such as the small gaps that exists between the surface of the moving piston and the surface of the engine cylinder. The combustion flame often fails to ignite the fuel entrapped in these small spaces. The unburnt fuel is then emitted to the atmosphere during the exhaust stroke. Another source is at the combustion chamber walls [17]. A quench layer containing unburnt and partially burned air fuel mixture is left at the wall when the flame is extinguished as it approaches the wall [17]. Engine oil deposited in a thin layer on the cylinder wall is also believed to absorb some hydrocarbon matter during combustion, which also avoids being burnt. Particulate matter has been reduced significantly since the introduction of non-leaded fuel and is more a problem with the operation of compression ignition engines.

Due to the random nature of the combustion process, the pressure developed inside the combustion chamber after ignition varies from one cycle to the next. An explanation for this phenomenon is presented below.

2.2.6 Cycle by Cycle Variations in Combustion

It has been assumed so far that a uniform air fuel mixture is ignited in the engine cylinder from cycle to cycle. During practical engine operation a homogeneous air fuel mixture rarely occurs even though engine components are designed to thoroughly mix the air fuel mixture. This phenomenon can easily be verified by examining the pressure variations inside the cylinder over a number of different engine cycles, shown in Figure 2-10 below.

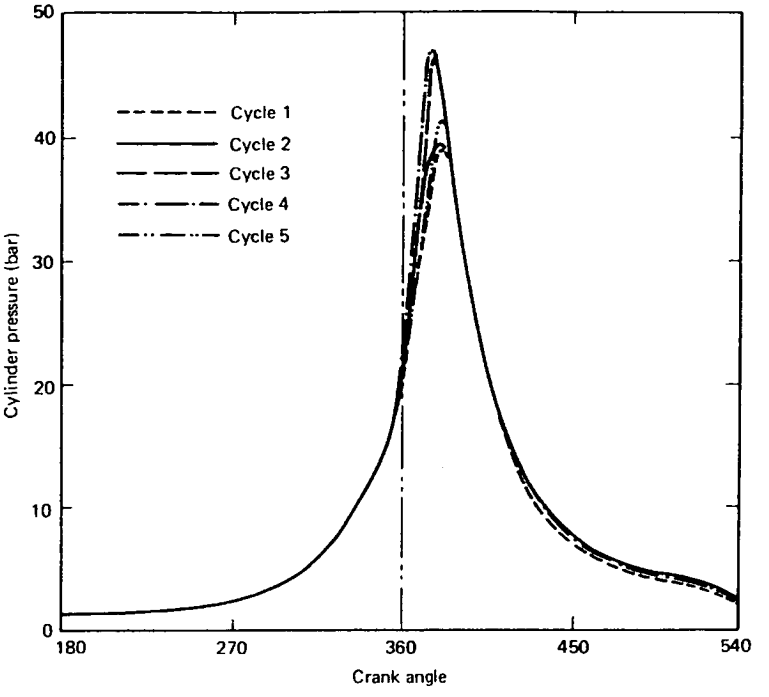

Figure 2-10 Cylinder pressure diagrams for successive cycles, illustrating the variations in peak pressure [21]

The variations in peak pressure, shown above, are called cycle by cycle variations or cyclic dispersion. Such variations exist due to turbulence within the cylinder varying from cycle to cycle, the air fuel mixture not being homogenous and the exhaust gas recirculation not completely mixing with the air fuel mixture charge [21]. Turbulence inside the engine combustion chamber occurs in a random way, which results in different local air fuel mixtures existing at the location of the spark plug from cycle to cycle. These mixture variations significantly effect the flame nucleus formation stage of combustion resulting in different rates of flame propagation throughout the mixture for successive cycles. In multicylinder operation the mixture distribution flow rates to each cylinder is also not uniform resulting in what is known as cylinder to cylinder variations.

The next section reviews how the AFR effects engine performance described in terms of engine power, fuel economy, engine efficiency and the composition of the exhaust gas emissions.

2.3 SI Engine Performance

2.3.1 Factors that Effect SI Engine Performance

Three major engine-operating variables are recognised in literature to govern the performance of an IC SI engine. These are, spark timing, the proportion of recycled exhaust gases that constitute the total amount of the inducted combustion mixture for the control of NO_x emissions and in particular the lambda ratio or fuel equivalence ratio [17]. The importance of spark timing on combustion formation was briefly covered in Section 2.1.5, and exhaust gas recirculation was discussed above in Section 2.2.5. The effect of the air fuel ratio on engine performance is the focus of the remaining part of this survey. Engine performance comparisons are usually gauged by comparing engine-operating characteristic over a wide range of engine loads and speeds. The engine operating parameters that are generally investigated include different definitions of engine efficiency, engine torque or power, fuel consumption and exhaust gas emission composition. The effect of the lambda ratio on engine power, fuel efficiency and exhaust gas composition will be discussed in some detail below.

2.3.2 The Effect of the Air Fuel Ratio on Engine Performance

It has long been realised that the basic performance of any reciprocating engine is a function of the air and fuel that flow through it. It has been shown that the air fuel mixture governs engine power output, fuel conversion efficiency, fuel consumption, and the type and quantity of exhaust gases emissions.

As mentioned in Section 2.2.4 above the air fuel ratio should be maintained as close as possible to the stoichiometric value in order to guarantee consistent engine combustion and therefore performance. However the combustion reaction, is able to proceed over a wide range of AFR's above or below the stoichiometric value. Different AFR values are used in engine operation depending on the desired engine performance criteria that is to be optimised. Choosing different values of the AFR greatly effects the combustion reaction resulting in changes in the amount of energy that is released and the types of emissions produced. Generally there are three engine-operating characteristics that are optimised, either on an

individual basis or collectively depending on the application and use of the engine and limitations imposed by various governmental authorities. These parameters are the engine power output, engine fuel consumption and the permitted level of engine emissions.

2.3.3 Engine Power, Fuel Consumption and Efficiency

Maximum power in SI engine operation occurs when the air fuel mixture inducted into the cylinders is slightly rich of stoichiometric. Peak power and maximum exhaust gas temperatures usually occurs at a λ value of approximately 0.90 ($\phi \cong 1.1$). Peak power occurs at this point due to the chemical process known as dissociation described above in Section 2.2.5. The increase in temperature because of combustion causes dissociation to occur, resulting in the presence of molecular oxygen in the combustion reactants. The available oxygen present, from dissociation, allows a small amount of additional fuel to be added to the air fuel mixture. This additional fuel undergoes combustion with the available oxygen producing a greater temperature and pressure rise inside the cylinder resulting in increased power. Engines operating with λ values on either side of $\lambda \cong 0.9$ ($\phi \cong 1.1$) output less power, this is shown below in Figure 2-11. Mixtures slightly rich of the stoichiometric mixture produce peak power, however fuel consumption increases also.

SI engines operating with air fuel mixtures just lean of stoichiometric have lower fuel consumption, produce less engine power and have lower exhaust gas temperatures in comparison to mixtures just rich of stoichiometric. Running an engine on lean mixtures also improves fuel conversion efficiency as a greater percentage of the fuels chemical energy is converted to piston mechanical work and less energy is lost to the atmosphere as high temperature exhaust gases. As the air fuel mixture becomes increasingly lean the resulting quality of the combustion reaction decreases significantly. There exists a threshold lean mixture value at which the air fuel mixture does not ignite resulting in combustion misfire. It occurs as there is insufficient fuel mixed with the air for the combustion reaction to proceed. Misfire should be avoided at all times as it has the potential to severely damage engine components in particular the piston and the engine cylinder. Misfire normally occurs at a λ value greater than approximately 1.30 ($\phi \cong 0.77$), however this value depends on the design of the engine in particular the combustion chamber geometry. Engine fuel consumption is

minimised when the Lambda ratio is equal to approximately 1.1 ($\phi \cong 0.90$). This is shown below in Figure 2-11.

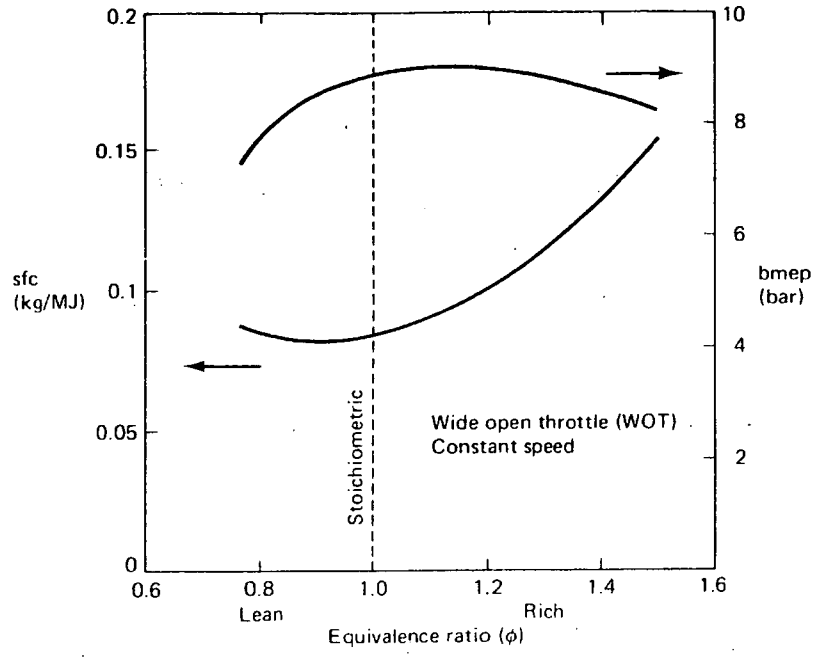

Figure 2-11 Response of specific fuel consumption (sfc) and power output to changes in AFR [21]

2.3.4 Effect of AFR on Emissions Products

As mentioned above it is impossible for complete oxidation to occur even during stoichiometric AFR engine operation due to chemical dissociation of carbon dioxide. A small fraction of non-oxidised compounds are always present in the exhaust gases, which is undesirable, as it is these exhaust gases that are the major contributors to urban air pollution. The most common forms of these undesirable pollutants are carbon monoxide (CO), nitric oxides (NO_x) and hydrocarbons (HC) in SI engine operation.

The lambda ratio is a critical factor that governs the composition of exhaust gas emissions generated by SI engines and also the temperature of the exhaust gases. In Section 2.2.5 above a brief explanation for the formation of these non-oxidised compounds was given, however the significance of the air fuel ratio on their formation was not provided. This section

highlights the importance of the air fuel ratio on pollutant formation. Figure 2-12 below shows the qualitative trends of NO, CO and HC pollutant formation with air fuel ratio variation.

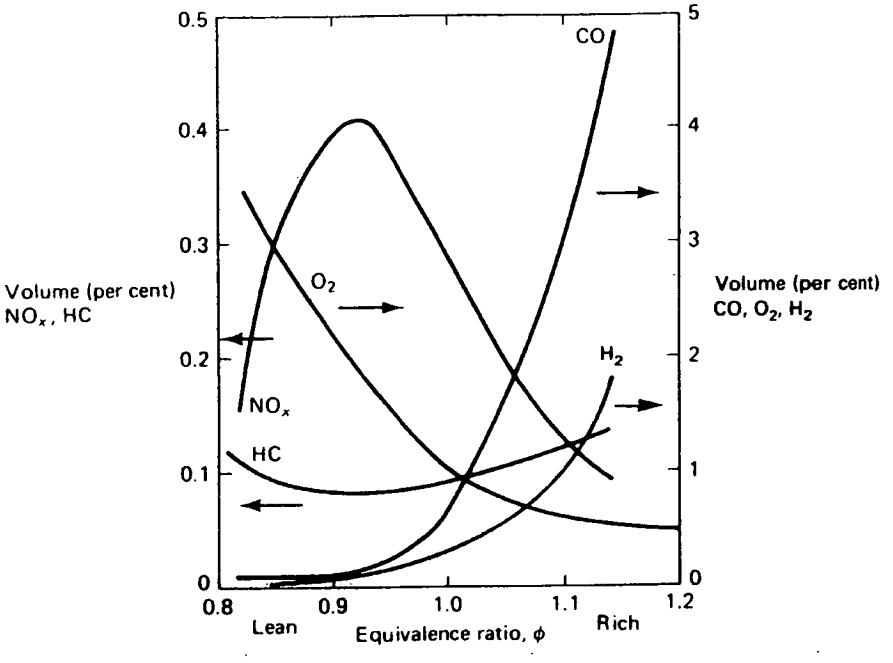

Figure 2-12 Spark ignition engine emissions for different AFR [21]

Lower emissions occur during lean mixture operation, as the AFR is greater than the stoichiometric value and there is additional air available for the complete combustion of all of the fuel. Due to this reason during lean burn combustion a large percentage of the final products are fully oxidised. The excess air present during combustion does not react and is present in the exhaust gases as oxygen and nitrogen. Figure 2-12 above, shows that CO and HC emissions are minimal during lean burn engine operation, until combustion quality becomes poor (and eventually misfire occurs) and HC emissions rise sharply [17]. There always exists some CO in the products due to dissociation. Lean mixture operation also produces products at lower temperatures and consequently the dissociation of CO_2 and H_2O molecules is smaller in comparison to slightly rich mixtures (see Section 2.2.5 Equations 2-8 – 2-10).

If combustion occurs in a fuel rich environment or with an AFR less than the stoichiometric value, there is insufficient oxygen to convert all of the hydrocarbon fuel into fully oxidised

products. As a result the reactants are composed of high levels of CO, HC, H_2 which increase nonlinearly with decreasing air fuel ratio or increasing equivalence ratio. Also during rich mixture operation, (especially just rich of stoichiometric), the combustion products are at high temperatures resulting in an increased rate of dissociation of CO_2 and H_2O molecules. The rate of NO formation is dependent primarily on cylinder temperature and flame speed and as a result maximum NO concentration occurs just lean of stoichiometric where there exists sufficient oxygen and relatively high combustion temperatures. This can be seen above in Figure 2-12.

Above it has been illustrated that the AFR has a significant effect on many engine performance variables. Selecting the appropriate AFR to enhance or optimise, one specific engine output parameter is often achieved at the detriment of others. For example increasing engine power increases fuel consumption. The next section reviews the factors that are considered when selecting the appropriate AFR for different engine operating conditions.

2.4 Selection of the Appropriate AFR

2.4.1 Factors involved in AFR Selection

As demonstrated above, the lambda ratio or equivalence ratio plays a definitive role in the determination of many engine performance criteria, including the power output, fuel consumption and the composition of engine emissions. The concept of a theoretical AFR (stoichiometric AFR value) has been introduced, illustrating its significance in terms of its importance in governing exhaust gas emissions composition and ensuring correct combustion. However, the optimum practical AFR for a spark ignition engines is that which gives the required power output with the lowest fuel consumption, consistent with smooth and reliable engine operation [17]. Power, low fuel consumption and reliable engine operation, in the past were the only key parameters that were considered for the selection of an appropriate operational AFR. Over the last four decades though, government imposed emission legislation has often dictated the use of a different AFR than that which optimises power and fuel consumption. Increasing government emission legislation has also required automotive manufactures to develop techniques and hardware that further reduce emissions, normally at

the detriment of engine performance. Such techniques include Exhaust Gas Recirculation (EGR), ignition timing delay and catalyst systems.

Additionally, what makes actual AFR selection difficult is that it is affected by the operational conditions placed on the engine by the driver. That is the engine input is derived from the drivers actions at the pedal. This is most conveniently measured in terms of the load placed on the engine and the engines operating speed. The throttle position at any particular time gives a good indication of the desired driving mode and therefore the response the driver requires from the vehicle.

During automobile operation the driver commands a wide range of different types of driving modes. The selection of the most appropriate AFR is crucial in these different driving modes in order to satisfy driver power requirements, engine fuel efficiency and government exhaust gas emission legislation. The selection of the ideal AFR in transportation vehicles is a continual compromise between these three variables relative to the requirements of the driver.

The engine mixture composition is generally selected according to two engine-operating conditions. These are at wide-open-throttle (WOT) or full engine load operation and part throttle or part engine operation. During WOT operation the mass airflow inducted into the engine is maximum due to the throttle valve being fully open. In such an instant the driver is requesting a sharp increase in engine power. It is paramount during such operating conditions that power output from the engine is maximum. Due to this, rich mixtures are used during WOT operating conditions. At part load or part throttle engine operation drivers often require less engine power (at a given speed) in comparison to WOT operation. Because of this engine power is sacrificed and the efficient use of the fuel becomes more significant. To increase the fuel efficiency of an engine, lean mixture operation is adopted, which is advantageous as it reduces the quantity of generated pollutants making it easier to meet exhaust gas emission legislation. Lean burn operation also improves the fuel conversion efficiency of the engine as described briefly in Section 2.3.3 above.

Exhaust gas emission legislation has existed since the 1960's and regulates the types of combustion products that are emitted to the atmosphere by automobiles. Due to this, lean or stoichiometric mixtures are used over the majority of the working range of the engine. The general approach taken by the automotive manufactures is to enrich the fuel mixture to just

rich of stoichiometric when wide open throttle is approached to satisfy driver power requirements and to use lean mixtures at lighter loads when fuel efficiency is more crucial. Mixtures can be leaned out by either diluting the mixture with additional air or by recycling a fraction of the exhaust gases (EGR) which reduces NO_x formation (see Section 2.2.5). The percentage of EGR is normally zero at light loads, increases to a maximum at mid load and decreases to zero as WOT is approached so maximum power can be obtained [17]. The variation of EGR with respect to intake mass airflow rate is provided below in Figure 2-13.

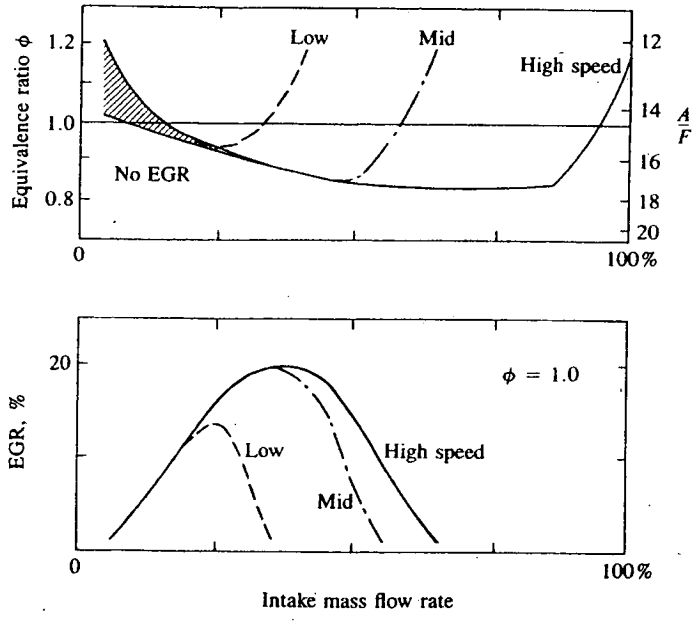

Figure 2-13 Top diagram shows equivalence ratio variation with intake mass flow rate at low, mid and high engine speeds. Bottom diagram shows EGR schedule as a function of intake flow rate for low, mid and high speeds for stoichiometric operation. [17].

Approximately a decade after emission legislation was first introduced in the USA, a number of new provisions were included to the legislation which meant that using a combination of both ignition timing delay and EGR was no longer adequate in meeting the stricter legislation requirements, without compromising reliable engine operation. The imposed stricter legislation led to the development of catalyst systems and automobiles since have been fitted with catalytic converters, devices which chemically convert the partially oxidised combustion products into completely oxidised compounds before expelling them to the atmosphere. The

peak operating efficiency of the catalytic converter is strongly linked to the automobiles working air fuel ratio. The relationship between the catalytic converters peak efficiency and the AFR has now become the critical factor in the determination of an automobiles optimum operational AFR. This will be described in more detail in Section 2.6.

Controlling the amount of air and fuel that enters the combustion chamber of an engine, that is the AFR, is a challenging and complex task. The hardware that is used in AFR control has undergone significant changes within the last two decades. The carburettor, the standard fuel metering device of the past, has been replaced by the more advanced Electronic Fuel Injection (EFI) system in modern automobiles. The carburettor was replaced by EFI primarily because of the need for improved AFR control due to the introduction of stricter emission standards. Below the conventional hardware components involved in mixture preparation will be discussed in some detail with special reference to EFI and engine management systems.

2.5 Components Used in AFR Control

2.5.1 Conventual Hardware Used in AFR Control

In SI engines the air and the fuel are usually mixed together in the intake system prior to entry to the engine cylinder, using a carburettor or fuel injection system [17]. Before approximately 1980 the carburettor was the most common fuel-metering device used as the fuel managing system in automobiles. The operation of the carburettor will be briefly described below for completeness.

The carburettor is positioned upstream of the throttle plate of an automobile and incorporates a converging diverging nozzle also known as a venturi in its design. As air is drawn into the engine it passes through the venturi and the velocity of the air stream increases (satisfying the continuity equation), until a maximum velocity is reached at throat of the venturi (the position at which the cross sectional area of the venturi is minimum). The rise in air velocity (dynamic pressure) at the throat of the venturi is offset by a decrease in the static pressure (expansion) of the air stream in order to satisfy the Bernoulli equation.

The pressure differential that is set up between the carburettor inlet and the throat of the nozzle is dependant upon the mass air flow rate passing through the venturi [21]. That is as more air is inducted into the engine more fuel is also drawn into the carburettor. The pressure difference causes a vacuum to exist between the throat and inlet, which is sufficient to draw an amount of fuel into the carburettor for that specific particular airflow rate. The fuel is released into the throat of the venturi by the fuel discharge tube, which is connected to a fuel reservoir which incorporates a float and needle valve assembly to ensure a constant level of petrol in the float chamber [17].

Discharging the fuel at this position has two significant advantages in terms of the fuel mixing with the air stream. The air attains maximum velocity at the venturi throat and this promotes maximum fuel atomisation into the air and the minimum pressure at this point promotes maximum fuel evaporation [21]. Mixing of the air and the fuel continues in the intake manifold. Figure 2-14 depicts an elementary carburettor.

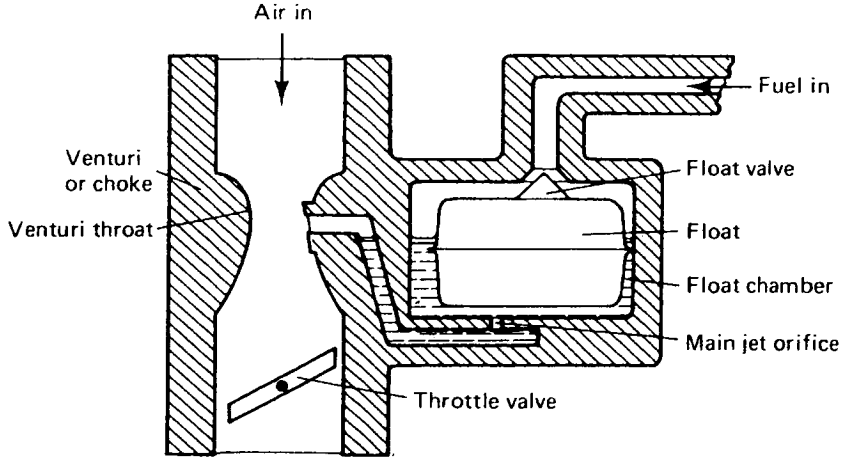

Figure 2-14 The layout of an elementary carburettor [21]

However, the major problem associated with the operation of the carburettor is that the amount of fuel drawn in at the venturi is not proportional to the quantity of airflow inducted into the engine at different operating engine speeds ie the AFR is constantly changing at different engine speeds. To compensate for this either additional fuel or air is added to the inducted air stream under certain driving conditions in order to maintain the required AFR.

A number of modifications have been made to the carburettor in an attempt to alleviate fuelling problems, in an effort to provide improved accuracy in the control of the AFR during different driving conditions. These modifications were necessary to minimise AFR excursions and thus maintain reliable and smooth engine operation, to improvement engine fuel consumption and to reduce exhaust gas emissions. Such modifications led to the carburettor becoming an extremely complicated mechanism. Compensations were implemented into the design of the carburettor for different driving modes and conditions including at engine idle, accelerator and power enrichment and a chock mechanism for cold starting [31].

However successive amendments to the emission standards, resulted in the carburettor becoming obsolete in its application due to its inability to achieve the air fuel mixture control demands required to pass emission legislation. Automotive manufactures developed fuel injection, a new fuel supplying technique that provided improved air fuel mixture control in comparison to the carburettor. Using fuel injection automotive manufactures were able to satisfy the emission legislation requirements. Early fuel injection systems were controlled mechanically, but the usual form of control is now electronic [21]. Figure 2-15 depicts the transition from the carburettor to fuel injection systems.

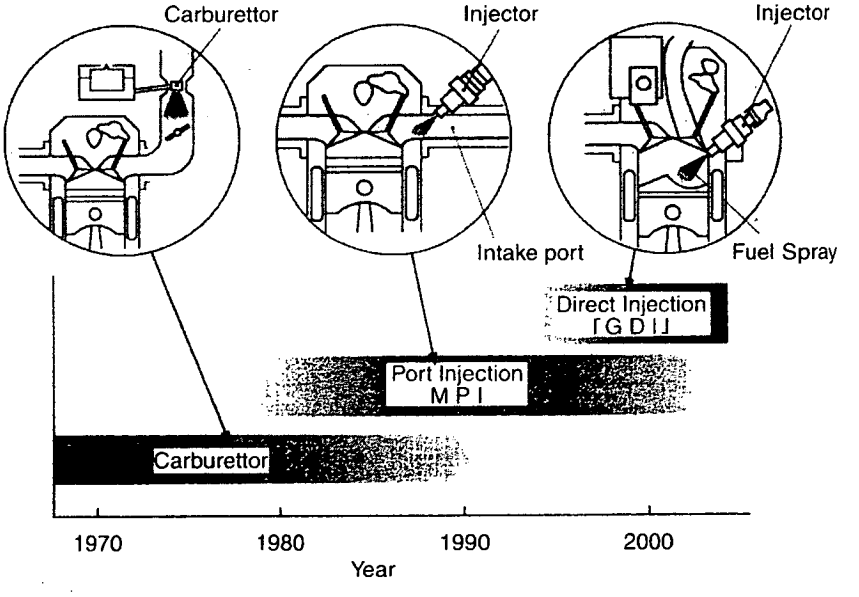

Figure 2-15 Transition of Fuel supply technologies from the carburettor to the fuel injection systems [23]

The major components of the Electronic Fuel Injection (EFI) will be described below.

2.5.2 Electronic Fuel Injection Systems

Electronic fuel injection systems were first introduced approximately two decades ago and today they have become the conventional fuel metering system adopted by automotive manufactures. Fuel injection systems offer superior control of the air fuel mixture in comparison to the carburettor technology, and therefore can provide increased reliability in engine operation, improved fuel efficiency and compliance to current emission standards. The basic operating principal of the fuel injection system is that if petrol is supplied to an injector at a constant pressure then the amount of fuel injected will be directly proportional to the injector open time [23]. Thus, fuel calculations can be performed based on fuel time rather than fuel volume [30]

There are two main types of fuel injection systems, single point injection systems and multipoint injection systems. These two types of fuel injection systems are shown below in Figure 2-16.

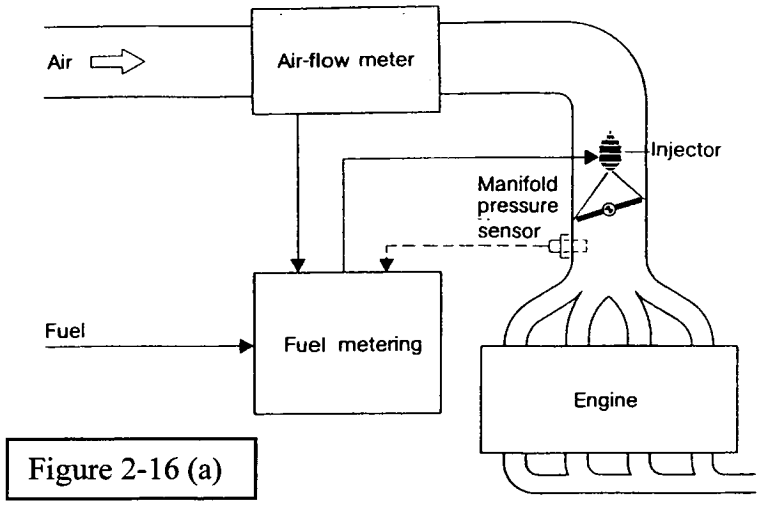

Figure 2-16 (a)

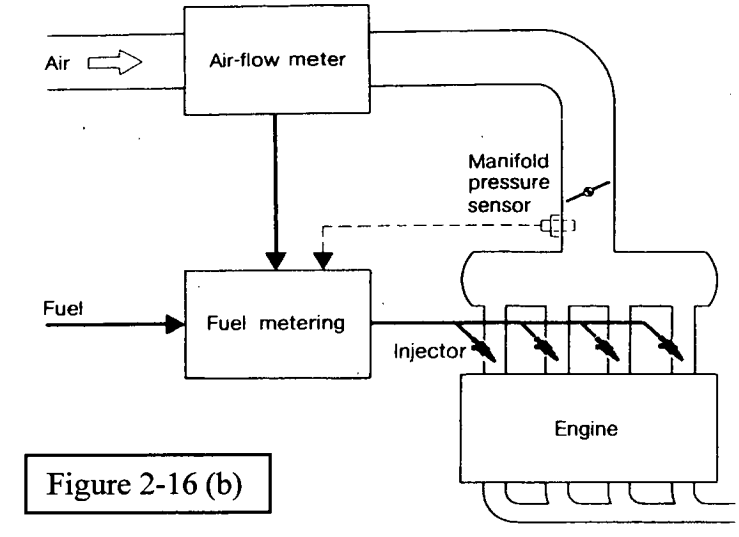

Figure 2-16 (b)

Figure 2-16 (a) depicts a single point fuel injection system, (b) depicts a multipoint fuel injection system [23]

Single point fuel injection systems are composed of a single fuel injector that delivers fuel upstream of the throttle into the inlet manifold. This system simply replaces the carburettor with an electronic fuel injector. Multipoint fuel is a more complicated injection system consisting of one fuel injector for every engine cylinder. Multipoint fuel injection systems have become the standard fuel delivery systems used in modern automobiles as they provide more accurate and quicker delivery of the fuel into the engine cylinders, hence engine response is more rapid [32].

2.5.3 Major Components in Fuel Injection Systems

Fuel injection systems consist of two sub systems, the fuel delivery system and the fuel management system. The fuel delivery sub system consists of a fuel pump, fuel filter, fuel rail, and one or more electromagnetic fuel injectors. The fuel control sub system consists of number of engine sensors and a microprocessor. The microprocessor controls the fuel injector opening time and thus controls the amount of fuel delivered to the individual engine cylinders.

Fuel is pumped from the fuel tank and passes through a fuel filter to the fuel rail. The main components of the fuel delivery system are shown below in Figure 2-17.

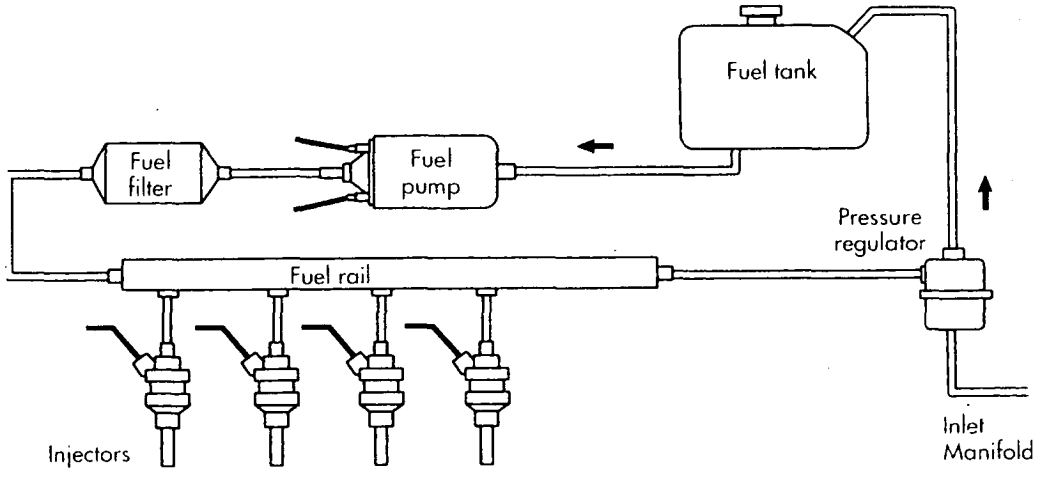

Figure 2-17 The main components in the fuel supply system [23]

Each fuel injector is essentially an electronically actuated valve [30]. When the fuel injector is activated, an electromagnet moves a plunger that opens the valve allowing pressurised fuel to squirt through a tinny nozzle [30]. The nozzle of a fuel injector is designed to atomise the fuel and deliver it in the form of a fine misty spray on the back of the closed inlet valves. The time the fuel injector is open is determined by the duration of the activation signal from the ECU. At the commencement of the induction stroke fuel is drawn into the combustion chamber and mixes with the inducted air. The fuel pressure regulator maintains a constant differential pressure of approximately 2.5 to 3 bar across each injector relative to the pressure

of the inlet manifold. A self-adjusting valve contained within the pressure regulator compensates for fluctuations in the manifold air pressure.

Fuel injection systems are controlled by a microprocessor called an Electronic Control Unit (ECU) also referred to as an engine management system. Figure 2-18 (below) shows a simplified fuel injection and injection block diagram depicting the inputs to and outputs from the ECU. Engine sensors provide information regarding the actual engine operating conditions to the ECU. The most commonly used sensors include, a mass air flow sensor, one or more oxygen or lambda sensors, a throttle position sensor, an engine temperature sensor, voltage sensors, a manifold absolute pressure sensor and an engine speed sensor [30]. The information from these sensors is received by the ECU, which then controls the fuel injector opening time thus metering the appropriate amount of fuel into the cylinders per engine cycle.

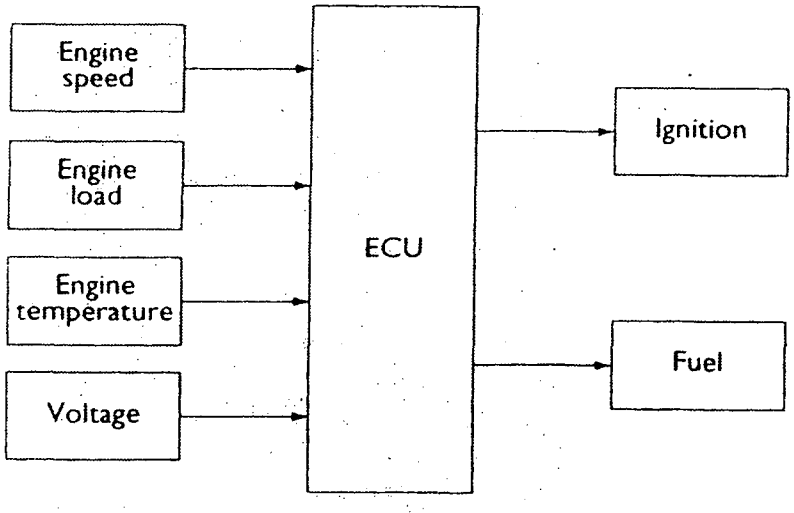

Figure 2-18 General block diagram of the inputs to the ECU and the controlled outputs of the delivered fuel and ignition timing [23]

Multipoint fuel injection systems can delivery the fuel to the engine in one of two ways, either simultaneously or sequentially. Simultaneous fuel injection involves the fuel injectors firing or opening at the same time and delivering equal amounts of fuel to all cylinders. Sequential injection system injects fuel on the induction stroke of each cylinder in the engine firing order [23]. Figure 2-19 (below) compares the operation cycle of each method.

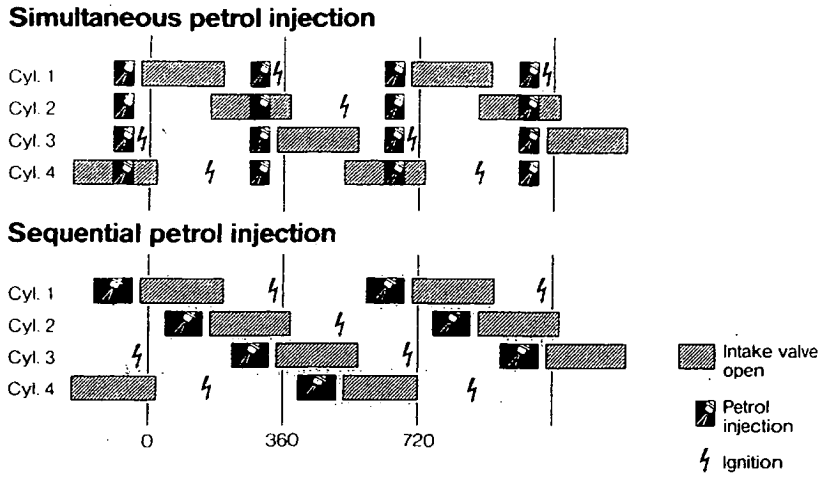

Figure 2-19 A comparison between simultaneous and sequential injection strategies [23]

A brief overview of the major physical components of the electronic fuel injection systems was presented above. The following section defines the term engine management and describes in more detail how these components are actually controlled.

2.5.4 Engine Management

"Engine Management is the science of equipping and calibrating an engine to achieve the cleanest possible exhaust stream while maintaining top performance and fuel economy and continuous diagnosing of system faults. However the focus on those priories often varies around the world, reflecting differing government regulations, customer expectations and driving conditions and a host of vehicle types and content levels." [33].

Engine management is performed by the ECU and its primary assignment is to furnish the torque requested by driver while at the same time ensuring maximum fuel economy and minimum emissions [17]. Modern engine management systems are responsible for the control of a wide range of engine subsystems, including lambda control, ignition timing control, dwell angle control, evaporative emission control, knock control, EGR control, camshaft control, vehicle control including ABS, traction control and stability control etc.

The discussion below will be limited to lambda control and the ignition timing is accomplished in a typical engine management system.

2.5.5 Lambda & Ignition Timing Control

In modern multipoint fuel injection systems AFR control is primarily achieved by controlling both the engines fuelling and ignition requirements by receiving engine data from a variety of sensors. The primary sensor inputs used by the ECU in the determination of the injector opening time and ignition timing are the engine operating speed and engine load. As mentioned in Section 2.4.1, above there are many factors governing the actual air fuel mixture that is used during different engine operating conditions. The ideal engine air fuel mixture is decided over a wide range of engine operating conditions and is represented as a function of engine load and speed.

A complex non-linear relationship exists between the engine load, speed and the engine fuelling requirements. In practice, the most convenient way in determining the non-linear relationship is through non-dynamic map modelling [34]. This involves extensive stationary experimental engine testing and tuning over a wide range of engine speeds and loads with the use of engine dynamometer. This testing develops an engine characteristic map or schedule, which graphically depicts the relationship between the fuel injector opening time for specific engine load and speed values. The engine map represents the optimum air fuel mixture schedule that satisfies the power and fuel economy demands of the driver, while at the same time meeting exhaust gas emission standards and maintaining smooth and reliable engine operation.

The engine map is represented as a three dimensional cartographic map as shown below in Figure 2-20 and is stored in the read only memory of the ECU in the form of a look up table.

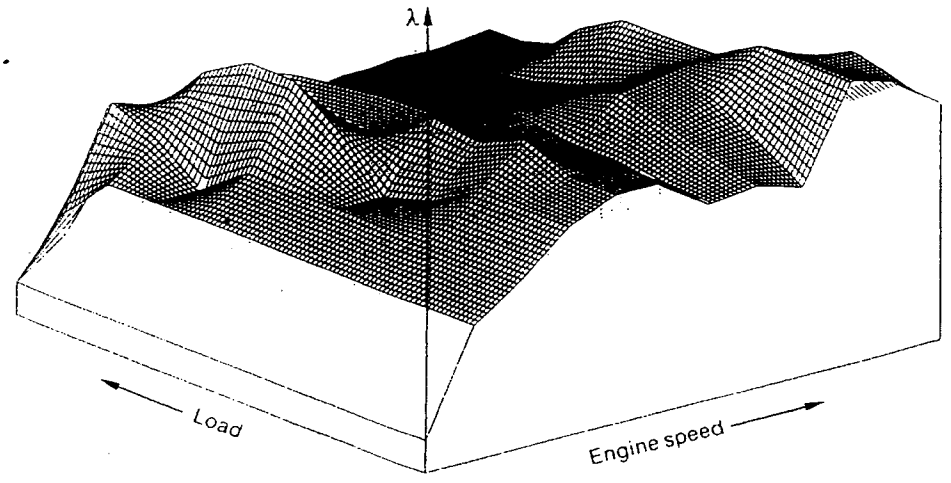

Figure 2-20 Cartographic map used to represent how information on an engine's fuelling requirements are stored [23]

Either the base injection opening time or the desired lambda λ value is located on the z-axis depending on the method used in the determination of the engine load. Figure 2-18 above shows that the lambda value or injection time is mapped as a function of both engine speed and load. These quantities are labelled on the x-axis and y-axis and form a conventual two dimensional grid. The ECU simultaneously reads in the data from the speed and load sensors and then "looks up" the base injector opening or pulse width from the schedule map stored in the ECU memory for those specific engine operating conditions. Look up tables such as those used with fuel injection systems are referred to as a feedforward control structures that operate in open loop control. It is often difficult to build an open loop controller that will be suitably accurate under all conditions [32]. Due to this in modern automobiles, the open loop control algorithm is supplemented by a feedback law using a signal from a lambda sensor to improve overall control of the air fuel ratio [9]. This arrangement will be described in more detail in Section 2.6.

Linear interpolation is used to determine the injection opening time when the signalled engine speed and load inputs are between points in the engine map. The interpolation accuracy therefore strongly depends on the complexity of the underlying grid and the degree of non-linearity [35]. Where there is a high degree of non-linearity the grid should be more closely

meshed while in areas of smooth non-linear behaviour a small number of grid data may be sufficient [33].

A non-dynamic modelling process is also undertaken to develop the nonlinear relationship that exists between ignition timing and engine load and speed. Likewise extensive testing and calibration during the design phase of the engine, is also required to map the spark advance schedule [25]. This schedule is stored on the ECU in a look up table format and the desired output is computed in a similar manner as that employed with fuel injection valve opening time. Figure 2-21 below depicts a typical ignition timing engine map. Unlike the look up tables for the injection timing, which are supplemented by feed back control, most spark advance controllers today are simply open systems which measure a number of parameters that affect the spark advance and compensate for their effects [25].

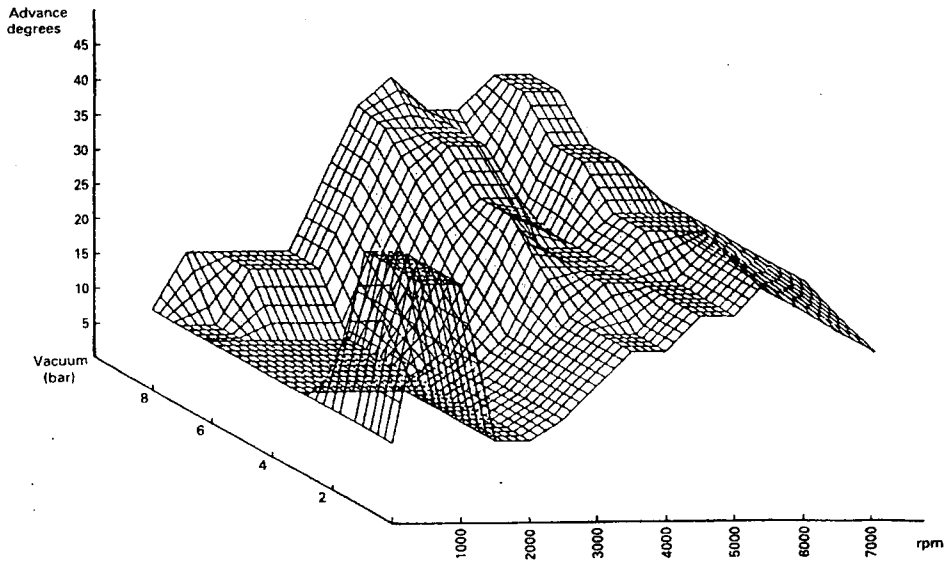

Figure 2-21 The ignition timing map, as a function of engine speed and inlet manifold pressure as used in engine management systems [21]

Compensation and correction factors are introduced by the ECU to improve overall engine performance and reliability and these will be discussed in the following section.

2.5.6 ECU Corrections & Compensation Factors

The ECU computes the appropriate amount of fuel to be injected into the engine cylinder by determining the current engine load, that is the amount of air that is drawn into the engine at any given time. There are two basic methods used in determining the engine load and this leads to two different types of electronic fuel injection control strategies [21]. There are those that measure the load directly using a mass air flow meter and those that calculate it indirectly using a manifold absolute pressure sensor. Mass Air Flow (MAF) systems are at present nearly always realised using a hot wire or hot film sensors [36], [37]. Fuel injection systems based on the latter are called speed density systems and rely on look up tables for the desired lambda value and the steady state volumetric efficiency of an engine over a wide range of operating conditions [12]. There are also Throttle-Density Systems, which are simply Speed-Density systems that have been modified to use a throttle position sensor in the calculation of the mass airflow rate [12].

Corrections need to be made to the base injector time determined from the engine load and speed information. The first correction is for air temperature as the density of air changes with temperature and the second is an allowance for the current driving condition represented by the throttle position. The ECU depending on its complexity then compensates for after start enrichment (choke), acceleration enrichment, weakening on deceleration, cut-off on overrun, reinstatement of injection after cut-off, correction for battery voltage variation, just to name a few [23]. These correction factors are stored on the ECU in the form of three-dimensional nonlinear maps and encompass corrections for both fuelling requirements and ignition timing and are normally a function of two of the following, engine cooling temperature, manifold air pressure or rate of change of throttle position. A modern upper class vehicle contains about fifty, three-dimensional maps to realise complex functions like engine management and emission control [38]. The ECU determines the actual pulse width by multiplying the base pulse width, determined from the main fuelling look up table by applicable correction factors.

The compensation factors described above, adjust for different engine operating conditions by referring to correction values contained in feedforward look up tables. Tightening of emission legislation has meant feedforward compensation alone is insufficient in controlling

the AFR and meeting exhaust gas pollution levels. In response to this automotive manufactures have been forced to develop other methods and new components to reduce exhaust gas emission pollution levels. Today all automobiles supplement the feedforward control strategy, described above, using close loop control using a feedback signal from a lambda sensor complimented with the use of a catalytic converter. This approach has proved significant in the reduction of pollution and will be described below.

2.6 Closed Loop Control of Fuel Injection Systems & Catalyst Emission Systems

2.6.1 Closed Loop AFR Control

Current emission regulations have almost made mandatory closed loop control of the air fuel mixture in conjunction with a three-way catalytic converter [23]. Present AFR control technologies do not control the air fuel mixture of each engine cylinder but control the average AFR of all cylinders [7] [39]. A typical feedback control, such as that used in AFR control, has the feature that the output quantity (control variable) is measured and then compared with a desired value, and the resulting error is used to correct the systems output [40]. Fuel injection closed loop feedback control consists of a lambda sensor, which is mounted downstream of the confluence point[1] in the exhaust manifold. It is not physically possible to directly measure the AFR inside the combustion chamber instantaneously and delays are introduced in the measurement due to time it takes the exhaust gases to reach the mounting position of the sensor.

There are two types of lambda sensors used in feedback control applications. The switching Exhaust Gas Oxygen (EGO) sensor, which tells the ECU if the air fuel mixture is rich or lean of stoichiometric and the Universal Exhaust Gas Oxygen (UEGO) sensor which signals the actual operating air fuel ratio value to the ECU. Both types of sensors are operational only above a certain temperature range approximately 250-300 °C. Heaters are used to realise this temperature during cold start operation and closed loop control is only initialised once this

[1] where the individual emission collection pipes for each cylinder converge to form the single exhaust pipe

temperature has been reached. Before this time, the ECU uses open loop feedforward control to regulate the AFR. The UEGO sensor is slowly replacing EGO sensors in modern automobiles due to their ability to provide the actual AFR value [32].

Both these sensors measure the average AFR of all the engine cylinders by analysing the composition of the exhaust gases. This information is then "fed back" as an input to the ECU, which then regulates the engines operating AFR to the desired AFR using a Proportional (P) or Proportional Integral (PI) controller during steady state and idle speed control conditions [7], [36]. The P or PI controller adjusts the fuel pulse width by a small amount in the direction that will bring the engines AFR towards the desired stoichiometric value.

Using the feedback signal from a lambda sensor as the only means in controlling, the AFR is not feasible as the sensor has a large 'sensing' time, due to the exhaust gas transport delay. This is the time it takes the exhaust gases to reach the sensors mounting point in the exhaust manifold. Thus lambda based feedback control compliments the feedforward look up table control strategy described above. The main purpose of feedback control is to compensate for variations from engine to engine, variations in fuel and changes due to engine wear and aging. In modern vehicles, it is also used to adapt or update the engines fuelling map over time [41].

Corrections that are made to the fuel pulse width, because of feedback from the lambda sensor is stored to the memory of some modern ECU's. The corrections are stored with reference to the engine speed and load conditions at which the fuel adjustment was calculated. This is advantageous as the data in the fuel look up tables is adjusted over time, meaning that a smaller amount of correction is required the next time the engine experiences the same set of operating conditions. A typical lambda feedback control system is shown below in Figure 2-22.

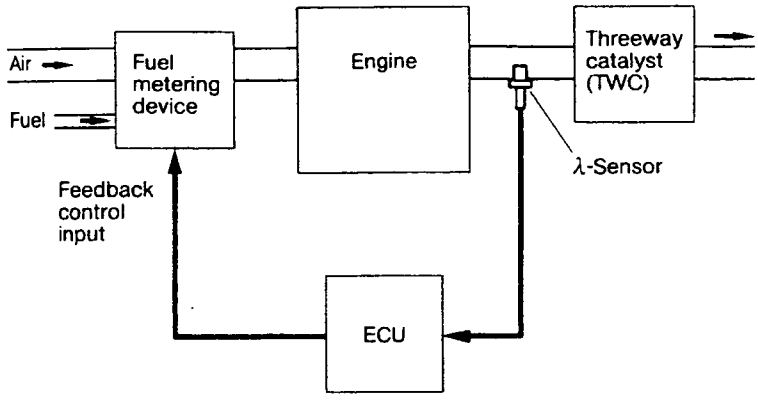

Figure 2-22 Closed Loop Feedback control showing the lambda sensor upstream of the three way catalytic converter

The feedback from the lambda sensor and its associated correction to fuelling is critical to maintain the maximum conversion efficiency of the catalytic converter and thus minimise exhaust gas emissions. The next section will briefly discussed the importance of the catalytic converter in reducing pollutants and illustrates that its effectiveness is closely related to the AFR.

2.6.2 Three Way Catalytic Converter

The Three Way Catalytic Converter (TWCC) is a device that has been developed by automobile manufactures to reduce the amount of automobile generated pollution and thus abide by exhaust gas emission legislation. A three-way catalytic converter is a device that treats the exhaust gases by chemically converting the damaging pollutants into more environmental friendly compounds before they are expelled into the atmosphere. Catalytic converters are installed upstream of the muffler in the exhaust system.

As discussed in Section 2.2.5, NO_x, CO, HC pollutants are formed during the combustion reaction between a hydrocarbon fuel and oxygen. The purpose of the catalytic converter is to use a catalyst, usually a noble metal, to oxidise the CO and HC compounds and reduce the NO compounds. Platinum is the catalyst used to oxidise HC to H_2O and CO to CO_2. Rhodium is used to reduce NO to N_2. The actual chemical reactions will not be presented here.

The conversion efficiency of the TWCC is dependant upon two factors, the AFR and the TWCC temperature. The ideal operating temperature of the TWCC is about 400-800 °C [23]. During times of engine cold start, electrical heating elements are used to bring the TWCC to the optimum temperature range and minimise the heating delay.

In order for the catalytic converter to operate at its highest efficiency for conversion of all the three gases (HC, CO, NO_x) the average AFR must be maintained within less than 1 percent of stoichiometry [38]. This small operating range is known as the lambda operating window or catalytic converter operating window [38]. This lambda window is usually defined for when the catalytic converter is operating at an efficiency above 80 % [17]. Figure 2-23 below is a graph of lambda (λ) verses the exhaust gas emissions both before and after the catalytic converter.

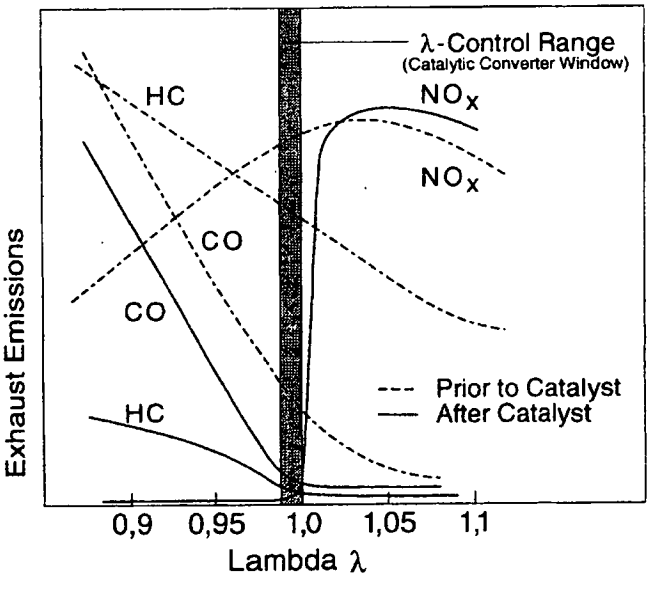

Figure 2-23 Lambda effect on exhaust gas emissions prior to and after catalyst treatment [38]

When the lambda ratio is equal to one the conversion efficiency is approximately 90%, which represents the point at which the conversion of the three pollutants is maximum. Figure 2-23, above illustrates that the conversion efficiency of the catalytic converter is highly dependent upon the AFR. Research [3] has shown that even small deviations around the stoichiometric value can result in a severe loss in the efficiency of the catalytic converter. Even a 1%

variation of the AFR may cause up to a 50% reduction in catalytic converter efficiency [3], [4]. The next section reviews some of the reasons as to why conventual engine control systems are unable to prevent deviations in the AFR around the stoichiometric value, especially during transient engine operation, thus limiting the effectiveness of the catalytic converter.

2.7 Deviations in the Air Fuel Ratio Using Conventional Engine Control

Conventional engine control technologies such as feedback loop control strategies are unable to avoid large AFR excursions during transient engine operation, that is during periods of engine acceleration, deceleration, and engine load variations [32]. Conventional AFR control algorithms perform poorly during transient conditions as they are based on look up tables, which are, developed by stationary or non-dynamic modelling techniques. Many researchers have examined why AFR variations occur during transient driving conditions [26] [8], [9], [10]. The main reason for AFR deviations is due to the fact it is very difficult to accurately estimate the airflow at the engine cylinder ports, especially during transient operating conditions [11]. It is also difficult to place the fuel in the intake manifold at the necessary location and at that instant [12]. This is because during transient conditions the fuel injected does not equal the fuel flow into the cylinders of the engine and the air mass flow either calculated or measured upstream of the throttle does not correspond to the actual air mass flow inducted into the engine.

These two effects have been known for a long time and are called the wall-wetting phenomenon and the manifold-filling phenomenon [32] respectively. The wall-wetting phenomenon occurs when some of the injected fuel becomes deposited on the manifold wall instead of entering the engine cylinders immediately. The manifold filling phenomenon occurs during transient conditions when the port air mass flow and throttle air mass flow are different because of the filling and emptying of the intake manifold volume. A number of researchers have developed and revised mathematical models to try and compensate for these two effects and these will be looked at in the next chapter.

Other factors that make it difficult to obtain tight control of the AFR in transient driving conditions include engine pumping fluctuations, poor engine sensor response time and ECU computational time delays. These factors will be briefly described below.

In the intake manifold, pressures and flows oscillate because of the periodic motion of the piston and valves and these resulting variations are often referred to as pumping fluctuations [42], [43]. The pumping fluctuations introduce noise into the Air Mass Flow Related signals (AMFR) encompassing manifold air pressure sensors and mass air flow sensors. This sensor noise is undesirable in the control of the AFR. Current fuelling strategies ignore this problem and fail to condition the signals in an attempt to remove the fluctuating noisy component of the sensor measurements [32]. Serious aliasing problems should be expected if no special measures are taken during the sampling/processing of the AMFR measurements [32]. Some researchers have proposed step moving average filters and extended Kalman Filters which have built into them a priori dynamic description of the mean AMFR signals as well as a statistical description of the noise in an attempt to remove the noise from AMFR sensor signals [44].

Sensor response time also has a significant impact on the performance of AFR controllers [32]. Hot wire Mass air flow meters (MAF) which are the most popular choice with automotive companies can have a response time anywhere between 30 ms and 0.5 sec. This is a relatively large response time in comparison to manifold absolute pressure sensors (MAP) which has a response time of 1 ms [45]. Another problem associated with mass airflow sensors is that they are unable to determine the air flow direction and therefore they can give a false reading when engine back flow or flow reversal occurs. Engine back flow is caused by engine pulsations due to the periodic motion of the pistons.

There is a significant transport delay associated with the readings from the Lambda sensor in feedback AFR control strategies. This transport delay is known as the lambda feedback control transport delay and exists because it takes time for the exhaust gases to travel from the exhaust valve to the position of the oxygen sensor mounted in the exhaust manifold. Thus, the readings from the lambda sensor actually provide delayed AFR information on previous engine events rather than the current engine event. This phenomenon severely limits the response time of the ECU controller [32]. It takes about 3 1/2 engine strokes before the burnt

exhaust gases enter the exhaust manifold and a further 2 to 20 ms before they reach the lambda sensor [32].

AFR excursions are also apparent due to the time delay associated with the fuelling calculation and the subsequent time needed to delivery the fuel into the engine cylinders. This involves three separate time delays, computation duration, injection duration and start of injection delay. Computation time delay is the time it takes for the ECU to determine the appropriate amount of fuel that should be injected with the calculated or measured air mass flow. This time delay is usually about 15 ms long [46]. Injection duration is the delay associated with the injector actuation. This delay is usually between 2-15 ms long [32]. Start of injection delay (SOI) is the time that is required to wait until the the inlet valves are fully closed before injection is initiated. The ECU delays injection until the hot inlet valves are closed as this is the optimal moment for fuel injection as a greater proportion of the fuel evaporates and enters the combustion chamber directly than in comparison to open valve injection. The SOI delay varies continuously and can be equal in the worst case to 15 ms [32].

The cumulative sum of all the time delays associated with fuel delivery described above can total in the worst case over 100 ms or 0.1 sec [32]. Conventional AFR feedback control strategies are adequate during steady state engine operation, however during transient operation the time delays mentioned above result in large AFR excursions and poor TWC efficiency. The time delays associated with fuel delivery become critical during transient conditions, as during these periods there are two types of disturbances possible on the engine which can not be immediately detected and which move the actual air mass flow inducted into the engine away from the ECU estimated value. These disturbances are driver derived and are observed as fast changes on the external load (torque) on the crankshaft (and consequently a change in engine speed) and a change of throttle position (and consequently a change in mass air flow) [32].

During realistic transient driving conditions, such as during peak hour traffic, the accelerator (throttle angle) can be changed on a time scale as low as 50 ms to 100 ms [40]. This suggests that in the worst case there can be as many as two movements of the accelerator pedal before the injection of fuel. The ECU bases its fuel calculation on delayed sensor measurements and delivers fuel based on previous engine events. During steady state, engine operation control

of the AFR is adequate, as there are no imposed changes on engine operation. However during highly transient-driving conditions, the engine controller is always trying to "catch up" to the drivers wishes and with the current technology this can only be achieved a short period after the driver engages steady state engine operation. This is most evident in a tip in tip out throttle actions. The value of the AFR as a result of this fast throttle action leans out and then becomes rich due to the time delays associated with the controllers measurement, estimation and delivery of the fuel. Conventual AFR controllers at present do not have the required control bandwidth to be able to immediately detect and control the fuel delivery during the minimum throttle rise time (50 ms) [32].

2.8 Summary

The above chapter has provided a comprehensive overview of the reciprocating SI engine. In particular the review concentrated on the significance of the AFR and its effect on a number of engine operating and performance characteristics. As highlighted above, current AFR control strategies and additional components are unable to avoid deviations in the AFR during transient conditions. As a result this has prompted a great deal of research into engine modelling in order to develop mathematical descriptions of the physical fuelling problems. The purpose of such analytical models is to compensate for dynamic air and fuelling effects and thus maintain better control of the AFR. The purpose of the next chapter is to provide a review of some of these models in particular describe the Mean Value Engine Model which has become the prominent nonlinear engine model used extensively throughout automotive research.

3 MEAN VALUE ENGINE MODELLING & NEURAL NETWORK MODELS

This chapter reviews the research that has been undertaken in the field of conventional analytical engine modelling and describes the Mean Value Engine Model's (MVEM's) in mathematical detail. The aim of analytical engine modelling is to represent the entire engine plant in terms of mathematical expressions so that a better understanding of the processes involved can be established and thus a greater degree of control can be gained over critical engine operating variables such as the AFR. Linear engine models were the first to be developed, however such models were too basic and idealistic in representing the complex nonlinear nature of practical engine operation. Subsequently nonlinear models began to emerge that were better suited to cope with the complexities and relationships involved in 'real world' engine operation.

Of these models one has become very popular with automotive researchers due to the high accuracy in which it can characterise engine parameters. This is Hendrick's et a; [1] MVEM, and is discussed in some detail below. The complexities associated with the implementation of the MVEM's to real world conditions are raised, also the need for an alternative control strategy to replace the shortly to be inadequate conventional models currently in use. A review of recent research into the application of Artificial Neural Networks to SI engines is also presented in this chapter. A detail description of the MVEM's is deemed necessary as a large amount of Artificial Neural Network engine related research, is inspired by MVEM's with a significant number of papers incorporating specific relationships directly into their research.

3.1 Engine Modelling

In the 1970's, Hazell and Flower [47], were among the first to develop discrete engine models [48] and since then there has been a large amount of research interest shown in the modelling of engine processes. IC engines are highly nonlinear systems and as a result engine modelling is a very complicated and difficult task involving a number of interrelated and interdependent variables. In the late 1970's and early 1980's nonlinear dynamic engine models started to emerge that were accurate over wide speed and load engine operating

ranges. At present there is one nonlinear dynamic engine model that has gained wide accepted in literature, has proven accuracy and to be a good basis for engine design and control [49]. This model was first presented by Hendricks and Sorenson in 1990 [1] and is referred to as the Mean Value Engine Model (MVEM). Over the past decade this model has been revised and optimised, increasing its accuracy in the prediction of engine parameters and its capacity to be applied to a wider range of engine configurations. This model will be described in some detail below and is based on the equations and description presented in [1], [50], [51].

3.2 Mean Value Engine Modelling (MVEM) of SI Engines

The Mean Value Engine Models (MVEM's) are simplified dynamic engine models, which are based on collections of physical models of the most important engine subsystems [1]. The MVEM developed by Hendricks and Sorenson [1] has been strongly influenced by work presented by other researchers such as Rasmussen [52], Aquino [53], Hires and Overington [54], and Fozo [55]. MVEM's are intended to operate as predictors of the averages rather than cycle to cycle values of the most important engine states and variables [1].

The MVEM's consists of mathematical expressions of the three most important dynamic subsystems, which describe the behaviour of the fuel mass flow, the intake manifold filling dynamics and the acceleration of the crankshaft [48]. MVEM does not allow a distinction between single cylinders or positions of the crankshaft, but a display of the dynamic behaviour of interesting states [47]. Each of the engine subsytems, namely the fuel flow evaporation model, the manifold filling dynamics model and the crankshaft dynamics model will be individually described below on a mathematical basis.

3.2.1 MVEM Time Scaling Relationships and State Variables

MVEM's are composed of instantaneous and time developing analytical relationships. Instantaneous relationships only take one or two engine cycles for equilibrium to be reached. For time developing relationships, equilibrium is attained in 10 to 1000 engine cycles. Instantaneous relationships are expressed as time independent algebraic equations while time

based differential equations are used to describe time developing relationships. State variables are those which are determined by integrating the differential equations, which are used to describe time developing relationships of the engine [1].

3.2.2 Fuel Flow Evaporation Dynamic Submodel

This model describes the path of the fuel from the injector into the combustion chamber. As mentioned briefly in Section 2.7 not all of the injected fuel directly enters the combustion chamber when the intake valve opens, this due to the wall wetting phenomena. When fuel is injected into an engine, a fraction of the fuel vaporises $(1-X_f)$, mixes with the inducted air and enters the combustion chamber directly. The remaining portion of the injected fuel (X_f) is deposited on the walls of the intake runners. This deposited fuel is referred to as the fuel film. Mathematical expressions have been developed to describe the wall wetting phenomena. The expressions below are based on monitoring the fuel mass entering the cylinders and are based on the assumption that only fuel vapour enters the combustion chamber, that is no liquid fuel directly enters the combustion chamber. The total mass of fuel entering the engine is therefore equal to the fraction of the injected fuel that vaporises and mixes with the air and the quantity of fuel that evaporates from the fuel film.

$$\dot{m}_{ff} = \frac{1}{\tau_f}\left(-\dot{m}_{ff} + X_f \dot{m}_{fi}\right) \qquad \text{Equation 3-1}$$

$$\dot{m}_{fv} = (1-X_f)\dot{m}_{fi} \qquad \text{Equation 3-2}$$

$$\dot{m}_f = \dot{m}_{fv} + \dot{m}_{ff} \qquad \text{Equation 3-3}$$

where, $\dot{m}_{fv}$ = is the fuel vapour mass flow

$\dot{m}_{ff}$ = is the rate of change of the evaporating fuel film mass flow

$\dot{m}_f$ = is the total fuel mass flow that enters the combustion chambers

X_f = is the portion of fuel that is deposited on the walls of the intake runners

τ_f = is the evaporation time constant for the fuel film

The parameters τ_f, X_f are operating point dependent and thus the model is nonlinear in spite of its linear form [49]. The parameters τ_f, X_f can not be measured directly by any means and are highly dependent upon the temperature of the inlet air, the temperature of the fuel and the temperature of the manifold walls [56]. The variables τ_f, X_f are normally mapped for a specific engine as a polynomial function of engine speed and the intake manifold pressure over a wide range of operating temperatures and engine conditions. The parameter τ_f has a value generally in the range of 0.25-0.75 seconds while X_f has values within the range of 0.1 – 0.5 seconds, [57], [47], [48].

Other models have been developed that describe the wall wetting phenomenon. One of these is the Aquino model [51], which is based on monitoring the fuel film mass deposited on the intake rather than the mass of fuel. The Aquino model is also uses the parameters τ_f, X_f which have the same physical meaning and function as in Hendricks' et al [1] model presented above. With the correct mapping strategy for the parameters, Hendricks' et al [1] MVEM and the Aquino model provides more or less an equally good description of the fuel flow dynamics [48].

The mathematical expressions that describe the fuel flow submodel are rarely used directly in conventional engine control systems [49]. Transient Fuel Compensation (TFC) has been developed which is based on the above expressions, with the aim to take into consideration the wall-wetting phenomenon and adjust the fuel injected accordingly. That is fuel is either added or subtracted from the base amount determined by the ECU in an attempt to cancel out the dynamic effects of the fuel evaporating from and being deposited onto the intake manifold runners. As a result of this compensation the fuel mass that actually enters the engine is closer to the amount of fuel requested rather than a quantity less than or greater than the desired amount.

The TFC mathematical expressions for Hendricks' et al [1] model for the fuel flow dynamics are presented below.

$$\ddot{m}_{fi}' = \frac{1}{\tau_f}\left(-\dot{m}_{ff}' + X_f \dot{m}_{fi} \right) \qquad \text{Equation 3-4}$$

$$\dot{m}_{fi} = \frac{1}{(1-X_f)}\left(\dot{m}_{fu} - \dot{m}_{ff}' \right) \qquad \text{Equation 3-5}$$

where, $\ddot{m}_{fi}'$ = is the second rate of change of the projected fuel film mass flow.

$\dot{m}_{ff}'$ = is the rate of change of the projected fuel film mass flow

τ_f, X_f = have the same meaning as above

A transient method of mapping the above parameters of the compensators is suggested in [49].

3.2.3 Manifold Filling Dynamics Submodel

This model mathematically describes the path of air that is inducted into the engine. During transient engine operation the mass flow rate at the throttle, which is normally used to calculate the amount of fuel to inject, is not equivalent to the mass of air that actually enters the engine cylinders known as the port air mass flow rate. This is because of the manifold filling phenomena, which was introduced in Section 2.7 above. Figure 3-1 shows the effect of the manifold filling phenomena for a tip in tip out throttle action, illustrating the difference between the throttle air mass flow rate and the port air mass flow rate.

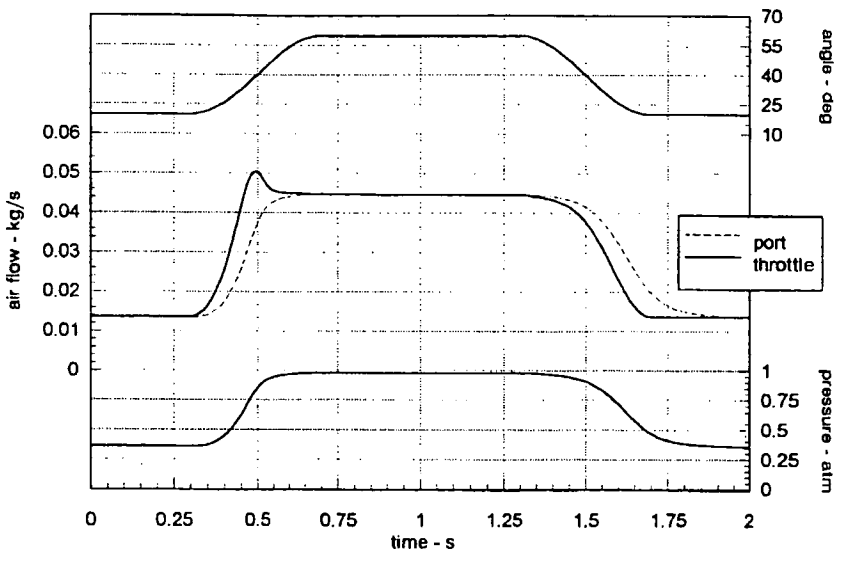

Figure 3-1 Tip in tip out throttle action and its effect on the throttle air mass flow rate and the port air mass flow rate [2].

The mathematical model of the port air mass flow rate will be described below.

If the conservation of mass is applied to the intake manifold that is the volume of space between the throttle plate and the engine valves one obtains,

$$\dot{m}_{at} = \dot{m}_{ap} + \dot{m}_{am} + \dot{m}_{EGR} \qquad \text{Equation 3-6}$$

where,

$\dot{m}_{at}$ = air mass flow rate passed the throttle plate

$\dot{m}_{ap}$ = air mass flow rate at the engine, which represents the actual mass flow rate inducted into the engine

$\dot{m}_{am}$ = rate of change of the mass inside the intake manifold

$\dot{m}_{EGR}$ = exhaust gas recirculation mass flow rate

Assuming the contents inside the intake manifold obey the Perfect Gas Law and assuming the pressure inside the manifold is uniform we can apply,

$$p_m = \rho_m R T_m \qquad \text{Equation 3-7}$$

$$p_m V_m = m_{am} R T_m \quad \text{as} \quad \rho = \frac{m}{V} \qquad \text{Equation 3-8}$$

where, p_m = Intake manifold air pressure

V_m = Volume of intake manifold

m_{am} = Mass of air in intake manifold

R = Universal gas constant

T_m = Intake manifold air temperature

Taking derivative of Equation 3-8 with respect to time and assuming that the time derivative T_m is negligible in comparison to the time derivative of p_m, one obtains

$$\frac{d}{dt} p_m V_m = \frac{d}{dt} m_{am} R T_m \qquad \text{Equation 3-9}$$

Equation 3-9 can be rearranged into the following form

$$\dot{m}_{am} = \dot{p}_m \frac{V_m}{R T_m} \qquad \text{Equation 3-10}$$

Equation 3-10 can be substituted into Equation 3-6 to obtain.

$$\dot{m}_{th} = \dot{m}_{ap} + \dot{p}_m \frac{V_m}{R T_m} + \dot{m}_{EGR} \qquad \text{Equation 3-11}$$

Equation 3-11 above is often expressed in the following form.

$$\dot{p}_m = \frac{R T_m}{V_m} \left(\dot{m}_{th} - \dot{m}_{ap} - \dot{m}_{EGR} \right) \qquad \text{Equation 3-12}$$

Thus the port air mass flow is a function of the following parameters.

$$\dot{m}_{ap} = f^{n}\left(\alpha, T_m, n, p_m, \dot{m}_{EGR}, \dot{m}_{th}\right)$$

The expression in equation 3-12 is referred to as the isothermal port air mass flow model and has been derived on the basis of mass conservation assuming that the intake manifold temperature is known instantaneously and is equal to the ambient and the EGR temperatures [58]. It is assumed in the derivation of this equation that there is no heat transfer to the surroundings and that the intake manifold temperature is uniform and constant [56]. In practice the ambient, intake manifold and EGR temperatures are not equal. The EGR temperature can easily approach 200 °C and the EGR flow can compose 25 % of the total fluid flow entering an engine [48].

3.2.4 Determination of the Air Mass Flow Rate through the Throttle

The mass flow rate through the throttle into the intake manifold can be determined in one of two ways. It can be measured directly using a mass air flow meter placed upstream of the throttle plate to within an accuracy of less than or equal to 3 % or calculated assuming that that the flow of the air through the throttle plate can be described as the flow of compressible medium through a converging diverging nozzle or an orifice. The equations describing a compressible medium through a converging diverging nozzle are presented below.

$$\dot{m}_{at} = C_d A_{th} P_0 \sqrt{\frac{2}{RT_0}\psi} \qquad \text{Equation 3-13}$$

where, C_d = Discharge coefficient

A_{th} = Area at the throttle, which is expressed as nonlinear function of throttle plate angle

The term $C_d A_{th}$ is a nonlinear function of the throttle angle [58]

where, $\psi = \psi\left(\frac{p_m}{p_0}\right)$ is described by

$$\varphi = \left(\frac{p_m}{p_0}\right)^{\frac{1}{k}} \sqrt{\frac{k}{k-1}\left(1-\left(\frac{p_m}{p_0}\right)^{\frac{k-1}{k}}\right)} \qquad \text{Equation 3-14}$$

For pressure ratios below the critical pressure the ratio $\left(\frac{p_m}{p_0}\right)$ is described by

$$\frac{p_m}{p_0} = \left(\frac{2}{k+1}\right)^{\frac{k}{k+1}} = 0.528 \text{ when k = 1.4 for air} \qquad \text{Equation 3-15}$$

For choked flow φ_{max} is described by

$$\varphi_{max} = \left(\frac{2}{k+1}\right)^{\frac{k}{k+1}} \sqrt{\frac{k}{k+1}} \qquad \text{Equation 3-16}$$

Hendricks' et al [55] has modified the expressions of the converging diverging nozzle approach and proposes an alternative method for determining the mass airflow at the throttle plate. Hendricks' model is based on a number of constants, which have to be determined experimentally and are specific to the experimental engine. The model equations are presented below.

$$\dot{m}_{at}(\alpha, p_i) = m_{at1}\frac{p_a}{\sqrt{T_a}}\beta_1(\alpha)\,\beta_2(p_r) + m_{at0} \qquad \text{Equation 3-17}$$

$$\beta_1(\alpha) = 1 - \alpha_1 \cos(\alpha) - \alpha_0 \qquad \text{Equation 3-18}$$

$$p_r = \frac{p_m}{p_a} \qquad \text{Equation 3-19}$$

$$\beta_2(p_r) = \sqrt{1 - \left(\frac{p_r - p_c}{1 - p_c}\right)^2} \qquad \text{if } p_r \geq p_c \qquad \text{Equation 3-20}$$

&

$$\beta_2(p_r) = 1 \qquad \text{if } p_r < p_c \qquad \text{Equation 3-21}$$

where $m_{at1}, m_{at0}, \alpha_1, \alpha_0, p_c$ are constants and $p_c = 0.4125$

Look up tables are employed for the expressions in equations 3-17, 3-18 in model based engine controllers [50]

The modified isentropic converging diverging nozzle model presented above is too inaccurate for actual use [32]. The reason for this is that the flow of the air splits along two paths across the plate (one large dominant flow and one residual flow) [32]. Chevalier et al [59] has presented a more accurate model to determine the mass air flow at the throttle plate, which takes these factors into consideration, but will not be presented here.

Chevalier's model was shown to calculate the air mass flow rate to within an accuracy of less than 3 % the actual flow over the entire operating range upto a $p_r \cong 1$ [32]. However errors of 50 % where encountered at throttle angles above 77 degrees and unavoidable at wide-open throttle operation or when p_r approached 1. Errors in excess of 10 % of the actual air mass flow rate were encountered at throttle angles of 40-60 degrees ($p_r \cong 0.95$-0.98) [32]. The model presented by Chevalier is inappropriate for MVEM for conditions when p_r is close to 1 [32]. This limits the application of the model to real world engine operating conditions as throttle angles of and exceeding 40-60 degrees are commonly encountered during normal driving conditions.

3.2.5 Determination of the Port Air Mass Flow Rate

The speed density equation, mathematically, presented in Equation 3-24, is used to calculate the port air mass flow in many engine management systems. The speed density equation

assumes the engine acts as an air pump and therefore is a function of the engine speed, engine displacement and the engines volumetric efficiency, which is nonlinear parameter.

Volumetric efficiency is defined as the volume flow rate of air into the intake system divided by the rate at which volume is displaced by the piston [17]. Engine cylinders do not get completely charged or filled by air during the induction process due to dynamic losses in the intake manifold, ports and the valve system [60].

$$\eta = \frac{120\, m_{ap}}{\rho V_d n} \qquad \text{Equation 3-22}$$

where, m_{ap} = is the port air mass flow rate which is actually inducted into the engine

V_d = is the displacement of the engine

n = is the engine speed (rpm)

ρ = is either the density of atmospheric air or the density of the air inside the intake manifold

The volumetric efficiency of an engine is a dimensionless parameter, which measures the effectiveness of the induction process of a specific engine [17].

The density of the air inside the intake manifold can be determined by applying the Perfect Gas Equation, assuming the pressure inside the manifold is uniform.

$$\rho_m = \frac{p_m}{RT_m} \qquad \text{Equation 3-23}$$

Substituting Equation 3-23 into Equation 3-22 and rearranging for m_{ap} one obtains the speed density equation.

$$m_{ap} = \frac{V_d n}{120} \frac{p_m}{RT_m} \eta \qquad \text{Equation 3-24}$$

Conventionally the nonlinear volumetric efficiency term in the speed density equation is determined through extensive stationary engine testing over a wide range of engine speeds and load conditions. Conventional engine controllers employ look up tables to determine the volumetric efficiency usually in terms of engine speed and load information provided by sensors.

Hendricks' et al prefers not to model the volumetric efficiency (η) directly but rather the quantity $\eta\, p_i$.

$$\eta\, p_i = s_i(n)\; p_i + y_i(n) \qquad \text{Equation 3-25}$$

where $s_i(n)$ and $y_i(n)$ are positive, weak functions of the crank shaft speed and $y_i \gg s_i$ [48]. This expression holds for many engines and was derived physically in [48], [55].

3.2.6 Crankshaft Speed State Equation

The final MVEM describes the crankshaft dynamics. This model is derived using the conservation of rotational energy on the crankshaft. Energy is transferred to the crankshaft by the torque produced from the air fuel combustion reaction.

The rate of change of rotational kinetic energy of the crankshaft is equal to the actual power that is available to accelerate the crankshaft [1]. The actual power that rotates the crankshaft is equal to the torque (power) generated by the combustion reaction minus any frictional torque losses that are present in mechanical couplings of the piston cylinder arrangement. Pumping and friction losses dissipate the rotational kinetic energy and some of the available energy goes into the load [1].

$$\frac{d}{dt}\left(\frac{1}{2} I n^2\right) = I n \dot{n} = -\left(P_f + P_p + P_h\right) + H_u\, \eta_i\, \dot{m}_f (t - \Delta\tau_d) \qquad \text{Equation 3-26}$$

where, P_f, P_p, P_h = friction, pumping and load power losses

H_u = fuel heating value

η_i = indicated efficiency, a function of (p_i, n, λ)

$\dot{m}_f$ = cylinder port fuel mass flow

t = time

τ_d = mean injection/torque time delay

I = scaled moment of inertia of the engine

n = engine speed (rpm)

$\dot{n}$ = time rate of change of engine speed

Equation 3-29 can be arranged in terms of $\dot{n}$ to obtain the Crankshaft Speed State Equation

$$\dot{n} = -\frac{1}{I\,n}\left(P_f[p_i, n] + P_p[p_i, n] + P_b[n] \right) + \frac{1}{I\,n} H_u\, \eta_i[p_i, n, \lambda]\, \dot{m}_f(t - \Delta\tau_d)$$

Equation 3-27

The rate of change of engine speed is a function of the following parameters.

$$\dot{n} = f^n\left(p_m, n, \theta, \lambda, \dot{m}_f \right)$$

Equation 3-28

The frictional, pumping and load powers are given by regression equations derived from well-known physical arguments as functions of p_i, n [56]. These equations along with the functions developed for indicated efficiency can be found in [55]. The quantities $I, \Delta\tau_d, \dot{m}_f$ are given by the following expressions.

$$I = I_{ac}\left(\frac{2\pi}{60} \right)^2$$

Equation 3-29

where, I_{ac} is the actual moment of inertia for a port injected engine

The mean injection/torque time delay can be approximated as the mean time delay between mixture ignitions [1] and for a four cycle SI engine this is expressed as.

$$\Delta\tau_d = \frac{60}{n}\left(1 + \frac{1}{n_{cyl}}\right) \qquad \text{Equation 3-30}$$

where, n_{cyl} = is the number of engine cylinders

The rate of change of the crankshaft is governed by the amount of torque that is generated which is dependant upon the fuel flow to the engine, which in turn is dependant upon the desired operational air fuel ratio. By rearranging the lambda ratio equation, an expression can be developed for the cylinder port fuel mass flow, ie.

$$\lambda_{des} = \frac{\dot{m}_{ap}}{14.64\,\dot{m}_f} \qquad \text{Equation 3-31}$$

$$\dot{m}_f = \frac{\dot{m}_{ap}}{14.64\lambda_{des}} \qquad \text{Equation 3-32}$$

Equation 3-32 assumes that there is ideal fuelling, assuming no transient fuel film compensation. λ_{des} is the desired operating lambda ratio for those particular operating conditions. The cylinder port mass airflow in Equation 3-32, is calculated by rearranging Equation 3-1.

The MVEM mathematical expressions presented above provide a good theoretical means to describe and analyse the physical processes that occur during engine operation. However, some of the mathematical functions of the MVEM are quite complex, as they are dependent upon nonlinear parameters. The values of these nonlinear parameters can only be determined by applying curve fitting techniques to highly accurate experimental engine data over a wide range of engine operating conditions. The overall accuracy of the MVEM and the complexities associated with their application to real world engine control implementation will be the focus of the next section.

3.3 Complexities with Conventional Mean Value Engine Models

The MVEM's presented by Hendricks' et al [1], use a number of differential equations to describe the three major engine subsystems. The overall engine model has been validated experimentally on a test bed comprising of a 1.1 Litre Ford Central Fuel Injection (CFI) SI Engine in both static and transient engine testing conditions over the engines entire speed and load ranges. The model has shown to estimate various engine state variables to within an accuracy of 2 %, during both static and transient engine testing, which is comparable to the accuracy of a typical engine dynamometer [1].

Although the model is very accurate, there are a number complexities involved with MVEM's which have prevented them from totally replacing current look up table based control strategies. One reason is because the many of the equations of the MVEM's are a function of a number of nonlinear "fitting constants". In order to determine values for these parameters and hence develop a valid MVEM, comprehensive engine testing and data acquisition is required and thorough data analysis needs to be conducted involving regression fitting. After this the model then has to undergo subsequent validation to see if the regression fitting process is adequate and the model meets a desired level of estimation accuracy. If this is not met, further engine testing is required to fully define conditions where estimation accuracy is poor. This process must occur over a wide range of engine speeds, load conditions and engine temperatures.

The estimation accuracy of Hendricks' MVEM's relies on extensive and time consuming engine testing and detailed processing of the collected data, which often makes the approach difficult to implement in some instances [6]. The equations of the various subsystems of the MVEM are physically based and thus the model has to be "calibrated" to the specific engine under investigation. The amount of engine testing which is used to calibrate or match/map the MVEM to a specific engine greatly effects the performance of the model in terms of its estimation accuracy. Using all the MVEM in a production engine controller would require a human intensive, laborious and an exhaustive calibration process similar or greater than what is currently required in the development of conventional engine fuel maps. The dominant reason an extensive amount of engine testing is required is because the MVEM differential

equations are functions of nonlinear variables that vary strongly with engine operating conditions.

Hendricks' intended to develop mathematical expressions of the MVEM that were based on the least number of fitting constants where possible, while still ensuring a model that fully described the engine subsystems and possessed high accuracy in the estimation of the engine variables. The advantage of developing expressions based on minimum number of fitting constants is that it reduces the complexity of the model calibration process. However, the complex nature of the modelling problem requires the use of some fitting constants to adequately describe the engine subsystems. Both the fuel flow evaporation dynamic submodel and the crankshaft dynamic subsystem are strongly dependent upon fitting constants.

The fuel flow evaporation dynamic submodel, which describes the path of fuel to the engine combustion chamber is a function of a number of fitting constants, variables that can not be measured or quantified directly. These nonlinear fitting constants include the parameter X and the time constant τ, which are described above in Section 3.2.2.

Practically it is not possible to directly measure the fuel film flow or the fuel vapour flow and therefore the total amount of fuel that actually enters the engine cylinders. The parameters X, τ unlike many other nonlinear parameters such as volumetric efficiency of the model can not be determined from steady state engine measurements. This means that the parameters X, τ can only be found using optimum fitting procedures by applying classical and advanced statistical identification techniques based on the maximum likelihood [1]. Values for the X, τ have to be determined over a wide range of engine operating conditions and are both dependant on engine operating temperature. The X parameter is represented as a function of the throttle position $(X(\alpha))$ for a series of different operating points and specific engine temperature using curve-fitting techniques.

Algebraic functions for the crankshaft dynamic submodel parameters, P_f, P_p, P_b, η_i and for the manifold filling dynamics parameters $\eta_{vol}, \dot{m}_{at}$ are developed in terms of the engine state variables from data collected from steady state engine measurements [1]. These parameters are approximated as polynomial functions of one or more of the following variables, engine

speed, manifold and exhaust pressure and lambda ratio and rely on correction terms to account for certain physical occurrences, such as engine pumping losses. The polynomial coefficients are estimated by employing advanced curve fitting techniques using regression analysis on data collected from engine measurements. A great effort is expended in finding the physically correct regression variables before even attempting to make a regression fit [1]. Even once a regression fit has been obtained, more effort is necessary in testing the statistical hypothesis that the correct and optimum number of regression terms are used and that the functional representation used is minimal [1].

This fitting process and subsequent validation is time consuming as it is based on a model optimisation process that seeks the most accurate model using "educated trial and error". This process can become difficult, as there are a large number of parameters that have the potential to be changed. Changing the degree or power of the curve fitted polynomial can have a significant effect to the fitting performance of the mathematical function to the collected experimental data. In addition, the polynomial expressions developed by the curve fitting process can only be regarded as an approximation or an estimate of the modelled engine parameters to within a certain accuracy range. The accuracy of these models will vary over time due to engine wear and aging and model performance will also differ due to engine manufacturing tolerances. The only way to update the algebraic functions over time is to compensate for aging effects and this would require a similar engine testing and model calibration process that was necessary in the development of the model in the first place.

It is unlikely that MVEM's will be implemented in their entire mathematical forms in modern engine management systems. As a result it is unlikely that MVEM's will be able to completely fill the void needed to meet the exhaust gas emission targets of the next decade. Consequently, there is a need to find alternatives to the MVEM's or better ways of representing them. Alternatives MVEM's should have the potential to accurately estimate engine variables with a reduced amount of development time. The following section highlights the inadequacies of convention AFR control systems and demonstrates a need for research into potential alternative engine modelling techniques.

3.4 Need for Intelligent Engine Modelling Techniques

Precise control of the AFR is critical in modern engine operation for optimum engine performance and for minium engine emissions [61]. If the automotive industry does not develop additional methods and or strategies to improve AFR control it may encounter problems meeting future exhaust gas emission legislation. Automotive manufactures must not only abide by tightening government emission legislation but at the same time satisfy consumer demands in providing a reliable engine that runs smoothly, has low fuel consumption and delivers sufficient power [6].

Currently feedforward look up table control algorithms with a feedback signal provided by a lambda sensor is used together with a catalytic converter in the control of the AFR and automotive emissions. This technology is only able to obtain tight control of the AFR during steady state engine operation as described in detail in Section 2.7. The aim of future fuel injection control systems is to maintain tight control of the AFR ratio in all driving conditions, both in steady state and transient engine operation. This is particularly important, as the use of catalytic converters is compulsory in today's modern automobiles due to successive amendments to the emission legislation. The catalytic converter is widely regarded as the critical device that until now has maintained and regulated exhaust gas emission levels below the targets set out in legislation.

The maximum efficiency of a catalytic converter is achieved only when the engine is constantly operating at the stoichiometric AFR value as described in Section 2.6.2 (14.64) [3], [4], [62]. The conversion efficiency is also very sensitive to changes in the AFR, as a ± 1 % deviation from the stoichiometric AFR value may result in up to a 50 % reduction of the efficiency of the catalytic converter in reducing pollutants [3], [4]. To minimise automotive generated pollution it is therefore paramount that future fuel injection control systems can precisely determine the correct amount of air entering the engine and hence be able to inject the correct amount of fuel, in order to maintain the AFR to within this ± 1 % boundary of the stoichiometric AFR in all driving conditions.

Until now the existing fuel injection systems have been able to control the AFR to a sufficient level to meet current emission legislation and satisfy the demands of the consumer. Further

amendments to the exhaust gas emission legislation over the next few years will significantly stretch the capabilities of the conventional control strategies in maintaining sufficient control of the AFR. As an example the state of California in the USA, which has the strictest emission legislation in the world, in 2003 will introduce legislation requiring 10 % of all production vehicles to be zero emission vehicles [13], [60]. The remaining 90% of vehicles manufactured will need to reduce their allowable levels of exhaust pollution by as much as 60-84% of current legislative values [13] [60].

The first signs of the inadequacy of conventional fuel injection systems in the control of the AFR are already apparent with standard engine control technologies unable to avoid large AFR excursions during transient operation as described in Section 2.7. Conventional AFR control algorithms perform poorly during transient conditions as they are based on look up tables, that are developed by non-dynamic modelling techniques.

To meet tightening emission legislation automotive manufactures have so far primarily focussed on improving the hardware side of the fuel injection control system, by developing more advance sensors of higher accuracy and lower response times, more precise fuel injectors and implementing ECU's with faster microprocessors. Very little progress has actually been made by automobile manufactures in developing and implementing totally new techniques or algorithms of controlling the hardware of the fuel injection system. More advanced AFR control systems have been published in literature, however automotive manufactures as yet have not implemented these methods in full scale ECU production.

This is evident, as the control of most modern fuel injection systems are still based or rely heavily on feedforward look up tables, the operating principals of which have basically remained unchanged over the past decade or more. Hybrid engine controllers are now emerging which are partially based on simplified MVEM's subsystems and look up tables. This development has taken approximately a decade since the complete MVEM was first published. However there are a number complexities involved with the MVEM's which prevent them from being implemented in an engine management system in their entire form, as the sole engine control algorithm. These were as described above in Section 3.2.

Until now, the increasing demands of emission legislation have been met simply by approaching the control problem in a more comprehensive and detailed manner through the

introduction of a larger number of compensation factors that attempt to improve the poor performance of modern engine controllers during transient engine operation. Additional looks up tables are employed to reduce the effect of cold start operation, and different types of transient throttle operation. The outcomes of this approach has resulted in a significant increase in the amount of engine testing, tuning and calibration work necessary in the development of additional compensation maps and as a result a large rise in the cost of engine model development.

Legislation is also being introduced requiring maintenance of low emission levels over the lifetime of a vehicle [59]. This is an additional challenge, as fuel injection systems are developed for new engines and most are unable to adapt to the changing engine characteristics over time [59]. Over the life of the engine the control system becomes outdated as a result of engine wearing. Currently feedback control from a lambda sensor compensates for age and wearing effects and for variations in engine to engine manufacturing tolerances. However, feedback control is unable to correct AFR excursions during transient operation due to the large time delay associated with its signal, as described in Section 2.6.1.

In order to achieve precise control of the AFR in all driving conditions a new "smarter" control strategy is required, that is not simply a variation on the feedforward look up table based strategy and thus is removed from the problems associated with such a control algorithm. A more sophisticated approach is needed that is easily adaptable over the life of the engine, the accuracy of which does not rely upon extensive and laborious engine testing and which can provide accurate control during transient engine operation.

Artificial Intelligence, in the form of Artificial Neural Networks is one suitable alternative that has the potential to totally replace the conventional look up table fuel injection control systems and perhaps revolutionise AFR control. Neural Networks are ideally suited to such an application due to their proven ability in capturing complex highly nonlinear relationships. The major advantages of neural networks will be discussed below highlighting their significant advantages over alternative control strategies.

3.5 The Advantages & Strengths of ANN

ANN have a number of significant advantages over conventional modelling techniques and are ideally suited to engine modelling and control due to their proven ability to characterise complex highly nonlinear systems with a high degree of accuracy. Neural networks offer a different way to analyse data and to recognise patterns within data, than traditional computing methods [63]. ANN have also been used in problem solving situations which were found to be to difficult to handle by conventional control techniques, especially those which are hard to characterise [64]

The main advantages of ANN over conventional modelling techniques, is in their capacity to model nonlinear systems without relying on existing analytical relations between input and output variables. Hence, the input variables to neural networks are not restricted to those for which mathematical relationships already exist. Below is a summary of the major characteristics of ANN's. The information presented here is primarily based on the ideas presented in [62], where the advantages and strengths of ANN are discussed under the following headings in some detail.

3.5.1 Generality

Neural networks are learning systems and their ability to model a process is dependent upon the training data. A major strength of ANN's is their flexibility to be applied to a variety of different problems without the need to change the way they operate. Another benefit of ANN's is that it is easy to implement such models in both hardware and software. This is mainly due to ANN being simple in all aspects of their design and configuration. ANN are composed of a number of simple processing elements called neurones. The architecture of ANN's is relatively simple, and communication between various components is uncomplicated, communicating through a rich set of interconnections with variable weights or strengths [65].

3.5.2 Adaptively

Neural networks learn to reproduce a response for a given input [62]. When an ANN receives new or unseen inputs they have the potential to adapt to produce the right output for the given input. Likewise if certain inputs are no longer received by the model and hence no longer acted upon the ANN over time will forget the relationships between the outdated input and output creating more room for the learning of new patterns. ANN's are taught a number of basic skills or instincts regarding the system it will model. Once these basic skills have been established the model can be placed in the control environment where it has the potential to develop and update its skills in real time by relearning the relationship that exists between the input and output from feedback provided by sensors. Such a capability is advantageous in complex changing environments where it is impractical or too expensive to reprogram the control systems.

3.5.3 Feature Selection

Neural networks have the ability to detect correlations and recognise trends between input data and a specific output. A major advantage of neural networks is that decisions are made on the basis of identifying relevant trends in data. Consequently irrelevant information such as noise, which is a random distortion and has no recognisable pattern or association with the desired output is ignored and hence has no bearing on the ANN solution. Computers on the other hand are not capable of recognising even simple patterns and the accuracy of the control response is dependent upon the quality of information presented [61]. That is ANN can detect and pick out those features or trends in data that influence the response of certain outputs [62].

3.5.4 Tolerance

Neural networks are tolerant against damage, because each component of the network contributes a small part to the output, which reduces the importance of individual components [62]. This means if part of the neural network becomes damaged the network will not immediately fail, but will continue to operate using its available processing power. Also ANN's have the ability to operate with missing input information, which may arise due to possible sensor failure. In such circumstances the ANN produces the optimal or best results it

can, based on the information made available to it. As expected the output of ANN models is less accurate and of a lower quality during operating conditions involving network damage or missing input data. As mentioned above ANN's are also tolerant against noisy input data.

3.5.5 Imprecision

In the real world it is not possible to find exact or perfect solutions to many problems due to financing, time constraints or the complexity of the problem at hand. In practical applications ANN's are becoming very attractive and popular as they can provide good solutions to difficult problems quickly and with small development times, reducing implementation costs which is a crucial factor in industrial applications.

3.5.6 Self Programming

NN are not programmed how to do things, they are taught what to do [62]. This makes system development easier, if there is little knowledge about the actual complexities involved with the problem and hence if an accurate analytical model is difficult to develop. As a result ANN have been likened to "black boxes" as the actual system model which the network utilises in arriving at a solution is unknown. ANN have been successfully implemented in situations where conventional techniques have failed due to programmers over complicating the control problem [62].

The advantages of neural network modelling are evident from the information presented above. The next section reviews some of the recent research that has been conducted using neural networks in the control of the AFR and the prediction of other engine parameters. The review demonstrates some of the advantages of using neural networks in the modelling and control of various engine parameters.

3.6 ANN Applied to Engine Modelling & Engine Management Systems

Applying neural network models to vehicle engine management systems is not novel and a significant amount of research has already demonstrated the advantages of using neural networks models over convention look up table based engine management systems [66]. This

is clearly illustrated by [6], [67] who replaced conventional engine lookup tables with a Neural Network model equivalent and demonstrated an increase level in performance when the Neural Network model was used, due to their nonlinear interpolation capabilities. However there have not been many papers published using neural networks directly as controllers of engines [56].

Research into the application and viability of neural networks in the modelling of SI engines first appeared in the early 1990's. Since then a large amount of research has been published on the application of neural networks into engine fault diagnosis, such as [14] and the possible replacement of specific sections of the engine control strategy software with neural network based systems [64].

Many researchers have attempted to represent the physical subsystems of the MVEM's using neural network modelling [56]. Thus, the description of the MVEM provided above is considered essential for the thorough understanding of current research that will be reviewed below. Presented below is a review of research that has been published in the area of neural network IC SI engine modelling and control over the past decade. The literature review has shown that neural network engine related research can be distinguished into two main groups, on the basis of the types of sensors used in the research. Research based on conventional automotive sensors is considered a group while research based on unconventional sensors is considered a seperate group. Unconventional sensors encompass cylinder pressure sensors, for example [68], [69] and using the spark plug as a "sensor" to analyse the ionisation current [70], [71].

The focus of this review is on research undertaken into the application of neural network modelling to the prediction and control of engine management parameters, using only conventional sensors, currently used in engine management systems. The review is primarily concerned with research dealing with the control of the AFR of IC SI engines using neural networks.

Alippi et al [4] investigated the use of recurrent neural networks in the prediction and control of the air fuel ratio. The recurrent neural network consisted of 15 inputs and a single output. The inputs to the neural network included two delays for the manifold pressure, engine speed, and throttle position at times t, t-1, t-2 and three delays of output dynamic, the predicted AFR

at time t-1, t-2, t-3. Training data consisted of simulated and real data obtained from an Alfa Romeo 1.3 L engine decimated at 30 Hz. Simulated data was corrupted by a white noise with an intensity 3 % of the amplitude of the signal.

The neural network architecture was optimised by varying the number of hidden layers and the number of neurons per layer. Selection of the optimum neural network architecture was based on the prediction accuracy of the models, defined in terms of the mean percentage error. The final model predicted the AFR to within a mean percentage error accuracy of 1.27 % and its architecture consisted of a single hidden layer with 15 neurons.

Control of the AFR is achieved by using a neural network model, which receives inputs of manifold air pressure at time t, t-1, engine speed at time t, throttle position at t and t-1 and the integrated error between the desired AFR and the a neural network predicted AFR at time t, t-1,t-2 to estimate the fuel injector opening time. The neural network control structure was validated using simulated and real transient engine data consisting of tip in tip out movements of the throttle. Four different AFR control validation experiments were conducted on the test engine and it was found that the neural network model based controller outperformed the conventional controller in maintaining the AFR to the optimum stoichiometric value.

The comparison between the two controllers was made, by recording the number of times the controlled AFR deviated from the desired AFR by 3 %. Averages of the four experiments show that the conventional controller was found to be outside the desired AFR operating range 3.46% of the testing time while the neural network control structure was outside the this zone on average 0.83% of the testing time. This demonstrates the obvious potential of neural network based control schemes in AFR control.

Dong et al [72] demonstrated the application of neural network modelling to detect soft failures of sensors and actuators automobile engines. Wong developed a dynamic two layer feedback neural network to predict manifold pressure, using three feed forward inputs and a single feedback input. The three feed forward input variables consisted of the mass air flow rate, EGR valve position and engine speed and the predicted manifold pressure value was used as the feedback input to the network. The architecture of the neural network consisted of four input neurons, sixteen hidden layer neurons and a single output layer neuron. The neural network was trained using the back propagation technique.

The neural network training and testing data was collected on an experimental testing vehicle under normal city and highway driving conditions. A fault was introduced into the data by using a fault generator. Two separate data sets were collected one with a simulated manifold pressure sensor reading 80 % of the true value. A second set of data was collected using a fault of the same nature introduced into the EGR reading, which had the effect of increasing the manifold air pressure by approximately 5 %.

After training the neural network model was able to identify a normal vehicle sensor output from a faulty output and thus be able to diagnose a fault. The performance of the network was validated using a separate data set. The authors of the paper suggest the neural network can predict the manifold pressure accurately, however fail to provide any information regarding the actual error margin in network prediction.

For fault diagnosis the authors believe the best method, especially for small changes in the manifold pressure output, with the EGR fault generated data is to use the residual variance, the variance of the difference between the predicted and measured manifold air pressure values. The authors confirm this by providing graphical evidence illustrating that the variance from the EGR faulty data is significantly greater than the variance of the normal data set. The authors also confirm the accuracy of their model on data collected with different drivers at the wheel. The authors claim that the network is still able to detect faults when different driver are at the wheel. The research demonstrates the usefulness of applying neural network technology for engine modelling and diagnosis purposes.

Hodgson et al [2] developed a neural network model to predict the transient air mass flow at the engine intake ports. The authors of the paper applied the MVEM manifold filling emptying model relationship to describe the manifold filling dynamics and characterise the engines transient port air mass flow. The MVEM was implemented and calibrated on a 1.8 L port injected engine.

The air flow at the throttle in this research was estimated using the standard equations for the flow of a compressible fluid past an orifice. Two neural network architectures were employed for prediction purposes, namely a multilayer feedforward network that predicts the mass air flow and manifold pressure under steady state operation and a recurrent Elman network which predicts the transient port mass air flow at the engine ports. Backpropagation

was used to train the Elman network architecture and the Lavenberg Marquardt was used to train the feedforward network.

Real engine data acquired from dynamometer testing was used to train the neural network. The neural network training data set consisted of 48 static engine-operating points collected at various constant throttle and constant engine speeds by varying the load on the engine. Throttle position and engine speed were used as inputs to the feedforward neural network for the prediction of air mass flow. The architecture of the neural network consisted of two input neurons, two hidden layers of four neurons each and two output layer neurons, a 2:4:4:2 structure. The neural network was trained for a 1000 epochs and the model possessed a RMS error of 623 Pa in the prediction of the manifold air pressure and a RMS error of 4.7×10^{-4} kg/s in the prediction of the air mass flow.

The training data for the Elman network consisted of several tip in tip out examples generated from the air flow model [2]. There were three inputs to the neural network model, namely throttle angle, engine speed and mass air flow for the prediction of the transient port air mass flow. The RMS error for the prediction of the transient port air mass flow was not provided in the paper. However the authors detail that a more comprehensive set of data is required to adequately train the model during transient tip in tip out operations as the prediction accuracy of the model deteriorates when the unseen validating data differs from the training data set.

(74)
Asik et al [73] developed a neural network model to estimate the AFR and used the output of the model in a conventional closed loop AFR control system as the replacement for the feedback signal normally provided by an exhaust gas oxygen sensor. The authors believe that the estimator would be especially useful during cold start engine operation, as the feedback control signal from the lambda sensor is unavailable until it reaches a certain operating temperature and as a result the engine management systems operate in open loop control. The neural network AFR estimator could also be used as contingency feedback signal to the engine management system if the lambda sensor was not functioning due to failure.

Data was collected from the first 40 seconds of the standard Federal Test Procedure 1975 and used to validate the performance of the neural network model. Testing was conducted on a 4.6 L V8 engine mounted in a test car. The developed neural network architecture consisted of eight inputs, two hidden layers and one output the estimated AFR. The input parameters

consisted of engine speed, cylinder air charge, spark advance, engine coolant temperature, automatic transmission speed ratio and a metric derived from the crankshaft fluctuations induced by rapidly altering the fuel ijection pulse width. These inputs were selected based on prior system identification [71].

The neural network model was trained on data gathered during lean, rich and stoichiometric engine operation. The neural network estimator is more accurate in predicting the AFR than a regression estimator the authors developed previously and also shows better correlation with the actual AFR measured by a Universal Exhaust Gas Oxygen Sensor (UEGO). The neural network estimator has a tendency to underpredict the AFR generated by the UEGO sensor during lean and rich engine operation.

The AFR control structure was achieved by implementing a conventional PID controller and using the neural network estimated AFR signal to replace as the feedback signal provided by an UEGO sensor. The results indicate that the neural network PID control system has slightly improved performance in comparison to a similar control structure based on a previously developed AFR regression estimator.

[75]

Shayler et al [74] demonstrates the use of a back-propagation neural networks in the development and implementation of an open loop control of the AFR during transient engine operating conditions. A Transient Fuel Compensation model, based on Aquino's approached is replaced by a neural network model in this investigation.

The developed back-propagation neural network consisted of three inputs and a single output, the transient fuel compensation required. The inputs to the network included the engine airflow rate, the engine temperature and the fuel film mass deposited on the intake manifold runners. The fuel film mass was determined by considering the fuel injected during the last cycle and solving the differential equations based on the Aquino model. TFC is supplied until the calculated fuel film mass reaches the value for which the network learned to supply zero fuel for that air flow and temperature [54].

Training data consisted of nine transient data sets collected on a 1.8 L Zetec engine mounted on an engine dynamometer. Transient driving conditions were simulated by a tip in tip out movement of the throttle expressed in terms of change in normalised airflow rate.

An optimisation technique was used to determine the final architecture of the network. The network architecture that provided the least AFR deviation from the stoichiometric value during training was selected as the final model. The final 3:5:1 architecture is able to model the training data to within 0.1 AFR units.

The authors also present an alternative training method for the model without the need of prior knowledge of the intake port characteristics [54]. The architecture inputs, are the same, however the fuel film mass is determined by deriving a quadratic expression as a function of airflow rate. This trained neural network is able to reduce AFR excursions to below 1.2 AFR units for a range of validation transients. Results indicated acceptable performance with the benefit of vastly simpler calibration procedures the elimination of a number of look up tables and fast development time.

Beaumont and Frith [59] demonstrate the potential viability of using neural networks for adaptive transient AFR control. The inputs to the neural network model consisted of delayed and filtered engine measurements and the fuel pulse width, the output of the model is the AFR. The actual architecture of the developed model is not discussed. Information on the actual "relevant engine measurement" inputs to the model are also not presented. The model was trained using back-propagation to give six AFR predictions ranging from 0.13 to 0.23 seconds ahead of the current time [59]. The ahead of time prediction considers the time delay associated with the exhaust gas oxygen sensor measurement, which is dependent upon engine speed.

Unworn and worn simulated engine data was used in this research to train and validate the neural network model. The authors generated the simulated data from a Simulink simulation of the air, fuelling and exhaust dynamic engine processes, which had previously been validated, with experimental data. Transient engine data was generated in the simulation software by applying step changes to the throttle position. Eight sets of worn and unworn data were generated, at a sampling rate of 100 Hz, for 100 seconds. Before training commenced the "a realistic level of noise" was added to the simulated data. Four data sets were used for network training, two sets for intermediate network validation and the final two sets were kept as "unseen" for final network validation.

The author's definition of the AFR error is vague and the paper does not discuss the actual prediction accuracy of the developed neural network model. Graphical plots of the AFR error suggest it is less than 1 %. The authors suggest that the developed neural network models provide an accurate prediction of the AFR. The authors propose an AFR control strategy using the predicted AFR as an input to a nonlinear equivalent of a Generalised Minimum Variance (GMV) control law. The authors believe that ANN's are potentially a viable technology in adaptive AFR control.

-[63]

Shiraishi et al [60] used a cerebellar model articulation controller (CMAC) neural network to maintain the AFR at its stoichiometric value. The CMAC model developed, is based on the speed density method of estimating the mass flow rate at the intake valves. The CMAC neural network consists of two inputs, engine speed and manifold air pressure to predict the air mass flow at the intake valves. The authors assume that the manifold temperature is almost constant and changes in its signal are slow enough for the CMAC algorithm to adjust to the changes in its learning mechanism.

The initial weights for the CMAC model are based on values derived from previous research. The weights of the model are updated with feedback information from a switching exhaust gas oxygen sensor using a learning gain. The learning gain is set small enough for the weights to converge to the desired value to maintain the a stoichiometric AFR.

Training and validation was conducted on a 1988 Oldsmobile Cutlass Calais with a Quad-4 DOHC four cylinder engine. A toggle was mounted in the testing vehicle to switch the injector control signal between the vehicles standard ECU based controller with the developed CMAC controller. This was required in order to make a comparison between the effectiveness of the two different control strategies.

AFR control was achieved by using the mass airflow predicted by the CMAC model and calculating the injector opening. Transient engine operation was used to train and validate the AFR controller. This comprised of a number of tip in tip out throttle movements, ranging from a change in throttle position from 0 to 50 degrees in approximately ten seconds. This was achieved using a throttle position controller. The results indicate that the CMAC controller is comparable with the ECM under most operating conditions with as little as

thirty-minutes training and believe controller improvement can be achieved with additional training.

Majors et al [75] continued the initial work presented by Shiraishi et al [60]. The exact same experimental test rig was used to train and validate the controller with the exception that the switching exhaust gas sensor was replaced with a linear exhaust gas sensor. The weight adjustment learning algorithm used in [73] has been replaced. The new adjustment algorithm is based on a learning gain applied to the difference between the fuel required to maintain stoichiometric operation and the previous amount of fuel injected.

Experimental results based on tip in tip out operation indicate an improved performance in maintaining the AFR to the stoichiometric value. During one transient, the CMAC controller maintains the AFR to within the 1 % AFR operating window which is required to maintain catalytic converter efficiency above 80 %. With sufficient network training, the AFR deviation is lower with the CMAC control strategy than those experienced with the standard production ECU controller on the same transient data sets. The authors believe "the results demonstrate that the CMAC controller has excellent potential for good emission performance" [76]. The research illustrated that a neural network is capable of improving upon the AFR control performance of traditional fuelling control strategies under certain load and engine speed conditions.

Recent research using ANN's in automotive applications was presented above highlighting the advantages of using neural networks in the modelling and control of various engine parameters. The next section reviews the Neural Network Algorithms that will be used in this research, providing a description of the network's structure and learning algorithms.

3.7 Review of the Neural Network Algorithms Used in this Research – Back Propagation Network and Optimised Layer By Layer Network

Two types of multilayer perception feedforward neural network paradigms will be used in this investigation. These are the Backpropagation Neural Network and the Optimised Layer by Layer Neural Network. In this section, the important characteristics and features of

feedforward neural networks will be described and the particularities of each of the above networks will be discussed in terms of network structure and the learning algorithm used in network development.

3.7.1 Feedforward Networks

In a feedforward network, input activity signals propagate in one direction only, from the input stage through intermediate neurons to an output stage. This type of neural network has one input layer, one output layer, and any number of hidden layers in between [76], [77]. The basic architecture of a feedforward network is shown in Figure 3-2 with the main features labelled.

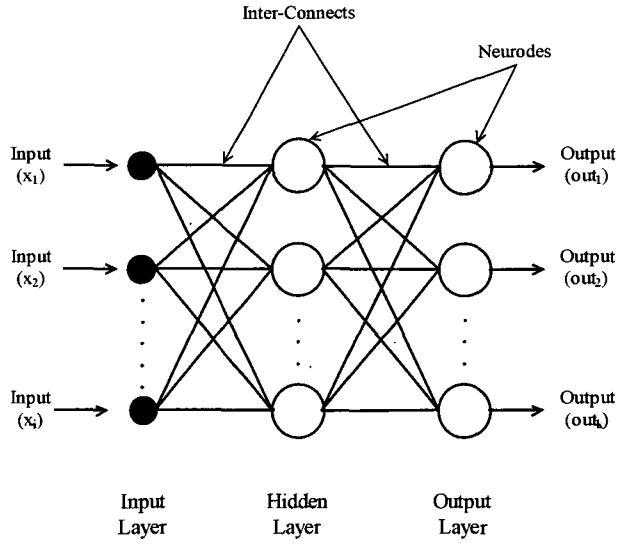

Figure 3-2 Basic Structure of a Multi-Layer Feedforward Network [77]

Each layer in the network contains neurons, which receive any number of inputs, process those inputs and send a single output to other neurons in the subsequent layer. The neurons in the input layer receive information from a knowledge base while the output layer neurons send information to the surrounding environment. The neurons in the hidden layer are the processing units of the network.

3.7.2 Backpropagation Network

Backpropagation is the most widely used of the neural network paradigms and has been applied successfully in applications studies in a broad range of areas. Backpropagation networks are multi-layered feedforward neural networks that are trained using the error backpropagation procedure, a supervised mode of training. Backpropagation is a systematic method for training multi-layered artificial neural networks and is a form of supervised training [78].

3.7.3 Architecture

The architecture of a backpropagation network, shown in Figure 3-3, consists of an input layer, one or more hidden layers and an output layer. There are i input nodes, j hidden nodes and k output nodes. All input nodes are connected to all hidden nodes through weighted connections, w_{ji}, and all hidden nodes are connected to all output nodes through weighted connections, w_{kj}.

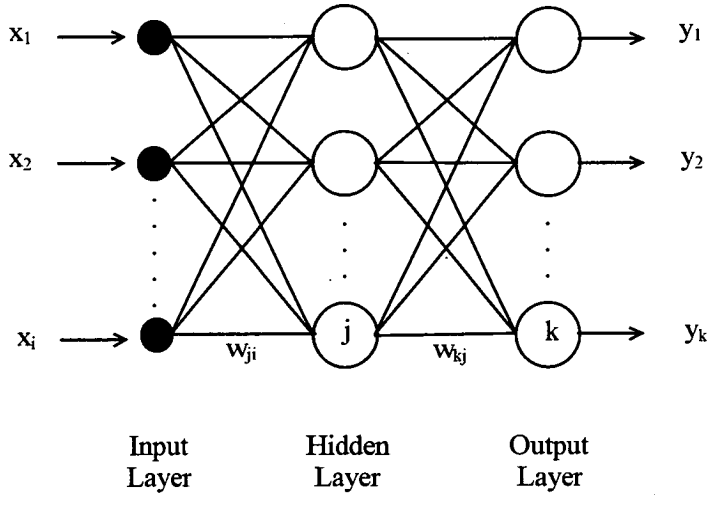

Figure 3-3 Basic Structure of a Backpropagation Network [77]

The sole function of the input neurons is to pass forward input patterns to neurons in the hidden layer. In this type of feedforward network there are no connections leading from a unit to units in previous layers, nor to other units in the same layer, nor to units more than one layer ahead [79]. Hence, every neuron in each layer communicates only with neurons in the

immediate following layer. Only the hidden layer and output layer neurons complete any type of processing. The neurons in these layers perform three functions; an input function, an activation function and an output function. The input function performs a summing of the inputs and synaptic weights. It is a linear function and is given by the equation:

$$net_j = \sum_j x_i w_{ji} \qquad \text{Equation 3-33}$$

where, net_j = weighted summed input to neuron j,
x_i = input to input node i to neuron j
w_{ji} = weight connecting input neuron i to hidden layer neuron j,

The most common activation function used in backpropagation networks is the logistic function, which is a nonlinear sigmoidal function given by the following equation:

$$y_k = f(net_j) = \frac{1}{1+e^{(-net_j)}} \qquad \text{Equation 3-34}$$

Hence, the input function summation is used in the processing performed by activation function. The purpose of the output function is to pass forward the output of the activation function. Hence, the output function is a linear function, and is equal to the output of the activation function.

3.7.4 Backpropagation Learning Procedure

Each training pattern presented to a backpropagation network is processed in two stages. In the first stage, the input pattern presented to the network generates a forward flow of activation from the input to the output layer. In the second stage, errors in the network's output generate a flow of information from the output layer backward to the input layer [77]. The error backpropagation procedure uses a gradient descent method which adjusts the network weights by an amount proportional to the derivative of the error function, this will be explained below [80]. The calculation of associated error for a given input pattern is

determined only after the forward propagation of the pattern is complete. That is, for each neuron in the output layer of the backpropagation network a single real number is output, which is compared to a target value presented with each input pattern. The error associated with this comparison is then used to update the weights for all interconnections from the output layer through to the hidden layers. Similarly, an error value is calculated for all neurons in the hidden layer immediately prior to the output layer, and subsequently, all weights are updated for interconnections that form inputs to this hidden layer. This process is completed until the all the weights between neurones have been updated in this manner.

3.7.4.1 Output Layer Weight Adjustment

Network connection weights are adjusted on the basis of minimising the error function, that is the error between the desired or target output and the actual output of the neural network. This is achieved by calculating the derivative (or slope) of the error function using the chain rule and finding where this curve is minimum. This is done by adjusting the network weights using an iterative process in the direction, which provides the greatest rate of decrease of the error until the minimum is found. Figure 3-4 below shows a representative error curve showing the nature of the iterative solution. In order to decrease the predictive error, positive and negative step adjustments are made to the value of the weights until the direction of the gradient becomes negative and ideally with sufficient weight adjustment converges to zero.

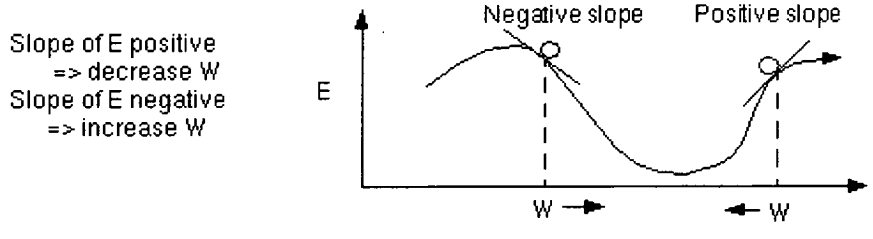

Figure 3-4 The effect of increasing or decreasing the network weights on error minimisation [81]

The error function is displayed below.

$$E(w) = \frac{1}{2}(t_k - y_k)^2 \qquad \text{Equation 3-35}$$

Applying the chain rule

$$\frac{dE(w)}{dw} = \frac{dE}{dy} \times \frac{dy}{dw} \qquad \text{Equation 3-36}$$

where $\frac{dE}{dy} = (y_k - t_k)$ Equation 3-37

$$\frac{dy}{dw} = f'(net) \qquad \text{Equation 3-38}$$

The gradient of the error function using the chain rule is often represented by δ, and is simple to compute for the output layer and somewhat more complicated for the hidden layers [82]. Considering firstly the output layer, for neuron *j* in the output layer, the error gradient is [79]:

$$\delta_k = (y_k - t_k) f'(net_k) \qquad \text{Equation 3-39}$$

where,

	y_k	=	$f(net_k)$ output value for unit *k*
	t_k	=	target value for unit *k*
	$f'(x)$	=	derivative of the sigmoid function, and
	net_k	=	$\sum_j z_j w_{kj}$ weighted sum of inputs to k

Hence, the quantity $(y_k - t_k)$ represents the difference between the network prediction and the target output while the derivative of the sigmoid function is used to scale the error. For the commonly used sigmoid function, the maximum value of the derivative corresponds to the point of maximum slope on the function curve. It is useful to reproduce a graph of the logistic function here along with a graph of the derivative of this function in order to highlight this important relationship, as shown below in Figure 3-5 (a), (b). It can be seen that by including the derivative term in the error value calculation, the error is scaled to make a larger correction when the weighted sum of the inputs is small, close to zero, and a smaller correction when the absolute value of the weighted sum of the inputs is large.

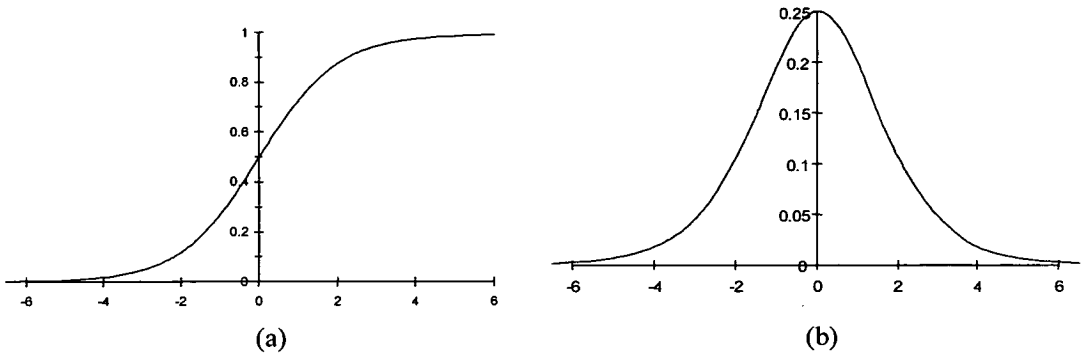

(a) (b)

Figure 3-5 (a) Logistic Function (b) Derivative of the Logistic Function

3.7.4.2 Hidden Layer Weight Adjustment

For hidden layer neurons, the associated input and output weighted connections are shown below in Figure 3-6 to illustrate the weights that are to be considered in the weight update for hidden layer neurons.

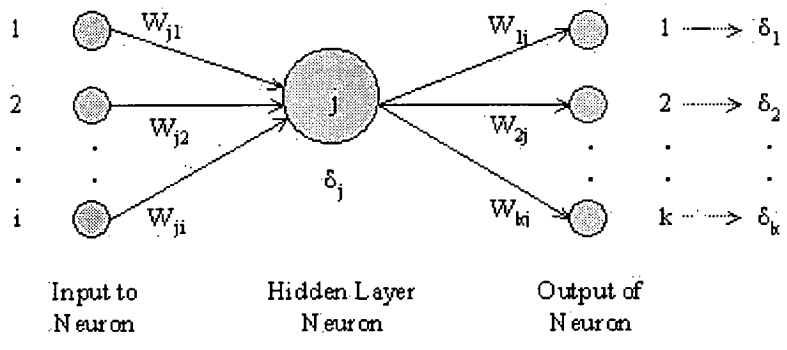

Figure 3-6 Hidden Layer Processing Neuron [79]

For neuron j in the hidden layer the error value calculation considers the weighted sum of the δ values of all neurons that receive output from neuron j. Hence, the error value calculation for the hidden layer is written as [79]:

$$\delta_j = \left[\sum_k \delta_k w_{kj}\right] f'(net_j) \qquad \text{Equation 3-40}$$

where w_{kj} = weight connection to neuron *k* from neuron *j*

The weight adjustment for the interconnections of the output and hidden layer neurons is now calculated using the respective δ values. Therefore, each interconnection weight is adjusted by considering the δ value of the neuron that receives input from that interconnection. Hence, the interconnection weight adjustment for w_k is written as [79]:

$$\Delta w_{kj} = \eta \, \delta_k \, z_j \qquad \text{Equation 3-41}$$

Likewise for w_{ji}

$$\Delta w_{kj} = \eta \, \delta_j \, x_i$$

where,
- w_{ji} = weight connection to neuron *j* from neuron *i*,
- z_j = $f(net_j)$ output of hidden layer node *j*
- x_i = input to input node i
- η = learning rate constant, $0 < \eta < 1$

It can be seen from Equation 3-42 that updating of interconnection weights is primarily based on three parameters, η, $\delta_{j/k}$ and z_j, x_i. As Δw_{ji} is proportional to δ_j then it follows that a large error value from neuron *j* will result in a large adjustment to its incoming weights. Similarly, large output values, x_i, will result in larger weight adjustments. The learning rate, η, in the weight adjustment equation is selected to reflect the desired convergence speed of the neural network. However, very large values of η lead to instability in the network and unsatisfactory learning while very small values of η give rise to an excessively slow learning rate. Sometimes the learning rate is varied in an attempt to produce a more efficient learning rate for the network; for example, allowing the value of η to begin at a high value and to decrease during the learning session can sometimes produce better learning performance [79].

One of the most popular ways to improve the convergence of the weight update is the introduction of a momentum term. The weight adjustment at each iteration is shown in the following equation and is referred to as the 'generalised delta rule' [83]:

$$\Delta w_{ji}^{k} = \eta\, \delta_j\, x_i + \alpha \Delta w_{ji}^{k-1} \qquad \text{Equation 3-42}$$

where, α = momentum term constant, $0 \leq \alpha < 1$

Δw_{ji}^{k} = weight update at iteration *k*

Δw_{ji}^{k-1} = weight update at iteration *(k-1)*

Through addition of the momentum term a portion of the weight update is not applied until the following iteration, resulting in dampening of oscillations in weight changes and improved convergence [84].

The weights of the network to be trained are typically initialised at small random values [85]. A well known initialisation heuristic for a feedforward network with sigmoidal units is to select its weights with uniform probability from an interval $(-\alpha, \alpha)$ [86]. A common procedure is to initialise weights to random values between -0.5 and 0.5, or between -1 and 1, or some other suitable interval [87]. Weight initialisation is an important procedure as it has substantial influence over network convergence. If all weights start out with equal values, and if the solution requires that unequal weight values be developed, the network may not train properly. Unless random factors, or the random character of input patterns during training, disturb the network, the internal representation may continuously result in symmetric weights. In particular, because the network weight update procedure incorporates the difference between a neuron output and the target output, if each neuron output within the network is the same value, due to equal valued weights, each weight change within the network will be identical and hence, the network weights will never differ. This is not desirable however, as most applications require uneven weights within the network, hence, a network with even weights will not produce accurate results.

3.7.5 Backpropagation Training Algorithm

The training procedure for a backpropagation network is as follows [78]:

Step 1. Initialise the weights of the network at small random values.

Step 2. Start the learning cycle by exposing the network to a certain input pattern, paired with the desired output.

Step 3. Compute the network's output, Equations 3-34 and 3-35, and compare it with the desired output so that the error can be calculated, Equations 3-40 and 3-41 for the output and hidden layers, respectively.

Step 4. Adjust the weights of the network using the error backpropagation algorithm so that a certain amount of the detected error is removed, Equation 3-42, or 3-43 if a momentum term is used.

Step 5. Repeat Steps 2 to 4 with all the input patterns and their correspondent desired outputs (training examples), until the RMS error is within a tolerable range. Compute the cumulative error.

3.7.6 Optimised Layer by Layer Neural Network Learning Algorithm

The Optimised Layer by Layer (OLL) multilayer perception neural network, like the backpropagation network described above is a feedforward neural network. However, there are two significant differences between the OLL neural network and the backpropagation network. The architecture of the OLL and the learning algorithm used to update the network weights of the OLL network are considerably different to the architecture and training procedure used with backpropagation networks. Below an overview of the architecture and learning algorithm of the OLL network is presented. A more detailed and mathematically comprehensive description is provided in [88].

The architecture of the OLL network, shown below in Figure 3-7, consists of an input layer, one or more hidden layers and an output layer. There are *M*, input nodes (equivalent to the i^{th} input node of the backpropagtion network), *H*, (equivalent to the j^{th} input node of the backpropagtion network) hidden nodes and k scalar output nodes. All input nodes are connected to all hidden nodes through weighted connections, W_{ji} and all hidden nodes are connected to all output nodes through weighted connections V_{kj}.

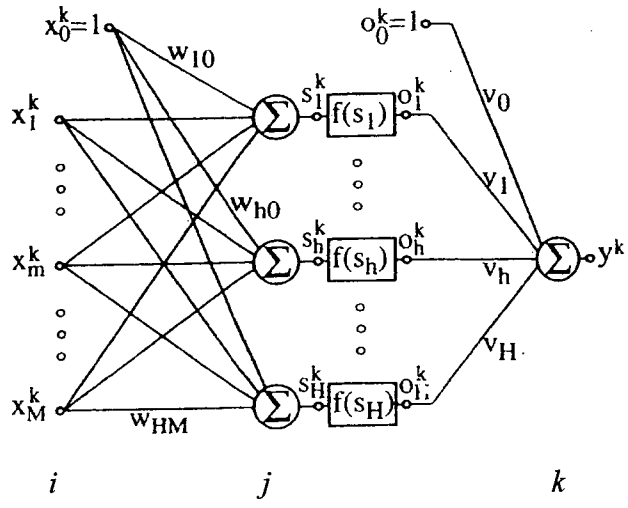

Figure 3-7 Basic Structure of the OLL Network [85]

Unlike the network architecture of the backpropagation paradigm the architecture of the OLL network is not symmetric about the hidden layer in terms of activation functions, as can be seen above in Figure 3-6. The architecture can be split into two different sections a nonlinear part and a linear part. This is achieved by employing two different types of activation functions. It uses a sigmoidal function in the non linear region between the input neurons and the hidden layer neurons and a linear function between the hidden neurons and the output neurones. The two activation functions are displayed below

$$f(net_j) = \frac{1}{1+e^{(-net)}}$$

$$f(net) = net_j$$

In order to describe the thresholds of the hidden layer and the output nodes in the same manner as the wights the node x_0 with fixed value 1.0 is added to the input layer and the node o_0 with fixed value 1.0 is added to the hidden layer [85].

3.7.7 Advantages of the OLL Network

The standard backpropagation algorithm presented above suffers from the typical handicaps of all steepest descent approaches, that is very slow convergence rate and the need for predetermined learning parameters limit the practical use of the algorithm [85]. The OLL network has been developed to overcome these problems. The OLL learning algorithm does this by reducing the optimisation of each layer, output, hidden and input to a linear problem, which can be solved exactly [85]. There are also no learning parameters, which have to be tuned by the user, such as the learning rate constant associated with backpropagation training [85]. Another major advantage is that the weights of each layer are modified dependant on each other but separately from all other layers [85].

3.7.8 OLL Learning Procedure

The network weights for the OLL network are also adjusted on basis of minimising the error function, the between the desired or target output and the actual output of the neural network.

3.7.8.1 Output Layer Weight Adjustment

For the output layer the error function is derived and set to zero and solved for v in order to find v^{opt}, the optimum values for the scalar weighted connection v at which error is minimum. From Section 3.7.4.1 the general form of the derivative of the error function for the output layer for unit k of the of the backpropagation network is:

$$\delta_k = (y_k - t_k) f'(net_k) \qquad \text{Equation 3-43}$$

For the OLL network, this is

$$\delta_k = \frac{dE}{dv} = \left(v^T o^k - t^k\right) o^k = 0 \qquad \text{Equation 3-44}$$

Comparing coefficients between Equation 3-43 and Equation 3-44

t^k = is equivalent to the target output of BP

$v^H o^k$ = is equivalent to the network output ie y^k of BP

o^k = is equivalent to $f'(net_k)$ of BP and is the scalar transformation function of the hidden layer of the OLL network

Equation 3-45 is a linear equation that can be solved exactly using matrix representation to find the optimum weight values for *v* which correspond to the minium error. As a result the iterative procedure used in the backpropagation is eliminated which reduces network training and development time. The matrix representation of this procedure is presented below.

$$Av = b$$

Equation 3-45

$$v^{opt} = A^{-1}b$$

where

$$A = \{a_{ij}\} = a_{ij} = \sum_{k=1}^{k} o_i^k o_j^k$$

$$b = \{b_i\} = b_i = \sum_{k=1}^{k} t^k o_i$$

Equation 3-46

3.7.8.2 Hidden Layer Weight Adjustment

The optimum weights for the hidden layer, the nonlinear section of the network architecture, are determined, by using a similar approach as that presented above. In order to achieve this, the nonlinear sigmoidal activation functions between the input neurons and the hidden layer neurons need to be transformed into a set of linear equations. Linearisation errors are introduced during the linear transformation of the sigmoidal activation function. As a result of the linearisation errors network optimisation can not be carried out in a single step [85]. An iterative procedure which alternatively optimises the output layer and the hidden layer has to be incorporated to compute the weights *v* and W** which minimise the error function [85] [89]. The Taylor series expansion is used to transform the nonlinear sigmoidal activation functions into a set of linear equations, resulting in a linearised network structure depicted below in Figure 3-8.

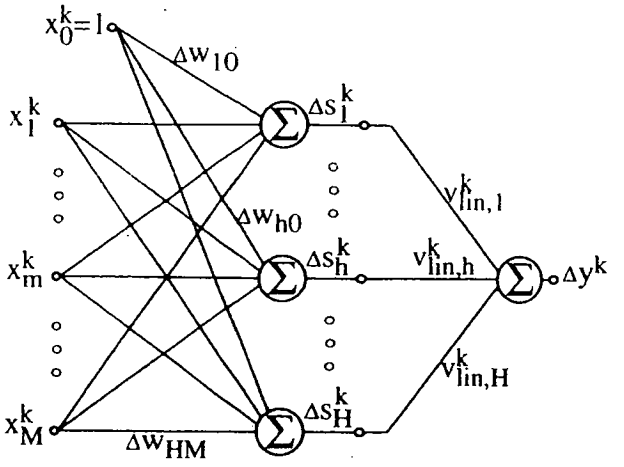

Figure 3-8 The linearised network structure of the hidden layer of the OLL network [85]

The modified cost function for the optimisation of the hidden layer is given by equation 3-47 and is composed of two separate error functions as seen below in Equation 3-48.

$$E_{hidden} = E_{linear} + \mu E_{pen} \qquad \text{Equation 3-47}$$

E_{hidden} = Overall Error function for the hidden layer

E_{linear} = Error function for the linearised sigmoidal functions

E_{prn} = Penalty term to account for the linearisation error

μ = is a weighting factor which determines the influence of the penalty term against the linear cost function

The optimium weight change, ΔW^{opt}, is found by taking the partial derivatives of E_{linear}, E_{prn} of Equation 3-48 with respect to $\Delta W^{op,}$ by using the chain rule and solving for when the above error functions are equal to zero. The result of this process is depicted below.

$$\frac{\delta E_{hidden}}{\delta w_{hm}} = \frac{\delta E_{linear}}{\delta w_{hm}} + \mu \frac{\delta E_{pen}}{\delta w_{hm}} = 0 \qquad \text{Equation 3-48}$$

$$\frac{\delta E_{hidden}}{\delta w_{hm}} = \sum_{i=0}^{M} \sum_{j=1}^{H} \alpha_{hm,ji} \Delta w_{ji} + \frac{\mu}{H} \sum_{i=o}^{M} c_{hmi} \Delta w_{hi} - \tilde{b}_{hm} = 0 \qquad \text{Equation 3-49}$$

Equation 3-50 is a set of $(M+1)\cdot H$ linear equations expressed in terms of the individual weight changes Δw_{hm} for the hidden layer connections. These sets of linear equations can be solved exactly using matrix notation, as for the output layer, to yield the optimum weight changes required for minimum network predictive error.

$$A\Delta W = b$$

Equation 3-50

$$\Delta W^{opt} = A^{-1}b$$

The to hidden layer weights are then updated according to Equation 3-51.

$$W_{new} = W_{old} + W^{opt}$$

Equation 3-51

m = 0,…,M h=1,…,H

Below is a summary of the OLL training procedure.

3.7.9 Optimised Layer By Layer Network Training Algorithm

The training procedure for the optimised layer by layer network is as follows [85]:

Step 1. Initialise the weights of the network *(W, v)* at small random values and choose an initial value for the penalty term μ in Equation 3-49

Step 2. Start the learning cycle by exposing the network to a certain input pattern paired with the desired output.

Step 3. Compute the network's output, RMS error, and compute the optimum output layer weights v^{opt} from Equation 3-46. Update the output layer weights, $v = v^{opt}$, and re-calculate the RMS prediction error from Equation 3-45.

Step 4. Compute the optimum weight changes for the hidden layer by minimising Equation 3-49 and using Equation 3-51. Re-calculate the RMS error (E) according to Equation 3-49 with the updated weight changes.

Step 5.

(a) Determine if $E_{test} < E$ then update the hidden layer connections using Equation 3-52, set $E = E_{test}$ and decrease the influence of the penalty term, ie $\mu = \mu_{tesr}\beta$, where $0 < \beta < 1$. Continue to step 6.

(b) If $E_{test} \geq E$, increase the influence of the penalty term, ie $\mu = \mu_{tesr}\gamma$, where $\gamma > 1$, and repeat step 5 (a)

Step 6. Repeat Steps 2 to 5 with all input patterns and their corresponding desired outputs (training examples) above until until the RMS error is within a tolerable range.

3.8 Summary

This chapter has provided an insight into Hendricks' [1] Mean Value Engine Models (MVEM) and presented some of the potential advantages of applying Artificial Neural Networks to nonlinear engine modelling. A review of recent research that has been published in the field of engine modelling using ANN's was also presented. The basic structure, features and operating principals of the Backpropagation and Optimised Layer by Layer Network algorithms were also provided. The next chapter provides an explanation of the rationale behind this investigation, describing the overall objectives of this research.

4 RESEARCH RATIONALE

The purpose of this investigation is to develop an Artificial Neural Network (ANN) model-based observer that represents the manifold filling dynamics and furthermore can estimate the port air mass flow into an engine during steady state and transient engine operating conditions. A simplified MVEM based on Hendricks' et al [1] analytical description of the manifold filling dynamics, as presented in Section 3.1.3, is used in this research.

The main reason for the presence of transient AFR deviations is due to the fact it is very difficult to accurately estimate the air flow at the actual engine cylinder ports especially during transient operating conditions. It is hoped the developed ANN model will have the capacity to accurately estimate the mass airflow at the intake ports of the engine in both steady state and transient conditions, which is essential in order to determine the correct amount of fuel to inject and hence maintain the desired AFR.

The objective of this research is not to simply replace conventional engine look up functions and tables, based on static experimental engine testing, with an equivalent ANN model. Nor does it rely solely on the superior nonlinear interpolation abilities of ANN in comparison to conventional look up table linear interpolation.

The aim of this research is to begin to develop a single complete static and dynamic engine model observer for the estimation of the port air mass flow. The two current conventional methods for determining the mass airflow in modern automobiles is to use either an air mass flow sensor or to employ a speed density system, these systems were outlined in Chapter 2. Mass flow sensors directly measure the air mass flow at the throttle however are unable to determine the port air mass flow. Speed density systems calculate an engine airflow that approximates the flow rate at the intake ports. This calculation is based on static engine measurements and consequently is unable to determine the port air mass flow during transient driving conditions. As highlighted in previous chapters there is a strong need for a system that can determine the port air mass flow in both static and dynamic operating conditions if automotive manufactures are to reduce transient AFR excursions and hence meet exhaust gas emission legislation targets of the decade.

Two types of Feedforward ANN paradigms are used in this investigation, namely the Backpropagation Neural Network and the fast converging Optimised Layer by Layer Neural Network. The Backpropagation algorithm is an established ANN, which has been used, extensively in a wide range of nonlinear modelling applications. The Optimise Layer by Layer network is a more recent network, which has been specifically designed and developed to overcome the short comings of the backpropagation network that primarily being its large convergence time. To the authors knowledge this is the first time the Optimise Layer by Layer Network has been applied to nonlinear engine modelling.

The performance of the individual ANN architectures in the estimation of the port air mass flow will be discussed and compared in this research. The overall goal is to find an optimum model, by altering the network architecture, that is the number of nodes and hidden layers and the inputs to each model. The optimum model will be selected on the basis of minimising the Root Mean Square percentage error between the model prediction[2] and target output[3], and also considering model computational time[4]. Model computation time is also considered in order to prevent solely maximising model accuracy.

4.1.1 Model Input Selection

The intention of this research is to develop an ANN model that has the future potential to be easily implemented and integrated into the control system of a modern vehicle. Therefore, inputs to the ANN models were limited to those engine parameters that are conventionally used in engine management systems and thus those for which affordable sensors are produced on a large scale. A modelling exercise is required to identify the main engine parameters that affect the ANN model output the port air mass flow. Such an analysis has already been undertaken by Hendricks' et al [1], who highlighted that the port air mass flow rate is a function of the following commonly measured engine parameters, as discussed in Section 3.1.3.

[2] that is the mass airflow at the intake ports
[3] target output is calculated from a MVEM relationship, based on the conservation of mass airflow in the engine manifold
[4] the time in seconds it takes the model to complete the total learning and testing cycle

$$\dot{m}_{ap} = f^n\left(\alpha, T_m, n, p_m, \dot{m}_{EGR}, \dot{m}_{th}\right)$$

Accordingly the inputs to the ANN models are based on those presented above, excluding the exhaust gas recirculation flow rate, as this is not available on the experimental testing engine and the throttle mass air flow rate for reasons that are presented below in Section 4.1.2. Figure 4-1 below shows the inputs to the ANN model.

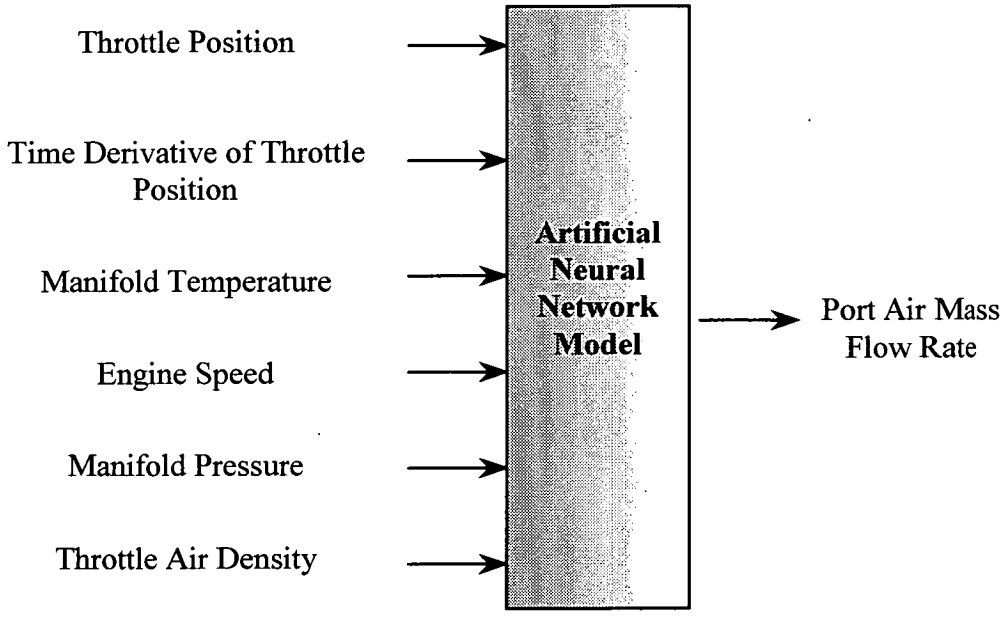

Figure 4-1 Inputs to the ANN model for the estimation of the port air mass flow rate

The inputs depicted above can be directly measurable by sensors or can be evaluated from sensor data. Throttle air density is a function of both atmospheric pressure and temperature and is included to compensate for variations in air density and hence the throttle mass airflow rate. A suitable look up table could be used to replace this input of the ANN model, in a similar fashion as that employed to compensate for such effects in modern automobiles.

The selection of time derivative of throttle position as an input to the ANN model was inspired by specific speed density systems that use this parameter for acceleration enrichment and deceleration enleanment compensation purposes. However, in this model it is simply used to represent if the engine is operating in a steady state or a transient driving condition. It

was also inspired by the Shayler et al [54] research who believes that engine mass air flow prediction might be possible by using throttle position as an input to a suitable ANN.

> "The throttle clearly moves a finite time before changes in the manifold pressure occur, so using throttle movement as an indication of immanent changes in MAP may be possible and an air flow anticipation scheme might be possible on this basis" [54]

In this research, the time differential of throttle position is included to provide an indication of changes in the time differential of manifold pressure.

Conventional control systems usually have difficulties dealing with the time differential of noisy or low resolution sensor readings as differentiation amplifies any error already present in the measurement [90]. As highlighted in Section 3.4 ANN's have the ability to cope with noisy sensor readings as decisions are made on the basis of identifying relevant trends in data. Any noise or errors introduced with the time differential of the throttle position will be uniform across all calculations and therefore the ANN will still be able to recognise patterns associated with its input.

When the time derivative of the throttle position is non-zero, the manifold pressure is also non-zero and hence the mass airflow at the engine ports is not equal to the mass airflow at the throttle. The movement in the throttle position represents a changing driver derived input to the system, which directly effects the behaviour of the manifold absolute pressure and hence the air mass flow rate.

The time derivative of the throttle position is a critical input to the ANN model. Without this input the ANN model would be unable to distinguish between steady state engine operation (when the flow at the throttle is equal to the flow at the engine ports) and transient engine operation (when the flow at the throttle and the flow at the ports differ due to the manifold filling phenomenon). Selecting such an input enables the model to be able to identify the appropriate time to apply compensation for the manifold filling dynamics based on the isothermal model developed by Hendricks' et al [1].

However even during periods of constant throttle operation there are small fluctuations in the manifold pressure. These small fluctuations can be considered insignificant in comparison to the large manifold pressure excursions that occur during fast throttle transients. It is hoped that the ANN model will be able to correlate the magnitude of the throttle position derivative to the magnitude of $\dot{p}_m$ and hence compensate the effect this parameter has in the calculation of the port air mass flow equation. The effectiveness of this parameter in establishing this correlation will be assessed by conducting a predictive importance analysis of the developed ANN models to determine if the rate of change of throttle position contributes to model prediction. Predictive importance analysis is concerned with investigating the increase in generalisation error when a variable is omitted from the training set [91].

4.1.2 Port Air Mass Flow Calculation

The port air mass flow can be described using Hendricks' [1] isothermal MVEM relationship, which is based on the conservation of mass principal, as described in Section 3.1.3. It assumes the pressure and temperature inside the manifold are constant at any particular time.

$$\dot{m}_{ap} = \dot{m}_{at} - \dot{m}_{am} - \dot{m}_{EGR} \qquad \text{Equation 4-1}$$

A simplified version of the MVEM is used in this research. The $\dot{m}_{EGR}$ term is removed, as the experimental testing engine does not have EGR, thus eliminating some of the complexities involved with large variations in the manifold temperature. The revised MVEM used in this research is provided below.

$$\dot{m}_{ap} = \dot{m}_{at} - \dot{m}_{am} \qquad \text{Equation 4-2}$$

where $\dot{m}_{am} = \dot{p}_m \frac{V_m}{RT_m}$ Equation 4-3

The complete port air mass flow relationship to be used in this research is provided below.

$$\dot{m}_{ap} = \dot{m}_{at} - \dot{p}_m \frac{V_m}{RT_m} \qquad \text{Equation 4-4}$$

When the throttle position remains constant, representing a steady state engine operation, the time derivative of the throttle position is equal to zero and the time derivative of the manifold pressure is also approximately zero. During such operating conditions the port air mass flow model observer will simply be predicting the throttle mass airflow rate as the manifold flow rate is insignificant. This can be illustrated by examining Equation 4-4 above, noting that when $\dot{\alpha} = 0, \dot{p}_m \cong 0$ therefore Equation 4-4 reduces to.

$$\dot{m}_{ap} = \dot{m}_{at} \qquad \text{Equation 4-5}$$

Therefore it is irrational to use the mass air flow rate as a model input as during instances of constant throttle operation the model will simply be outputting an input which is pointless. However when the time derivative of the throttle position is non-zero, it is hoped the model will be able to recognise that the engine is in transient operation and apply suitable compensation for the manifold air mass flow of Equation 4-3.

4.1.3 Significance of the Research in Enhancing AFR Control

This research attempts to explore the feasibility of using ANN for the estimation of the port air mass flow as means to enhance AFR control. If the port air mass flow rate can be accurately predicted over a wide range of engine operating conditions the fuel pulse width (injector opening time t_{io}) can be determined from the lambda relationship presented in Section 2.2.3, assuming the desired operating lambda value is known in advance. Typically, for minimum exhaust gas emissions, the optimum AFR occurs at stoichiometry or when the $\lambda = 1$ as this represents the point at which the conversion efficiency of the catalytic converter is maximum. Therefore, if the port air mass flow output from the ANN model $\left(\dot{m}_{ap}^{NN}\right)$ can be integrated with respect to time for when the intake valves are open, as suggested in [47], then

one can obtain the actual amount of air that enters the combustion chamber $\left(m_{ap}^{NN}\right)$. This is shown mathematically below.

$$m_{ap}^{NN} = \int_{dt}\left(\dot{m}_{at} - \dot{m}_{am}\right)dt \qquad \text{Equation 4-6}$$

If m_{ap}^{NN} is known it is possible to determine the correct amount of fuel to inject $\left(m_{fi}\right)$ and thus calculate the ideal fuel injection opening time $\left(t_{io}\right)$ in order to sustain the desired AFR during transient operating conditions. This calculation does not include any compensation for the fuel film developing on the intake runners.

$$m_{fi} = \frac{m_{ap}^{NN}}{14.64\lambda} \qquad \text{Equation 4-7}$$

$$t_{io} = \frac{m_{fi}}{\dot{m}_{inj}} \qquad \text{Equation 4-8}$$

4.2 Summary

This chapter has provided the reader with the objectives of this research, the inputs paramters that will be used in the developed ANN models and how the port air mass flow will be calculated. The next chapter provides a description of the experimental setup that will be used to collect the necessary data required to train and test the developed ANN model.

5 DESIGN & DEVELOPMENT OF EXPERIMENTAL TEST RIG

In developing an ANN model, extensive testing must be undertaken to compile a comprehensive collection of experimental data. This is necessary as it is the experimental data gathered on the dynamic response of the automotive engine during different operational testing conditions that forms the foundation for the training and testing of the ANN models. In this research the ANN model must be presented sufficient engine data so that it can accurately estimate the port air mass flow over a wide range of engine operating conditions. The accuracy and reliability of any developed ANN model is therefore dependent upon the accuracy, relevance and correctness of the data collected during experimental testing. The correctness of the data is conditional to the establishment of an appropriate, reliable and accurate measuring system. With this in mind careful consideration was given to the selection of appropriate automotive sensors and the precision of the data acquisition system for this project.

This chapter describes the experimental setup that is used to obtain the associated engine data that is necessary to adequately train and test the ANN models. This chapter provides a description of:

(i) The experimental engine
(ii) The custom made engine intake manifold
(iii) The engine management & fuel injection system
(iv) The Data Acquisition System
(v) Engine Sensors &
(vi) Testing dynamometer

5.1 Experimental Engine

A 2000 Kawasaki Ninja ZX6, was used as the experimental test bed for this investigation. Figure 5-1 shows the experimental testing engine.

(a) (b)

Figure 5-1 (a) Experimental test engine mounted in a Kawaski ZX6 Ninja motorbike
(b) The separate Kawaski ZX6 Ninja engine

An overview of the engine specifications are displayed in the Table 5-1 below. The full engine specifications, along with drawings are presented in Appendix D.

Kawaski Ninja ZX6 Engine Specifications	
Serial Number	ZX600 FE071487
Type	4 stroke, 4-cylinders inline
Cooling System	Liquid cooled
Bore & Stroke	66 x 43.88 mm
Displacement	599 cc
Compression Ratio	12.8:1
Maximum Horsepower	81.6 kW
Maximum Torque	65.6 Nm @ 10,000 rpm
Valve Train	4 valves per cylinder, DOHC, Chain drive to camshafts
Firing Order	1-2-4-3
Lubrication System	Forced lubrication (wet sump)
Spark Plug	NGK CR9E

Table 5-1 2000 Kawaski ZX6 Ninja Engine Specifications [92] [93]

This engine is the power plant for the 2001/2002 University of Tasmania's FSAE Race Car. Figure 5-2 shows the research engine installed and mounted in the 2002 Race Car.

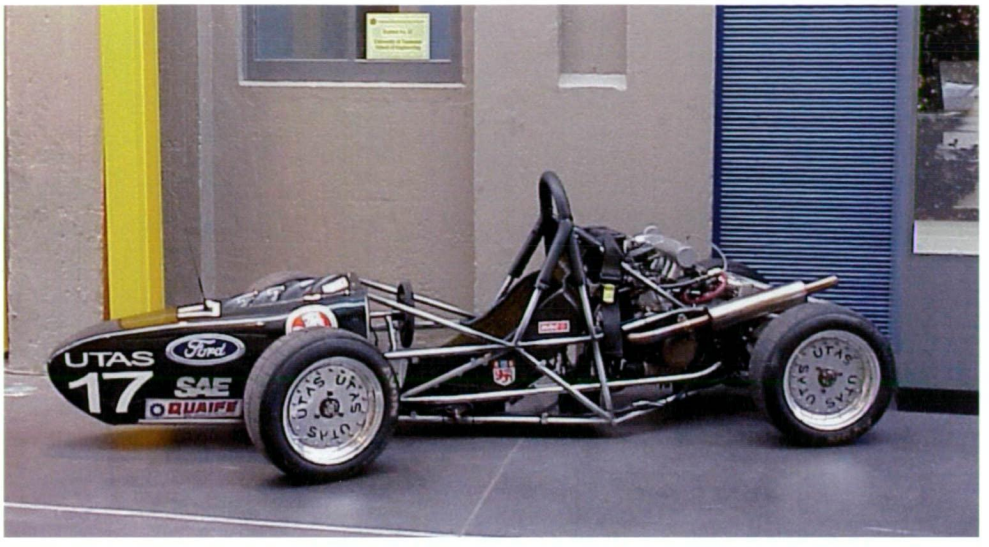

Figure 5-2 Picture of the 2001-2002 FSAE Race Car

Experimental engine data will be collected with the engine mounted to the Race Car. Engine data will be gathered using a chassis dynamometer, the details of which are described below in Section 5.4. Fuel is normally delivered to such a motorbike engine by a bank of four carburettors, one for each cylinder. For this research a fuel injection system is necessary and this required a custom made intake manifold to be designed and manufactured.

5.1.1 Custom Built Intake Manifold

The intake manifold consists of four straight runners, 50 mm in length and 36.5 mm in diameter. The plenum chamber is rectangular in shape, fabricated by folding 3-mm aluminium sheet. A multi-point fuel injection system is used by mounting four Bosch (Part Number 0280 150 790) injectors directly above each intake runner so that they sprayed directly down the intake runner at the back of each intake valve. This greatly reduces the likelihood of a fuel film developing on the intake runners. Figure 5-3 shows the custom-built intake manifold that will be used in this investigation. The exact manifold volume, defined from throttle plate to intake valves, is 2.98 Litres measured by filling the intake manifold with water. The volume of the entire intake system is approximately five times the size of the

research engines total displacement. The engine is throttled upstream of the plenum chamber with a 50 mm diameter butterfly style throttle body.

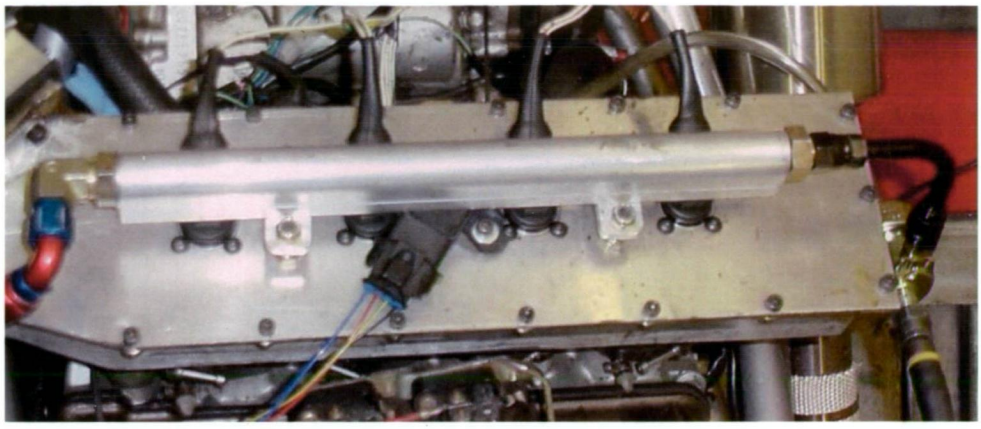

(a)

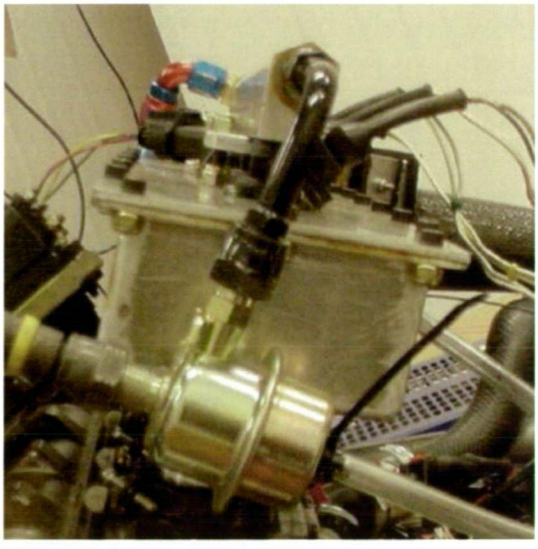

(b)

Figure 5-3 The custom built intake manifold mounted to the engine (a) top view, (b) side view

5.1.2 Engine Management & Fuel Injection System

A MoTeC engine management system was selected as being the most appropriate engine management system for this research as it possessed all the major operating characteristics of a conventional automotive manufacturer produced electronic fuel injection system. A

MoTeC M4-Pro system, shown below in Figure 5-4, was selected, as this system provided sequential injection and 3-D fuelling and ignition look up tables that were fully programmable.

Figure 5-4 MoTeC M4 Pro Engine Management System

The MoTeC system also provided the additional option of either operating in open loop lambda control or closed loop lambda control using feedback information provided by a lambda sensor. The MoTeC ECU is manufactured to ISO 9001 quality control standards. The main inputs and outputs of the engine management system are shown below in Figure 5-5.

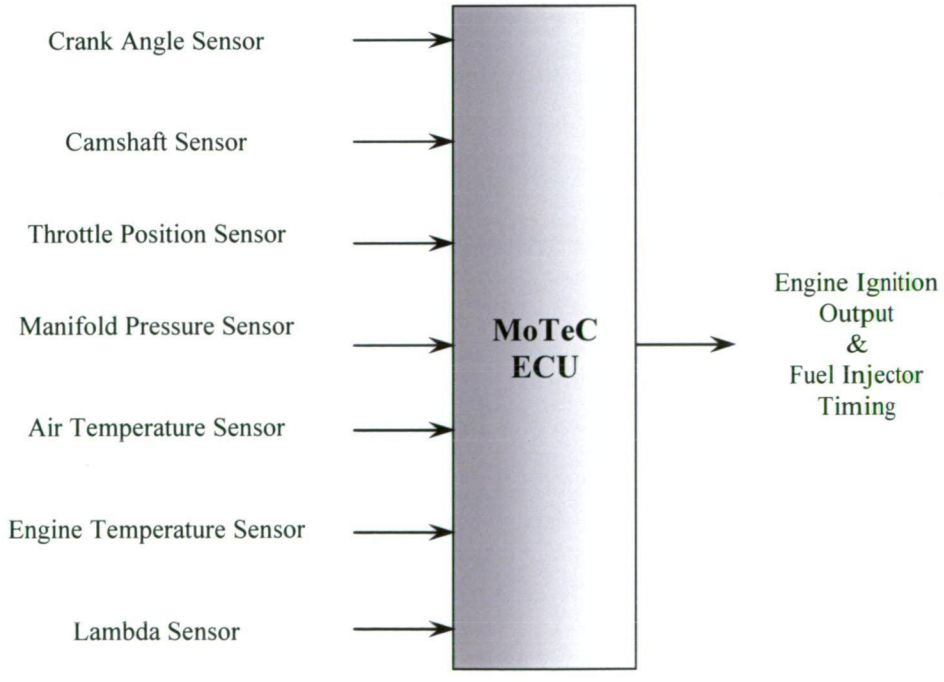

Figure 5-5 Inputs & Outputs of the MoTeC M4 Pro Engine Management System

Additional inputs and outputs are available on the MoTeC engine management system, however these have no effect in controlling the engine injection/ignition timing.

A MoTeC engine management system like conventional engine management systems determines the amount of fuel to inject by calculating the engine speed and load then extracting the corresponding fuel injection time from a 3D look up table [93]. Two different sensor inputs can be used to characterise the engine load, a manifold air pressure sensor, or a throttle position sensor. In this research the throttle position sensor input was selected to represent engine load and was used together with engine speed in the development of the fuelling and ignition maps. The ECU comes with its own software for fuel injection configuration purposes and the associated development of the 3D engine fuelling and ignition maps. The specifications of the MoTeC M4 Pro ECU are provided in Appendix E.

5.2 Data Acquisition System

A MoTeC Advanced Dash Logger (ADL) was selected as the Data Acquisition System (DAS) for this investigation as any ECU generated engine data could be directly obtained via an RS232 serial link between the two devices. The unit, shown below in Figure 5-6, is a compact DAS suitable to manage the on-board acquisition of data from the selected automobile sensors.

Figure 5-6 The Research DAS, MoTeC Advance dash Logger (ADL)

The layout of the complete DAS is also shown below in Figure 5-7

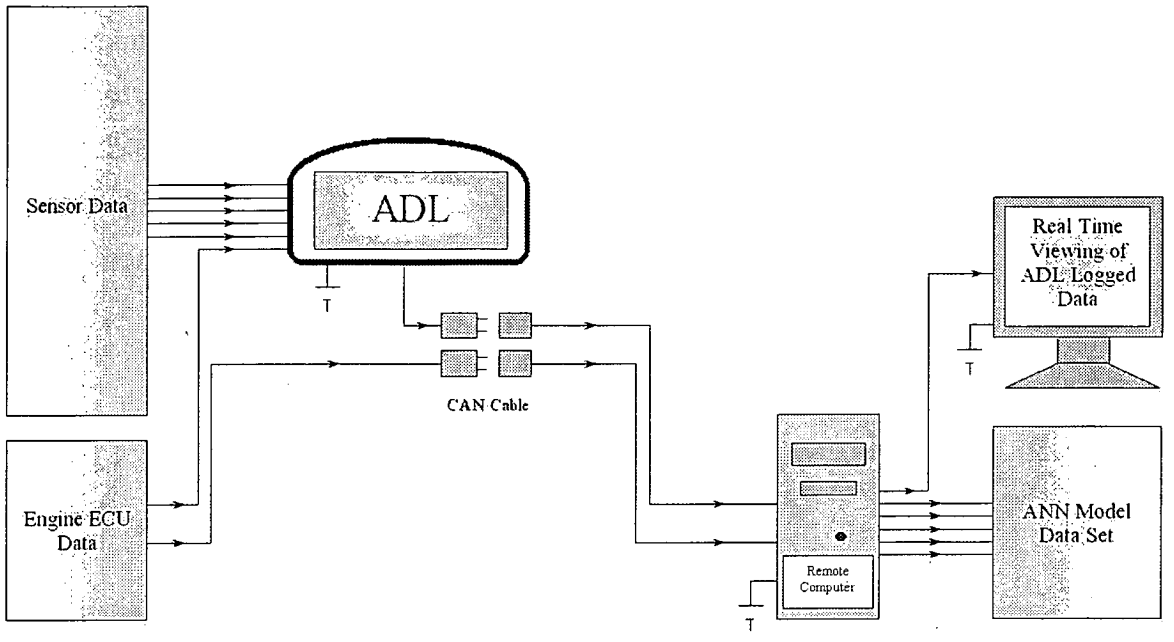

Figure 5-7 Diagram of the complete DAS

The ADL also serves as a programmable dash display unit for the test vehicle and supports 14 analog inputs, 10 digital inputs, one RS232 serial input and 4 auxiliary outputs in its current configuration. ECU based engine data is received by the ADL through the RS232 input and all other sensor inputs for this investigation use the available analog ADL inputs. The ADL incorporates a high speed 32-bit microprocessor and has 1Mb storage capacity. Logged ADL data files are downloaded to a PC via the computer's parallel port using a high speed CAN communication cable at a rate of 19 sec/MB. The MoTeC ADL is manufactured to ISO 9001 quality standards.

The ADL comes with two windows based programs, these are the Dash Manager Software Package and the Interpreter Analysis Software Package. The Dash Manager Software primarily deals with the configuration of the ADL and is used to retrieve any data stored on the ADL memory. This program allows sensor channel properties to be selected, enables sensor calibration, and all other ADL configuration features.

The Interpreter Software Package, is used to analyse the collected data. This program allows the graphical representation of the collected data, and has many additional features, including a number of mathematical functions, which can be used for parameter conditioning, the development of mathematical formulas and for providing statistical information. This program also has the ability to export acquired ADL data files into Microsoft Excel, using a comma separated (*.csv), format. The specifications of the MoTeC ADL are provided in Appendix F.

5.3 Sensors

The engine parameters listed below have either been identified as ANN model inputs or are required to be measured as they are needed in the calculation of the model output, the port air mass flow.

- Throttle Position
- Manifold Pressure & Temperature
- Atmospheric Pressure
- Throttle Air Mass Flow Rate & Throttle Air Temperature
- Engine Speed

Sensor selection was limited to conventional automotive sensors that are currently used in modern engine management systems. Sensors were selected on the basis of resolution, accuracy, response time and the availability of a manufacturer produced sensor calibration characteristic curves. The availability of sensor calibration curves was considered important, as any effort to calibrate the sensors with the equipment available at hand would significant reduce the accuracy of the sensors. This section is not intended to give detailed information on how the sensor operates, its purpose is to give a brief overview of some of the technical specifications of each sensor. Bosch produces all sensors that have been selected for this research.

5.3.1 Throttle Position Sensor

An analog Bosch Throttle-valve angular position sensor Part Number 0 280 122 001 was chosen for the measurement of the throttle position. The throttle valve angular position sensor is a potentiometric sensor, which has a linear characteristic curve. The rotor of the sensor is attached to the throttle valve shaft and is mounted on the throttle valve housing. As the throttle valve rotates it generates a voltage proportion to the throttle valves angle of rotation [94]. The sensor specification brochure is presented in Appendix G-1. This particular type of throttle position sensor has an accuracy of ± 3 % and a typical response time in the order of 0.1 ms [90], [95].

This sensor is required as an input to the MoTeC engine management system and as such must be calibrated using the associated ECU software. The procedure involved simply taking a voltage reading of the sensor when it was at 0 degrees (no depression of the throttle pedal) and then repeating the process when the butterfly was at wide-open throttle position (complete depression of the throttle pedal).

5.3.2 Manifold Air Pressure (MAP) & Manifold Temperature Sensors

An analog Bosch micromechanical hybrid design absolute-pressure sensor, Part Number 0 261 230 030, was selected to measure the manifold absolute pressure. This sensor has been specifically designed for measuring manifold absolute pressure. This sensor also has the advantage of an in built temperature sensor, which means that the manifold pressure and temperature can be measured, by the same measuring device at the same location in the intake manifold. The temperature sensor measures the temperature of the air that is drawn into the sensor for pressure measurement purposes [90].

A piezoresistive pressure sensor element and suitable electronic circuitry for signal amplification are used in the determination of the intake manifold pressure. . The MAP sensor has a manifold absolute pressure measuring range between 10 – 115 KPa. The sensor has been mounted on the top of the intake manifold. The pressure fitting and the temperature sensor extend into the manifold and are sealed of to atmosphere by O-rings [90]. The pressure sensor has an accuracy of ± 1% and a typical response time of 1 ms [91].

A Negative Temperature Coefficient (NTC) thermistor temperature sensor is integrated into the MAP sensor. The manifold temperature sensor has an air temperature measuring range between –40 –130 °C. The sensing element of the NTC temperature sensor is a resistor comprised of metal oxides and oxidised mixed crystals [90]. If the sensor is exposed to a shift in temperature the resistance of the sensor element changes dramatically and the input current increases, so long as the input voltage remains constant. This temperature sensor has a measurement accuracy of ± 2 % and a thermal time constant of 10 seconds [91]. The specification brochure for both these sensors is presented in Appendix G-2.

A calibration curve for the MAP sensor is provided in the specification brochure, presented in Appendix G-2. The characteristic curve for the MAP sensor is linear. The characteristic curve was inserted in the MoTeC dash manager software in a look up table format.

Information regarding the NTC temperature calibration curve was obtained directly from Bosch, this is also presented in Appendix G-2. The characteristic curve for the temperature sensor was also inserted into the MoTeC Dash Manager software in a look up table format.

5.3.3 Atmospheric Pressure Sensor

An analog Bosch absolute pressure sensor designed especially for the measurement of atmospheric pressure, Part Number 0 273 300 030 was selected for this purpose. It has an atmospheric pressure measuring range between 60 to 115 kPa. The pressure sensor has a measurement accuracy of ± 1% and a typical response time of 1 ms [91].

The linear calibration characteristic curve for the atmospheric pressure sensor is provided in specification brochure, presented in Appendix G-3. The characteristic curve was inserted into the MoTeC dash manager software.

5.3.4 Throttle Air Mass Flow Rate & Throttle Temperature

An analog Bosch hot-film air mass flow meter, Type HFM 5, Part Number 0 280 218 019 was selected to measure the mass airflow rate at the throttle. This sensor also comes with a

temperature sensor, which in this investigation will be used to measure the throttle air temperature before the throttle (approximately equivalent to atmospheric temperature). This mass air flow sensor has return flow detection which eliminates measurement errors associated with air flow reversible caused by the reciprocating motion of the pistons.

The sensor incorporates a heated element and as air is drawn into the engine the heated element dissipates its heat to the incoming air. As the airflow increases, the heated element dissipates a larger amount of heat to the inducted air. The resulting temperature differential is used as a basis to determine the air mass flowing past the sensor and hence entering the engine. This sensor has a mass airflow measuring range between 8 to 480 kg/h. and has a measurement accuracy of less than ± 3% and a typical response time of less than 30 ms [90], [91].

An NTC thermistor temperature sensor similar to the one used to measure the manifold temperature is used to measure the air temperature at the throttle. The temperature sensor has an air temperature measuring range between –40 – +130 °C. This temperature sensor has a measurement accuracy of ± 2 % and a thermal time constant of 10 seconds [91]. The specification brochure for both sensors is presented in Appendix G-4.

This mass air flow sensor has been calibrated to measure the volumetric flow rate rather than the mass airflow rate as the volumetric flow rate is independent of air density and therefore independent of the experimental testing pressure and temperature conditions. An mass airflow rate calibration curve for the sensor is provided in specification brochure, presented in Appendix G 4. The information presented in the specification brochure has been modified to develop a volumetric flow calibration curve for the sensor. The testing conditions at which the mass airflow rate calibration characteristic curve was developed were obtained from Bosch directly [96]. From this information and using perfect gas relationships the associated volumetric flow calibration curve can be directly calculated. This process is shown below.

$$\dot{m}_{at} = \rho_{at} Q_{at} \qquad \text{Equation 5-1}$$

$\dot{m}_{at}$ Throttle mass airflow rate (kg/s)

Q_{at} Throttle volumetric airflow (m^3/s)

ρ_{at} Throttle air density

Rearranging Equation 5-1 above in terms of Q_{th}

$$Q_{th} = \frac{m_{th}}{\rho_{th}} \qquad \text{Equation 5-2}$$

Using the perfect gas relationship, ρ_{th} can be expressed as:

$$\rho_{at} = \frac{P_{th}}{RT_{th}} \qquad \text{Equation 5-3}$$

In this research it is assumed $P_{th} \cong P_{atm}$. P_{atm} is measured by the atmospheric pressure sensor, described above and will be used in Equation 5-3.

The air mass flow calibration characteristic curve for this sensor was developed under the following atmospheric testing conditions.

Pressure	101.30	kPa
Temperature	20.00 °C	(293.15 K)

With this information the calibration air density can be determined from Equation 5-3.

$$\rho_{at} = \frac{101.30}{0.287 \times 293.15} \cong 1.204 \text{ kg/m}^3$$

Using Equation 5-2, Q_{th} can be calculated from the sensors' mass air flow characteristic curve. The volumetric calibration table is shown below in Table 5-2.

Mass Airflow Rate (kg/hr)	Volumetric Airflow (m^3/hr)	Voltage (V)
0	0	1.0000
8	6.6444	1.2390
10	8.3054	1.3644
15	12.4582	1.5241
30	24.9163	1.8748
60	49.8326	2.3710
120	99.6652	2.9998
250	207.6359	3.7494
370	307.3011	4.1695
480	398.6609	4.4578

Table 5-2 Volumetric flow rate calibration Data

Using the developed volumetric airflow rate calibration characteristic curve the sensor is now operating as a volumetric flow rate sensor rather than a mass air flow sensor.

5.3.4.1 Calculation of Compensated Air Mass Flow Rate

The experimental throttle air mass flow rate is calculated from Equation 5-1 by compensating for experimental ambient testing conditions. This involves using the volumetric flow rate output from the sensor and multiplying this value by the experimental testing density calculated from Equation 5-3. The experimental testing air density is determined by using the pressure and temperature information collected by the atmospheric temperature sensor and the throttle temperature sensor (assuming $P_{at} \cong P_{atm}$).

5.3.5 Engine Speed

Engine Speed is determined from the standard motorbike crankshaft angle sensor. This sensor is an inductive sensor, which is mounted above the teeth of the crankshaft. The crankshaft wheel is composed of eleven teeth. When the crank-angle sensor generates eleven pulses the MoTeC engine management system identifies that the crankshaft has undergone one revolution. This information is then converted into an engine speed in revolutions per minute by the MoTeC ECU. The crankshaft sensor has a an accuracy of less than 1 % and a response between 0.3 ms [91]

5.4 Testing Dynamometer

As the experimental engine is mounted to a Formulae SAE Race Car, all testing was conducted on a Chassis Dynamometer. An engine/chassis dynamometer is designed to apply a variable load to an engine and measure the resultant engine torque and power output. The chassis dynamometer used in this investigation is produced by DynoDynamics, model Dynomax 450 4WD. This specific chassis dynamometer has a power measuring limit of 450 kW (600 Hp), which is many times greater than the maximum power output of the experimental engine. The dynamometer uses a load cell to measure engine torque and has a power resolution of 0.1 kW. The full specifications of the experimental testing dynamometer is presented in Appendix H. The dynamometer testing facility is less than a year old, is not used excessively and hence the dynamometers operational accuracy is considered reliable and its repeatability good. Figure 5-8 shows a picture of the dynamometer testing facility used in this investigation.

Figure 5-8 Dynamometer control panel

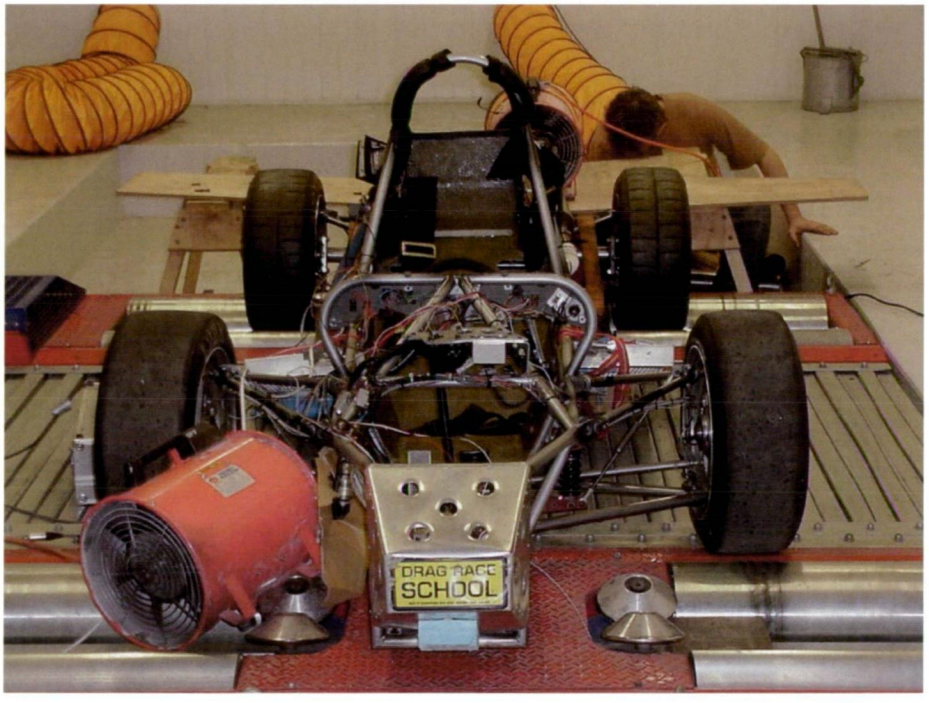

Figure 5-9 Race car mounted on the chassis dynamometer

This particular dynamometer uses an eddy current or absorber or a "brake" to apply load on the engine. When the current supplied to the coils of the absorber is increased the magnetic field increases which in turn increases the resistance to the rotor spinning inside the armature. This has the effect of reducing engine speed, equivalent to driving a vehicle up an incline. Eddy current brakes have the advantage varying engine load rapidly.

5.5 Summary

This chapter provided a description of the experimental setup, which will be used to collect the necessary steady state and transient engine data required for the development of the ANN models. Details regarding the data collection procedures and the experimental data testing range, are addressed in the following chapter.

6 CHAPTER 6

6.1 Experimental Testing Matrix

ANN transient engine modelling research, to date, has relied on some or all of the training or validation data sourced from engine simulation programs [59]. Other research simply present theoretical models or approaches without providing sufficient evidence through experimental validation to support their ideas or rationale [47], [97]. In this research it is considered paramount to use only real valid engine data, acquired through chassis dynamometer engine testing.

In this research the feasibility of developing an ANN engine model that has the capacity to adequately estimate the port air mass flow during periods of steady state and transient driving conditions is to be illustrated. In order to achieve this, two different forms of engine information must be collected, steady state and transient engine data, for network training and validation purposes. Consequently the experimental testing data matrix has been divided into, steady state engine data collection and transient engine data collection.

6.1.1 Sampling Rate

It is not possible to choose a sampling rate in the crank-angle domain with the current experimental setup and as a result data is to be decimated in the time domain. Selecting the optimum sampling rate is of importance as a low sampling rate of a highly variable data set can result in a loss of information, as the true variation is not presented in the sample. In selecting the rate of data decimation one must consider the correct sampling period that is sufficient to adequately distinguish all dynamic variations in the parameters under investigation while still maintaining measurement accuracy. Higher sampling rates than this optimum does not improve measurement accuracy, repeated sensor measurements are recorded.

In this study there are two distinctly different types of engine operational modes at which data is to be collected. In steady state engine operation there is only small fluctuations in the parameters of interest. However in transient engine operation the engine parameter vary on much smaller time scales. As a result two different sampling rates were chosen for the different engine testing modes. Data was decimated at 20 Hz in steady state testing, while data was decimated at 50 Hz in transient engine testing. The sampling rate for the transient case was selected on the basis of identifying the parameter with the highest frequency of change (varies on the smallest time scale) which is the manifold absolute air pressure. MoTeC recommends a sampling rate of 50 Hz when logging manifold pressure. The sampling rate of all data can be adjusted in the Dash Manager Software.

6.1.2 Calculation of the Port Air Mass Flow

The calculations required for the determination of the port air mass flow using Hendricks' [1] MVEM manifold filling equations and all associated parameter conditioning was conducted using Microsoft Excel. The time derivative of the throttle position and manifold absolute pressure were determined by developing differential mathematical functions in Microsoft Excel using numerical differentiation based on the accepted forward, backward and central difference formula. Details of which are provided in Appendix I.

Before model training commences it is necessary to consider the inherent accuracy of the port air mass flow calculation.

6.1.3 Consideration of Accuracy in Port Air Mass flow Calculation

Consideration must be given to the overall accuracy in the calculation of the port air mass flow. This is calculated based on the propagation of error in a function of several variables. Table 6-1, depicts the measurement error that is assigned to each variable involved in the port air mass flow calculation. The error limits for each parameter are based on the published accuracy of the associated sensors, presented in Chapter 5.

Equation Variable	Associated Measurement Error (%)
$\dot{m}_{th}$	3 %
P_m	1 %
$\frac{dP_m}{dt}$	3 %
T_m	2 %
V_m	5 %
R	Literature value used $0.287\ \frac{kJ}{kgK}$

Table 6-1 Variable assigned measurement error

The isentropic MVEM port air mass flow equation used in this investigation is:

$$\dot{m}_{ap} = \dot{m}_{at} - \dot{m}_{am} \qquad \text{Equation 6-1}$$

$$\dot{m}_{ap} = \dot{m}_{at} - \dot{p}_m \frac{V_m}{RT_m} \qquad \text{Equation 6-2}$$

Error associated with $\dot{m}_{am} = \dot{p}_m \frac{V_m}{RT_m}$ term is;

$$\left(\frac{E_{\dot{m}_{am}}}{\dot{m}_{am}}\right)^2 = \left(0.03^2 + 0.05^2 + 0.02^2\right)$$

$$E_{\dot{m}_{am}} = 0.0616 \text{ or } 6.16\ \%$$

Total error of $\dot{m}_{at} - \dot{p}_m \frac{V_m}{RT_m}$ is therefore;

$$\left(\frac{E_{m_{ap}}}{\dot{m}_{ap}}\right)^2 = \left(0.03^2 + 0.0616^2\right)$$

$$E_{m_{ap}} = 0.0685 \text{ or } 6.85\ \%$$

The above calculation suggests that the calculated port air mass flow is accurate to within ± 6.85 %. With the port air mass flow error margins established it is now possible to proceed with a description of the ANN model training and testing software and provide a definition of the errors used to evaluate and analyse the performance of the individual networks.

6.1.4 ANN Training & Testing Software

The University of Tasmania has developed Microsoft® Excel based ANN training and testing software primarily for manufacturing applications, as covered in [88]. This software was used in this investigation. The software operates in Microsoft Excel by first requesting the number of inputs and outputs of the ANN and how many lines of data encompass the training and testing data set. The software then generates a table based on this information and the associated data is then inserted into the worksheet. The software then proceeds to normalise the data. The program then presents a number of training options - such as ANN type, transfer function, number of neurons (nodes), and the percentage of training data that is to be withheld and used as testing data. Network training then commences. At the conclusion of network training there a number of analysing options available to the user, such as testing the network with new data, plotting graphs to compare network accuracy with testing data, evaluating RMS percentage errors, conducting model input importance analysis and evaluating total model training time.

6.1.5 Definition of Error Evaluation Criteria Used in this Investigation

In order to analyse and compare the performance of two or more ANN models it is necessary to define the errors that will be used to evaluate the prediction accuracy of the developed models. Three different error measures are used to analyse and evaluate the performance of the different ANN algorithms. These are the average RMS error, the average RMS

percentage error and the model percentage error. The mathematical definitions of the three types of error are provided below:

$$AverageRMS_{ERROR} = \sqrt{\frac{1}{N}\sum_{n=1}^{N}\left(y(n)-t(n)\right)^2} \qquad \text{Equation 6-3}$$

$$AverageRMSPercentage_{ERROR} = \sqrt{\frac{1}{N}\sum_{n=1}^{N}\left(\left[\frac{y(n)-t(n)}{t(n)}\right]\times 100\right)^2} \qquad \text{Equation 6-4}$$

$$PercentageError = \left(\frac{y(n)-t(n)}{t(n)}\right)\times 100 \qquad \text{Equation 6-5}$$

where $y(n)$ = ANN model output

$t(n)$ = Actual target output

N = Number of data patterns

The average RMS error is used to determine the optimum number of training iterations and the optimum model architecture. It is calculated using the normalised data set values. The average RMS percentage error and model percentage error both use the original experimental data values in their calculation. The average RMS percentage error is used to compare how accurate the model output is relative to the measured target output. Model percentage error is employed to investigate the overall model error distribution for the optimum model. As can be seen the average percentage RMS error calculation is different from the average RMS error as it replaces the deviation between model output and actual output with the model percentage error. A description of the network training process will be provided below.

6.1.6 Process of Selecting Optimum ANN Architecture

The optimum ANN model for both steady state and transient conditions was determined through an iterative (trial and error) procedure, by manipulating the architecture of the model in an effort to find the model that best estimated the input data.

The identification of the five input parameters and the single output of the ANN model, as discussed in Chapter Four has fixed the number of nodes at five on the input side and one on the output side of the developed ANN. Hence manipulating the model architecture involved adjusting the number of nodes and number of hidden layers of the network, over a suitable interval, until a configuration was arrived at which minimised the RMS prediction error.

Below, the prediction performance of the two different ANN paradigms, namely BP and OLL, will be discussed. The steady state port air mass flow engine models will be analysed first, followed by the transient engine port air mass flow models.

6.2 Steady State Engine Port Air Mass Flow Prediction

This section individually appraises the steady state engine port air mass flow prediction performance of the two ANN models, namely BP and OLL. During periods of steady state engine operation the port air mass flow is a strong function of the throttle air mass flow rate, as there are only small changes in the manifold pressure. However, there still exists some deviation in the manifold pressure due to the reciprocating motion of the pistons. Below the steady state data collection procedure and any parameter, conditioning is explained. The selection of the optimum ANN architecture and the effect of the number of training iterations on the RMS error are also discussed. The BP network will be analysed first followed by the OLL network.

6.2.1 Steady State Engine Data Collection

Table 6-2 illustrates the steady state experimental testing sites, expressed as a function of engine speed and throttle position, used to train and validate the neural network models.

Throttle Position (%)	RPM						
	4000	*5000*	*6000*	*70000*	*8000*	*9000*	*10000*
20	X	X	X	X	O	O	O
40	X	X	X	X	X	X	X
50	X	X	X	X	X	X	X
60	X	X	X	X	X	X	X
80	X	X	X	X	X	X	X
100	X	X	X	X	X	X	X

Table 6-2 Table illustrating the steady state testing sites, represented by X, at which data was collected.

For each data point, the engines throttle angle was fixed and the dynamometer load was adjusted accordingly so the engine was operating at the desired speed for data collection to commence. At 20 % throttle position it was not possible for the engine speed to exceed 7000 rpm no matter what dynamometer load was applied. Once steady state engine operation had been reached, determined by observing when the real time output of the engine sensors provided relatively constant readings, data logging was initiated, by switching a toggle located on the dash of the race car.

The sampling rate during steady state conditions was set at 20 Hz for all logging parameters. At each testing site, data was recorded for fifteen seconds, which is equivalent to 300 patterns of data.

6.2.2 Steady State Data Parameter Conditioning

In order to reduce the training data size and hence the ANN model training time, a moving average taken over three was introduced into the raw collected data to generate the static back propagation data training and testing sets. This resulted in 100 data points for each testing site and a complete training data set of 3900 data points. An additional twenty point moving average was introduced into the back propagation training data set to generate the Optimise

Layer by Layer training and testing data set. This provided five data points for each testing site.

Two different training sets were deemed necessary, as a preliminary investigation based on the three point moving average data for both the BP and OLL ANN models disclosed that BP presented significantly better prediction results. As a result a smaller set of data was generated and used to train both models and in this case the prediction of the OLL model improved significantly, however the prediction of the BP model deteriorated. To be fair to both models and to eliminate any bias in the training methodology, separate sized training data sets, both based on the same set of data (the OLL data set being an average of the BP data set) were used in an attempt to enhanced the individual models prediction.

The testing data for both models was identical, so that a valid prediction comparison between the models could be made. The testing data was formed by selecting one of the five data points of the OLL training set, resulted in 39 testing validation data points. This data was withheld during the training process. This subsequently reduced the training OLL data set to four data points at each testing site 156 training data points in total.

6.2.3 Prediction Using the Back Propagation Algorithm

The number of training epochs was selected by using the standard approach, by undertaking an investigation in to how the RMS model output error varies with the number of training epochs. As expected this error reduces until it converges to a specific RMS error value after a certain number of training epochs. Further training past this particular epoch number does not improve the accuracy of the model it actually has a detrimental effect of increasing model training time. A common way to observe and determine the optimum training epoch number is to construct a graph of RMS model output error against training epoch/iteration number. The Figure 6-1 shows the variation of RMS output error with increasing training epoch number.

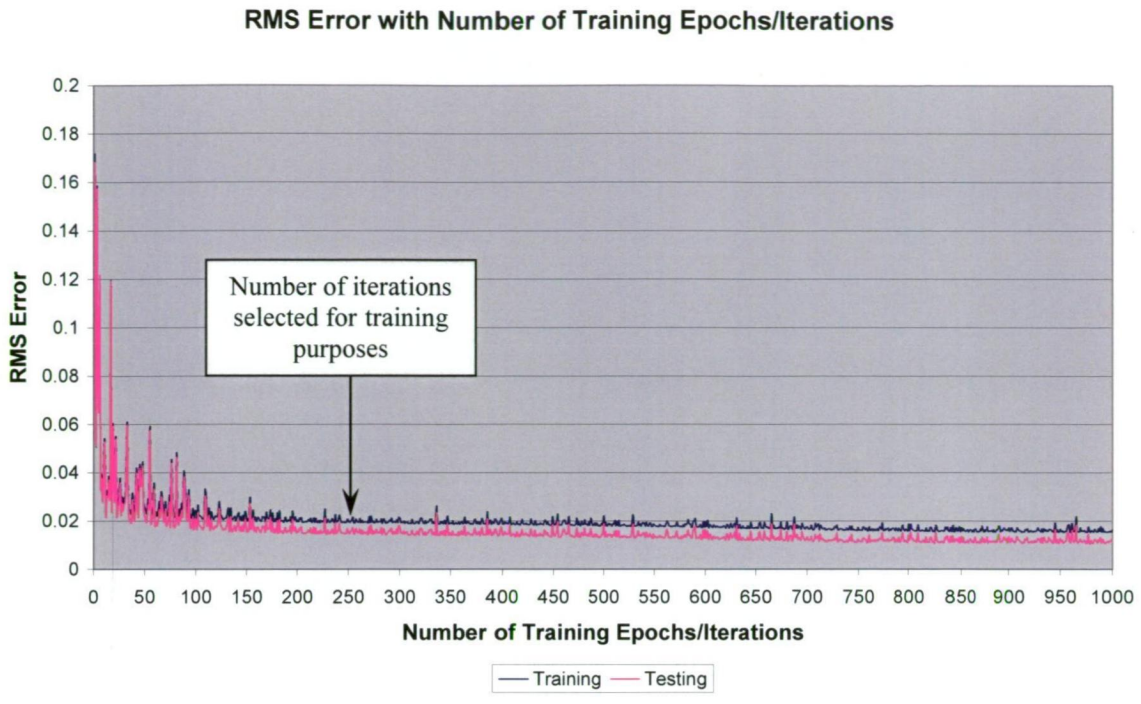

Figure 6-1 The effect the number of training iterations has on RMS error

The RMS error as shown above in Figure 6-1, is calculated from the normalised data set. The RMS error calculated from the normalised data set and the RMS error based on the real actual values are proportional to each other and hence either one can be used for the purpose of this investigation. When selecting the appropriate training epoch number one must take into consideration that a model can become over trained and when this occurs the model can lose its ability to generalise from the data it was trained on. With this in mind, the number of BP model training epochs was chosen based on minimising model training time, maximising the models generalisation abilities and minimising the RMS model output error. The above three selection criteria all carried equal importance in the decision making process. For the BP network, 250 training iterations were selected as the number training epochs that provided the best compromise between all three selection criteria. This is the number of training epochs at which the RMS error starts to converge to its steady state error value as identified in Figure 6-1.

Figure 6-1, is typical of most curves of this nature, depicting a rapid decline in model output error during the initial stages of training (first fifty iterations). With increasing training iterations prediction accuracy slowly improves until the accuracy reaches almost steady state

with only very small improvements in accuracy with increasing training after this point. In Figure 6-1 this is at approximately 250 training iterations.

6.2.4 Selection of Optimum Network Architecture

Both single layer and two layer Back Propagation models were investigated in this study and their associated architectures manipulated in an endeavour to find the overall optimum configuration which minimised the RMS percentage error. For the single layer BP network only the number of nodes in the first layer could be manipulated. However, the number of nodes in both layers of the two layer BP model could be adjusted independently of each other. The hidden layer nodes were adjusted between the range of 2-10 nodes for both layers of the two-layer BP model and between 2-10 for the single layer BP model. These node boundaries were chosen as it is generally accepted that with increasing network size the generalisation abilities of the ANN model deteriorates, conversely generalisation is enhanced if the smallest number of neurones are used in the model architecture [54]. A sigmoid transfer function was selected for training purposes, as it is widely known that the port air mass flow is a highly non-linear function. Table 6-3, below, summarises the range of nodes investigated and other parameters involved in model training.

Model	BP 1 Layer	BP 2 Layers
Inputs	5	5
Output	1	1
Training Epochs	250	250
Transfer Function	Sigmoid	Sigmoid
Number Nodes 1st Layer	2-10	2-10
Number Nodes 2nd Layer	-	2-10

Table 6-3 Summary of model parameters investigated

The best way to present the results of the above investigation is through graphical means. Figure 6-2, below shows the RMS error calculated from the normalised data for different BP architectures, based solely on the training data and Figure 6-3, below based solely on testing data.

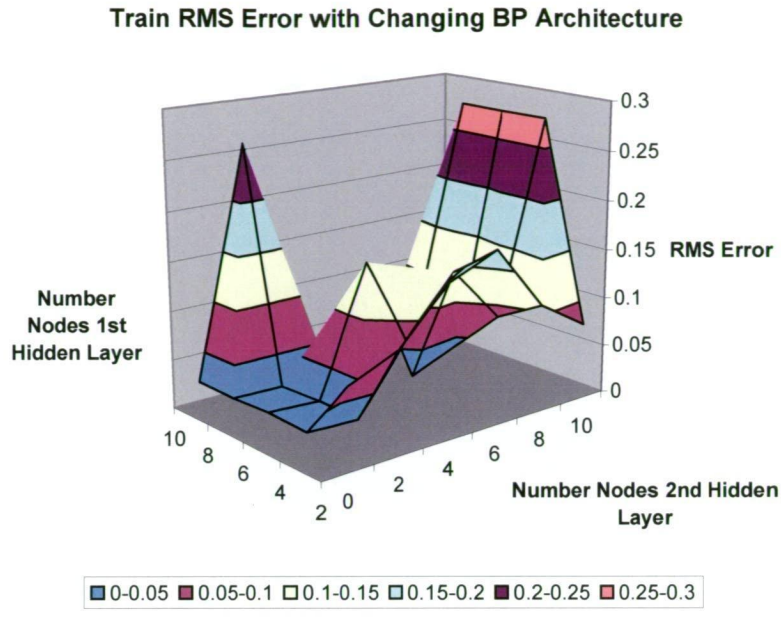

Figure 6-2 Training RMS error with changing BP architecture

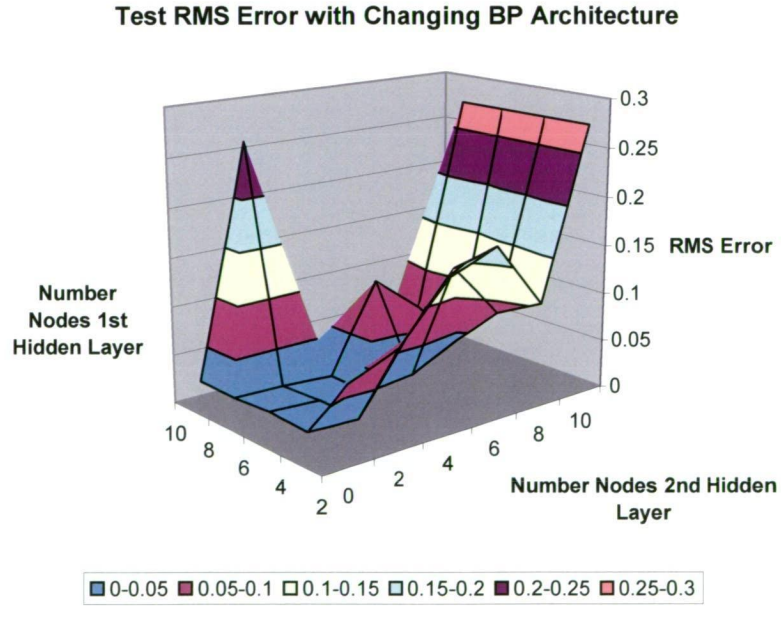

Figure 6-3 Testing/validation RMS error with changing BP architecture

Figure 6-2 and Figure 6-3, show the effect of varying network architecture on the RMS error. The general shape of the two Figures is quite similar, however the magnitude of the error

does not correlate in all positions. This is especially clear in comparing the error magnitude of the middle region of the two figures.

The above investigation revealed that the same network architecture produced the minimum RMS error for both the training and testing data. The optimum network architecture is composed of eight first layer nodes and four second layer nodes, resulting in a final model architecture of 5:8:4:1. The model's prediction performance in terms of average RMS percentage error based the original data values was calculated to be 2.87 % and 1.79 % for the training and testing data respectively. It is interesting to note that the testing percentage error is less than the training error. Intuitively one would expect this to be the other way round. The network prediction accuracy will be analysed in greater detail below.

6.2.4.1 Back Propagation Prediction Accuracy

The steady state port air mass flow prediction accuracy of the optimum 5:8:4:1 BP network will be analysed in this section only in terms of how well the network estimates the training data set. Section 6.2.5 will analyse the performance of each model, by comparing the accuracy to which the BP and OLL network models can predict the testing data set, which is identical for both models. Such a comparison can not be undertaken on the training data set as the training data is not identical for both models as explained above in Section 6.2.2 and hence a direct comparison can not be justified.

The accuracy of each network is evaluated both qualitatively and quantitatively. The qualitative analysis involves graphing the actual port air mass flow target output together with the ANN model output. How well the two curves correlate to one another can be determined in this manner. The quantitative analysis involves statistically analysing the actual and predicted data by developing percentage error deviation histograms to observe model error bias. The BP training results are provided below.

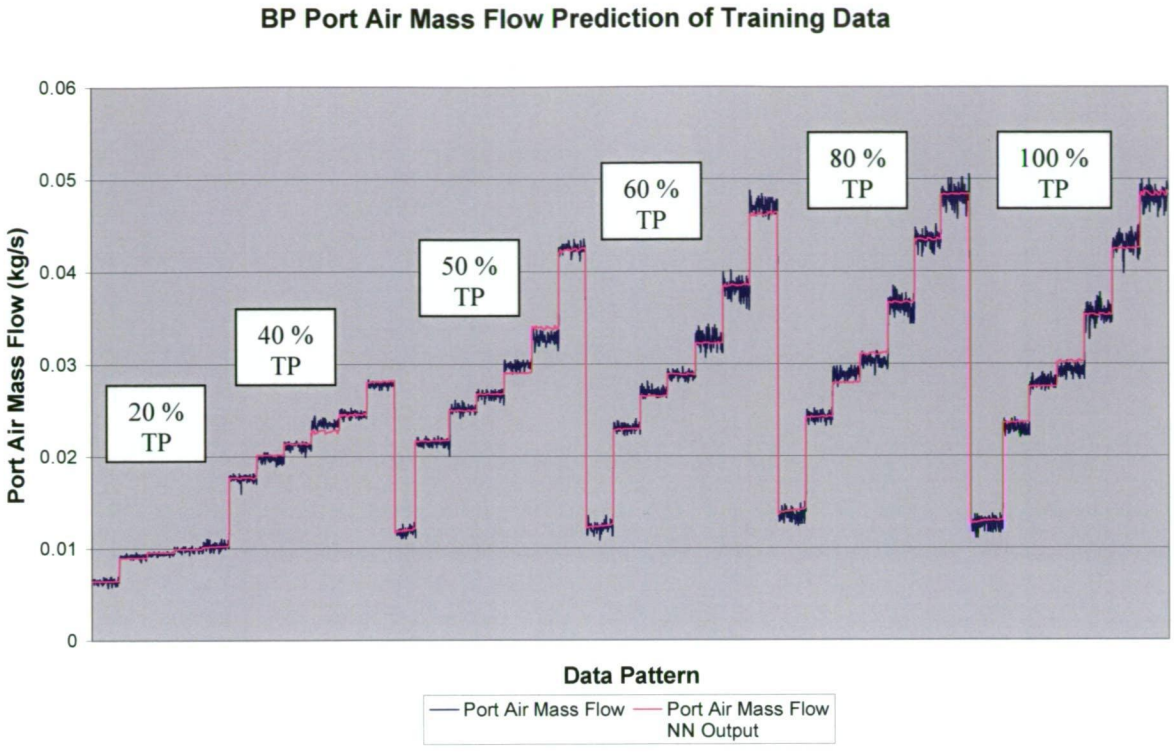

Figure 6-4 BP Training data results comparing actual port air mass flow with the ANN output. TP refers to Throttle Position

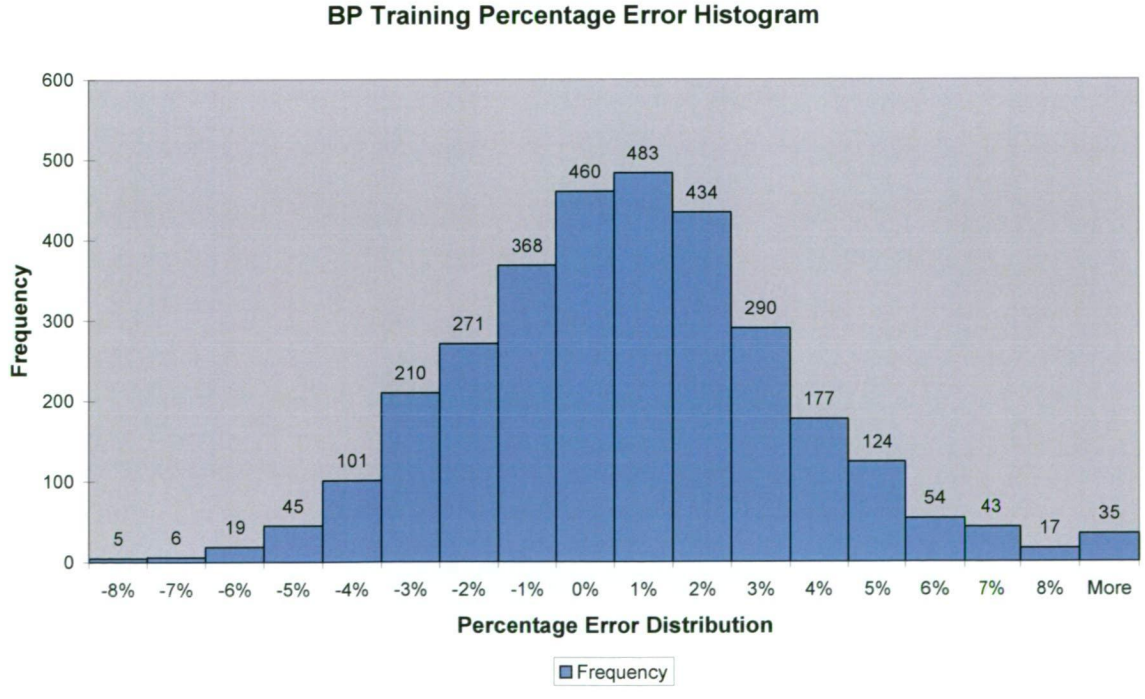

Figure 6-5 BP Training data percentage error deviation histogram

In Figure 6-4, the stepwise behaviour of the curve, represents each different testing site, that is a change in engine load at a specific throttle position, producing the desired experimental testing engine speed. At each throttle position there are seven steps, 20 % being an exception, corresponding to the seven testing engine speeds investigated, ranging from 4000 to 10000 rpm, increasing in increments of 1000 rpm.

Observing Figure 6-4 it can be clearly seen that the developed network predicted the actual calculated port air mass flow rate values at each testing site quite well. The network in most instances predicts approximately the average flow rate at each particular tested engine speed and throttle position, with only very small fluctuations in the model output signal in comparison to the calculated port air mass flow.

The percentage error histogram, shown in Figure 6-5 approximates a normal distribution, with a slight positive bias. This suggests that the model more frequently estimates values higher than the actual port air mass flow rates based on the training data. 52 % of all training data is estimated to be greater than the actual port air mass flow rate, 33% of the training data is under estimated by the model, leaving 15 % of the time when the model predicts zero (0-0.49 %) port air mass flow rate error. The developed ANN model can predict the training data to within a ± 3 % error band, approximately 81 % of the time.

An engine would run richer a greater proportion of the time than leaner, if this model was used in a online control situation, which is advantageous for engine power requirements but detrimental to engine fuel economy and engine emission production. Ideally it would be more advantageous to produce a model that slightly under predicts the port air mass flow rather than over predicts while still maintaining vehicle driveability as this would increase engine fuel economy and potentially reduce emissions[5].

6.2.5 Prediction Using OLL Algorithm

The procedure used to determine the optimum number of training iterations for the BP network was also employed to determine the required number of training epochs for the OLL

[5] Emissions are minimised when the engine is operating at a lambda value of 1 as this is the point at which the catalytic converter efficiency is maximum.

network. Figure 6-6 shows the variation of RMS output error with increasing training iterations for the OLL network.

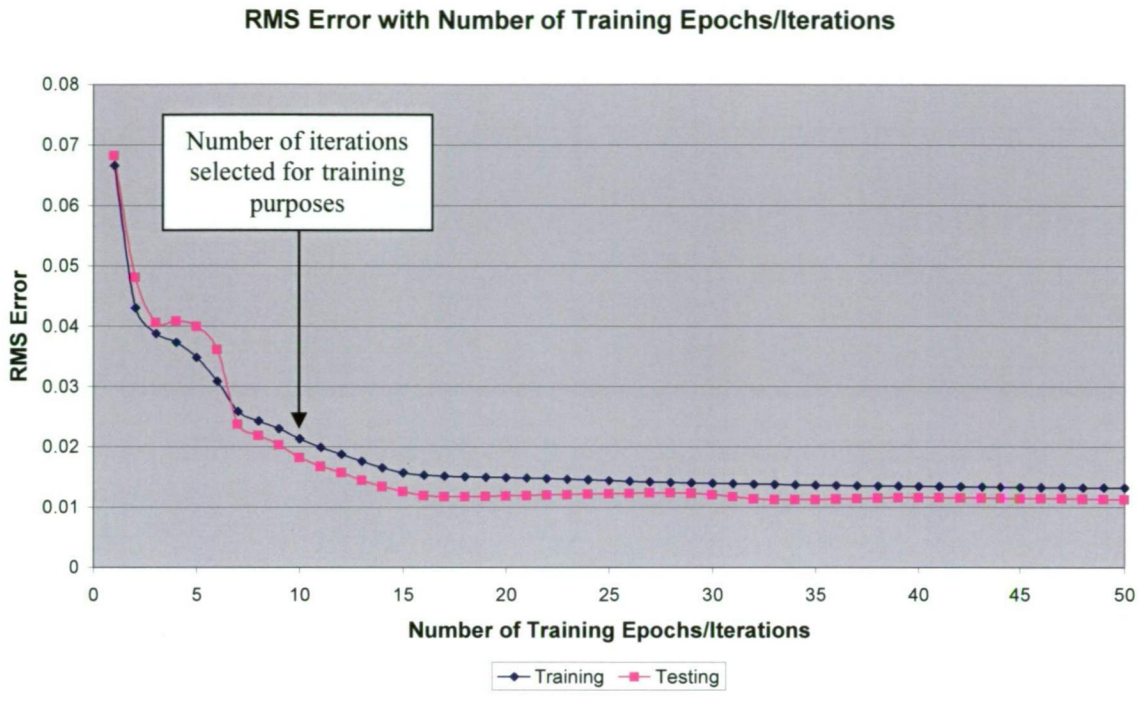

Figure 6-6 The effect the number of training iterations has on RMS error

Previous experience with the OLL model at the University of Tasmania has found that the number of training epochs should not exceed fifteen as further training above this number causes the network to quickly loose its generalisation capabilities. With this in mind and considering the selection criteria highlighted in Section 6.2.3 above, 10 training epochs were selected for training purposes, as highlighted in Figure 6-6. This initial investigation also illustrates the fast convergence rate of the OLL algorithm, (only taking approximately 15 epochs) in comparison to the BP paradigm (taking approximately 250 iterations) before the model converges to a steady state error value. The OLL network has a fast convergence due to the method used to calculate the optimum weight connections between each layer of the model. The OLL model solves for the weight connections by linearising the transfer function rather than relying on an iterative, trial an error approach as used by the BP algorithm. The training methodologies for each network are discussed in more detail in Chapter 3, Section 3.6.

6.2.6 Selection of Optimum Network Architecture

In this study only single layer OLL models were investigated and their associated architectures manipulated in an endeavour to find the overall optimum configuration, which minimised the RMS percentage error. The following results were obtained by adjusting the first layer nodes over the range of 2-20 nodes. As above for the BP training a sigmoid transfer function was selected for training purposes. Table 6-4, below summarises the range of nodes investigated and other parameters of interest, which are related to model training.

Model	OLL 1 Layer
Inputs	5
Output	1
Training Epochs	10
Transfer Function	Sigmoid
Number Nodes 1st Layer	2-20

Table 6-4 Summary of model parameters investigated

The best way to present the results of the above investigation is through graphical means. Figure 6-7, below shows the RMS prediction error for different BP architectures, based solely on the training data set and Figure 6-3, below based solely on testing data set.

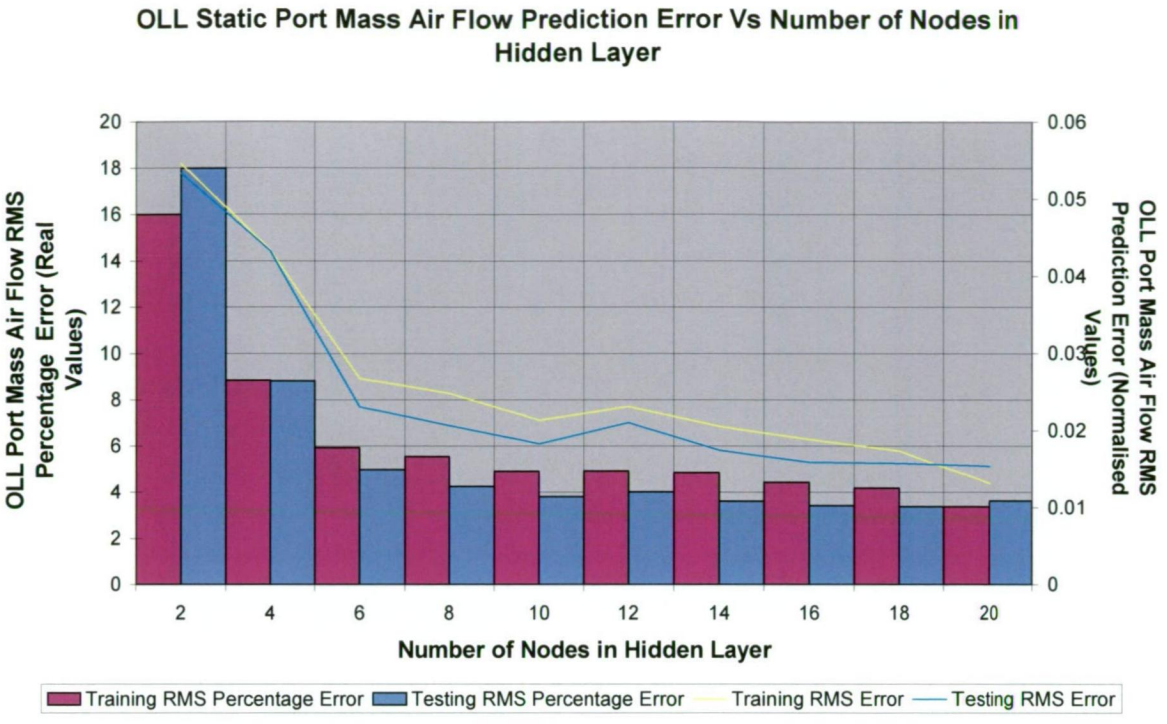

Figure 6-7 Training/testing data RMS based on normalised data / Percentage RMS error based on original magnitude with changing OLL architecture

Figure 6-7 illustrates that increasing the number of hidden layer nodes decreases the training and testing RMS error. Minimum RMS error for both the training and testing data sets occurs with a model architecture of 5:20:1. One would expect that further increasing the number of nodes in the hidden layer would further reduce the prediction error. It was decided to limit the investigation to this number of nodes in an attempt to maximise the generalisation capabilities of the developed network model and to minimise the associated training time.

The resultant RMS percentage error calculated on the original data values rather than on the normalised values is quite small at 3.37 % and 3.62 % for the training and testing data respectively. The network prediction accuracy will be analysed in greater detail below.

6.2.6.1 Optimised Layer by Layer Prediction Accuracy

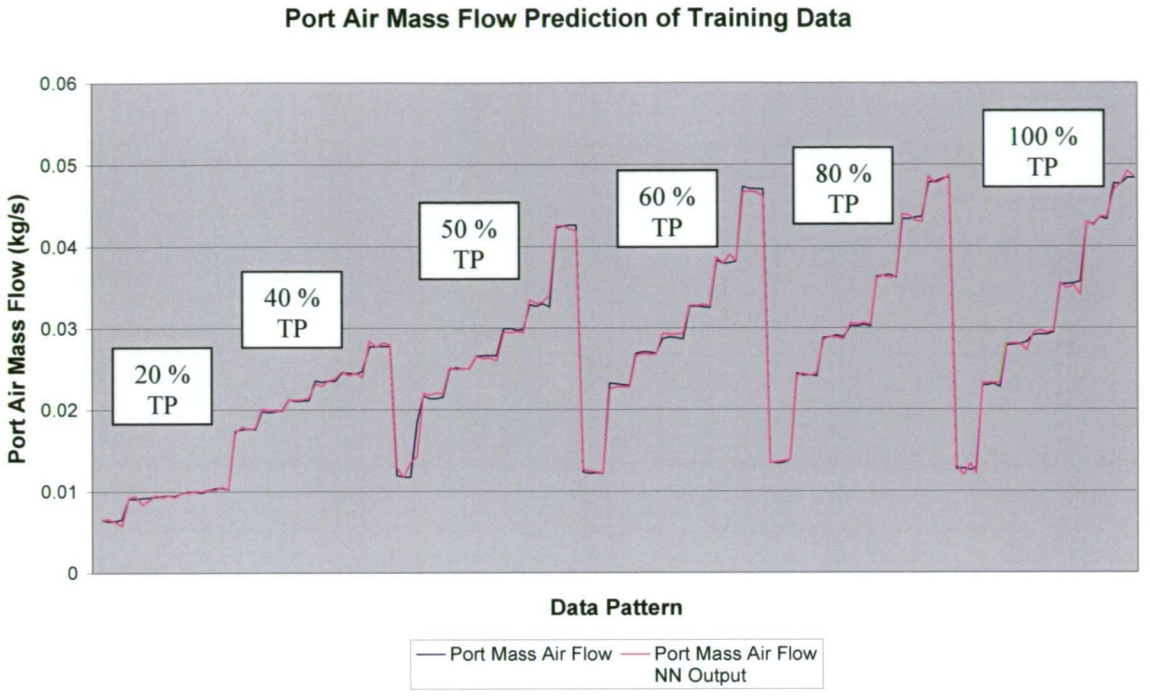

Figure 6-8 Training data results comparing actual port air mass flow with the ANN output

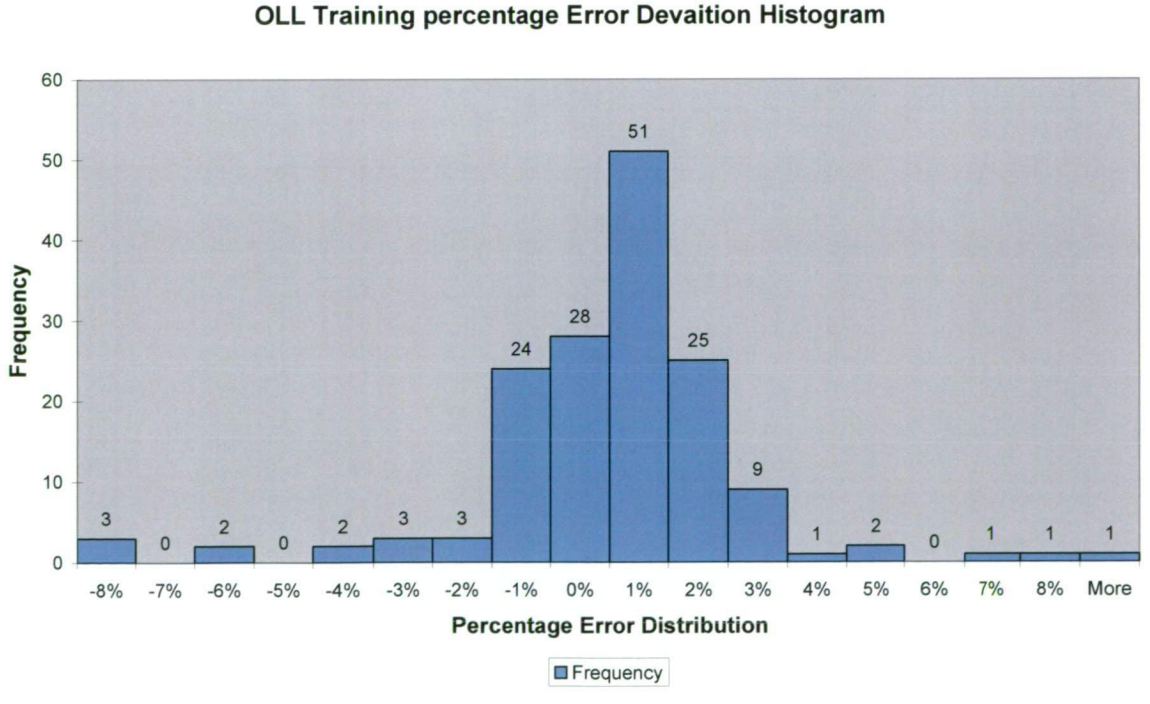

Figure 6-9 Training data percentage error deviation histogram

As before in Figure 6-4 shown above, the stepwise behaviour of Figure 6-8, represents the different engine throttle and load sites used for training and testing purposes. The training data for the OLL network is an average of the BP training data as explained above.

Observing Figure 6-8 it can be clearly seen that the developed network predicted the actual port air mass flow values reasonably well. The percentage error deviation histogram, as shown above in Figure 6-9, shows that the error distribution approximates a normal distribution, with a positive bias. This suggests that the OLL model more frequently estimates values higher than the actual port air mass flow rate. 58 % of all training data is estimated to be greater than the actual port air mass flow rate, 24 % of the training data is under estimated by OLL model, leaving 15 % of the time when the model predicts zero percentage error deviation. The developed ANN model can predict the training data to within a ± 3 % error band, approximately 91 % of the time.

6.2.7 Comparison of the Established BP & Developed OLL Steady State Models

As mentioned above it was not possible to directly compare the steady state BP and OLL models based on their training data set, as it was not exactly the same. However the unseen testing data for each model is identical and thus the testing prediction performance of each model can be compared directly. The results of this comparison are displayed below using the same graphical techniques employed above.

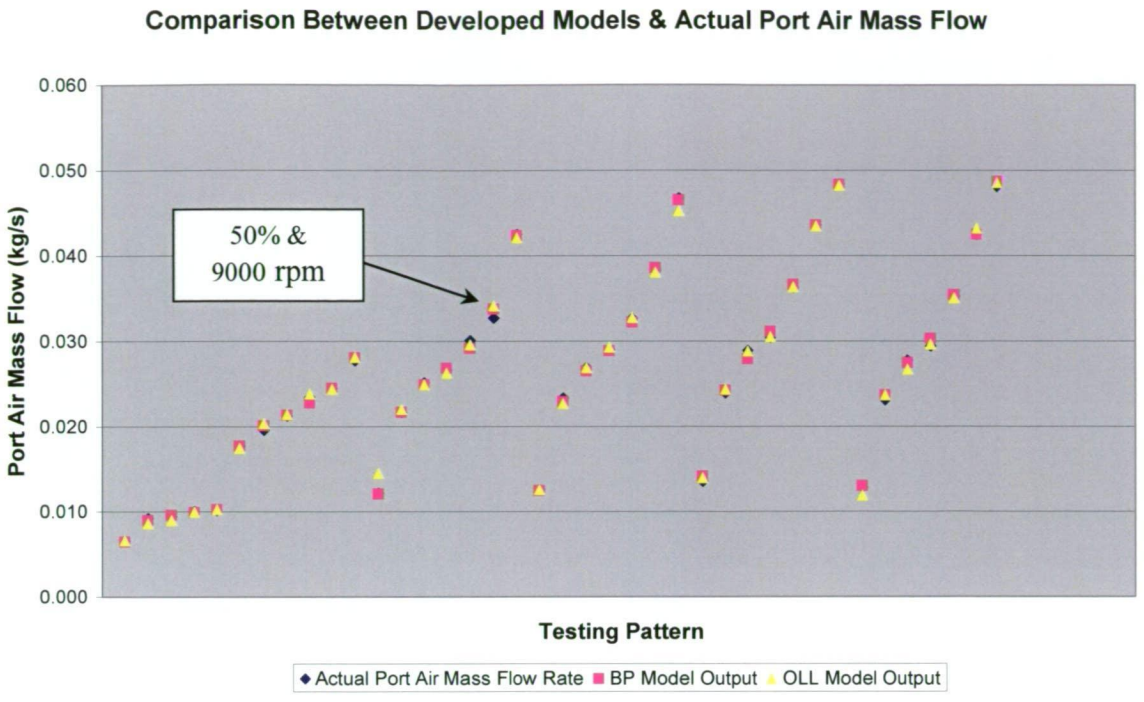

Figure 6-10 Actual Port Air Mass Flow and BP/OLL Model Predicted Port Air Mass Flow

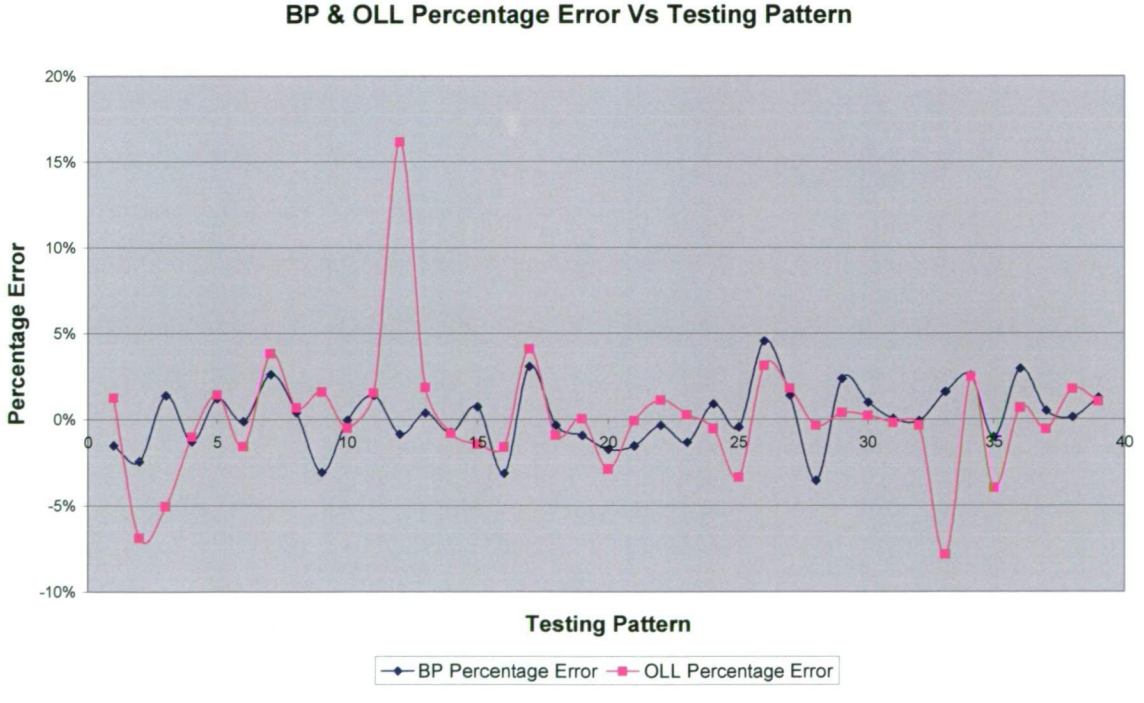

Figure 6-11 Percentage error against training pattern

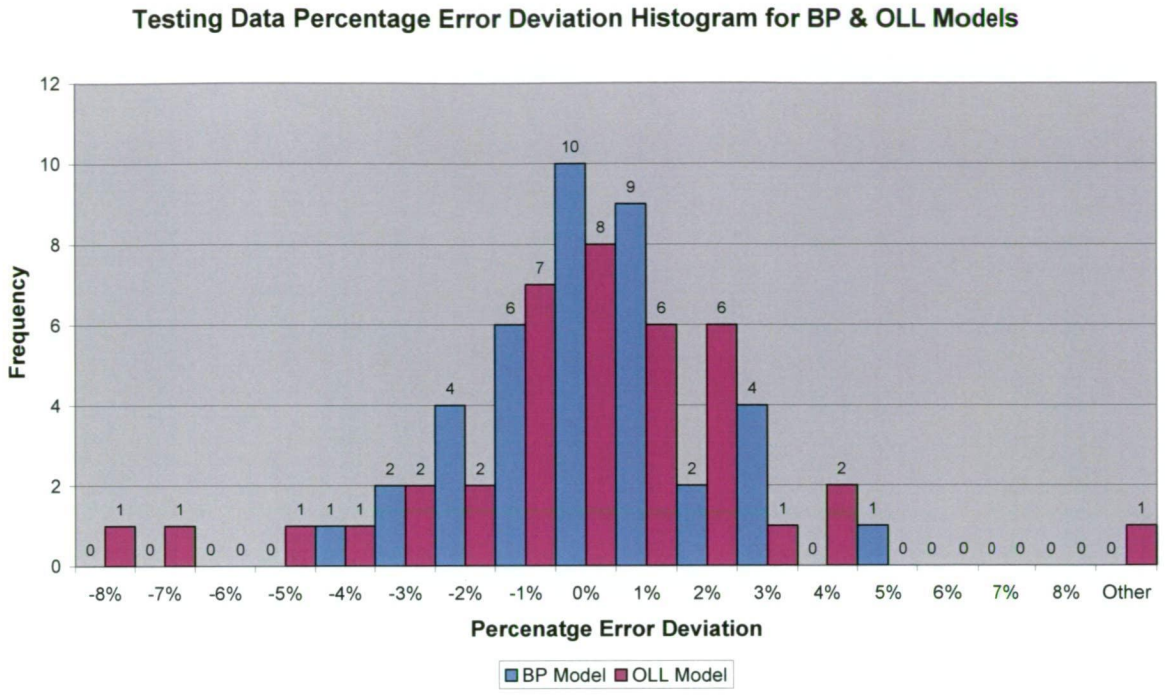

Figure 6-12 BP and OLL static Models, testing data percentage error deviation histogram

Above in Figure 6-10, the testing data is composed of a single point at each experimental throttle and load condition. This data remained unseen during the model training process. Generally, both the BP and OLL developed models can predict the unseen testing data quite well. The BP model has an average RMS percentage error calculated from the original data values of 1.79 %, compared to 3.62 % for the OLL model. On this basis alone it is clear that the BP network is more accurate at predicting the steady state port air mass flow rate. Figures 6-10 and 6-11 also illustrating that the BP model provides a more precise prediction.

Based on the worst case scenario the BP model predicts the target output to within ± 5 %, while the OLL model can only predict the testing data to within approximately ± 16 % (+ 16% / -8%). The OLL model has a greater tendency for large percentage error excursions, in comparison to the BP model and hence the reason for its greater RMS error value in comparison to the BP model. To illustrate this the worst absolute percentage error excursion, for the BP model is 4.55 % compared to 16.15 % for the OLL model. One interesting validation point, highlighted in Figure 6-10 above, is at 50 % throttle position with the engine operating at 9000 rpm. Both models find it difficult to adequately predict the port air mass

flow rate at this particular operating condition with both models over estimating the target value.

Figure 6-12 compares the percentage error distribution of each model. As can be seen the OLL model's percentage error is greater than ± 5 % on three occasions. With the exception of these three points, the OLL model's percentage error distribution is comparable to the BP models percentage error distribution. Two of these excursions occur at the beginning of a new throttle position value experimental testing sites. The percentage error deviation distribution of both models approximately represents a normal distribution, with the BP & OLL networks both exhibiting a slight positive bias. The BP model is able to predict approximately 26 % of all the testing data to within zero percentage error, while the OLL model can only predict 21 % of the testing data to within zero percentage error. The BP model can predict the testing data to within a ± 3 % error band, approximately 95 % of the time, which is an increase of 14 % in comparison to the value calculated based on the training data. In comparison, the OLL model can predict the testing data to within a ± 3 % error band, approximately 82 % of the time, which is a decrease of 9 % in comparison to the training data value.

The results above clearly indicate that the most accurate and precise model in predicting the stationary port air mass flow (throttle air mass flow) is the BP network. The accuracy of the results suggests that ANN can adequately represent steady state engine mass airflow maps and thus confirms what Hodgson et al [2] found in the same field of study. The results also support Blomqvist et al [6] rationale in comparing steady state developed ANN based engine fuelling strategies to conventional ECU look up table algorithms under certain transient testing conditions.

6.3 Transient Engine Operation Port Air Mass Flow Prediction

It was shown above that ANN's can adequately predict the steady state port air mass flow rate to within a reasonable accuracy. This section appraises the potential of the Backpropagation and Optimised Layer by Layer neural networks in predicting the transient port air mass flow which is a more challenging task due to the time changing characteristics of model input and

output variables. During periods of highly transient engine operation the changes in the manifold pressure are large and the manifold filling phenomena becomes significant and consequently effects the amount of airflow at the engine ports.

The transient data collection procedure and the any conditioning that was performed on the collected experimental data will be explained in the following section. The selection of the optimum ANN architecture will then be appraised followed by the effect of the number of iterations on the RMS error. The investigation will conclude by analysing the prediction accuracy of the separate ANN models. The BP network will be analysed first followed by the OLL network.

6.3.1 Transient State Engine Data Collection

Transient state engine data was collected at a constant dynamometer load. The dynamometer load chosen limited the engine speed to 10,000 rpm at 100 % throttle position, which is 2500 rpm below the speed limiter for the engine. This load condition was chosen mainly to prevent damaging the engine during the long periods of experimental testing. Transient data collection was composed of a number of tip in tip out throttle angle scenarios at various throttle position magnitudes. It was decided that a random excitation on the accelerator pedal would represent more closely a real valid driving condition and eliminate any preconceived knowledge in being able to set a throttle transient schedule that could enhance ANN model training and hence improve prediction performance. The innovation in making the experimental test rig suitable for both static and transient conditions has enabled the testing to be carried out over a large range of driving conditions. Realistic driving behaviour was simulated by varying the dynamic engine parameters in such a manner to best represent transient engine operation. Using such a transient schedule is a much more difficult in terms of model training than using idealised repetitive square wave tip in tip out scenarios that other authors have based similar research upon [4], [59], [60], [73]. Transient data was measured at a sampling rate of 50 Hz.

Transient data collection in this instance does not solely refer to repetitive throttle movements, but also periods at which the throttle is constant for a small period of time. With this in mind periods of constant throttle operation can be considered a special case of transient

engine operation, represented when the derivative of the throttle position is equivalent to zero. As a result transient engine operation covers the whole spectrum of potential throttle positions available as inputs to the system. The diagram below shows the testing and training transient throttle position movement at which the ANN models were trained and validated on.

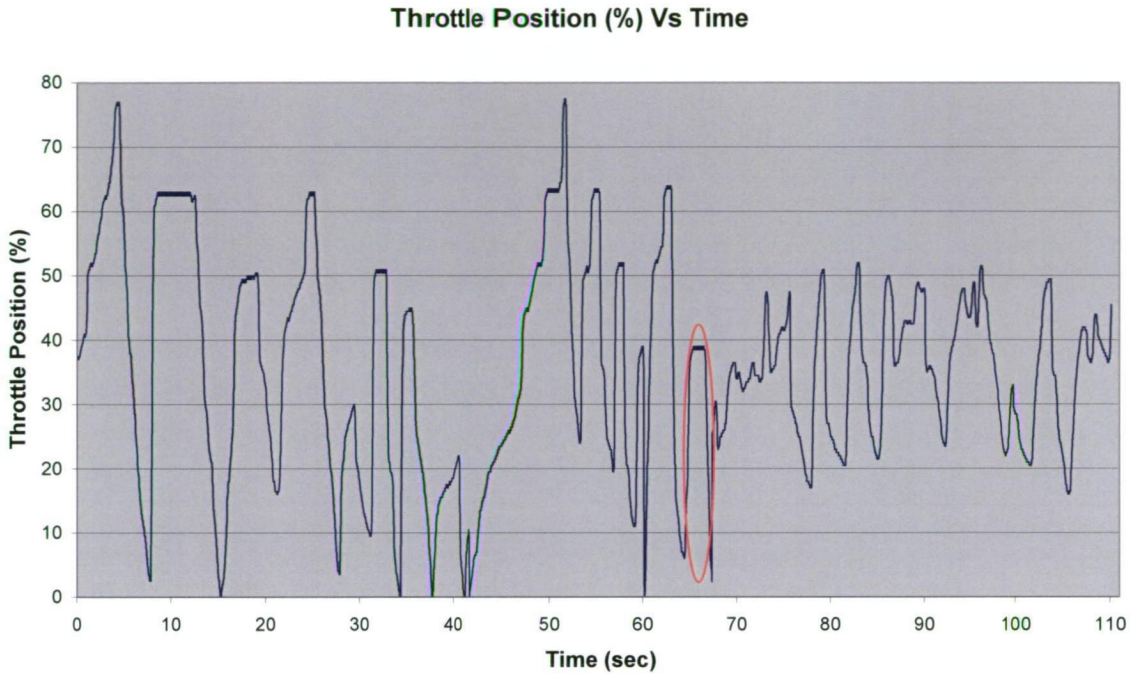

Figure 6-13 Transient Throttle Position Training/Testing Schedule

Figure 6-14 shows a comparison between the calculated port air mass flow and the actual throttle air mass flow for the highlighted throttle movement of Figure 6-13 above.

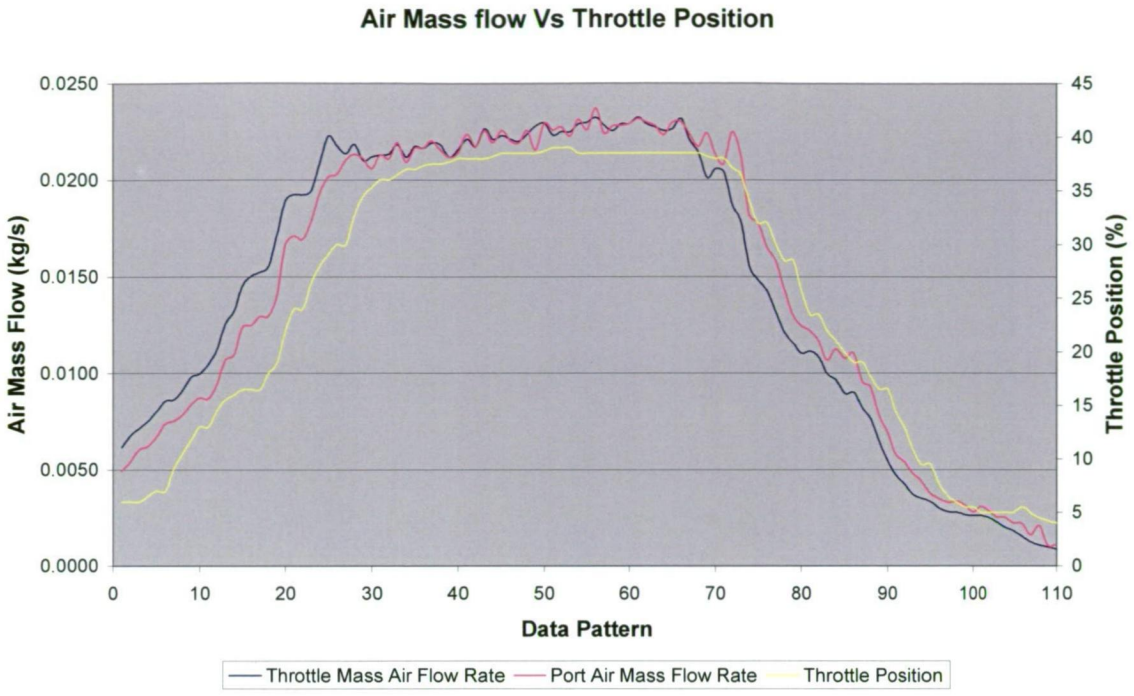

Figure 6-14 Air Mass Flow Vs Throttle Position

It can be seen above in Figure 6-13, that there are no obvious identifiable trends or repetitive throttle excitation movements, which could improve model predictive performance due to associated trends in the training and testing data. Zero throttle positions are also included in the training and testing data sets as they encompass normal driving throttle conditions. Such throttle positions are common during periods of braking and engine coasting. The variation of the port air mass flow in Figure 6-14 is typical of a tip in tip out throttle action and the profile of Figure 6-14 compares favourably with the idealised profile of Figure 3-1.

The throttle transients used to train and test the ANN models are more severe than the largest throttle transients of the EPA's US Federal Test Procedure (FTP75) drive cycle. This is a realistic test schedule that simulates stop and go urban driving conditions. All automobiles driving in the USA must comply to the exhaust gas emission regulations based on this driving cycle. The first sixty seconds of FTP Cycle 2 are shown below for comparative purposes and according to Weeks et al [87] the largest throttle transients of the FTP 75 drive cycle occur in this period.

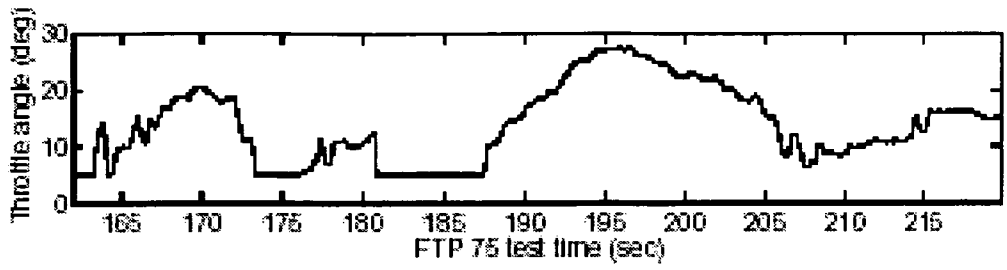

Figure 6-15 First 60 seconds of Cycle 2 FTP 75 driving cycle [87]

The training data and testing data was developed from two different transient logged files combined together with a complete time duration of approximately 110 seconds. The throttle was adjusted between the ranges of 0 and approximately 80 % of full throttle.

6.3.2 Transient Data Parameter Conditioning

The only parameter conditioning conducted on the raw data was that long periods of constant throttle operation were removed to reduce the training and testing data set in an effort to maximise the frequency of transient data present within the training and testing data set. Apart from removing large periods of steady state data, no parameter conditioning was conducted on the experimental data. Only the raw non-manipulated data was used in the ANN model training and testing process. The total size of the training and testing data set was 5507 data sets of experimental conditions.

Five percent of the training data (276 data points) was chosen to make up the testing data. The software randomly extracts the testing data points from the training data sets and this data is withheld from the training process. The training data set is randomly presented during the training process to reduce the likelihood of the network learning any trends within the data. Unlike the steady state training process both the BP and OLL network models have been trained and tested on the exact same experimental data. As a result there is no need to analyse each model separately. Analysing and presenting the results of each model together enhances model comparison. The proceeding model analysis also introduces an additional assessment criterion, the model computational time, which will be used in the selection of the optimum network architecture.

Model computation time is the actual time it takes for the model to complete the total learning and testing cycle and is measured in seconds. The model achieving minimum RMS percentage error with a realistic computation time is ranked as the most suitable for this specific application. That is the optimum model architecture will be chosen on the basis of which model produces the least RMS error, with a suitable model computational time. Computational time has been incorporated into the selection criteria as it is the aim of this investigation to find the most suitable network for future online modelling purposes. An online model requires a high level of accuracy and must also have fast processing and learning times.

As with the steady state port air mass flow prediction, an investigation into determining the required number of training epochs and the selection of the optimum network architecture is necessary. The same techniques used to determine the number of training epochs and the optimum architecture for the steady state port air mass flow model have also been used below to determine these characteristics for the transient data set. To avoid repetition, the results and outcomes of each investigation will be presented only. It is necessary to determine the significance of the throttle derivative as an input to the transient engine model and decide wether this input contributes to the prediction of the port air mass flow.

6.3.3 Throttle Position Derivative Model Importance Investigation

An analysis is required to determine if the derivative of the throttle position is a contributing parameter in the prediction of the port air mass flow for each model. This involves undertaking a predictive importance analysis for each model. Predictive importance is concerned with the increase in generalisation error when a variable is omitted from the training set [88]. The result of this investigation for both the BP and OLL models is presented below in Table 6-5.

PREDITIVE IMPORTANCE RESULTS			
Ranking	*Parameter*	*Contribution Percentage (%)*	
		BP	OLL
1	Throttle Position (TP)	81.70	81.70
2	RPM	10.10	10.10
3	Air Density	2.90	2.90
4	Derivative TP	2.60	2.60
5	Manifold Temp	2.60	2.60

Table 6-5 Contribution of models input parameters on prediction

There are no non-contributing parameters in either of the developed models. This is to be expected as all the model input parameters for the exception of the derivative of the throttle position are identical to those engine parameters identified by Hendricks' et al [1] in modelling the mass air flow rate inducted into an engine.

As can be seen from Table 6-5 the throttle position and the engine speed are the two most important factors governing the engine port air mass flow. This was anticipated as the throttle mass air flow which is the dominate term in the port air mass flow equation is a stronger function of throttle position and engine speed in comparison to the other terms. For the same reason atmospheric air density is weighted slightly ahead of both the throttle position derivative and the manifold temperature as it directly effects the throttle air mass flow rate ($\dot{m}_{at} = \rho_{at} Q_{at}$). The derivative of the throttle position and manifold temperature are ranked lowest, as both are variables of the manifold mass airflow rate equation which is a variation of the perfect gas relationship. The impact of this term in the overall port air mass flow expression is small in comparison to the throttle air mass flow.

The above investigation confirms that the throttle position derivative is not a redundant input for the port air mass flow model. This is because if the throttle derivative input is excluded the RMS prediction percentage error of the model increases.

6.3.4 Number of Epochs Selected for Training

The graphs of RMS error against increasing epoch/iteration number for both the BP and OLL networks are provided below in Figures 6-16 and 6-17 respectively. The RMS error shown in these graphs is calculated from the normalised data set. As identified in the figures below, 250 iterations were selected for the BP model and 10 iterations were chosen for the OLL network for training purposes. The chosen number of training iterations for both models occurs after model RMS error convergence has been reached. As low as five training iterations could have been selected for the OLL network as it is at this point at which the RMS error converges. The same number of training iterations have been selected for both the steady state and transient testing scenarios. It is interesting to note that both models converge to approximately the same RMS error value of 0.025. However as is clearly evident in Figures 6-16 and 6-17 the OLL network converges to this value at a much faster rate in comparison to the BP network. The reasons for the fast convergence of the OLL algorithm is discussed above in Section 6.2.5.

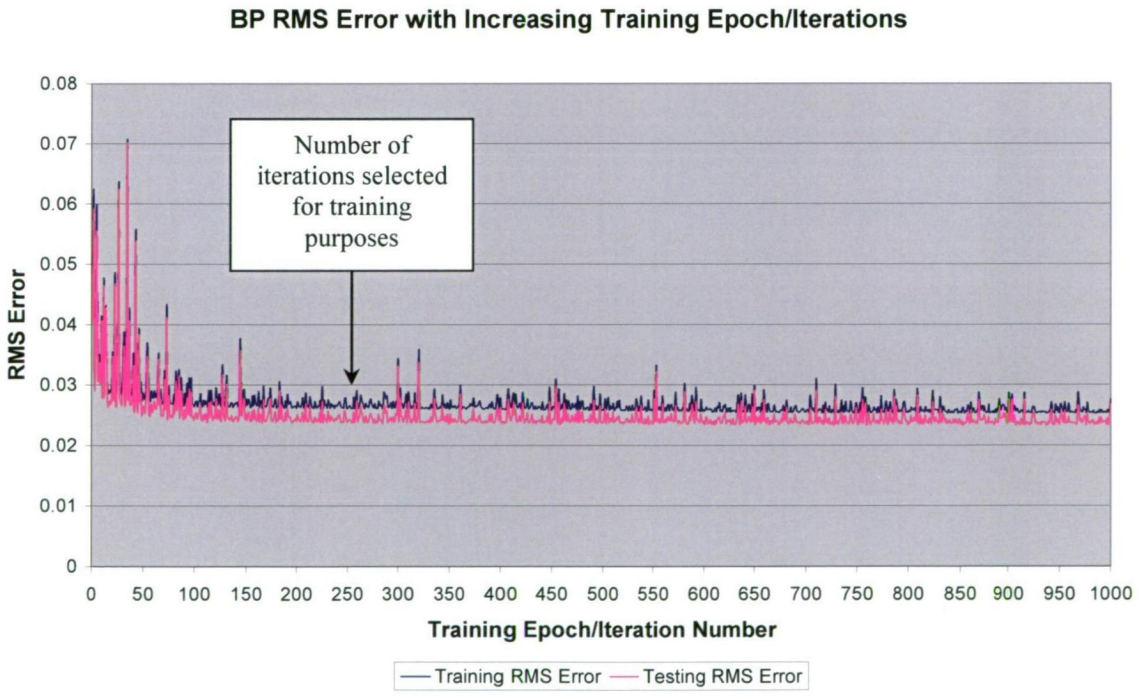

Figure 6-16 The effect increasing the number of training iterations has on the BP networks average RMS error

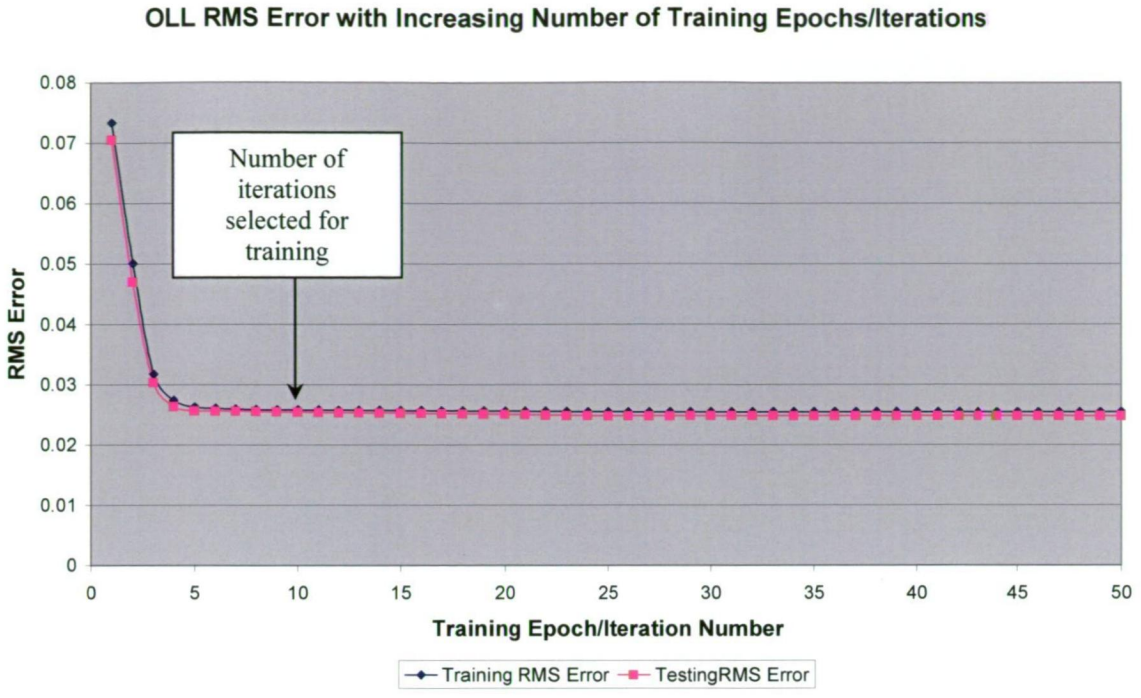

Figure 6-17 The effect increasing the number of training iterations has on the OLL networks average RMS error

6.3.5 Selection of Optimum Network Architecture

Manipulation of the individual model's network architecture was conducted in the same manner as described above in Section 6.2.4, for the BP network and Section 6.2.6, for the OLL network.

Table 6-6, below summarises the range of nodes investigated for each model and other parameters important to model training.

Model	BP 1 Layer	BP 2 Layers	OLL
Inputs	5	5	5
Output	1	1	1
Training Epochs	250	250	10
Transfer Function	Sigmoid	Sigmoid	Sigmoid
Number Nodes 1st Layer	2-10	2-10	2-20
Number Nodes 2nd Layer	-	2-10	-

Table 6-6 Summary of transient model parameters investigated

6.3.5.1 BP Training & Testing

Figures 6-18 & 6-19, below show the training and testing RMS error calculated from the normalised data values for the different BP architectures.

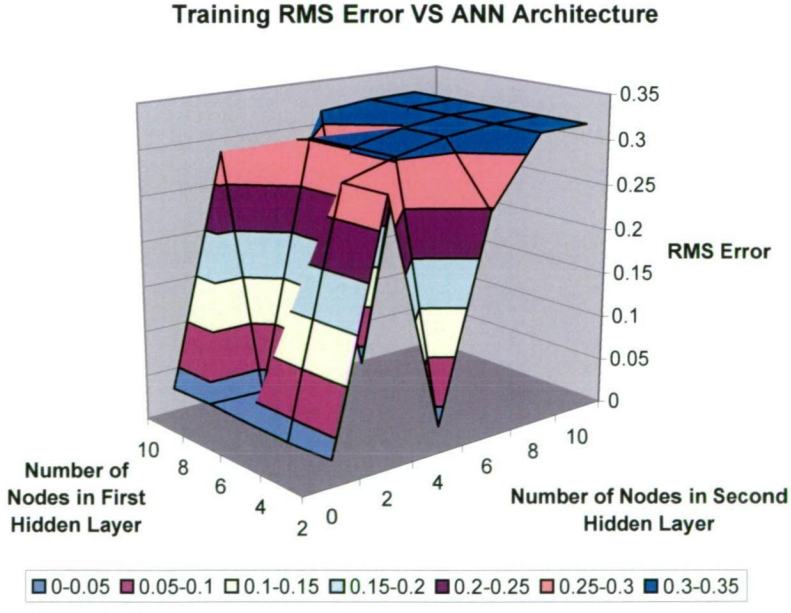

Figure 6-18 Training RMS error with changing BP architecture

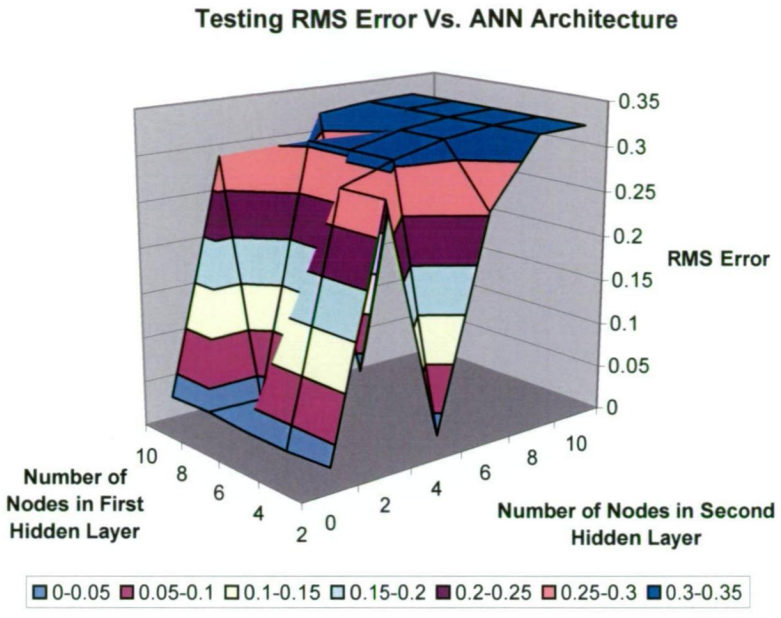

Figure 6-19 Testing RMS error with changing BP architecture

The general shape and error magnitude profiles of Figures 6-18 & 6-19 are almost identical. The above investigation revealed that the same network architecture produced the minimum RMS error for both the training and testing data. The optimum network architecture is composed of six first layer nodes and zero second layer nodes, resulting in a final model architecture of 5:6:1. The model's prediction performance in terms of RMS percentage error based on the original data values was calculated to be 8.86 % for training and 7.56 % for the testing data. Model computational time was determined to be approximately 23 seconds.

6.3.5.2 OLL Training & Testing

Figure 6-20 depicts the training and testing RMS error with changing OLL network architecture.

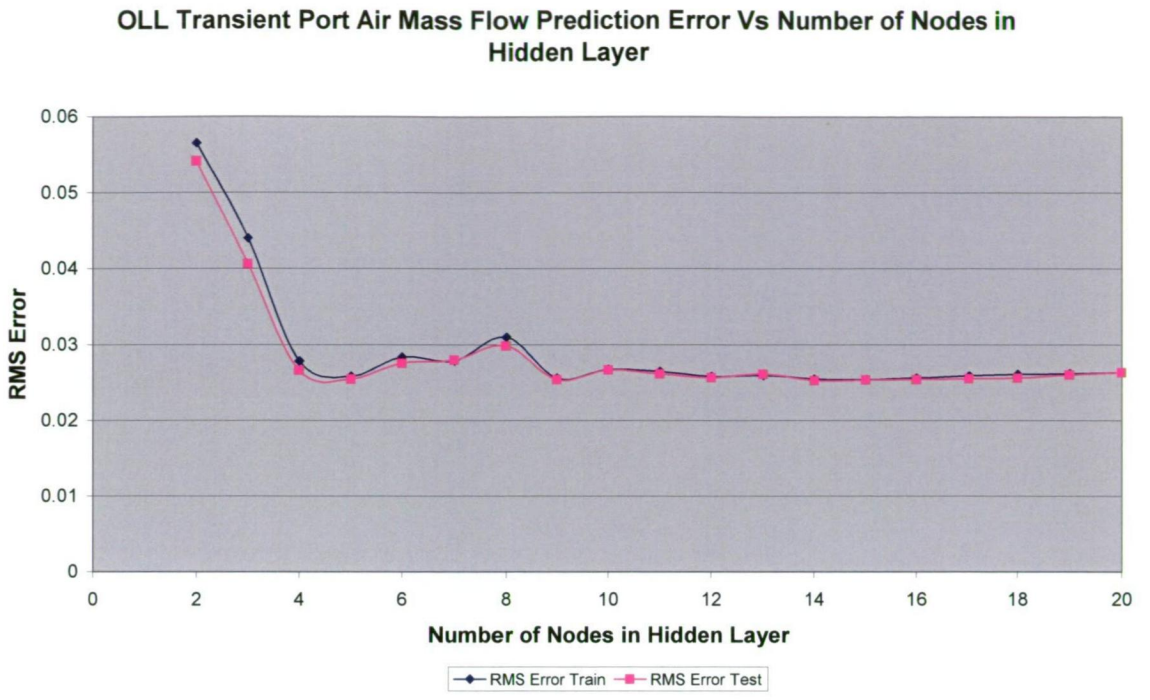

Figure 6-20 Training/Testing RMS error with changing BP architecture

The optimum network architecture based on RMS error alone is composed of fourteen first layer nodes resulting in a 5:14:1 model. However, based on minimising both RMS error and computational time the 5:5:1 model is the more appropriate model. The 5:5:1 model is slightly more inaccurate in terms of RMS error with training and testing RMS errors of 0.02583 and 0.02546 compared with 0.02547 and 0.02528 for the 5:14:1 model. However, the 5:5:1 model in terms of computation time is over seven times faster than the 5:14:1 model, (5.74 s compared to 42.29 s).

The model's prediction performance in terms of RMS percentage error based on original values was calculated to be 177.52 % and 11.10 % for the training and testing data respectively.

Below in Table 6-7, is a summary of major outcomes of the investigation.

Model Parameter	BP	OLL
Architecture	5 : 6 : 1	5 : 5 : 1
RMS Error Training Set (%)	8.86	177.52
RMS Error Testing Set (%)	7.56	11.10
Computation Time (s)	23.01	5.74

Table 6-7 Summary of results for investigation into optimum BP and OLL model architecture

The information presented above in Table 6-7 suggests that the BP model is able to predict the target output to a higher level of accuracy in comparison to the OLL network. However, the computational time of the BP network is significantly larger than that of the OLL model. Although the OLL training error is large in comparison to the BP model training error, a closer investigation into the error distribution of each model, reveals that the error margins of the above two models are much closure than the raw RMS error values shown above indicate.

6.3.6 Training Error Comparison of the Developed BP & OLL Transient Models

As with the steady state port air mass flow analysis, transient model accuracy is evaluated both qualitatively and quantitatively. Figure 6-21 is a graph comparing the BP & OLL model outputs to the training port air mass flow data values. Individual graphs of the BP model output and the OLL model output compared to actual training port air mass flow are provided in Appendix A.

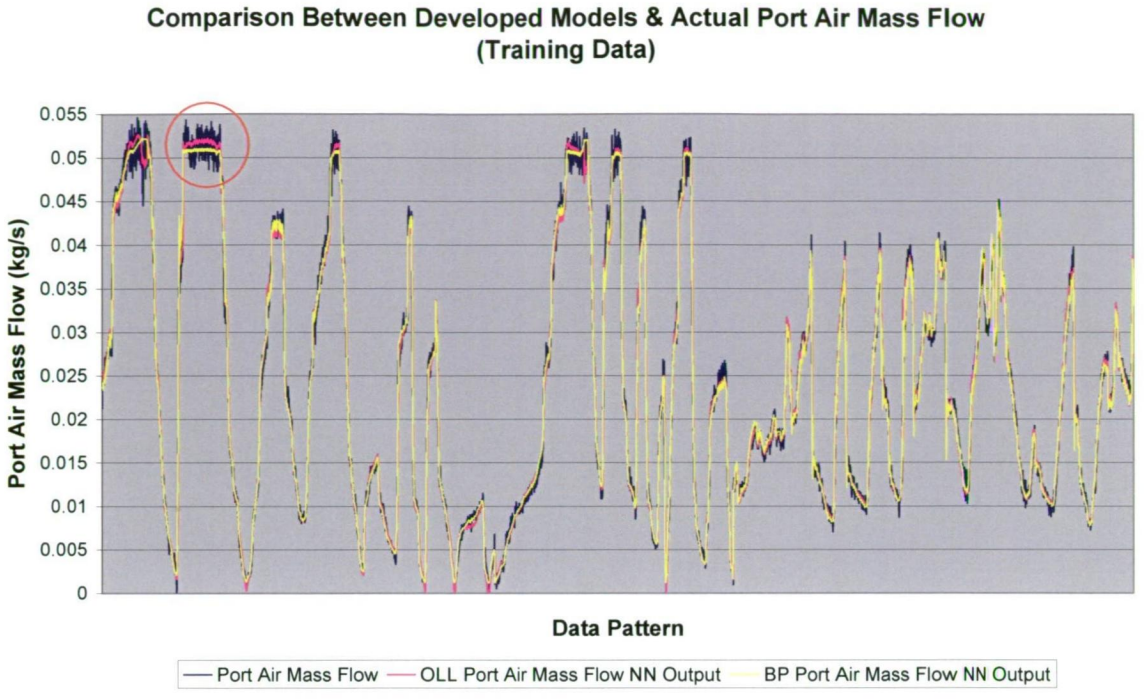

Figure 6-21 Comparison between developed models & actual port air mass flow based on the training data

Figure 6-21 illustrates that there is no significant qualitative difference between the individual model output and the actual port air mass flow output, as both curves correlate well to the actual port air mass flow output. This is also confirmed from observing the individual model prediction to actual output curves shown in Appendix A. The OLL model has a tendency to over predict large port air mass flow values and under predict low port air mass flow values in comparison to the BP models output. Both models during periods resembling steady state engine operation predict the average port air mass flow value. This is most clearly evident during the initial period after the second throttle transient, highlighted by a red circle in Figure 6-21. The training percentage error histograms for both models is provided below in Figures 6-22, 6-23.

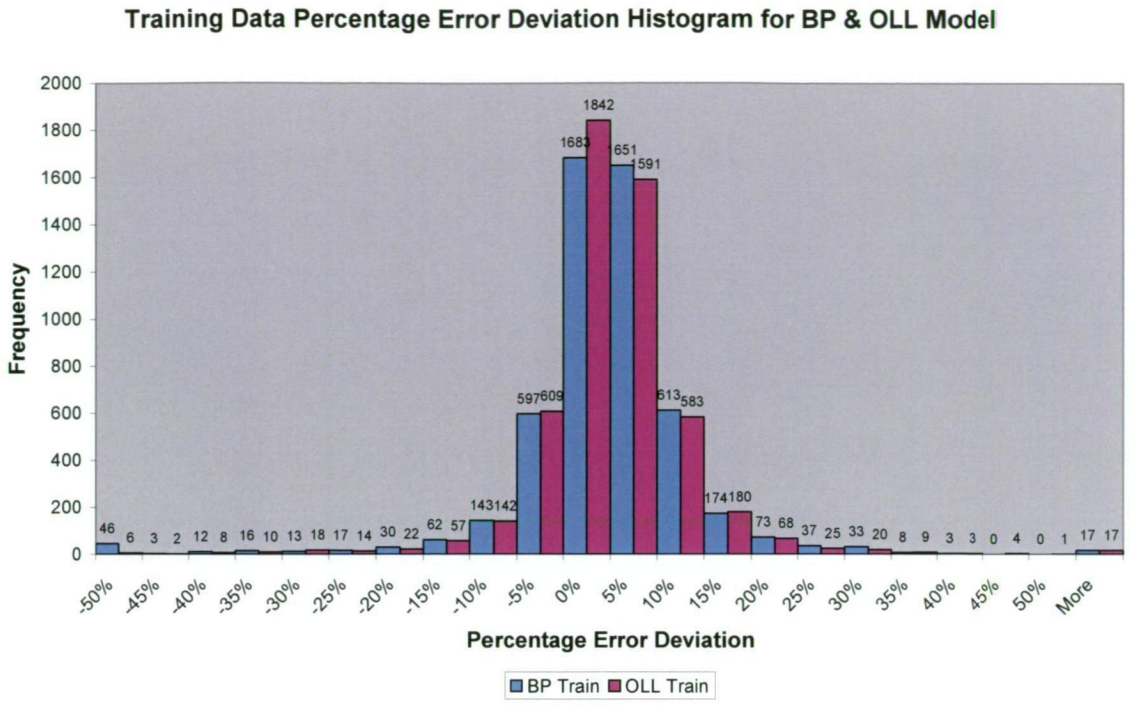

Figure 6-22 BP and OLL models, training data percentage error histogram at 5% increments between ± 50 %

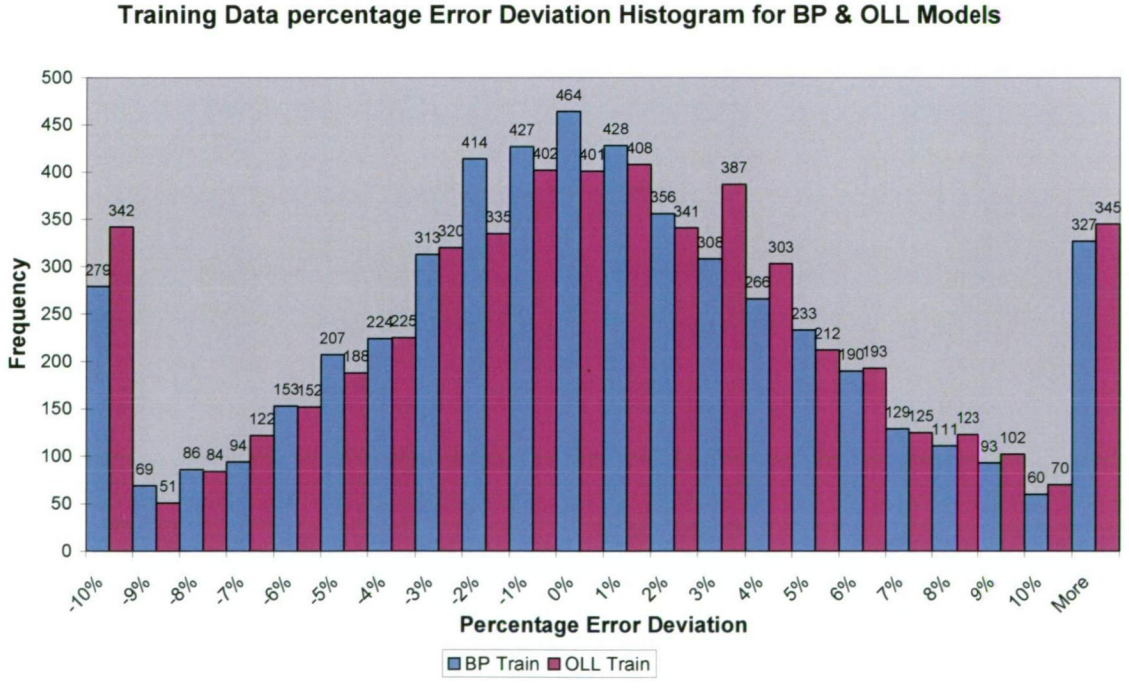

Figure 6-23 BP and OLL models, training data percentage error histogram at 1 % increments between ± 10 %.

Figures 6-22 and 6-23 compare the percentage error deviation distribution of each model between ± 50 % at increments of 5 % and ± 10 % at increments of 1 %. The error boundary range of both the transient BP and OLL models are significantly larger in comparison to the error ranges of the steady state engine data models. The error data scatter is within a training error range of ± 8 % for the steady state engine data, while the transient data requires a range of ± 40 % to adequately display the approximately the same proportion of data. This discrepancy is to be expected as transient engine operation is significantly more complex than steady state engine operation and as a result model prediction accuracy would intuitively be higher.

From Figure 6-22 the shapes of both the BP and OLL algorithms are quite similar approximately resembling a normal distribution. Both the deviation histograms for the BP and OLL models have a negative bias. Approximately 48 % of all the training data is located in the negative region of the percentage error histogram for the BP model while 49 % of all training data is located in the negative region of the OLL histogram. Additional information regarding the distribution of the training data is provided below in Table 6-8. This information has been calculated using the data presented in Figure 6-23.

Percentage Error	**BP**	**OLL**
	Percentage of Training Data (%)	
0 %	8.87	7.67
0 - ± 3 %	51.80	49.59
0 - ± 5 %	69.58	67.33
0 - ± 10 %	93.75	93.40

Table 6-8 Training data categorised into certain percentage error boundaries

Table 6-8 shows that the BP model is approximately 1-2 % more accurate than the OLL model over the first three error boundaries investigated, however between the range of 0 - ± 10 % both models are of similar accuracy in terms of what proportion of data falls within this percentage error range. Both transient models require an error margin between ± 0-10 %, which is three times the size of what is needed for the steady state case (± 0-3%) to encompass approximately 90 percent of the training data. The profile of Figure 6-23, the

percentage error histogram between the range of 0 - ± 10 % approximates a normal distribution. From the results provided above in Table 6-8, the training errors of the BP and OLL models do not appear to be significantly different which is in disagreement with what the training RMS error values indicate.

The reason for this is not obvious from looking at Figure 6-22. However in Figure 6-23 there are a number of data points that are labelled under the heading "More". These data points all fall outside the 50 % percentage error margin. An investigation into the magnitude of these data points for both models yields some interesting results.

It was found that the average RMS percentage error for these data points for the BP network was 76 % compared to 1832 % for the OLL network. This clearly explains the large discrepancy between the overall training RMS error of both models. It was also observed that in both instances these large percentage errors occur when predicting data points of very small throttle positions, predominantly of magnitudes less than 2 %. Based on the RMS error results it can be said that the OLL model is inadequate in predicting the port air mass flow during periods of small throttle operation.

With this in mind a new average RMS percentage error value was calculated for both models. Data composed of throttle angles of less than 2 degrees was eliminated from this calculation. The new RMS error for the BP was calculated to be 7.88 %, which in comparison to the original RMS value of 8.86 % represents a reduction of 0.98 %. The new RMS error value for the OLL model was calculated to be 9.26 %, which is nineteen times smaller than the original RMS value of 177.52 %. This illustrates the enormous impact this small amount of training data, composing approximately 2 % of the total training data set has on the RMS error calculation for this particular model. This phenomenon will be further discussed below in light of its significance in an online engine prediction application.

6.3.7 Testing Error Comparison of the Developed BP & OLL Transient Models

Only the testing BP qualitative graph is shown below as the BP model graph is representative of the OLL model and thus it is believed that this single graph is sufficient in conveying the prediction trend of both models. Both graphs can be viewed in Appendix B.

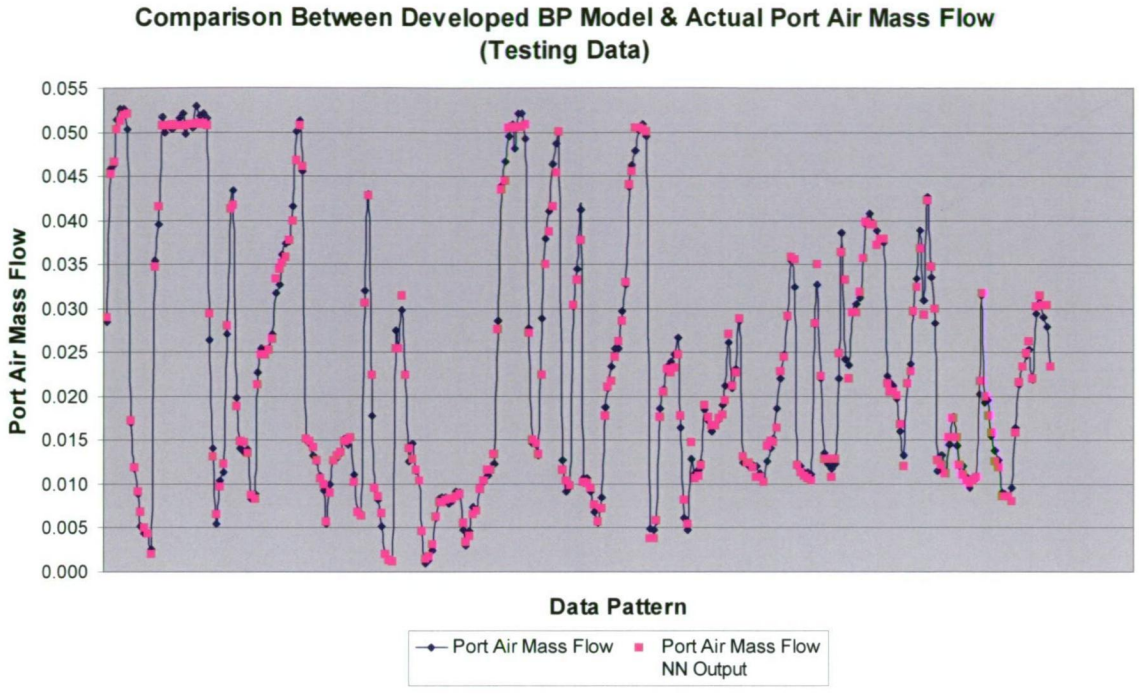

Figure 6-24 Comparison between developed models & actual port air mass flow based on the testing data

It is believed that displaying the results in such a manner above is more correct way of illustrating how close the model's prediction is to each testing data point in comparison to convention line based charts. Prediction of both models is quite good based on this type of evaluation, however a quantitative analysis needs to be undertaken to gain a better understanding of how accurate the prediction of the BP and OLL models are relative to the actual port air mass flow. Percentage error deviation histograms have been developed for both models and are provided below.

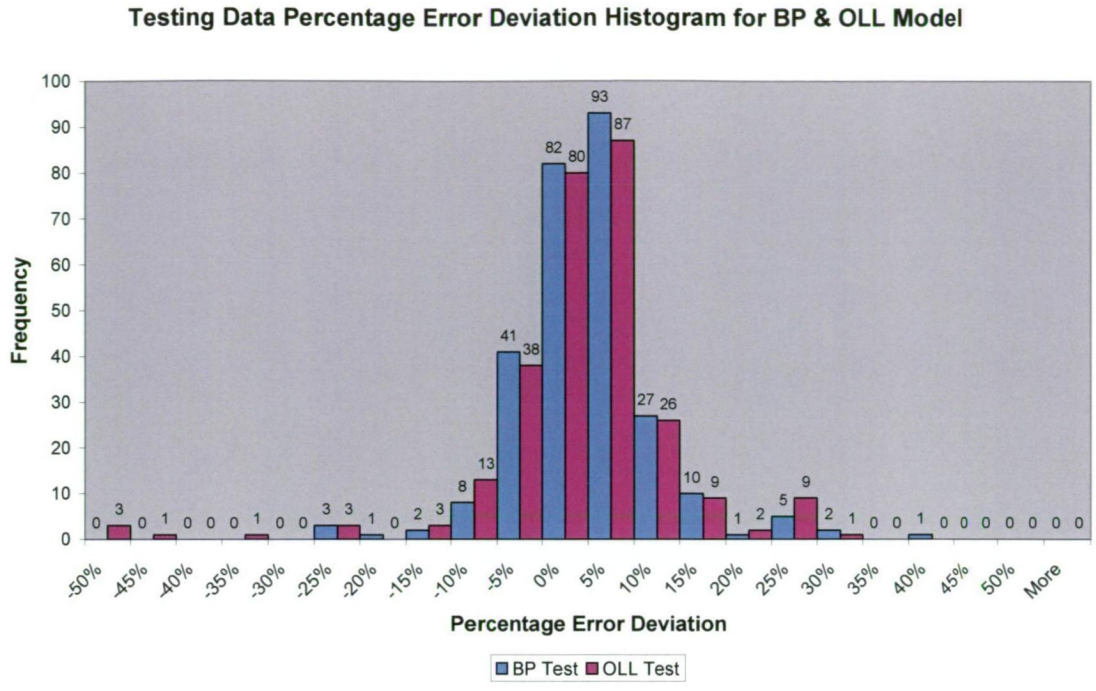

Figure 6-25 BP and OLL models, testing data percentage error histogram at 5% increments between ± 50 %

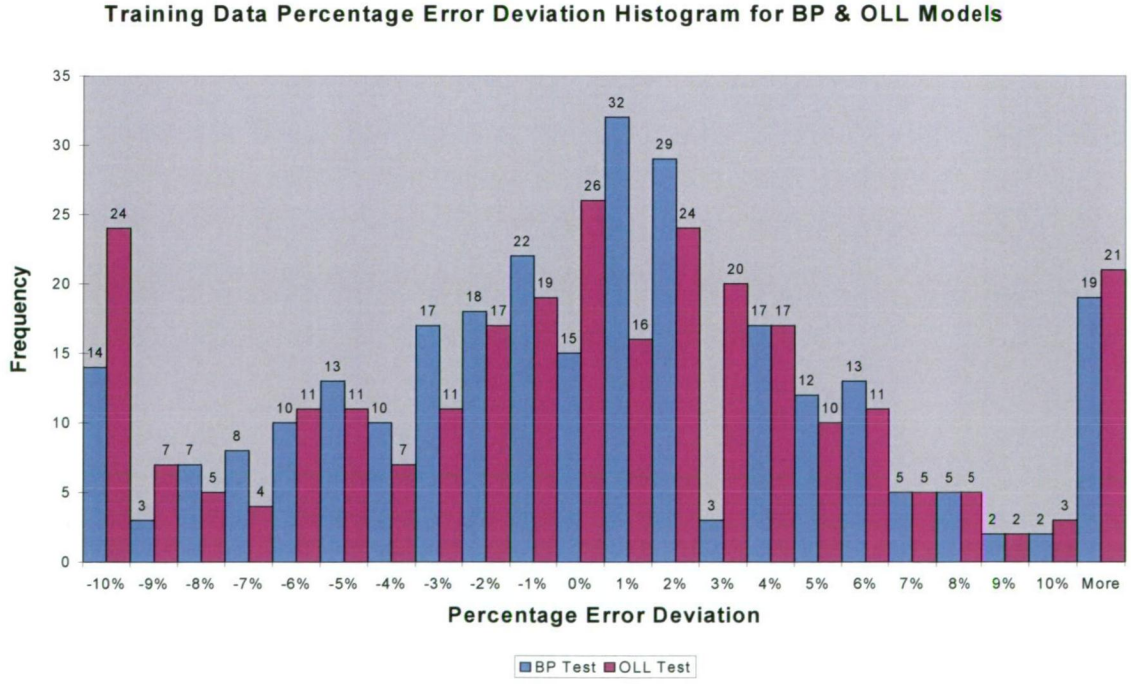

Figure 6-26 BP and OLL models, testing data percentage error histogram at 1 % increments between ± 10 %

Figures 6-25 and 6-26, compare the percentage error deviation distribution of each model between ± 50 % at increments of 5 % and ± 10 % at increments of 1 %. The error boundary range of both the transient BP and OLL models is less than the training error boundaries. This is to be expected as the testing RMS error is less than the training RMS error for both models. Intuitively one would not expect the RMS error for the testing data to be less than the training data. It is interesting to note that there is only a small difference between the transient testing RMS percentage errors of the BP and OLL models in comparison to the difference that exists between the training RMS percentage error values. The reason for this is due to the testing data being composed of only two points at which the throttle position is less than 2 %[6] where the OLL model prediction is highly inaccurate. Although there were only two such points in the testing data at each point the OLL model as expected predicted a value with a significantly larger percentage error than the BP model. The average difference between the models percentage errors at these two points was 37.9 %.

Once again the profile of Figure 6-25 resembles a normal distribution. The BP model has a very slight negative bias while the OLL model has a very slight positive bias. The frequency values of Figure 6-26 are scattered in a more random fashion in comparison to the other error histograms constructed in this study. Although there is no obvious most frequently occurring value to which the error distribution is maximum, the subsequently trend in both the above BP and OLL model profiles do loosely resemble normal distributions. The correlation though is not as well defined in comparison to other histograms developed above. Figure 6-26 does illustrate that the OLL model has a greater tendency to predict values with larger percentage error deviations in comparison to the BP model, as seen by comparing the frequency of occurrence between the two models at –10 %.

Table 6-7, below illustrates what percentage of the training data that lies within the percentage error ranges of 0 %, 0 to ± 3 %, 0 to ± 5 % and 0 to ± 10 %, calculated from information presented in Figure 6-26.

[6] The ANN software randomly choses the training and testing software and the author did not arrange the data to improve model accuracy.

Percentage Error	BP	OLL
	Percentage of Training Data (%)	
0 %	5.44	9.42
0 - ± 3 %	49.28	48.19
0 - ± 5 %	68.11	64.49
0 - ± 10 %	93.12	92.39

Table 6-9 Testing data categorised into certain percentage error boundaries

Although the testing RMS values for both models are lower in comparison to the training RMS values the proportional of data falling within the above percentage error margins is slightly smaller in comparison to the training data. There is little separating the different models in terms of the proportion of data that lies in the above error boundaries, as can be seen by comparing the values in Table 6-7. However comparing the testing and training RMS percentage errors of both models clearly indicates that the BP model is more accurate than the OLL model.

The next section reviews the developed port air mass flow ANN models for online training and prediction purposes. The poor prediction accuracy of the models at low throttle predictions is analysed and the possible practical consequences of this phenomenon discussed. An investigation is also undertaken to determine the most appropriate model for transient online training and prediction.

6.4 Evaluation of the Developed Dynamic Models

6.4.1 Prediction Accuracy at Low Throttle Positions

An investigation is necessary to find the cause as why both the models, but in particular the OLL model, are inaccurate in predicting small throttle position data. This is to be investigated by analysing the percentage error and absolute error over the entire throttle position range. This is to be conducted by developing the appropriate graphs of percentage

error against throttle position and difference in prediction[7] against throttle position for both models. These graphs can be viewed in Appendix C, and indicate that the ANN predicted output to actual target output deviation increases with increasing throttle position opening, however the percentage error increases with decreasing throttle position. The reason for this is due to the fact that at small throttle position openings the actual port air mass flow value approaches zero (ie its value is close to zero). Although the prediction difference is small at small throttle positions, relative to the actual port air mass flow value the percentage error becomes significantly large. As expected the largest percentage error excursions occur at throttle position of zero percent. It can be seen from Appendix C, graphs C-1, C-2, that the BP model at low throttle positions overpredicts the actual port air mass flow, while the OLL model has a tendency to underpredict the port air mass flow model at low throttle positions.

It is difficult to assess the significance of such a deviation on engine operation without implementing the model online in a non control scenario and observing the deviation between model and actual port air mass flow results. The majority of the time the BP network over-predicts the port air mass flow at low throttle position values. This would increase the fuel consumption of the engine. The OLL model underpredicts the port air mass flow at low throttle positions, which would decrease engine fuel consumption. Low throttle position engine operation can not be ignored as it frequently occurs throughout normal driving conditions. These include during times of coasting where the throttle position is small or zero and during normal braking periods.

Current engine management systems during phases of deceleration and coasting actually employ what is known as fuel cut off. This occurs when the throttle is closed and the engine speed is above a threshold value usually 1500 rpm [23]. When the engine speed falls to about 1000 rpm injection recommences according to the speed and load conditions of the engine. Figure 6-27 illustrates the strategy, which is used to control injection cut-out and reinstatement.

[7] Prediction difference is the difference between model full scale output and actual target output

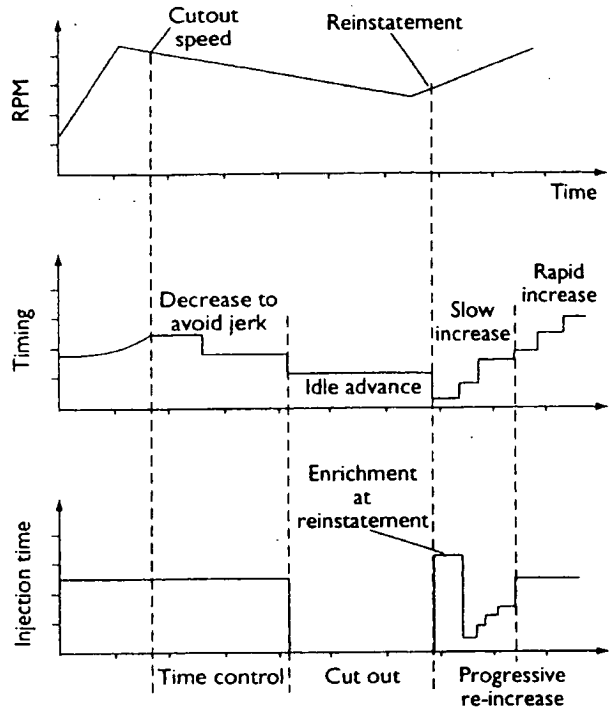

Figure 6-27 Strategy used to control injection cut-out and reinstatement [23]

If the network model was integrated into a conventional engine management system, fuel cut off would be employed in during potential throttle situations, overriding the signal from the ANN model.

An online investigation may demonstrate the need for an additional algorithm used in conjunction with the one of the above network models, for small throttle operating conditions. The hybrid system could either be composed of an additional ANN trained at only low throttle openings or use an existing conventional look up table based control algorithm to compensate for the port air mass flow estimation during.

6.4.2 Incorporating an Intelligent Model for Online Monitoring

Conventional engine modelling is based only on steady state experimental engine data and transient driving conditions are compensated for by correction factors. The above networks are a preliminary investigation into developing a single model that can adequately estimate the port air mass flow during steady state and transient driving conditions.

This is a more complex engine-modelling task in comparison to what is presently done and consequently the training data for such a model must be more extensive. For control purposes, such an ANN model would require an extensive representation of all possible driving conditions. This would include what is already required presently for conventional model development but also would need to incorporate training data concerned with the rate of change of throttle position and the effect of dynamic load changes on the port air mass flow or other engine parameters of interest. Some transient engine testing is conducted currently as it is required to develop the transient compensation factors.

With this in mind the online model must not only be accurate but also have minimum computation time. Model computational time is particular important in this application as engine modelling is renowned for being a laborious human intensive task.

Both steady state and transient port air mass flow models were developed in this research. The BP model was slightly more accurate in predicting the port air mass flow in both cases. However, the OLL network has a significantly smaller computational time in comparison to the BP transient engine model. Model-training time is proportional to the cost associated with engine model development. Thus from an economic point of view the OLL model, which has the lowest training time, would be considered the more attractive prospect. This would be true if there was no significant statistical difference between the mean percentage errors of the BP and OLL networks.

This can be determined by undertaking a t-test on the percentage errors of the testing data of both the BP and OLL models, encompassing 276 data points. A t-test assesses wether the means of two populations with unknown means and unknown variances are statistically different from each other. The t-test is based on comparing a test statistic, t with a critical t value at a particular confidence level. More information regarding this statistical technique can be found in [98]. The results of this investigation are shown below in Table 6-10 and are based on a 95 % confidence level, which means that five times out of one hundred a statistically significant difference between means would be found if there was none [88].

Population	*BP Model*	*OLL Model*
Mean	-0.000935953	-0.01
Variance	0.005740157	0.012269
T calculated	1.559017899	
T critical	1.645	

Table 6-10 t-test statistical results

The above results indicate that the null hypothesis should be accepted (ie that is that there is no significant difference between the three population means) as the t value is less than the t critical value at a 95 % confidence level. This suggests that the two models exhibit statistically equivalent mean error. On this basis it can be strongly argued that the OLL should be incorporated for online monitoring, however further assessment needs to be undertaken to determine the accuracy of the OLL model at low throttle positions.

6.4.3 Practical Application of the Transient Neural Network Model

The main motivation in developing a model centred around the throttle position and its derivative is inspired by Strivender's [99] idea of not only controlling the path of fuel but also the path of air as an alternative solution to the AFR control problem [32].

The driver of an automobile has direct mechanical control of the accelerator pedal and moves it in such a manner corresponding to the engine load requirements deemed necessary by the driver. Consequently, it is not possible to predict future throttle positions unless the load requirements are known in advance, which they are not. Therefore there is always a computation and injection delay associated with current AFR control systems as described in Section 2.7.

A solution to this problem has been suggested by many authors [9] [32] [54] who described a system involving the use of electronic throttle control. It is believed it may be possible to delay the requested throttle motion for a short period time equal to the computation and injection delay. The result of doing this means that the throttle position is known some time in advance providing sufficient time for a suitable feedforward engine model to estimate the

amount of air being inducted at future engine operating conditions and fuelling adjusted accordingly [32] [54].

The ANN model developed above would be ideal for such an application, as the critical input to the model is the throttle position and its derivative. The other inputs of the developed port air mass flow models namely, engine speed and air density are time developing variables that reach equilibrium in 10 or more engine cycles at times [1]. Thus using the current values of the engine speed and air density would be insignificant in the estimation of the future port air mass flow. This is because there would be only small changes in the engine speed and air density over the time scales associated in the calculation of the future port air mass flow estimation.

6.5 Concluding Remarks

Two different ANN's, namely the BP and OLL models were trained to estimate the port air mass flow in both steady state and transient engine operating conditions. In each case extensive analysis was undertaken in an attempt to find the optimum architecture for both models. The models were compared both qualitatively relying on graphical analysis and quantitatively involving histograms and statistical techniques for comparing population means. Both models predicted the actual values well, however the BP model in both steady state and transient engine operating conditions performed slightly better in comparison to the OLL network. A t-test determined that there was no statistical difference between the mean error of both models based on the transient testing data at a 95 % confidence level. However, the computational time of the fast converging OLL model was significantly smaller than the BP network based on the transient data.

It was determined that the rate of change of throttle position is a contributing parameter to the transient model and its inclusion improves prediction. Both models had difficulty in predicting low throttle position data (low port air mass flow values) in terms of percentage error. In terms of deciding which model is best suited for online prediction implementation further investigation is required to assess the potential of both models. However, the fast convergence OLL model would significantly decrease training and testing time in comparison

to the BP model and on this basis from an economic viewpoint it is the more attractive model at this stage.

7 FINAL CONCLUDING REMARKS & PROPOSED FUTURE WORK

The literature survey has highlighted that there is a critical need for new algorithms that can offer more precise control of the AFR in all engine operating conditions. Conventional AFR control techniques in the near future will be unable to meet exhaust gas emission regulations, because they are reaching their optimisation limits and further improvements to such models is becoming harder to achieve. Current AFR technologies, involve feedforward look up tables, supplemented by feedback control supplied by a signal from a lambda sensor and the use of catalytic converters. However, such systems are unable to provide tight control of the AFR during transient engine operation. The aim of future fuel injection control systems is to maintain tight control of the AFR ratio not only in steady state engine operation but also in transient engine operation, where large AFR excursions are most prevalent. Conventional AFR control algorithms perform poorly during transient conditions as they are based on look up tables, that are developed through non-dynamic experimental testing.

This study has presented a preliminary investigation into the development of Artificial Neural Networks Models in the prediction of both the steady state and transient port air mass flow. The main aim was to assess the potential of using Artificial Neural Networks for the development of a complete engine model that could accurately predict the port air mass flow during both steady state and transient engine operation. Two different ANN models have been investigated for this purpose namely the Backpropagation algorithm, both single and two layer models and the fast converging Optimise Layer by Layer algorithm.

The objective of the research has been to determine the most suitable ANN for online prediction purposes. Therefore, the most appropriate model was not selected solely on the basis of minimum RMS percentage error alone. The most suitable model was the one, which achieved the optimum combination of minimum error and minimum computation time. The model input parameters have been limited to those engine parameters that are conventionally measured in the control of the AFR. The inputs to the ANN models were selected from those engine parameters previously identified by Hendricks' et al [1] to model air mass flow inducted into an engine. A comprehensive investigation has been carried out in both the steady state and transient engine operating conditions in an attempt to determine the optimum

ANN architecture. This involved determining the ideal number of training iterations for each model and the optimum number of nodes in the hidden layer for each model.

The optimum BP and OLL models exhibit high prediction accuracy when exposed to the nonlinear complex and discontinuous mathematical function that is the port air mass flow, either in steady state or transient engine operating conditions. The training data in all cases has been presented to each network in a manner, which minimised the training error.

The optimum architectures for the BP and OLL models for the steady state port air mass flow prediction were found to be 5:8:4:1 and 5:20:1 respectively. The BP model was found to be approximately twice as accurate as the OLL model based on the testing RMS percentage error. The BP model had an average testing RMS percentage error of ± 1.79 % while the OLL model had an average testing RMS percentage error of ± 3.62. The computation time of both models could not be directly compared, as both models did not have exactly the same amount of training data. The steady state port air mass flow ANN prediction results are very promising and indicate the feasibility of potentially replacing convention look up tables with ANN model equivalents.

It has been determined through a predictive importance analysis that the rate of change of throttle position is a contributing model parameter for the prediction of the transient port air mass flow. The accuracy of the transient port air mass flow prediction is generally poorer than the steady state case but this is to be expected, as it is a more complex modelling problem. The transient throttle schedule used to train and test the developed models appears to be more demanding than the throttle positions used in the FTP 75 driving cycle.

The optimum architectures for the BP and OLL models for the transient port air mass flow prediction were found to be 5:6:1 and 5:5:1 respectively. The BP model had an average testing RMS percentage error of ± 7.56 % while the OLL model had an average testing RMS error of ± 11.10. However, the computation time of the BP model is four times larger than the OLL model. A t-test has been undertaken to determine if the mean testing percentage errors of the developed BP and OLL models were significantly different. The results of this statistical analysis indicate that there is no significant difference between the mean percentage errors of the two models based on a 95 % confidence level. Hence, this suggests that the

OLL model is more suitable for online implementation due to its superior computation time in comparison to the BP model.

Both models exhibit large percentage errors at low throttle positions. Although the predicted to actual deviation is small during periods of small throttle operation, relative to the actual port air mass flow value (which is very close to zero) the percentage error becomes significantly large. It is encouraging that the poor performance of the developed ANN models at low throttle positions may not be significantly detrimental to engine operation due to the fuel cut off phenomena which occurs at zero throttle operation. However too fully assess these effects an online model investigation is required.

At this stage, the level of accuracy of the developed transient models is outside the range required for the precise AFR control that is needed to maximise catalytic converter efficiency and hence minimise exhaust gas emissions. If the developed models were incorporated for transient AFR control at best they could control the AFR ratio to within approximately ± 10 %, which is far greater than the ± 1 % accuracy required for optimum catalytic converter efficiency. However, the developed transient models illustrate great potential for automotive engine fault diagnosis applications. There is also the potential to use such models as virtual sensors that are activated if automotive sensor failure occurs. The redundant virtual sensing system would provide sufficient time for the driver to undertake an appropriate set of evasive actions to deal with the automotive fault and reduce the chances of disturbing additional traffic. The need for such an automotive redundant sensor system has been identified by Atkinson et al [14] who suggests that an ultra low emissions vehicle operating with an engine sensor failure for one day may produce more emissions than a fully functional system does in a year.

The use of artificial neural networks as engine modelling tools was found to be extremely promising with both the developed BP and OLL port air mass flow neural networks models providing good quantitative predictive capabilities given the preliminary nature of this investigation. This preliminary investigation suggests the developed transient models in their current form do not have the required accuracy to completely replace conventional engine control systems with transient correction factors. The steady state models results are very promising and could be regarded as potential candidates for replacing engine look up tables.

It is believed with the development of more advanced artificial neural network algorithms the accuracy of transient ANN engine models will improve considerably.

7.1 Future Work

Future work in this area would encompass developing offline ANN engine models for a standard automobile engine with a factory developed engine control unit, complete with exhaust gas recirculation (EGR) control. The adiabatic port air mass flow equation could be applied to such an experimental engine and the full effect of EGR could be accurately modelled. However, additional engine inputs would be required for model development including EGR valve position, which would give an indication of the mass air flow of EGR entering the intake manifold and the EGR temperature. Future work may also encompass applying other ANN algorithms for transient engine modelling. This may possibly include appropriate recurrent ANN algorithms that may be better suited to model the transient behaviour of the modelling problem.

It is recommended that research should also commence into developing ANN models with the intention of predicting the manifold air pressure and or its derivative. The output of such ANN model could be used to compensate for dynamic manifold filling effects by correcting the signal of a mass air flow sensor or speed density system. Achleitner et al [100] and Gerhardt et al [101] have undertaken similar research by using conventional feedforward observer based techniques to correct for the manifold filling phenomena.

The future experimental test field would require a programmable stepper motor (or electronic throttle control) so that the rate of change of the throttle position could be adjusted and controlled in a more accurate manner at set increments over a predefined range. Xu [8] used such an arrangement and varied the rotational speed of the throttle plate between 50 to 150 degree/s through a gear box. It is proposed that future data collection process would involve exciting both the rate of change of throttle position and the engine load. This could be done by dividing the engine map up into various load and engine speed sites, as done in this research, and at these experimental testing sites undertaking a wide range of throttle transients at various rotational throttle speeds.

REFERENCES

[1] E Hendricks, S. C. Sorenson, "Mean Value Engine Modelling of Spark Ignition Engines", SAE Technical Paper 900616, 1990

[2] J Hodgson, Dr H R M Sadek, Professor A D Hope, "Neural Networks in Engine Management", Southhampton Institute UK, 95ME022, 1995

[3] C D Falck, J J Money, "Three Way conversion catalyst: effect of closed loop feedback control and other parameters on catalyst efficiency", SAE paper No. 800462, 1980

[4] C Alippi, C De Russis, V Piuri, "A Fine Control of the Air fuel Ratio with Recurrent Neural Networks", IEEE Instrumentation & Measurement Technology conference St Paul Minnesota , USA, May 18-21 1998

[5] N Anderson, "More Emissions than the manufactures report", Ny Teknik 1999 (46) : 20-21, 1999. See http://www.rototest.com/Rotonews/

[6] D Blomqvist, S Byttner, U Holmberg, T Rognvaldson, "Different Strategies for Transient Control of the Air-Fuel Ratio in a SI Engine", SAE Technical Paper 2001-01-2835, 2000

[7] R C Turin and H. P. Geering, "On-line Identification of Air Fuel Dynamics in a Sequentially Injected Engine", SAE 930857, 1993

[8] Hongming Xu, "Control of A/F Ratio During Engine Transients", SAE paper 1999-01-1484, 1999

[9] N.F. Benninger, G Plapp, "Requirements and Performance of Engine Management Systems Under Transient Conditions", SAE paper 910083, 1991

[10] H S Braun, G Kramer, M Thiessen, "Engine Dynamic Response – A New Goal in Engine Control Application", SAE Paper 881155, 1988

[11] T Sekzawa, S Takahashi, M Shioya, T Ishii, S Asano, "Development of a Highly Accurate Air Fuel Ratio Control Method Based on Internal State Estimation", SAE paper 920290, 1992

[12] E Hendricks, M Jenson, P Kaidantzis, P Rasmussen, T Vesterholm, "Transient A/F Ratio Errors in Conventional SI Engine Controllers", SAE paper no 930856, 1993

[13] T Y Chang, D P Chock et al, "Urban and Regional Ozone Air Quality: Issuers Relevant to Automobile Industry", Critical Review Environmental Control, Vol 22, 1992

[14] C M Atkinson, T W Long, E L Hanzevack, "Virtual Sensing: a Neural Network-based Intelligent Performance and Emissions Prediction System for On-board Diagnositics and Engine Control", SAE paper 980516, 1998

[15] D Butler, "Traction Control Using Artificial Neural Networks", Masters Thesis, University of Tasmania, 2002

[16] G Heron, "Estimation of Brake Force on an Open Wheel Racing Car Using Artificial Neural Networks", Masters Thesis, University of Tasmania, 2002

[17] H Cunningham, "Roll Over Parameters Prediction Using Neural Networks", Masters Thesis, University of Tasmania, 2002

[18] How Stuff Works, Internal Combustion Engines,http://www.howstuffworks.com/, Jan 17 2003

[19] V. L. Maleev, "Internal Combustion Engines Theory and Design", McGraw-Hill, 1945

[20] J. B. Heywood, "Internal Combustion Engine Fundamentals", McGraw-Hill Series in Mechanical Engineering, 1988

[21] M. J. Moran, H. N. Shapiro, "Fundamentals of Engineering Thermodynamics", John Wiley & Sons New York, 1998

[22] R. S. Benson, N. D. Whitehouse, "Internal Combustion Engines", Vol 1,2, Pergamon Press, 1979

[23] R. S. Benson, Edited by J. H. Horlock, D. E. Winterbone, "Thermodynamics and Gas Dynamics of Internal Combustion Engines", Vol 1, Oxford University Press, 1982

[24] R Stone, "Introduction to the Internal Combustion Engines", The Macmillian Press Ltd, 1992

[25] Supervising Editor R. B. Bucat, "Elements of Chemistry Earth Fire and Water" Vol 2, Australian Academy of Science, 1987

[26] T Denton, "Automotive Electrical and Electronic Systems", Arnold Publishers, 2000

[27] McGraw-Hill, "Encyclopaedia of Science and Technology", 8th Edition, Combustion, Vol 4 p 202-205, 1997

[28] L Eriksson, 'Spark Advance for Optimium Efficiency," SAE paper No. 1999-01-0548, 1999

[29] P Berggren, A Perkovic, "Cylinder Individual Lambda Feedback Control in an SI Engine", Examination Degree Performed at University of Technology Linkoping Sweden, 1996

[30] R Morrison, R Boyd, "Organic Chemistry', Prentice Hall Inc, New Jersey, 1992

[31] E Hendricks, M Jenson, P Kaidantzis, P Rasmussen, T Vesterholm, "Transient A/F Ratio Errors in Conventional Engine Controllers", SAE Technical Paper No. 930856, 1993

[32] How Stuff Works, Carburettor, http://www.howstuffworks.com/, Nov 2002

[33] How Stuff Works, Fuel injection Systems, http://www.howstuffworks.com/, Nov 2002

[34] Press Release, Delphi Energy & Engine Management Systems, Presentation to SAE, 1998

[35] A Chevalier, C Vigild, E Hendricks, "Predicting Port Mass Flow of SI Engines in Air/Fuel Ratio Control Applications", SAE paper No. 2000-01-260, 2000

[36] H. Holzmann, Ch Halfmann, R Isermann, "Representation of 3D Mappings for Automotive Control applications using Neural Networks and Fuzzy Logic", Proceedings of the 1997 IEEE International conference on Control Applications Hartford, CT October 5-7 1997

[37] R Sauer, "Hot Film Air Mass Meter – Low Cost Approach to Intake Measurement", SAE Technical Paper No. 880560, 1988

[38] W C Follmer, "Frequency Domain Characterisation of Mass Air Flow Sensors", SAE Technical Paper No. 880561, in SP-737, 1988

[39] Robert Bosch GmbH, "Automotive Handbook", Dusseldorf, Germany, VDI, 1993

[40] A Amstutz N Fekete and D Powell, "Model-Based Air Fuel ratio Control in SI Engines with a Switch Type EGO Sensor", SAE 940972, 1994

[41] G F Franklin, J D Powell and A Emami-Naeimi, "Feedback Control of Dynamic Systems", Addison Wesley Pub Co 1987 p 495

[42] R K Jurgen, "Automotive Electronics Handbook", 2nd Edition, Society of Automotive Engineers, 1999

[43] E Hendricks, M Jenson, A Chevalier, and T Vesterholm, "Conventional Event Based Engine Control", SAE 940377

[44] E Hendricks, A Chevalier, M Jenson, "Conventional Event Based Engine Control", Practical Problems and Solutions, SAE 950008

[45] E Hendricks and A Chevelier, "Emerging Engine Control Technologies, 29 th ISATA Conference on Automotive Electronics", June 1996, Florence Italy

[46] E Hendricks, "Errors in Hot Wire MAF Measurement Systems", Revised Interim Report, the Technical University of Denmark 1992

[47] L. Trajkovski, "Computer Controlled Engine Management System", Masters Thesis, the Technical University of Denmark, Institute of Automation 1997

[48] P A Hazell, J O Flower, "Discrete Modelling of Spark Ignition Engines for Control Purposes", Int. J. Control, vol 13 no 4 pp 609-623, 1971

[49] J A Cook, B K Powell, "Modelling of an Internal Combustion Engine", IEEE Control Systems Magazine, 1988

[50] U Lenz, D Schroeder, "Transient Air Fuel Ratio Control Using Artificial Intelligence", SAE paper 970618. 1997

[51] E Hendricks, D Engler, M Fam, "A Generic Mean Value Engine Model for Spark Ignition Engines", Institute for Automation, DTU, 2001

[52] E Hendricks, T Vesterholm, Kaidantzis, P Rasmussen et al, "Nonlinear Transient Fuel Compensation", SAE Technical Paper No. 930767

[53] I Rasmussen, "Emissions from Cars", PhD Dissertation, The Laboratory for Energetic, The Technical University of Denmark, Lyngby, Denmark, 1971

[54] C F Aquino, "Transient A/F Control Characteristics of the 5 Litre Central Fuel Injection Engine", SAE Technical Paper 810494, 1981

[55] S D Hires, and M T Overington, "Transient Mixture Strength Excursions – An investigation of their Causes and the Development of a Constant Mixture Strength Fuelling Strategy", SAE Technical Paper 810495,1981

[56] S R Fozo and C F Aquino, "A Transient A/F Characteristics for Cold Operation of a 1.6 litre Engine with Sequential Fuel Injection", SAE Technical Paper 880691, 1988

[57] P J Shayler, M S Goodman, T Ma, "Transient AFR Control of an SI Engine Using Neural Networks", SAE Technical Paper 960326, 1996

[58] E Hendricks and S. C Sorenson, Modelling of the Intake Manifold Filling Dynamics, SAE technical paper No. 960037

[59] E Hendricks, J B Luther, Model and Observer Based Control of Internal Combustion Engines, Institute for Automation Technical University of Denmark (DTU) DK-2800 Kongens Lyngby, Densmark, 2000

[60] A Chevalier and M Muller, On the Validity of Mean Value Engine Models During Transient Operation, SAE paper no 2000-01-1261, 2000

[61] J B Burl, "A State Model for the Air Fuel Ratio", http://www.ece.mtu.edu/faculty/burl/kut/Engine%20Controls/FuelControl.doc, Jan 2003

[62] A.J. Beaumont, "A.M. Frith, Adaptive Control of Transient Air Fuel Ratio Using Neural Networks", 94EN001, Isata Conference, 1994

[63] H Shiraishi, S Ipri, D Cho, "CMAC Neural Network for Fuel Injection Control", American Control Conference San Fransisco June, 1993

[64] D Anderson, G McNeill, "Artificial Neural Networks Technology, Kaman Sciences Corporation", 258 Genesse Street Utica, New York 13502-4627, 1992

[65] J Stader, "Applying Neural Networks, Artificial Intelligence Applications Institute", University of Edinburgh 80 South Bridge Edinburgh EH1 1HN UK, August 1992

[66] M Caudill, C Butler, 'Understanding Neural Networks – Computer Explorations", Vol 1: Basic Neural Networks, MIT, 1992

[67] D Lowe, C Zapart, "Point-Wise Confidence Interval Estimation by Neural Networks: A Comparitive Study based on Automotive Engine Calibration", Neural Computing & Applications77-85, Springer-Verlag London Ltd, 1999

[68] R Isermann, N Muller, "Modelling and Adaptive Control of Combustion Engines with Fast Neural Networks", Darmstadt University of Technology Institute of Autoatic Control Laboratory of Control Systems and Process Automation Landgraf-Georg-Str. 4, D-64283 Darmstadt Germany Tel: 49/6151-162114, fax 49/6151-293445, RIsermann, NMueller@iat.tu-darmstadt.de, 2000

[69] M L Traver, R J Atkinson, C M Atkinson, "Neural Network-Based Diesel Engine Emission Prediction Using In-cylinder Combustion Pressure", SAE paper 1999-01-1532, 1999

[70] M C Sellnau, F A Matekunas, P A Battiston, C F Chang et al, "Cylinder Pressure Based Engine Control Using Pressure Ratio Management and Low Cost Non-Intrusive Cylinder Pressure Sensors", SAE Paper200-01-0932, 2000

[71] M Hellring, T Munther, T Rognvaldsson, N Wicksrom et al, "Spark Advance Control Using the Ion current and Neural Soft Sensors", SAE Technical Paper 1999-01-1162, 1999

[72] A Linde, M Taveniku, B Svensson, "Using Neural Networks for Air Fuel Ratio Estimation in Two-Stroke Combustion Engines", Chalmers University of Technology Goteborg Sweden and Halmstad University, Halmstad Sweden, 1998

[73] D W Dong, J J Hopefield, K P Unnikrishnan, "Neural Network for Engine Fault Diagnosis", Computation and Neural Systems California Institute of Technology, Pasadena CA 91125, 1998

[74] J. R.Asik, J M Peters, G M Meyer and D X Tang, "Transient A/F Estimation and Control Using a Neural Network", SAE Technical Paper 970619, 1997

[75] P J Shayler, M S Goodman, T Ma, "Transient AFR Control of an SI Engine Using Neural Networks", SAE Technical Paper 960326, 1996

[76] M Majors, J Stori, D Cho, "CMAC Neural Network for Fuel Injection Control", IEEE Control Systems June 0272-1708/94, 1994

[77] R P Lippman, "An Introduction to Computing with Neural Nets", IEEE ASSP Magazine, April 1987

[78] M J Willis, G A Montague, C Peel, "On the Application of Artificial Neural Networks for Process Control", Kluwer Academic Publishers London, 1995

[79] D H Rao, M M Gupta, H C Wood, "Neural Networks in Control Systems, Neural Networks: Theory, Technology and Applications", IEEE, 1996

[80] A J Weijters, G A Hoppenbrouwes, "Backpropagation Networks for Grapheme-Phoneme Conversion: A Non-Technical Introduction", Artificial Neural Networks, Springer-Verlag Berlin Heidelberg, 1995

[81] D E Rumelhart, J L McClelland, "Parallel Distributed Processing", Vol 2, MIT Press, Cambridge MA,1986

[82] G Orr, N Schroudolph, F Cummins, "Neural Network Lecture Notes", Willianette University, USA, 1999

[83] C R Jones, C P Tsang, "On the Convergence of Feed Forward Neural Networks Incorporating Terminal Attractors", IEEE, New York, 1996

[84] R Brunelli, "Training Neural Nets Through Stochastic Minimisation Neural Networks", Vol 7, No 9, pp 1405-1412, 1994

[85] H Ritter, T Martinetz, K Schulten, "Neural Computation and Self Organising Maps: An Introduction", Addison-Wesley Publishing Company, 1992

[86] J A Freeman, D M Skapura, "Neural Networks: Algorithms, Applications and Programming Techniques", Addison-Wesley Publishing Company Inc, 1992

[87] F Rosenblatt, "The Perceptron: A Probabilistic Model for Information Storage and Organisation in the Brain", Psychological Review, Vol 65, 1960 pp 386-408

[88] L Fausett, "Fundamentals of Neural Networks: Architectures, Algorithms and Applications", Prentice Hall International, Inc.,1994

[89] S Ergezinger, E Thomsen, "An Accelerated Learning Algorithm for Multilayer Perceptrons": Optimised Layer by Layer, IEE Transactions on Neural Networks, Vol 6, No 1 Jan 1995

[90] P Grassberger, I Procaccia, "Measuring the Strangeness of Strange Attractors", Physicia D, Vol 9 pp 189-208, 1983

[91] R W Weeks, J J Moskwa, "Transient Air Flow Rate Estimation in a Natural Gas Engine Using a Nonlinear Observer", SAE Technical Paper 940759, 1994

[92] F Frost, "Neural Network Applications to Aluminium Manufacturing", PhD Thesis, University of Tasmania, 2000

[93] "Kawasaki Ninja ZX-6R Motor Cycle Service Manual", Kawaski Heavy Industries Ltd cionsumer Products & Machinery group, Part No 99924-1254-01, 2000

[94] MoTeC M4 & M48 Engine Management User's Manual, Electronic Performance Systems Pty Ltd, 2001

[95] Bosch Sensors Product Program 2001/2002, Robert Bosch GmbH Automotive Aftermarket Postfach 410960 D-76225 Karsruhe, htp://www.bosch.de/aad, 2001

[96] M H Westbrook, J D Turner, "Automotive Sensors," Institute of Physics Publishing, Bristol and Philadelphia, 1994

[97] Technical Customer Information Y 280 K16 892 E, Hot-film mass air flow meter, HFM5 - 4.7 with temperature sensor Part Number 0 280 218 019, Robert Bosch GmbH, 1999

[98] U Lenz, D Schroder, "Air Fuel Ratio Control for direct Injecting Combustion Engines Using Neural Networks", SAE Technical Paper 981060, 1998

[99] D C Montgomery, "Introduction to Statistical Quality Control", Sixth Edition, John Wiley and Son's Inc, 1991

[100] D L Stivender, "Engine Control – Basis of a Vehicular Systems Control Heirachy", SAE Technical Paper no. 780346, 1978

[101] E Achleitner, W Hosp, A Koch, W Schurz, "Electronic Engine Control System for Gasoline Engines for LEV and ULEV Standards", SAE Technical Paper No. 950479, 1995

[102] Gerhardt J, Benninger N, Wess W, "Torque Based System Structure of an Electronic engine Management System as a New Base for Drive Train Systems", (Bosch ME7 System) Aachener Kolloqium, Fahrzeug and Motorentech nik, Aachen Germany 20-22 October 1997

APPENDIX A TRAINING BP & OLL MODEL OUTPUTS

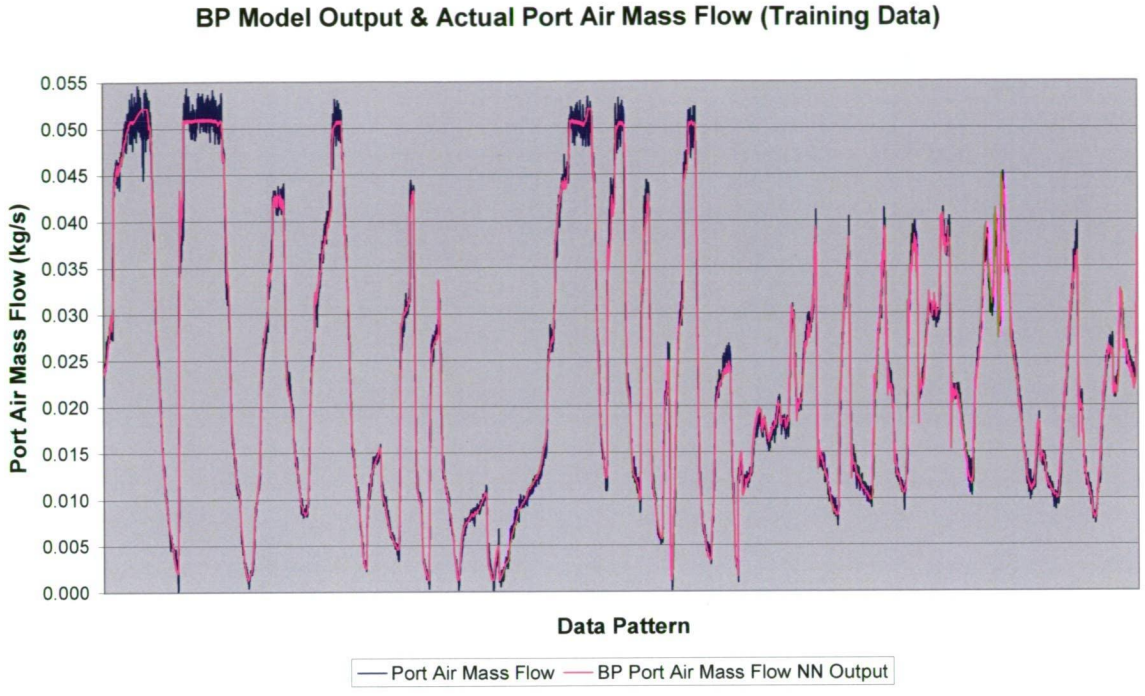

Figure A-1: Training BP model output Vs. actual port air mass flow

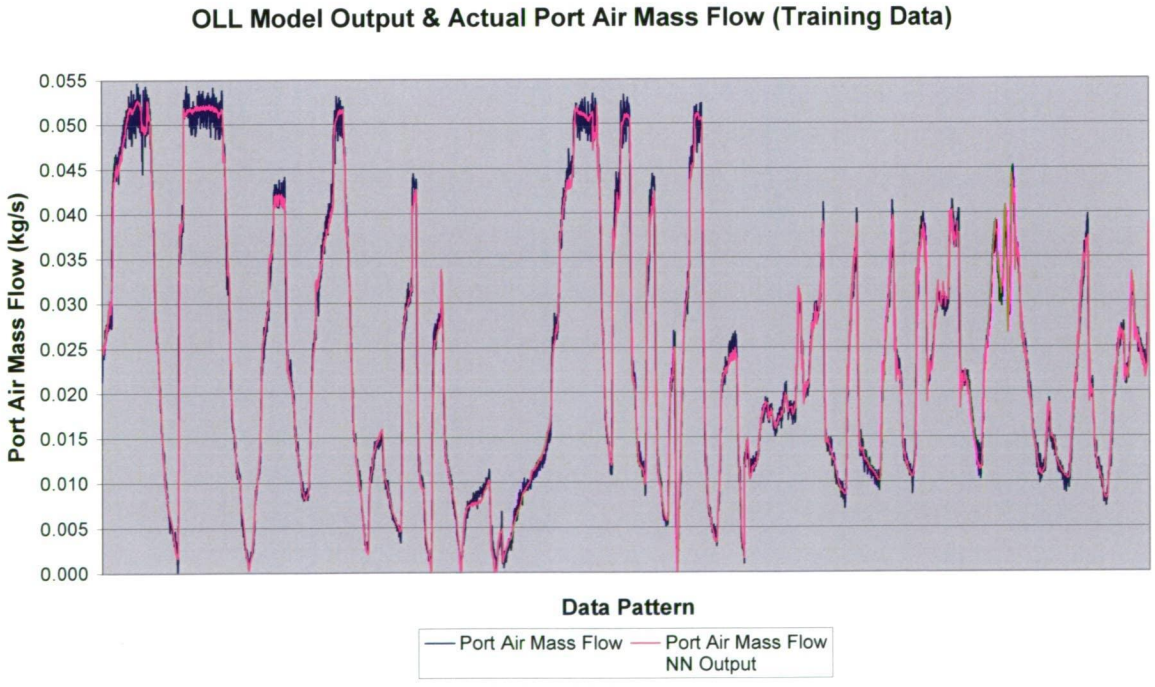

Figure A-2: Training OLL model output Vs. actual port air mass flow

APPENDIX B TESTING BP & OLL MODEL OUTPUTS

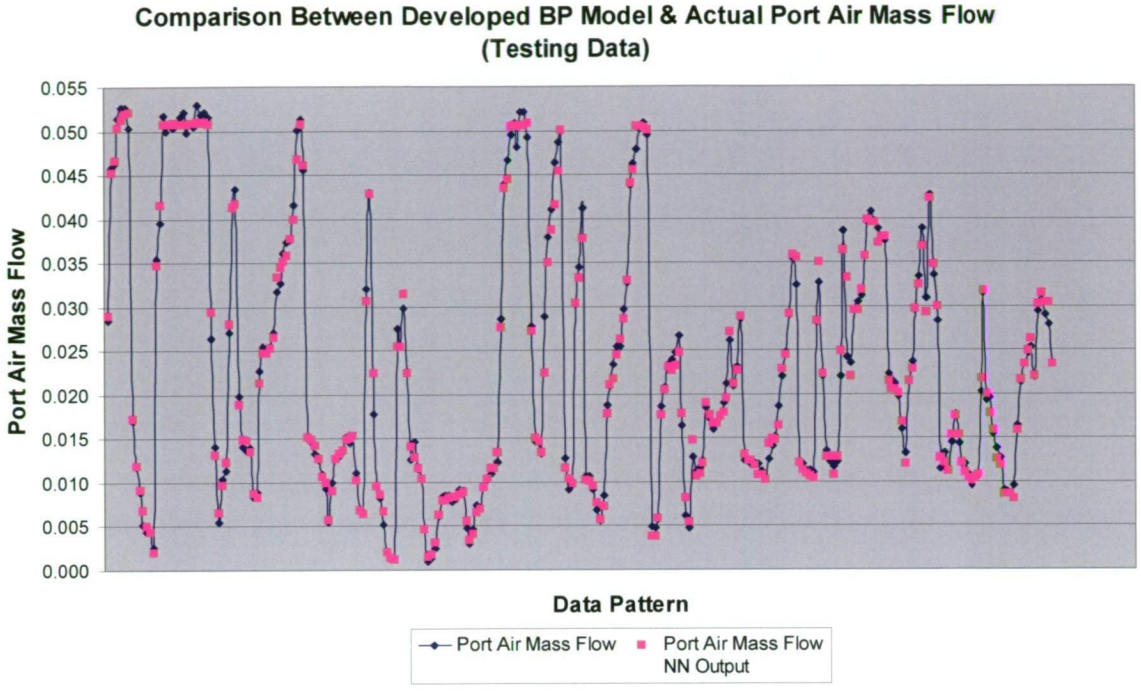

Figure B1: Testing BP model output Vs. actual port air mass flow

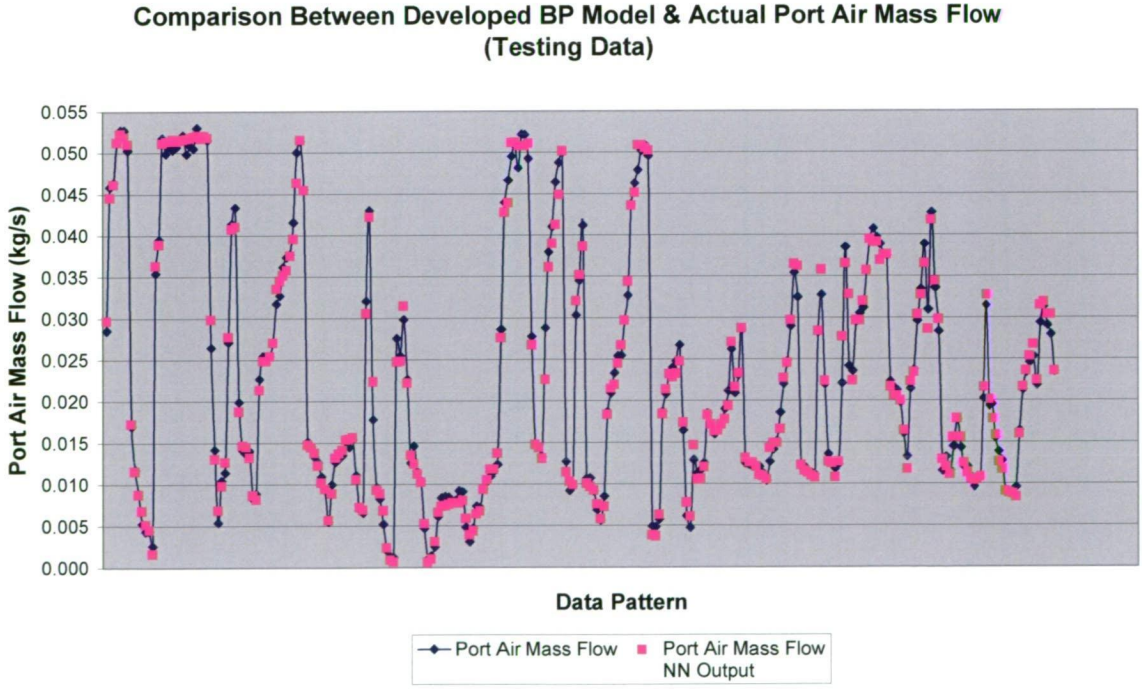

Figure B2: Testing OLL model output Vs. actual port air mass flow

APPENDIX C BP & OLL MODELS PERCENTAGE ERROR AND DEVIATION VS THROTTLE POSITION GRAPHS

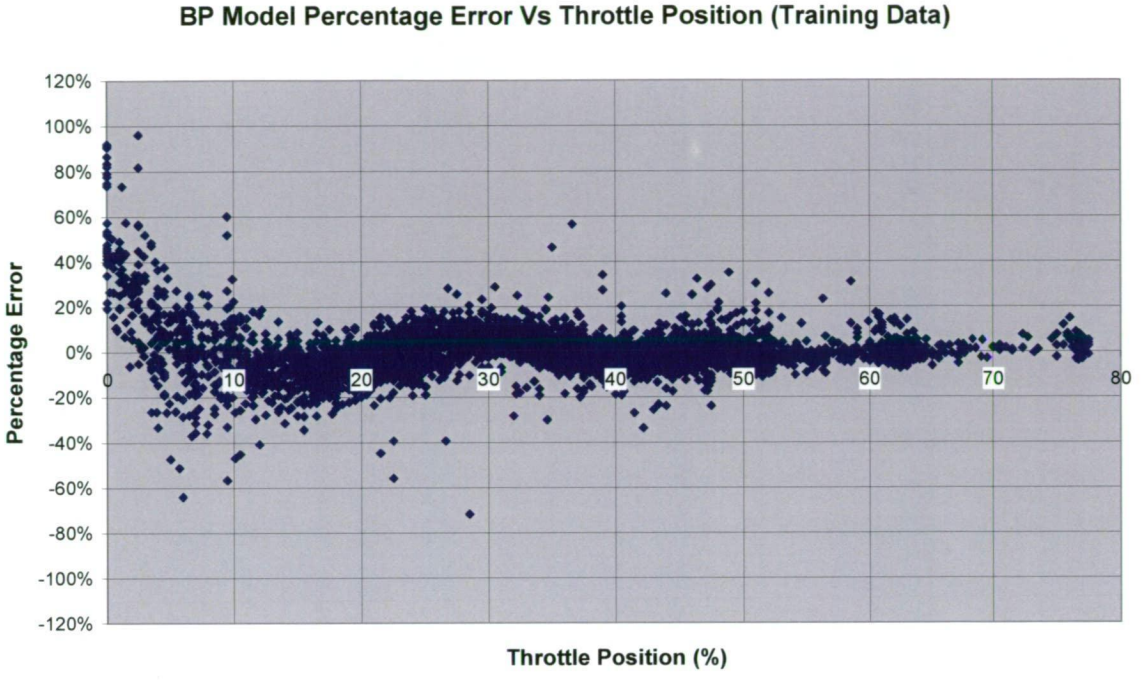

Figure C-1: Training BP model percentage error Vs throttle position

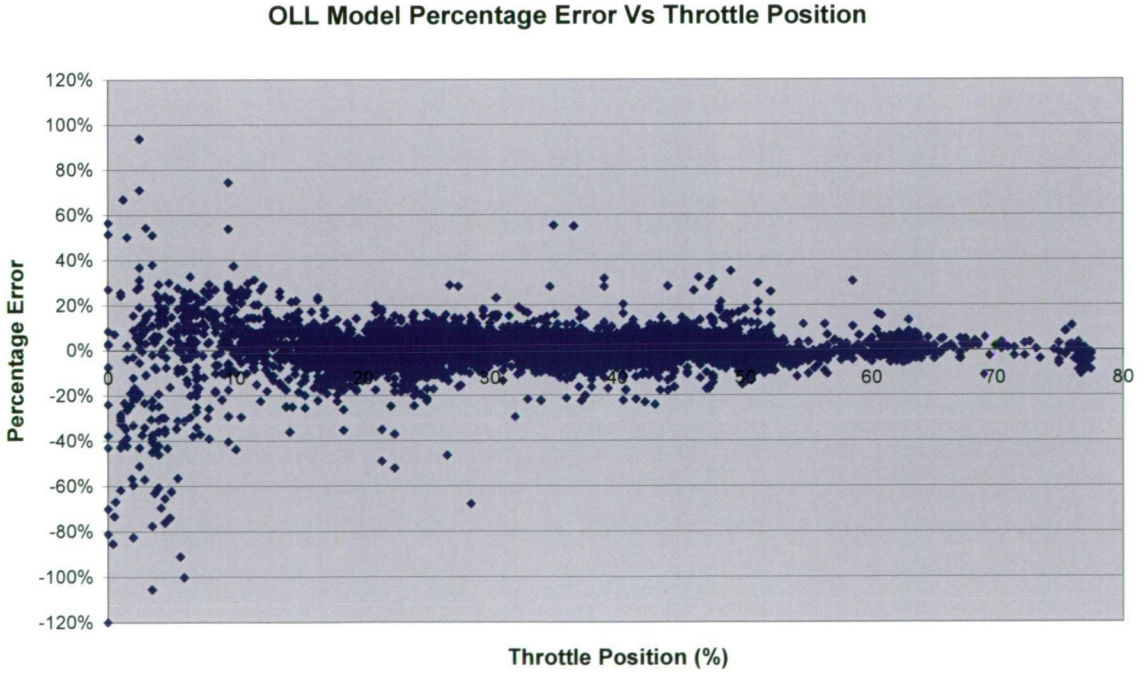

Figure C-2: Training OLL model percentage error Vs throttle position

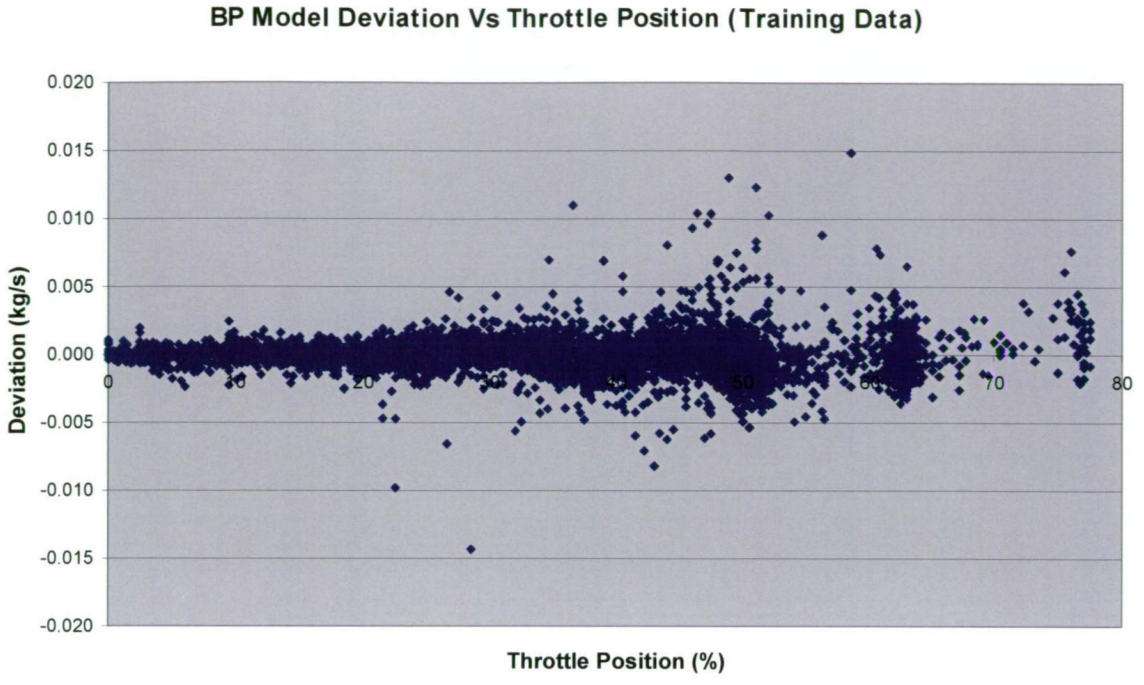

Figure C-3: Training BP model error deviation Vs throttle position

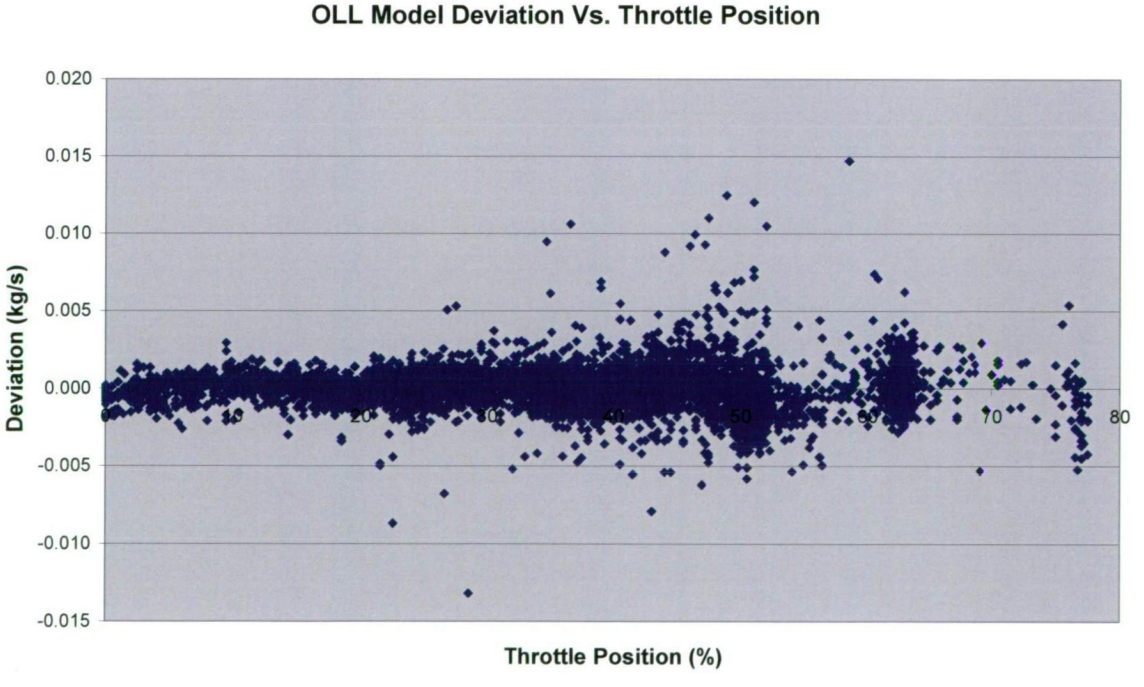

Figure C-4: Training OLL error deviation Vs throttle position

APPENDIX D ENGINE SPECIFICATIONS

D-1: Engine specifications

Engine:		
Type		4-stroke, DOHC, 4-cylinder
Cooling system		Liquid-cooled
Bore and stroke		66 x 43.8 mm
Displacement		599 mL
Compression ratio		12.8
Maximum horsepower		81.6 kW (111 PS) @12 500 r/min (rpm), (AS) 80.6 kW (109.6 PS) @12 500 r/min (rpm), (PR) 78.2 kW (106.3 PS) @12 500 r/min (rpm), (US) - - -
Maximum torque		65.6 N·m (6.7 kg·m, 48 ft·lb) @10 000 r/min (rpm), (AS) 64.6 N·m (6.6 kg·m, 48 ft·lb) @10 000 r/min (rpm) (FR)(US) - - -
Carburetion system		Carburetors, Mikuni BDSR 36R × 4
Starting system		Electric starter
Ignition system		Battery and coil (transistorized)
Timing advance		Electronically advanced(digital igniter)
Ignition timing		From 12.5° BTDC @1 300 r/min (rpm) to 42.5° BTDC @5 000 r/min (rpm)
Spark plug		NGK CR9E
Cylinder numbering method		Left to right, 1-2-3-4
Firing order		1-2-4-3
Valve timing:		
Inlet	Open	56° BTDC
	Close	80° ABDC
	Duration	316°
Exhaust	Open	61° BBDC
	Close	33° ATDC
	Duration	274°
Lubrication system		Forced lubrication (wet sump with cooler)
Engine oil:		
Grade		SE, SF or SG class
Viscosity		SAE10W-40, 10W-50, 20W-40, or 20W-50
Capacity		3.8 L

D-2: Engine top end exploded view

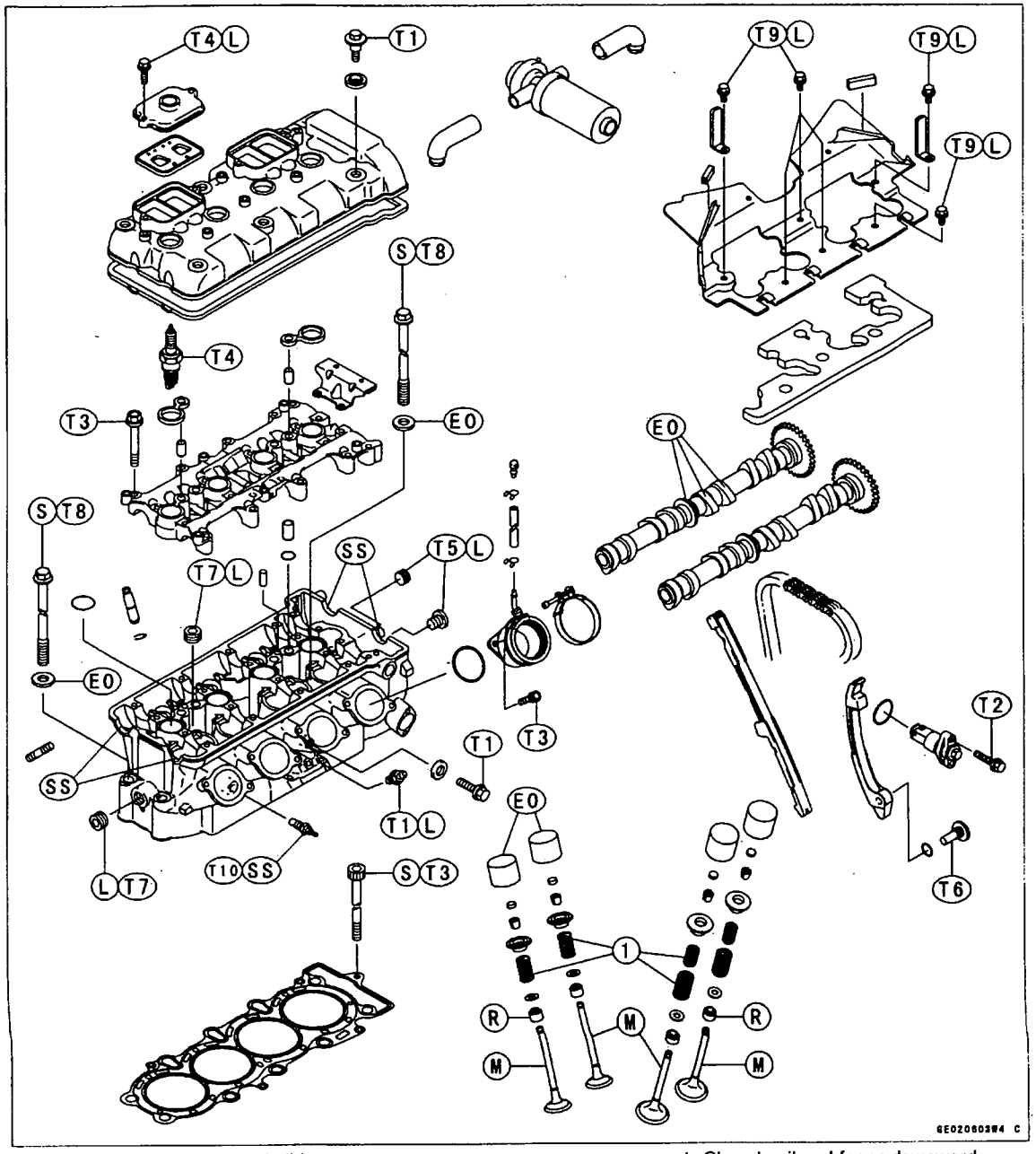

T1: 9.8 N·m (1.0 kg·m, 87 in·lb)
T2: 11 N·m (1.1 kg·m, 95 in·lb)
T3: 12 N·m (1.2 kg·m, 104 in·lb)
T4: 13 N·m (1.3 kg·m, 113 in·lb)
T5: 15 N·m (1.5 kg·m, 11.0 ft·lb)
T6: 25 N·m (2.5 kg·m, 18.0 ft·lb)
T7: 20 N·m (2.0 kg·m, 14.5 ft·lb)
T8: 49 N·m (5.0 kg·m, 36 ft·lb)
T9: 5.9 N·m (0.60 kg·m, 52 in·lb)
T10: 7.8 N·m (0.8 kg·m, 69 in·lb)

1. Closed coil end faces downward.
L: Apply a non-permanent locking agent.
M: Apply molybdenum disulfide grease.
EO: Apply engine oil.
SS: Apply silicone sealant.
R: Replacement Parts
S: Follow the specific tightening sequence.

D-3: Engine crankshaft exploded view

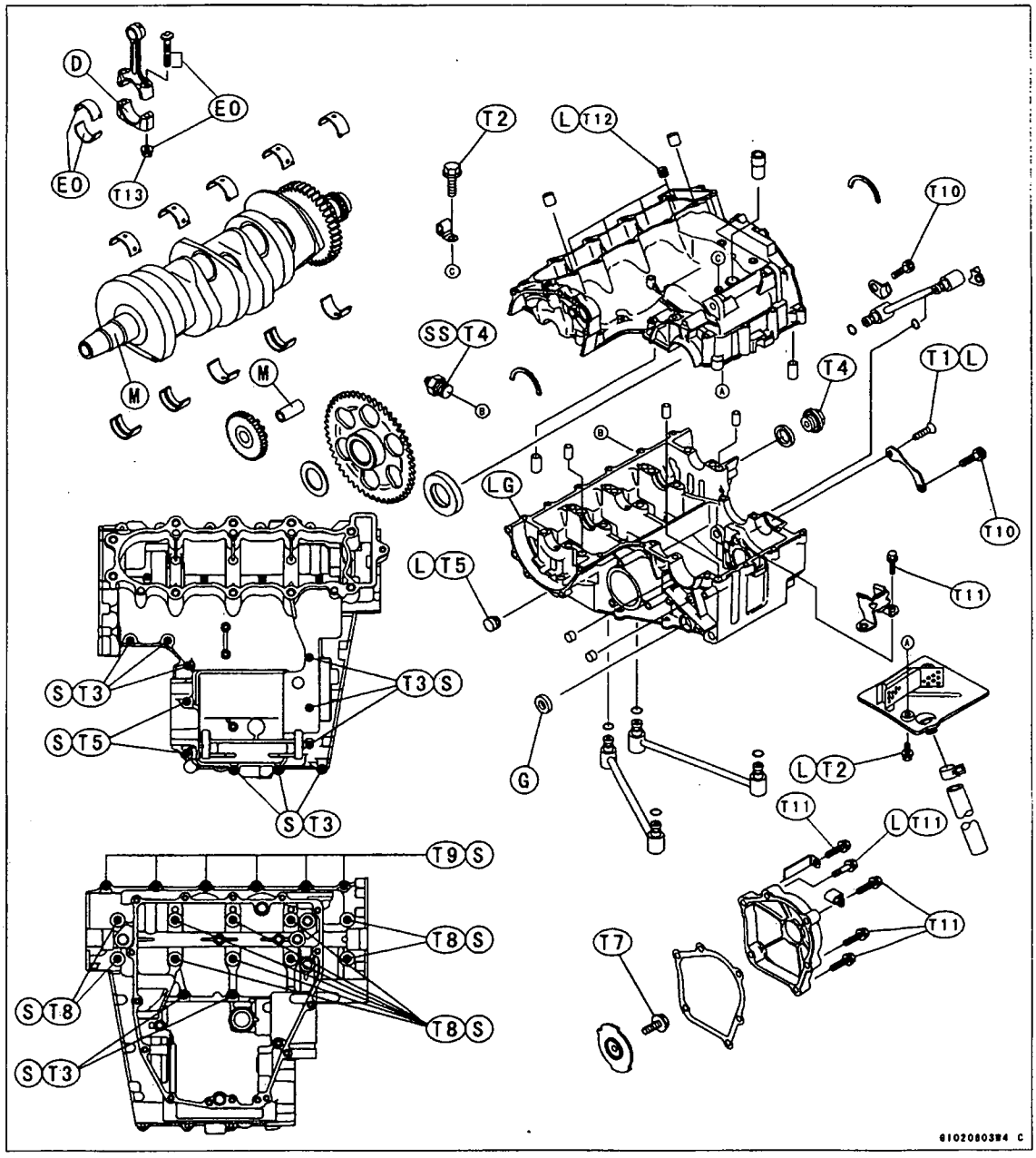

T1: 5.4 N·m (0.55 kg·m, 48 in·lb)
T2: 9.8 N·m (1.0 kg·m, 87 in·lb)
T3: 12 N·m (1.2 kg·m, 104 in·lb)
T4: 15 N·m (1.5 kg·m, 11.0 ft·lb)
T5: 20 N·m (2.0 kg·m, 14.5 ft·lb)
T6: 28 N·m (2.9 kg·m, 21 ft·lb)
T7: 40 N·m (4.0 kg·m, 29 ft·lb)
T8: 30 N·m (3.0 kg·m, 22 ft·lb)
T9: 18 N·m (1.8 kg·m, 13.0 ft·lb)
T10: 13 N·m (1.3 kg·m, 113 in·lb)
T11: 11 N·m (1.1 kg·m, 95 in·lb)
T12: 6.9 N·m (0.70 kg·m, 61 in·lb)
T13: See the text.

APPENDIX E MOTEC M4 ECU SPECIFICATIONS

E-1: ECU specifications

General

- Microprocessor 32 Bit 33 MHz with Time CO Processor
- Quality Standard ISO 9001
- Manufacturing Standard IPC-S-815-A Class 3 High Reliability
- Warranty 1 year Parts & Labour
- Burn In -50 to 70°C for 32 Hrs
- ECU Control Software stored in updatable FLASH memory
- High RFI Immunity
- Low heat generation
- Battery transient protection
- Environmentally sealed electronics
- Water proof connector with gold plated contacts
- Case Size 120 x 100 x 36 mm (4.7 x 3.9 x 1.4 inches)
- Weight 0.4 kg (14 oz)
- Cylinders 1,2,3,4,6,8,12
- Engines 2 stroke, 4 stroke, Rotary (1~4), Odd or Even fire
- Maximum RPM >15,000 RPM

Fuel Calibration

- Accuracy 0.00001 seconds
- All RPM & Load sites are user programmable
- Main Table (3D) 40 RPM sites x 21 Load sites (840 points)
- End of Injection (3D) 20 RPM sites x 6 Load sites
- Overall Trim ±99 %
- Individual Cylinder Trim ±99 %
- Individual Cylinder Tables (3D) 20 RPM sites x 11 Load sites
- Hi / Lo Injector Balance (3D) 20 RPM sites x 11 Load sites
- Hi / Lo End of Injection (3D) 20 RPM sites x 11 Load sites
- Eng Temp & Air Temp comps
- MAP modifier compensation
- Two Auxiliary compensation
- Injector Dead Time Compensation
- Accel Clamp, Decay & Sensitivity
- Deccel Clamp, Decay & Sensitivity
- Cold Start

Injection

- 4 group sequential
- User programmable injector current 0.5~12 Amps peak
- Battery Comp to suit any injector

Boost Control Calibration

- Main Table (3D) 20 RPM sites x 10 Throttle sites or 10 Gear sites
- Overall Trim
- Engine Temp & Air Temp comps
- One Auxiliary compensation

Ignition Outputs

- Up to 4 Ignition Outputs
- One output may drive up to 8 coils using the MoTeC Ignition Expander
- Versatile Ignition Interface allows connection to most OEM ignition systems including:
    - Nissan Multi Coil modules
    - GM EST DFI systems
    - FORD EDIS DFI systems
    - Mazda Rotary DFI modules
    - Many Others

Ignition Calibration

- Accuracy 0.25 degrees
- All RPM & Load sites are user programmable
- Main Table (3D) 40 RPM sites x 21 Load sites (840 points)
- Overall Trim ±99 %
- Individual Cylinder Trim ±99 %
- Individual Cylinder Tables (3D) 20 RPM sites x 11 Load sites
- Rotary Split 20 RPM x 11 Load
- Eng Temp & Air Temp comps
- MAP compensation
- Two Auxiliary compensations
- Dwell Time 20 RPM x11 Battery
- Odd fire engine capability Each Top Dead Centre angle may be specified Resolution 0.5 degree

Trigger Sensors

- Directly compatible with most OEM trigger systems including :
    - HALL, Magnetic and Optical types
    - Multi Tooth (eg Mazda and Toyota)
    - 1 or 2 Missing Teeth (eg Porsche)
    - Many other special types, eg. Ford Narrow Tooth, Nissan Optical, Harley Davidson

Data Logging

- Optional Logging memory allows logging of all ECU parameters
- Memory Size 512 KByte

- Logging Rate 1~20 sets / sec
- Logging Time 38 minutes at 5 sets / sec (28 Parameters+Diags) PC Software is available for analysis of the logged data.

Air Fuel Ratio Sensor

- High accuracy Wide Band Air Fuel Ratio Sensor Input (Optional)
- Range 0.75 to 1.20 Lambda
- Resolution 0.01 Lambda

Other Sensors

- Throttle Position, Manifold Pressure, Engine Temp & Air Temp
- 2 Auxiliary Sensor inputs
- 2 Digital / Speed Inputs

Special Functions

- Traction Control & Launch Control (2 wheel speed sensors) (or 4 sensors using the MoTeC TC Mux)
- Gear Change Ignition Cut
- Wide Band or Narrow Band Air Fuel Ratio Control (3D mapped)
- Over Run Boost Enhancement
- Warning Alarms (Sensor HI / LO)
- Gear Detection Ground Speed Limiting
- Dual RPM Limit
- Nitrous Oxide Enrich / Retard
- Air Conditioner Request
- Over Run Fuel Cut
- Sensor Calibration Tables RPM Limit Hard or Soft Cut Fuel and / or Ignition Cut

Auxiliary Outputs

- Four general purpose outputs (3 shared with ignition outputs)
- The outputs may be used for :
    - Turbo Wastegate Control
    - Idle Speed Control
    - Fuel Used Pulse
    - Tacho Output
    - Shift Light (Gear Dependent)
    - Driver Warning Alarm
    - RPM / Load dependant device
    - User Defined Table (20x11) with definable axis parameters
    - Slip Warning
    - Fuel Pump Relay
    - Thermatic Fan
    - Air Conditioner Fan or Clutch

Diagnostics

- Injectors Open Circuit, Short Circuit, Peak Current Not Reached
- Sensors Open & Short circuit

- Operating Errors RPM Limit Exceeded, Injector Overduty, Over Boost, Low Battery, REF Error etc.

Operating Conditions

- Internal Temp Range -10~85°C
- Ambient Temp -10~70°C (Depending on load & ventilation)
- Operating Voltage 6~22V DC
- Operating Current 0.4 A max
- Reverse Battery External Fuse

Calibration

- PC Software is available for calibration

Telemetry Link

Optional Telemetry Link allows real time monitoring and data

E-2: ECU installation

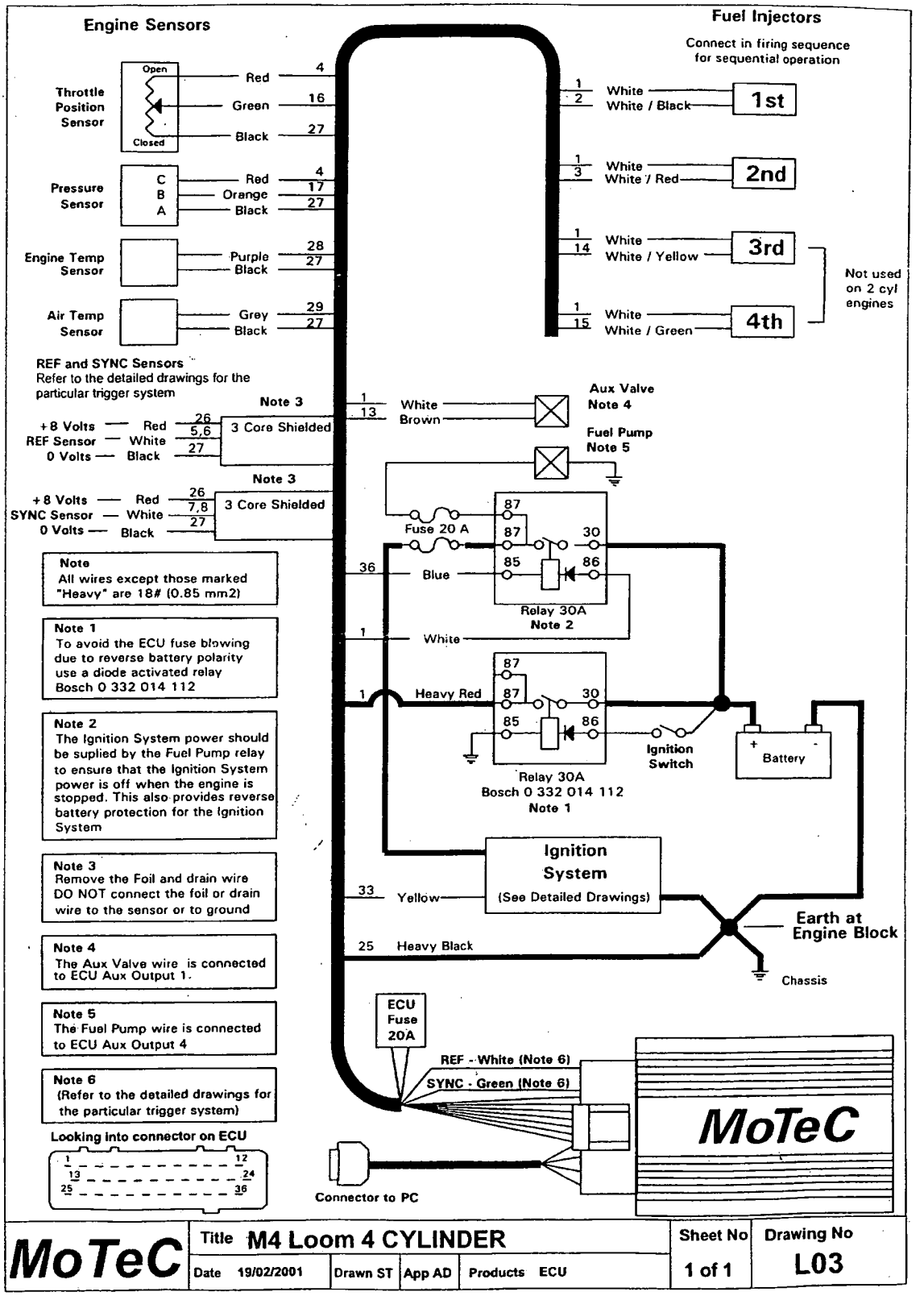

APPENDIX F MOTEC ADL SPECIFICATIONS

General

- Microprocessor: 32 Bit High Performance
- Manufacturing Quality standard to ISO9001
- Field updateable Operating System
- Non-volatile FLASH memory for data & operating system
- High RFI Immunity
- Rugged Aluminium Housing (IP-55, NEMA 4)
- 79 pin Autosport connector
- Operating Temperature: -10 to 70 DegC
- Operating Voltage: 7 to 22 VDC
- Operating Current: 0.3 A max.
- Weight: 385 gms (0.85 lbs)
- Size: 180mm x 91mm x 18mm (excluding connector)
- Reverse Battery and Transient Protection
- Warranty: 2 years Parts and Labour

Measurement Inputs

- 28 Analog Inputs (10 Standard):
  - 20 Analog Voltage (6 Standard)
  - 8 Analog Temperature (4 Standard)
  - 12 bit resolution, 0 to 15 VDC range
  - Update rate (Max. 8 channels): up to 1000 times/sec
  - Other inputs: up to 500 times/sec
- 4 Digital Inputs (2 Standard)
- 4 Speed Inputs (2 Standard)

  Digital & Speed
  - Switch to OV, logic signal, open collector (Hall Effect), or Magnetic
  - State & Counting (1MHz)
  - Period (1 micro sec)
  - Pulse width (1 micro sec)
- 4 Switch Inputs (4 Standard
- User definable sensor calibrations

Auxiliary Outputs

- 8 Digital Outputs (4 standard)
  - Open Collector (drives to ground) with pullup (10k ohms) to battery positive
  - On/Off or Pulse Width Modulation with variable Frequency and Duty Cycle

Air Fuel Ratio Measurement (Optional)

- 2 high accuracy Wideband Lambda (Air/Fuel ratio) inputs

- Resolution: 0.01 Lambda
- Temperature compensated
- Range: 0.75 to 1.2 Lambda

Data Logging

- Memory: 384k, 1MB, 2MB, 4MB, 8MB
- Non-volatile FLASH, field upgradeable
- Logging of any Analog, Digital, Serial, CAN bus or Calculated channel
- Maximum Logging throughput: 20k/sec
- 2 Burst Logging buffers with pre triggering (Large logging option only)
- Typical Unload Speed: 19 sec/MB, using parallel port of PC to CAN bus RS232 unload rates dependent on baud rate

Calculations

- Timers (0.01s, 0.1s, & 1s resolution)
- 2D and 3D Tables
- User conditions
- Math Functions: Differentiate, Integrate, Absolute, Min/Max
- Lap Time and Number
- Lap Gain/Loss
- Speed and Distance
- Gear Detection
- Fuel Prediction
- Tell-tales
- Running Min/Max

Display

- Custom LCD, High Contrast, High Temperature, Reflective
- Display any Analog, Digital, Serial, CAN bus channel or Calculated channel
- 3 Display Modes
- 70 Segment Bar graph:
    - Definable Range
    - Programmable Setpoint and Peak Hold point
- 4 Numeric Display Items
- 13 Digit Alpha Numeric Display area, 1,2 or 3 channels per line
- (20 scrollable lines per display mode)
- Alarm messages
- Channel display
- Descriptive text

Communication

- Serial RS232 Coms. (1200 to 115k baud)
- CAN data link (250Kbit to 1Mbit)
- Telemetry Link output (RS232)

Host Software

1. Dash Manager Software
2. Interpreter Analysis Software

3. Telemetry Software (Optional)

Computer Requirements

- IBM PC compatible running Windows 95/98 or NT4.0
- Pentium (Min.) 90MHz, 16MB RAM

APPENDIX G SENSOR SPECIFICATIONS

G-1 Throttle Position Sensor

8 Angular-position sensors BOSCH

Throttle-valve angular-position sensor

Measurement of angles up to 88°

φ / R

- Potentiometic angular-position sensor with linear characteristic curve.
- Sturdy construction for extreme loading.
- Very compact.

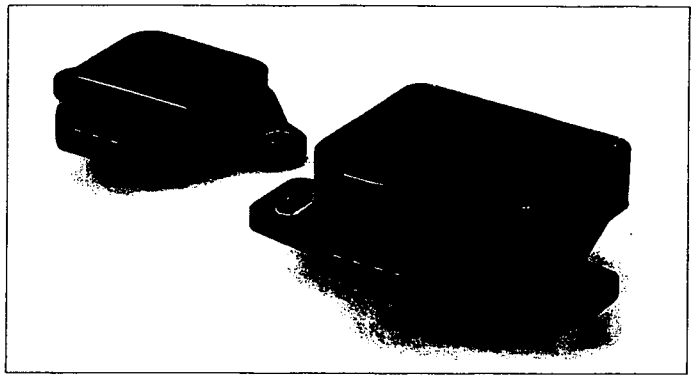

Application
These sensors are used in automotive applications for measuring the angle of rotation of the throttle valve. Since these sensors are directly attached to the throttle-valve housing at the end of the throttle-shaft extension, they are subject to extremely hostile underhood operating conditions. To remain fully operational, they must be resistant to fuels, oils, saline fog, and industrial climate.

Design and function
The throttle-valve angular-position sensor is a potentiometric sensor with a linear characteristic curve. In electronic fuel injection (EFI) engines it generates a voltage ratio which is proportional to the throttle valve's angle of rotation. The sensor's rotor is attached to the throttle-valve shaft, and when the throttle valve moves, the sensor's special wipers move over their resistance tracks so that the throttle's angular position is transformed into a voltage ratio. The throttle-valve angular-position sensor's are not provided with return springs.

Design
The position sensor 0 280 122 001 has one linear characteristic curve.
The position sensor 0 280 122 201 has two linear characteristic curves.
This permits particularly good resolution in the angular range 0°...23°.

Explanation of symbols
U_A Output voltage
U_V Supply voltage
φ Angle of rotation
U_{A2} Output voltage, characteristic curve 2
U_{A3} Output voltage, characteristic curve 3

Accessories for 0 280 122 001	
Connector	1 237 000 039

Accessories for 0 280 122 201	
Plug housing	1 284 485 118
Receptacles, 5 per pack, Qty. required: 4	1 284 477 121
Protective cap, 5 per pack, Qty. required: 1	1 280 703 023

Characteristic curve 1.
A Internal stop, L Positional tolerance of the wiper when fitted, N Nominal characteristic curve, T Tolerance limit,
φ_w Electrically usable angular range.

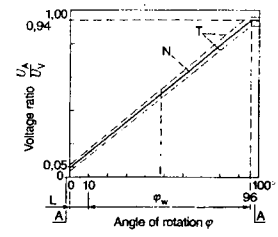

Characteristic curves 2 and 3.
A Internal stop,
φ_w Electrically usable angular range.

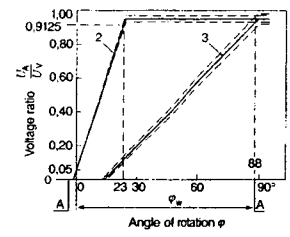

Technical data / Range

Part number		0 280 122 001	0 280 122 201
Diagram		1; 2	3
Useful electrical angular range	Degree	≤ 86	≤ 88
Useful mechanical angular range	Degree	≤ 86	≤ 92
Angle between the internal stops (must not be contacted when sensor installed)	Degree	≥ 95	–
Direction of rotation		Optional	Counterclockwise
Total resistance (Terms. 1–2)	kΩ	2 ±20 %	–
Wiper protective resistor (wiper in zero setting, Terms. 2–3)	Ω	710...1380	–
Operating voltage U_V	V	5	5
Electrical loading		Ohmic resistance	Ohmic resistance
Permissible wiper current	µA	≤ 18	≤ 20
Voltage ratio from stop to stop Chara. curve 1		$0.04 \le U_A/U_V \le 0.96$	–
Voltage ratio in area 0...88 °C Chara. curve 2		–	$0.05 \le U_{A2}/U_V \le 0.985$
Chara. curve 3		–	$0.05 \le U_{A3}/U_V \le 0.970$
Slope of the nominal characteristic curve	deg^{-1}	0.00927	–
Operating temperature	°C	–40...+130	–40...+85
Guide value for permissible vibration acceleration	$m \cdot s^{-2}$	≤ 700	≤ 300
Service life (operating cycles)	Mio	2	1.2

Dimension drawings.
A Plug-in connection,
B O-ring 14.65 x 2 mm,
C Fixing dimensions for throttle-valve housing, **D** Clockwise rotation [1]),
E Counterclockwise rotation [1]), **Ö** Direction of throttle-valve opening.
[1]) Throttle valve in idle setting.

F O-ring 16.5 x 2.5 mm, **G** 2 ribs, 2.5 mm thick,
H Plug-in connection, **I** Blade terminal,
K This mounting position is only permissible when the throttle-valve shaft is sealed against oil, gasoline, etc., **Ö** Direction of throttle-valve opening,
L Fixing dimensions for throttle-valve potentiometer.

0 280 122 001

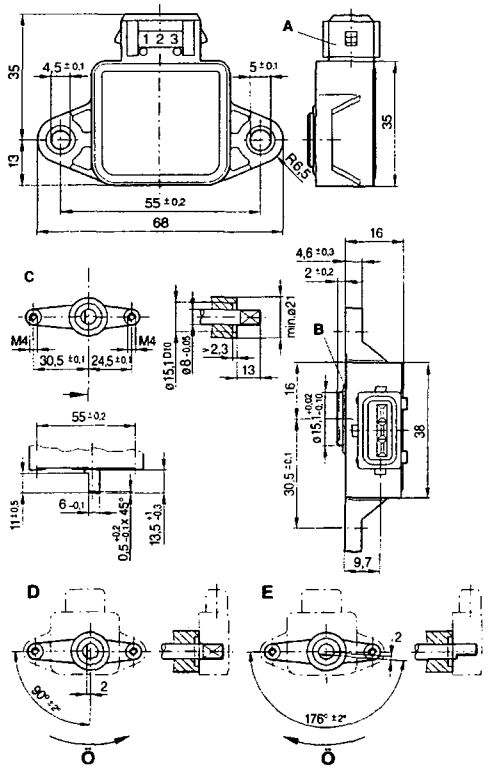

0 280 122 201

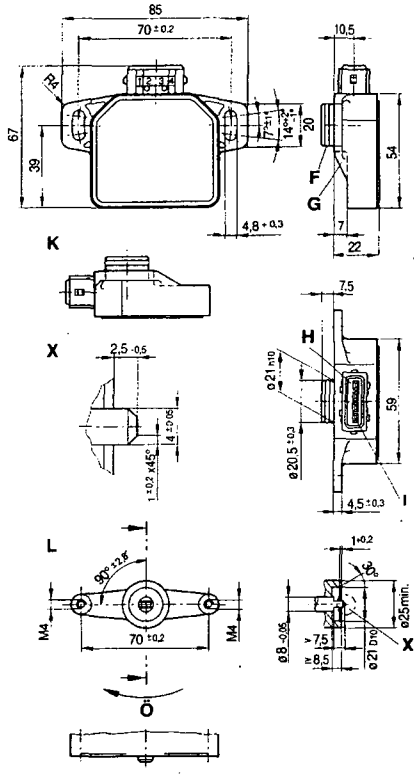

Diagram 1.

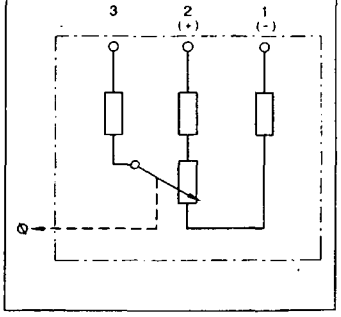

Diagram 2.

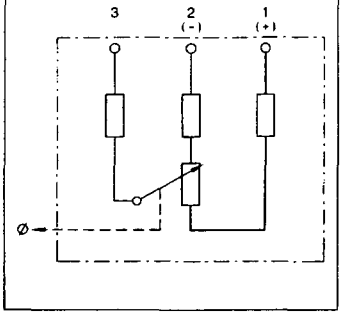

Diagram 3.
Throttle valve in idle setting.

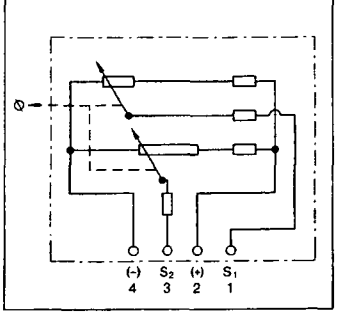

G-2 Manifold Pressure & Temperature Sensor

34 Pressure sensors BOSCH

Absolute-pressure sensors in micromechanical hybrid design

Measurement of pressures in gases up to 400 kPa

- High accuracy.
- EMC protection better than 100 V m^{-1}.
- Temperature-compensated.
- Version with additional integral temperature sensor.

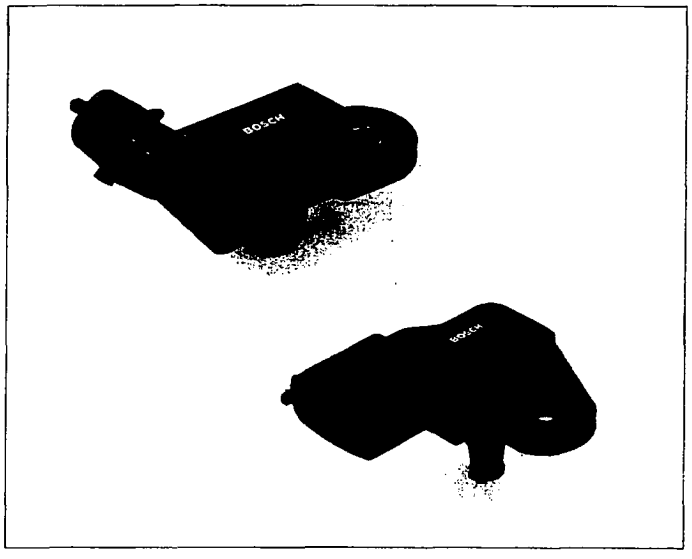

Applications
This sensor is used to measure the absolute intake-manifold pressure. On the version with integral temperature sensor, the temperature of the drawn-in air flow is also measured.

Design and function
The piezoresistive pressure-sensor element and suitable electronic circuitry for signal-amplification and temperature compensation are mounted on a silicon chip. The measured pressure is applied from above to the diaphragm's active surface. A reference vacuum is enclosed between the rear side and the glass base. Thanks to a special coating, both pressure sensor and temperature sensor are insensitive to the gases and liquids which are present in the intake manifold.

Installation information
The sensor is designed for mounting on a horizontal surface of the vehicle's intake manifold. The pressure fitting together with the temperature sensor extend into the manifold and are sealed-off to atmosphere by O-rings. By correct mounting in the vehicle (pressure-monitoring point on the top at the intake manifold, pressure fitting pointing downwards etc.) it is to be ensured that condensate does not collect in the pressure cell.

Range

Pressure range kPa (p_1...p_2)	Characteristic curve[1]	Features	Dimension drawing[2]	Order No.
10...115	1		1	**B 261 260 136**[3]
10...115	1		2	**0 261 230 052**
20...250	1		1	**0 281 002 487**
10...115	1	Integral temperature sensor	3	**0 261 230 030**
20...250	1	Integral temperature sensor	3	**0 261 230 042**
20...300	1	Integral temperature sensor	3	**0 281 002 437**
50...350	2	Integral temperature sensor	3	**0 281 002 456**
50...400	2	Integral temperature sensor	3	**B 261 260 508**[3]

[1] The characteristic-curve tolerance and the tolerance expansion factor apply for all versions, see Page 36
[2] See Page 37
[3] Provisional draft number, order number available upon enquiry. Available as from about the end of 2001

Accessories

Plug housing	Qty. required: 1[4]	**1 928 403 966**
Plug housing	Qty. required: 1[5]	**1 928 403 736**
Contact pin	Qty. required: 3 or 4[6]	**1 928 498 060**
Individual gasket	Qty. required: 3 or 4[6]	**1 928 300 599**

[4] Plug housing for sensors without integral temperature sensor
[5] Plug housing for sensors with integral temperature sensor
[6] Sensors without temperature sensor each need 3 contacts and gaskets. Sensors with integral temperature sensor each need 4 contacts and gaskets

Technical data

			min.	typ.	max.
Operating temperature	ϑ_B	°C	-40	–	+130
Supply voltage	U_V	V	4.5	5.0	5.5
Current consumption at U_V = 5 V	I_V	mA	6.0	9.0	12.5
Load current at output	I_L	mA	-1.0	–	0.5
Load resistance to U_V or ground	$R_{pull-up}$	kΩ	5	680	–
	$R_{pull-down}$	kΩ	10.0	100	–
Response time	$t_{10/90}$	ms	–	1.0	–
Voltage limitation at U_V = 5 V					
Lower limit	$U_{A\,min}$	V	0.25	0.3	0.35
Upper limit	$U_{A\,max}$	V	4.75	4.8	4.85
Limit data					
Supply voltage	$U_{V\,max}$	V	–	–	+16
Storage temperature	ϑ_L	°C	-40	–	+130
Temperature sensor					
Measuring range	ϑ_M	°C	-40	–	+130
Measured current	I_M	mA	–	–	1[1]
Nominal resistance at +20 °C		kΩ	–	2.5±5%	–
Thermal time constant	t_{63}	s	–	–	10[2]

[1]) Operation at 5 V with 1 kΩ series resistor
[2]) In air with a flow rate of 6 m · s^{-1}

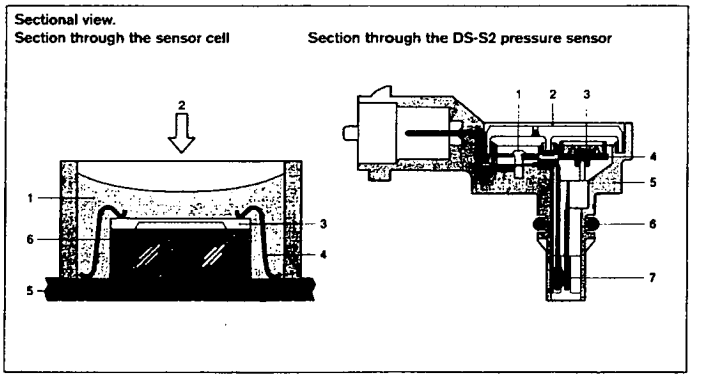

Section through the sensor cell.
1 Protective gel, **2** Pressure, **3** Sensor chip, **4** Bonded connection, **5** Ceramic substrate, **6** Glass base.

Section through the pressure sensor.
1 Bonded connection, **2** Cover, **3** Sensor chip, **4** Ceramic substrate, **5** Housing with pressure-sensor fitting, **6** Gasket, **7** NTC element.

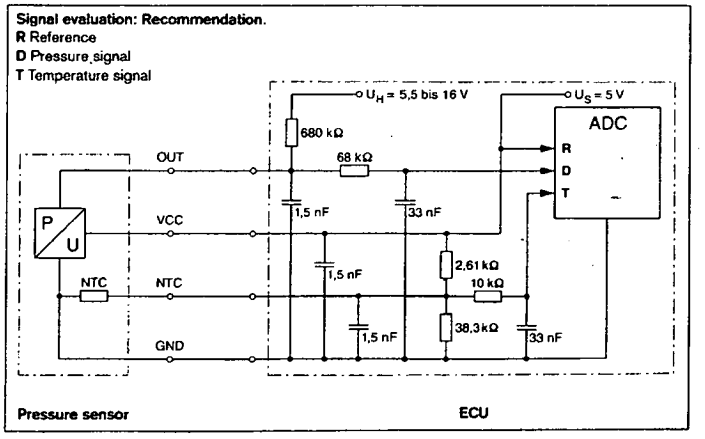

Signal evaluation: Recommendation.
The pressure sensor's electrical output is so designed that malfunctions caused by cable open-circuits or short circuits can be detected by a suitable circuit in the following electronic circuitry. The diagnosis areas situated outside the characteristic-curve limits are provided for fault diagnosis. The circuit diagram shows an example for detection of all malfunctions via signal outside the characteristic-curve limitation.

36 Pressure sensors BOSCH

Absolute-pressure sensors in micromechanical hybrid design (contd.)
Measurement of pressures in gases up to 400 kPa

Characteristic curve 1 (U_V = 5.0 V).

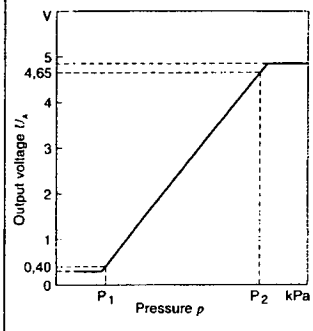

Characteristic curve (U_V = 5.0 V).

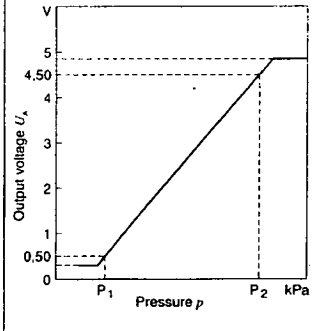

Characteristic-curve tolerance.

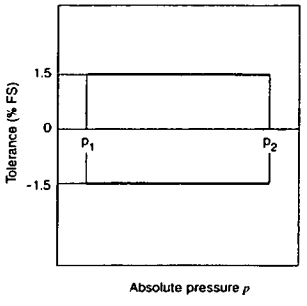

Tolerance-expansion factor.

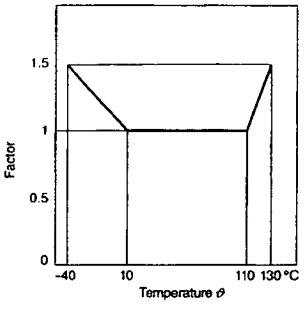

Temperature-sensor characteristic curve.

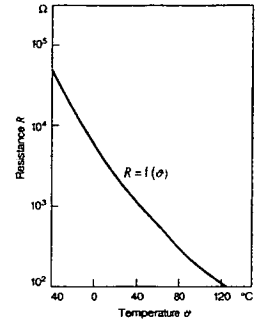

Explanation of symbols.
U_A Output voltage
U_V Supply voltage
k Tolerance multiplier
D After continuous operation
N As-new state

Dimensions drawings.

① Connector-pin assignment
Pin 1 +5 V
Pin 2 Ground
Pin 3 Output signal

② Connector-pin assignment
Pin 1 +5 V
Pin 2 Ground
Pin 3 Output signal

③ Connector-pin assignment
Pin 1 Ground
Pin 2 NTC resistor
Pin 3 +5 V
Pin 4 Output signal

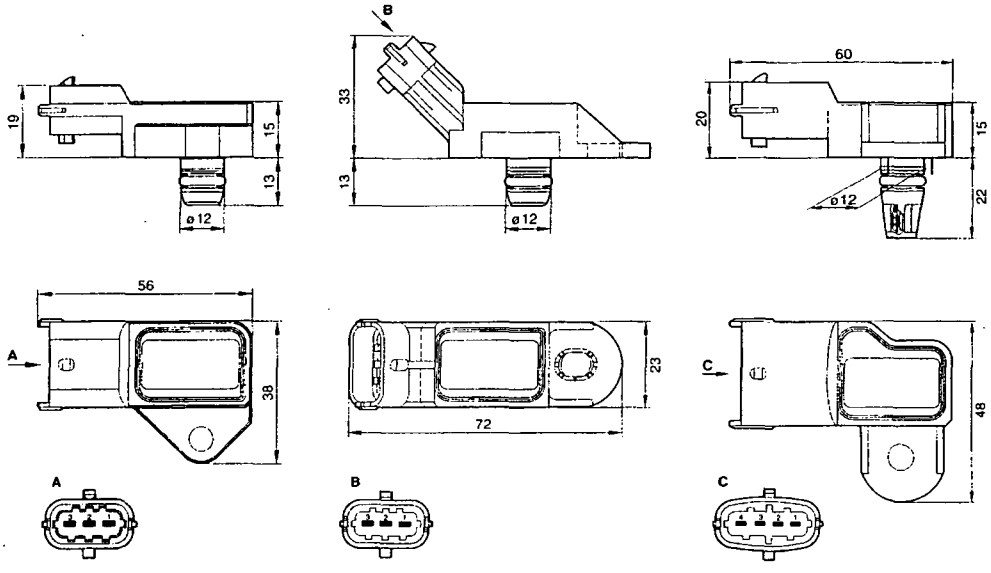

G-2 Manifold Temperature Sensor characteristic curve

3.2 Temperature sensor

Measurement of the resistance with measuring current ≤ 1 mA und after assimilation time ≥ 10 min at the temperatures -10, 20 and 80 °C.
Test limits according to the following table:

Temperature [°C]	Resistance [kΩ] min.	typ.	max.	Unit
-40 ± 1	39.18	48.55	57.92	kΩ
-30 ± 1	22.22	27.00	31.78	kΩ
-20 ± 1	13.24	15.67	18.10	kΩ
-10 ± 1	8.16	9.45	10.74	kΩ
0 ± 1	5.16	5.89	6.60	kΩ
10 ± 1	3.39	3.79	4.19	kΩ
20 ± 1	2.27	2.500	2.73	kΩ
30 ± 1	1.528	1.692	1.856	kΩ
40 ± 1	1.059	1.170	1.281	kΩ
50 ± 1	0.748	0.826	0.904	kΩ
60 ± 1	0.538	0.594	0.650	kΩ
70 ± 1	0.3917	0.4343	0.4769	kΩ
80 ± 1	0.2902	0.3224	0.3546	kΩ
90 ± 1	0.2171	0.2428	0.2685	kΩ
100 ± 1	0.1641	0.1852	0.2063	kΩ
110 ± 1	0.1254	0.1430	0.1606	kΩ
120 ± 1	0.0970	0.1116	0.1262	kΩ

G-3 Atmospheric Pressure Sensor

Absolute-pressure sensor for measuring atmospheric pressure

Measurement of temperatures from 60 kPa to 115 kPa

- SMD assembly.
- Low-profile micromechanics.
- Temperature-compensation.
- Integral signal amplification.

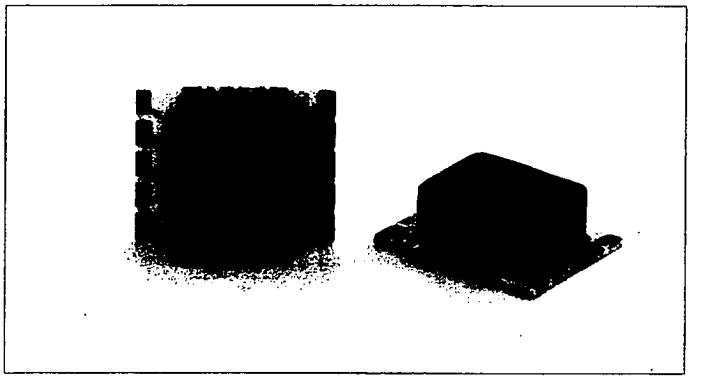

Design and function
This sensor comprises a temperature-compensated measuring element for determining the barometric absolute pressure. In this monolithic integrated silicon pressure sensor, the sensor element, and the respective evaluation circuitry with calibration elements are all united on a single silicon chip. The silicon chip is glued onto a hybrid substrate to facilitate automatic SMD assembly.

Explanation of symbols
U_V Supply voltage
U_A Output voltage (signal voltage)
k Temperature-error multiplier
ϑ Temperature
p_{abs} Absolute pressure
D Following endurance test
N Nominal status

Characteristic curves.

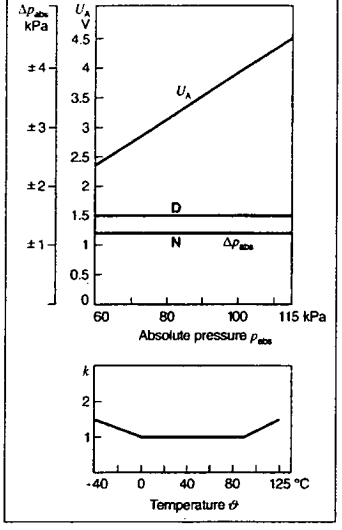

Block diagram.
E sensitivity, **O** Offset, **K** Compensation circuit, **S** Sensor bridge, **V** Amplifier.

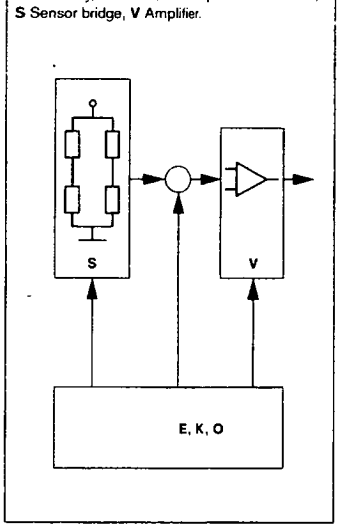

Technical data / Range

Part number			0 273 300 030		
			min.	typ.	max.
Pressure-measuring range	p_{abs}	kPa	60	–	115
Operating temperature range	ϑ_B	°C	–40	–	+125
Supply voltage	U_V	V	4.75	5.0	5.25
Supply current at U_V = 5 V	I_V	mA	6.0	9.0	12.5
Load current at output	I_L	mA	–1.0	–	0.5
Signal voltage	U_A	V	2.37	–	4.54
Voltage limitation at U_V = 5 V					
Lower limit	$U_{A\,min}$	V	0.25	0.3	0.35
Upper limit	$U_{A\,max}$	V	4.75	4.8	4.85
Response time	$t_{10/90}$	ms	–	–	1
Load capacity	C_L	nF	–	–	12
Signal evaluation: Recommendation					
Load resistance to U_V or ground	$R_{pull\text{-}up}$	kΩ	5	680	
	$R_{pull\text{-}down}$	kΩ	10.0	100	
Limit data					
Supply voltage, 1 min	$U_{V\,max}$	V	–	–	16
Pressure	p_{max}	kPa	–	–	160
Storage temperature	ϑ_L	°C	–40	–	130

Dimension drawings.
M Pin marking

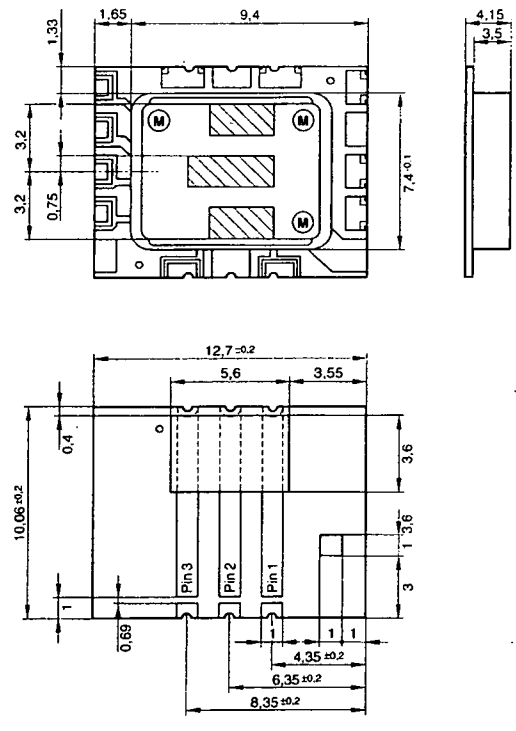

Connector-pin assignment
For operation, only the following pins are needed:
Pin 1 OUT output signal
Pin 2 GND (ground)
Pin 3 U_V supply voltage

G-4 Throttle Air Mass Flow & Temperature Sensor

56 Air-mass meters BOSCH

Hot-film air-mass meter, Type HFM 5

Measurement of air-mass throughflow up to 1000 kg/h

Q_m/U

- Compact design.
- Low weight.
- Rapid response.
- Low power input.
- Return-flow detection.

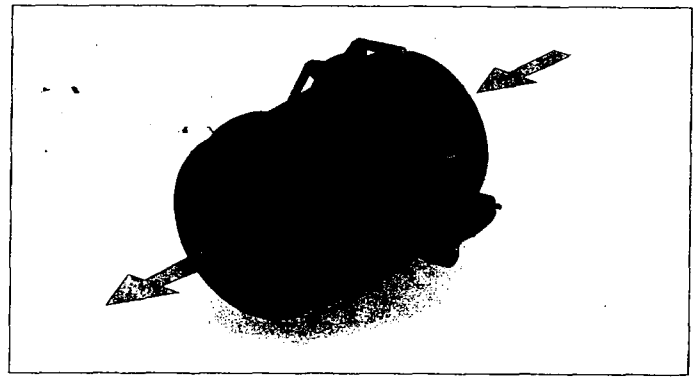

Application
In order to comply with the vehicle emission limits demanded by law, it is necessary to maintain a given air/fuel ratio exactly.
This requires sensors which precisely register the actual air-mass flow and output a corresponding electrical signal to the open and closed-loop control electronics.

Design
The micromechanical sensor element is located in the plug-in sensor's flow passage. This plug-in sensor is suitable for incorporating in the air filter or, using a measurement venturi, in the air-intake passages. There are different sizes of measurement venturi available depending upon the air throughflow. The micromechanical measuring system uses a hybrid circuit, and by evaluating the measuring data is able to detect when return flow takes place during air-flow pulsation.

Operating principle
The heated sensor element in the air-mass meter dissipates heat to the incoming air. The higher the air flow, the more heat is dissipated. The resulting temperature differential is a measure for the air mass flowing past the sensor.
An electronic hybrid circuit evaluates this measuring data so that the air-flow quantity can be measured precisely, and its direction of flow.
Only part of the air-mass flow is registered by the sensor element. The total air mass flowing through the measuring tube is determined by means of calibration, known as the characteristic-curve definition.

Technical data / range

Nominal supply voltage U_N	14 V
Supply-voltage range U_V	8...17 V
Output voltage U_A	0...5 V
Input current I_V	< 0.1 A
Permissible vibration acceleration	≤ 150 ms^{-2}
Time constant τ_{63} [1]	≤ 15 ms
Time constant τ_Δ [2]	≤ 30 ms
Temperature range	–40...+120 °C [3]

Part number	0 280 217 123	0 280 218 019	0 280 217 531	0 280 218 008	0 281 002 421
Measuring range Q_m	8...370 kg/h	10...480 kg/h	12...640 kg/h	12...850 kg/h	15...1000 kg/h
Accuracy [4]	≤ 3%	≤ 3%	≤ 3%	≤ 3%	≤ 3%
Fitting length L_E	22 mm	22 mm	22 mm	16 mm	22 mm
Fitting length L_A	20 mm	20 mm	20 mm	16 mm	20 mm
Installation length L	96 mm	96 mm	130 mm	100 mm	130 mm
Connection diam. D	60 mm	70 mm	80 mm	86/84 mm [6]	92 mm
Venturi ID	50 mm	62 mm	71 mm	78 mm	82 mm
Pressure drop at nominal air mass [5]	< 20 hPa	< 15 hPa	< 15 hPa	< 15 hPa	< 15 hPa
Temperature sensor	Yes	Yes	Yes	No	Yes
Version	1	2	3	4	5

[1] In case of sudden increase of the air-mass flow from 10 kg · h^{-1} auf 0,7 $Q_{m\,nominal}$, time required to reach 63% of the final value of the air-mass signal.
[2] Period of time in case of a throughflow jump of the air mass $|\Delta m/m| \leq 5\%$.
[3] For a short period up to +130 °C.
[4] $|\Delta Q_m/Q_m|$: The measurement deviation ΔQ_m from the exact value, referred to the measured value Q_m.
[5] Measured between input and output
[6] Inflow/outflow end

Accessories for connector

Plug housing	Contact pins	Individual gaskets	For conductor cross-section
1 928 403 836	**1 987 280 103**	**1 987 280 106**	0.5...1 mm²
	1 987 280 105	**1 987 280 107**	1.5...2.5 mm²

Note: Each 5-pole plug requires 1 plug housing, 5 contact pins, and 5 individual gaskets.
For automotive applications, original AMP crimping tools must be used.

Application
In internal-combustion engines, this sensor is used for measuring the air-mass flow so that the injected fuel quantity can be adapted to the presently required power, to the air pressure, and to the air temperature.

Explanation of symbols

Q_m	Air-mass flow rate
ΔQ_m	Absolute accuracy
$\Delta Q_m/Q_m$	Relative accuracy
τ_Δ	Time until measuring error is ≤ 5%
τ_{63}	Time until measured-value change 63%

Function diagram with connector-pin assignment.
1 Additional temperature sensor ϑ_u (not on version 4, Part number 0 280 218 008),
2 Supply voltage U_V, **3** Signal ground, **4** Reference voltage 5 V, **5** Measurement signal U_A.
ϑ Temperature-dependence of the resistor, R_H Heater resistor, U_K Constant voltage

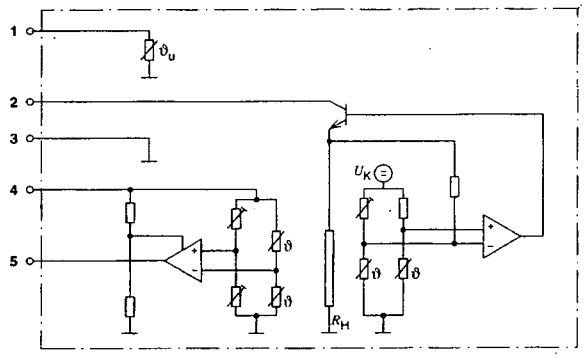

HFM 5 plug-in sensor design.
1 Measuring-passage cover, **2** Sensor,
3 Mounting plate, **4** Hybrid-circuit cover,
5 Hybrid, **6** Plug-in sensor, **7** O-ring,
8 Auxiliary temperature sensor.

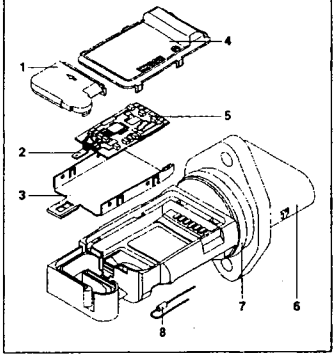

Output voltage $U_A = f(Q_m)$ of the air-mass meter

Part number	0 280 217 123	0 280 218 019	0 280 217 531	0 280 218 008	0 280 002 421
Characteristic curve	1	2	3	4	5
Q_m/kg/h	U_A/V	U_A/V	U_A/V	U_A/V	U_A/V
8	1.4837	1.2390	–	–	–
10	1.5819	1.3644	1.2695	–	–
15	1.7898	1.5241	1.4060	1.3395	1.2315
30	2.2739	1.8748	1.7100	1.6251	1.4758
60	2.8868	2.3710	2.1563	2.0109	1.8310
120	3.6255	2.9998	2.7522	2.5564	2.3074
250	4.4727	3.7494	3.5070	3.2655	2.9212
370	4.9406	4.1695	3.9393	3.6717	3.2874
480	–	4.4578	4.2349	3.9490	3.5461
640	–	–	4.5669	4.2600	3.8432
850	–	–	–	4.5727	4.1499
1000	–	–	–	–	4.3312

Air-mass meter output voltage.

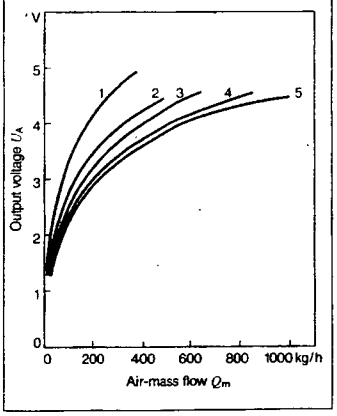

Temperature-dependence $R_\vartheta = f(\vartheta)$ of the temperature sensor

Temperature ϑ	°C	–40	–30	–20	–10	±0	10	20	30	40
Resistance R_ϑ	kΩ	39.26	22.96	13.85	8.609	5.499	3.604	2.420	1.662	1.166
Temperature ϑ	°C	50	60	70	80	90	100	110	120	130
Resistance R_ϑ	Ω	835	609	452	340	261	202	159	127	102

Temperature-resistance diagram of the temperature sensor.

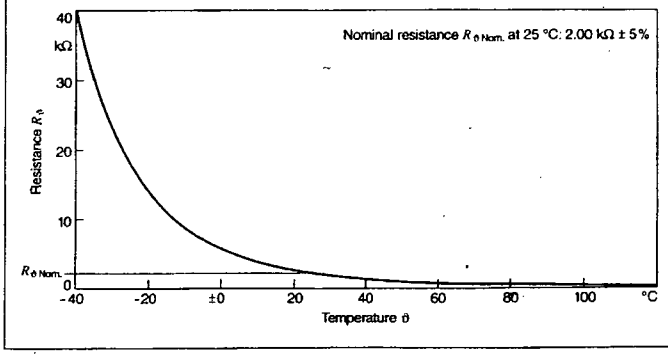

Dimensions overview of the HFM 5.
1 Plug-in sensor, **2** Throughflow direction,
3 Measurement venturi.

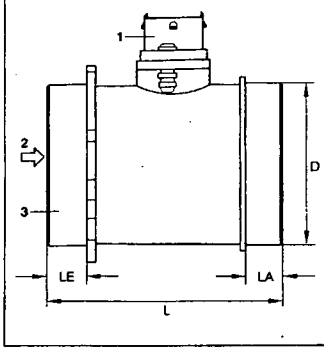

APPENDIX H DYNOMAX 450 4WD SPECIFICATION

DESCRIPTION & CAPACITY

- Maximum Power (per axle) 450 kW (600 HP)
- Maximum Power (combined) 900 kW (1200 HP)
- Power Resolution - 0.1 Kw
- Maximum Tractive Effort (per axle) - 11,000 (N) 2500 (lb)
- Maximum Tractive Effort (combined) - 22,000 (N) 5000 (lb)
- Maximum Roller Torque (per axle) - 1200 Nm (880 ft. lb)
- Maximum Roller Torque (combined) - 2400 Nm (1760 ft. lb)
- Force measurement - load Cell
- Maximum Speed - 200km/h
- Speed Accuracy - 0.3km/h
- Speed Sensing - Electronic
- Odometer Resolution - 0.1 Kilometre
- Dynamically Balanced - Retarders & Rollers
- Rollers - Knurled Drive Rollers (Square Cut)
- Roller Diameter: 218 mm
- Maximum Axle Weight - 4.5 Tonne
- Track Maximum - 2180 mm
- Track Minimum - 820 mm
- Wheelbase Ajustment - Hydraulic
- Maximum Wheel Base - 3300mm
- Minimum Wheel Base - 2100mm.
- Tie-Down Points - 8
- Bi-Directional - Yes
- Compensated Readings (Automatically) - Inlet Temp.
- Comp. Readings (Manually) - Humidity & Barometric.
- Graph Live to Screen - Yes

- (Optional) Control Cabinet - W900 x H1460 x D68O
- (Optional) Weight of Control Cabinet - 60kg
- Electrical Supply - AC 110/24OV 50/60HZ

FULL COLOUR COMPUTER DISPLAY

- High Quality Computer and Colour Monitor
- Colour lnkjet Printer

Main Screen Displays:

- Customer Details
- lnlet Air Temperature
- Test Details
- Distance Travelled
- Transmission Type
- Vehicle Details
- Dynamometer Status

Metric or Imperial Display of:

- Power
- Speed
- Tractive Effort

Large Bar Graphs and Digital Displays of:

- Power
- Tractive Effort
- Speed
- Front to Rear Load Balance

Graph Screen Display:

- Customer Details
- Test Details
- Vehicle Details

Graph Details:

- Speed x Power
- Speed x Tractive Effort
- Speed x Power & T. Effort
- 40 Preset Scales available
- Temporary Scales available, make your own scales to suit (Zoom In or Zoom Out)
- Live, see-as-you-go Graphing
- Full Auto Colour Graphs
- Multiple Graph
- Overlay/Comparison
- Recall - Overlay Previous Graphs

Computer Storage: of performance Graphs is automatically stored and may be displayed as:

- Speed x Tractive Effort
- Speed x Power
- Speed x Power & Tractive Effort

'Snapshot' of performance may be recorded displaying:

- Vehicle Repair History
- Speed
- Power
- Tractive Effort
- Inlet Air Temperature

COMMAND MODULE

- Lightweight Hand-held
- Use from within Vehicle

Displays:

- Desired Speed and Load
- Retarder Over Temp

Controls:

- Vehicle Speed
- Vehicle Load
- Wheelbase
- Screen Selection
- Snapshots
- Odometer Reset
- Roller Brake
- Balance Front to Rear
- Manual/ Auto load
- (Optional) Wheel Stabilisers
- Graph Acceleration Rate
- Graph Start
- Graph Finish

APPENDIX I NUMERICAL DIFFERENTIATION

(a) Differentiation using Difference Formulae

Differentiation $\Rightarrow$ slope of the curve at a point

Derivative at x_0	Difference Type
$\frac{dy}{dx} = \frac{y_1 - y_0}{h}$	Forward
$\frac{dy}{dx} = \frac{y_0 - y_{-1}}{h}$	Backward
$\frac{dy}{dx} = \frac{y_1 - y_{-1}}{2h}$	Central
$\frac{d^2y}{dx^2} = \frac{y_2 - 2y_1 + y_0}{h^2}$	Forward
$\frac{d^2y}{dx^2} = \frac{y_0 - 2y_{-1} + y_{-2}}{h^2}$	Backward
$\frac{d^2y}{dx^2} = \frac{y_1 - 2y_0 + y_{-1}}{h^2}$	Central

where h is the separation along the x axis